

Bioengineering functional organoid models across scales

Présentée le 26 avril 2024

Faculté des sciences de la vie
Unité du Prof. Lutolf
Programme doctoral en biotechnologie et génie biologique

pour l'obtention du grade de Docteur ès Sciences

par

Tania HÜBSCHER

Acceptée sur proposition du jury

Prof. D. M. Suter, président du jury
Prof. M. Lütolf, directeur de thèse
Prof. M. van den Brink, rapporteur
Dr J. Cowan, rapporteuse
Prof. L. Tang, rapporteur

“What we know is a drop, what we do not know is an ocean.”

Isaac Newton

Summary

The last two decades have seen the development of organoid models for many different tissues and organs. Organoids are three-dimensional organ-mimetics derived from stem or progenitor cells comprising various specialized cell types, resembling the architecture of their native organ on a smaller scale, and recapitulating some of its functions. They completely changed the cell culture world, offering highly interesting insights into basic research and beginning to demonstrate their potential for clinical applications. Despite all this, organoid growth relies on poorly controllable stem cell self-organization, which limits their reproducibility and size. Moreover, organoids often mimic only one compartment (e.g. the epithelium) of their native counterparts, and for some organs organoid models do not yet exist.

In this thesis, I introduce several bioengineering approaches to help overcome some of these limitations and obtain more robust and functional organoid models. Such engineering approaches were applied at different biological scales.

In chapter I, we induced for the first time the formation pathophysiologically relevant tumors in vitro in a highly observable setting based on cell responsiveness to light. With an optogenetic system driving Cre recombinase expression, we controlled the induction of cancer driver mutations in space and time in *Apc^{fl/fl};Kras^{LSL-G12D/+};Trp53^{fl/fl}* (AKP) colon organoids. A colon organoid-on-a-chip platform was then used to obtain a defined topology compatible with long-term studies and imaging. These bioengineering approaches provided us with insights into tumor initiation and development processes that would not have been possible with conventional cancer models.

In chapter II, I developed a new functional organoid model by applying knowledge gained from other organoids to the thymus, and, in particular, to thymic epithelial cells. The organoids were characterized in detail to show that the newly established culture conditions have the potential to preserve the functional ability of thymic epithelial cells to mediate thymopoiesis. I have demonstrated this by reaggregating thymic epithelial cells cultured as organoids with T cell progenitors and showing that T cell development in these reagggregates recapitulates to a large extent the process that occurs in the native thymus. In addition, when transplanted into mice, the reagggregates were capable of attracting new T cell progenitors, thus reproducing another important feature of the thymus in vivo. In general, this part aimed to bring the fields of organoid and immunology closer together.

In chapter III, we used bioprinting as a bioengineering strategy to create larger organoid constructs with a shape and cell type composition resembling their native organ. Specifically, centimeter-scale tissue constructs were printed that assembled different parts of the gastrointestinal tract in one functional epithelial tube. This chapter illustrates the possibility of

harnessing the native properties of cells, such as their self-organization capability, and of leveraging bioengineering approaches to extrinsically guide them.

Taken together, this thesis demonstrates the potential of combining different fields, such as biology and engineering, to advance basic research. It is hoped that the knowledge gained can be applied to human organoids in the future to develop new functional models for translational applications.

Keywords:

Organoids, Bioengineering, Stem cells, Organoid-on-a-chip, Colon, Cancer, Optogenetics, Immunology, Thymus, Thymic epithelial cells, T cells, Bioprinting, Self-organization, Macroscale, Multicellular

Résumé

Les deux dernières décennies ont vu l'arrivée des organoïdes pour modéliser différents tissus et organes. Les organoïdes sont des structures tridimensionnelles formées à partir de cellules souches ou progénitrices. Ils comprennent différents types de cellules, ressemblent en certains aspects à l'organe à partir duquel ils ont été dérivés et récapitulent même une partie de ses fonctions. Le monde de la culture cellulaire a été transformé par le développement des organoïdes. Ils ont amené un éclairage nouveau sur beaucoup de domaines de recherche fondamentale et commencent à montrer leur potentiel pour les applications cliniques. Malgré tout, le fait que la croissance des organoïdes soit basée sur la capacité des cellules souches à s'autoorganiser limite leur taille et leur reproductibilité. De plus, les organoïdes ne comprennent souvent qu'une partie des cellules d'un organe, par exemple l'épithélium. Et pour certains organes, il n'y a pas encore d'organoïdes qui ont pu être développés.

Dans cette thèse, je propose des approches de bioingénierie pour aider à surmonter certaines des limitations mentionnées ci-dessus et obtenir des organoïdes servant de modèles plus robustes et fonctionnels. Ces approches peuvent être appliquées à différentes échelles biologiques.

Au chapitre I, nous avons induit pour la première fois la formation des tumeurs reproduisant certaines caractéristiques physiopathologiques essentielles *in vitro*. Plus spécifiquement, nous avons modifiés les cellules pour qu'elles puissent répondre à des stimuli lumineux. Nous nous sommes basés sur un système optogénétique pour contrôler l'expression de la recombinaise Cre et ainsi l'induction de mutations cancéreuses pilotes (*Apc^{fl/fl};Kras^{LSL-G12D/+};Trp53^{fl/f}* ou AKP) dans le temps et l'espace dans des organoïdes de côlon. Nous avons aussi utilisé un modèle d'organe sur puce pour obtenir une topologie compatible avec l'imagerie et les études à long terme. Ensemble, ces approches de bioingénierie nous ont amené des connaissances nouvelles sur les processus d'initiation et de développement des tumeurs qui n'auraient pas pu être obtenues avec les modèles traditionnels.

Au chapitre II, en appliquant au thymus les connaissances acquises pour d'autres organes, j'ai généré un nouveau type d'organoïde fonctionnel avec les cellules épithéliales de thymus. J'ai caractérisé en détails ces organoïdes et démontré le potentiel des conditions de culture nouvellement établies à maintenir la fonctionnalité des cellules épithéliales de thymus, c'est-à-dire leur capacité à éduquer les lymphocytes T. J'ai aussi prouvé ceci en réagrégeant des cellules épithéliales de thymus cultivées sous forme d'organoïdes avec des cellules progénitrices de lymphocytes T. Par cette approche, j'ai pu démontrer que le développement et la maturation des lymphocytes T médiés par les cellules épithéliales de thymus *in vitro* ressemblaient à ce qu'il se passe dans le thymus *in vivo*. De plus, en transplantant ces

agrégats dans des souris, j'ai pu observer leur capacité à attirer de nouveaux progéniteurs de lymphocytes T, une autre caractéristique importante du thymus. De manière générale, cette partie avait pour but de rapprocher les domaines de l'immunologie et des organoïdes.

Au chapitre III, nous avons tiré parti de la bioimpression comme stratégie de bioingénierie pour générer des structures d'organoïdes plus grandes. Ces dernières présentaient des caractéristiques macroscopiques ressemblant aux organes à partir desquels les organoïdes avaient été dérivés et comprenaient plusieurs types de cellules. De manière plus spécifique, nous avons imprimés des structures tissulaires à l'échelle du centimètre, avons été capable de combiner différentes parties du tractus gastrointestinal en un tube, et avons démontré la fonctionnalité des tissus imprimés en testant leur réponse à divers stimuli. Ce chapitre a illustré la possibilité d'exploiter les propriétés des cellules, comme leur capacité à s'autoorganiser, et à les guider avec des techniques de bioingénierie.

Dans son ensemble, cette thèse démontre le potentiel de combiner différents domaines, comme la biologie et l'ingénierie, pour faire avancer la recherche fondamentale. Dans le futur, nous avons espoir que les connaissances acquises pourront être appliquées aux organoïdes humains et aider à générer de nouveaux modèles fonctionnels pour des applications cliniques.

Mots-clés:

Organoïdes, Bioingénierie, Cellules souches, Organoïdes sur puce, Colon, Cancer, Optogénétique, Immunologie, Thymus, Cellules épithélial du thymus, Lymphocytes T, Bioimpression, Autoorganisation, Echelle macroscopique, Multicellulaire

Zusammenfassung

Die letzten zwei Jahrzehnte erbrachten die Entwicklung von Organoidmodellen von vielen verschiedenen Geweben und Organen. Organoide sind aus Stamm- oder Vorläuferzellen gewonnene dreidimensionale Strukturen. Diese enthalten verschiedene Zelltypen, ähneln der Architektur von ihrem ursprünglichen Organ in kleinerem Massstab und rekapitulieren sogar einige seiner Funktionen. Diese Organoide haben die Welt der Zellkulturen weitgehend verändert, äusserst interessante Erkenntnisse in der Grundlagenforschung gebracht und ihr Potenzial für klinische Anwendungen aufgezeigt. Nichtsdestotrotz, beruht das Wachstum der Organoide auf dem Prinzip der Stammzellselbstorganisation, was sowohl ihre Reproduzierbarkeit als auch ihre Grösse einschränkt. Zudem verfügen Organoide vielfach über Zellen von nur einem Kompartiment (z.B. Epithelialzellen) und für einige Organe konnten noch gar keine echten Organoide entwickelt werden.

In der vorliegenden Thesis bringe ich Ansätze von dem Bioingenieurwesen ein, um einige dieser erwähnten Einschränkungen zu überwinden und robustere funktionelle Organoidmodelle zu erhalten. Solche ingenieurwissenschaftlichen Ansätze wurden auf verschiedenen biologischen Ebenen angewandt.

In Kapitel I haben wir zum ersten Mal pathophysiologisch relevante Tumore in vitro in einer beobachtbaren Umgebung induzieren können, basierend auf der Kapazität der Zellen auf Lichtstimulus zu reagieren. Dank einem optogenetischen System, welches die Expression von der Cre-Rekombinase anregt, kontrollierten wir die Induktion der Krebstreiber Mutationen in *Apc^{fl/fl};Kras^{LSL-G12D/+};Trp53^{fl/f}* (AKP) Kolonorganoide zeitlich und räumlich. Wir nutzten zudem eine Kolon-on-a-Chip Plattform, um einerseits Organoide mit einer definierten Topologie zu erhalten und um andererseits Langzeitstudien zu ermöglichen, welche mit Mikroskopietechniken kompatibel sind. Diese Ansätze des Bioingenieurwesens ermöglichten uns Einblicke in die Tumorentstehung und -entwicklung, die mit herkömmlichen Modellen nicht möglich gewesen wären.

In Kapitel II habe ich ein neues funktionelles Organoidmodell entwickelt, indem ich die aus anderen Organoiden gewonnenen Erkenntnisse auf den Thymus und insbesondere auf Thymusepithelialzellen angewandt habe. Ich habe die neu geschaffenen Organoide ausführlich charakterisiert und gezeigt, dass die Kulturbedingungen das Potenzial haben, die funktionelle Fähigkeiten der Thymusepithelialzellen zur Regulierung der Thymopoese in vitro zu erhalten. Ich habe dies durch die Reaggregation von den Thymusepithelialzellen von den kultivierten Organoiden mit T-Zell-Vorläufern bewiesen und gezeigt, dass die T-Zell-Entwicklung in diesen Reaggregaten den natürlichen Prozess, der im Thymus stattfindet, weitgehend imitiert. Darüber hinaus konnten die Reaggregate bei der Transplantation in

Mäuse neue T-Zell-Vorläufer anziehen und damit ein weiteres bedeutendes Merkmal des Thymus reproduzieren. Im Allgemeinen zielte dieser Teil der Arbeit darauf ab, die Bereiche Organoid und Immunologie einander näher zu bringen.

In Kapitel III setzen wir das «Bioprinting» (Biodruckerei) als Strategie des Bioingenieurwesens ein, um grössere Organoidkonstrukte mit einer makroskopisch relevanten Form sowie einer gewissen Zelltypdiversität zu erzeugen. Insbesondere haben wir zentimetergrosse Gewebekonstrukte gedruckt und konnten verschiedene Teile des Magen-Darm-Trakts in einer einzigen Röhre zusammenfügen. Wir haben die Funktionalität dieser gedruckten Gewebe demonstrieren können, indem wir ihre Reaktion auf verschiedene Stimuli getestet haben. Dieses Kapitel veranschaulicht die Möglichkeiten der Nutzung von den natürlichen Eigenschaften von Zellen, wie z.B. ihre Fähigkeit zur Selbstorganisation, in Kombination mit der Regulierung durch Ansätze des Bioingenieurwesens.

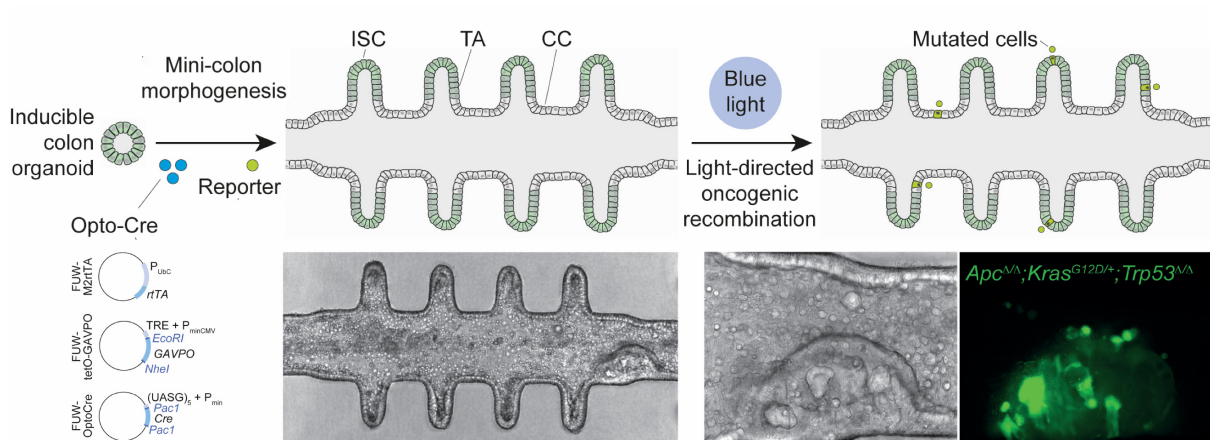
Insgesamt demonstriert diese Arbeit das Potenzial der Kombination von verschiedenen Bereichen wie die Biologie und das Ingenieurwesen, um die Grundlagenforschung voranzutreiben. Es bleibt zu hoffen, dass die gewonnenen Erkenntnisse in Zukunft auf menschliche Organoid übertragen werden können, um neue, funktionale Modelle für klinische Anwendungen zu entwickeln.

Schlüsselwörter:

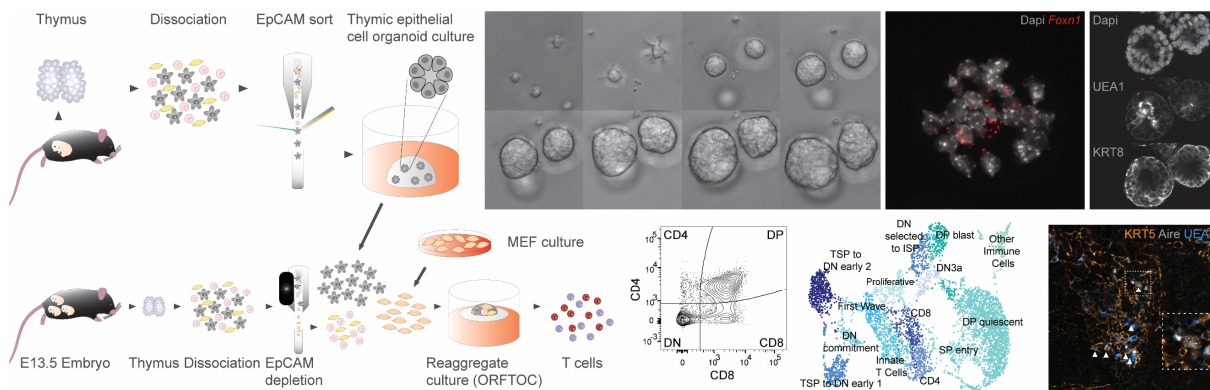
Organoid, Bioingenieurwesen, Stammzellen, Organoid-on-a-Chip, Kolon, Krebs, Optogenetik, Immunologie, Thymus, Thymusepithelzellen, T-Zellen, Bioprinting, Selbstorganisation.

Graphical summary

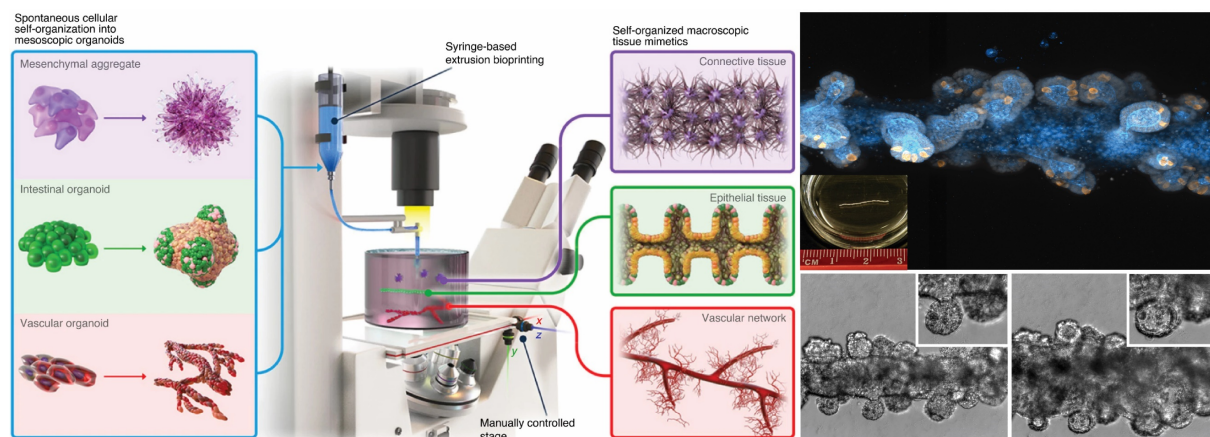
Chapter I



Chapter II



Chapter III



Contents

Summary	5
Résumé	7
Zusammenfassung	9
Graphical summary	11
Introduction.....	17
Chapter I – Optogenetic control over oncogenic mutations at the cellular level for studying tumor initiation and growth in a colon organoid-on-a-chip model	43
Abstract.....	46
Article.....	47
References	62
Acknowledgements.....	64
Author contributions.....	64
Extended data figures and supplementary videos.....	65
Methods.....	75
Chapter II – Development of a new type of organoids, thymic epithelial organoids, with preserved thymopoietic functionality ex vivo	87
Abstract.....	90
Article.....	91
References	102
Acknowledgements.....	107
Author contributions.....	107
Supplementary Materials	108
Materials and Methods	113
Chapter III - Bioprinting approach for guiding organoid self-organization for the generation of macroscale (multi)tissue constructs	125
Abstract.....	128
Article.....	129
References	143

Acknowledgements.....	145
Author contributions.....	145
Extended data figures and supplementary videos.....	146
Methods.....	158
Conclusion.....	171
Acknowledgements.....	183
Curriculum Vitae.....	187

Introduction

General introduction and objectives

The appearance of the term “stem cell” can be found already in the work of Ernst Haeckel in 1868¹. However, the pivotal discovery of stem cells properties is then consensually dated back to the 1960's, when Ernest McCulloch and James Till demonstrated that a population of hematopoietic cells could proliferate and form colonies upon transplantation into heavily irradiated mice². Stem cells are thus defined as cells that can proliferate (self-renew) and give rise to specialized progeny (differentiate)¹. Hematopoietic stem cells are an example of tissue-resident (or adult) stem cells. In 1981, Martin Evans and Matt Kauffman identified and cultured another type of stem cell, namely embryonic stem cells (ESCs) that they isolated from mouse blastocysts³. The list of stem cell types was completed in 2006, when Kazutoshi Takahashi and Shinya Yamanaka reprogrammed fibroblasts into so-called induced pluripotent stem cells (iPSCs)⁴. These three stem cell types differ not only in their origin, but also in their potency. Tissue-resident stem cells have the potential to give rise to multiple cell types, but within a specific lineage (e.g. hematopoietic cells), while ESCs and iPSCs are pluripotent and can give rise to all the cell types in the body.

Since the identification of stem cells, a lot of work has been undertaken to understand and recapitulate the environment allowing them to maintain their properties⁵. For ESCs and iPSCs, the main challenge consists in controlling their proper differentiation into the desired cell types. On the contrary, tissue-resident stem cells have the tendency to differentiate in culture, and identifying conditions maintaining their self-renewal capability remains an important goal today. In the body, tissue-resident stem cells reside in so-called niches, which provide biophysical and biochemical signals preserving their fate⁵. In 1975, James Rheinwald and Howard Green achieved for the first time the long-term culture of untransformed human cells, more specifically keratinocytes, by using fibroblasts as feeder layer. These cultures were organized in a way reminiscent of the native epidermis, with dividing cell types in the lower layer, and more differentiated cells in the superficial layers⁶. This work highlights the importance of supportive cell signals for stem cell maintenance and differentiation. A substantial part of the niche signals is also provided by the extracellular matrix (ECM), a complex assembly of proteins forming the scaffold supporting tissue organization *in vivo*⁷. Interestingly, a better understanding of the importance of the ECM was one of the key events leading from traditional two-dimensional (2D) to tridimensional (3D) cultures⁸.

While 2D cultures use plastic or glass plates to grow cells, 3D cultures involve either reaggregation techniques or a matrix such as scaffolds or hydrogels, which are often based on ECM proteins. Compared to standard 2D cultures, 3D cultures more closely recapitulate tissue properties such as stiffness and allow the formation of physiologically relevant multicellular structures⁹. The advent of 3D culture methods played a key role in the

development of organoids, which are defined as stem or progenitor cell-derived 3D structures that, on much smaller scales, recreate important aspects of the 3D anatomy and multicellular repertoire of their physiological counterparts and can recapitulate basic tissue-level functions⁸. Although mammary gland epithelium¹⁰ cultured in Matrigel, an ECM-based hydrogel, might be considered the first organoid, the field underwent drastic development building on the work of Hans Clevers and Yoshiki Sasai⁸ laboratories in the early 2000. Since then, organoids enable the modeling of many organs including optic cup and retina, brain (different cerebral structures), esophagus, stomach, intestine, colon, liver, pancreas, upper airways and lung, thyroid, prostate, kidney, mammary gland, heart, ear and skin (reviewed in ^{8,11,12}).

These new models offer great opportunities for both fundamental and translational research. For instance, organoids allow to study the processes by which cells self-organize and develop into multicellular structures¹³. They also serve as intermediate between very simple and high-throughput yet less physiologically relevant 2D cultures, and complex but relatively low-throughput animal models¹⁴. Since animal models can only recapitulate human physiology to a certain level, organoids derived from human cells present an interesting complementary axis for clinical trials. Not only can organoids be derived from human cells, but this can also be done in a patient-specific setting, opening many possibilities for personalized treatments. For instance, a screening on organoids was recently used to guide therapeutic decision on a patient with a rare cystic fibrosis-causing mutation¹⁵. Another focus area of today's research is cancer, and a link between organoid drug sensitivity and patient treatment response starts to be established¹⁶.

Despite the aforementioned great promises, organoids still present several limitations. Their self-organization properties can also be a disadvantage as they lead to high heterogeneity in terms of shape, size, and cell type composition¹⁷. Furthermore, most organoids only mimic one compartment of their native organ (e.g. the epithelium) and lack supportive stromal cells such as fibroblasts or vasculature, as well as immune cells, which can all be of crucial importance to organ development and function. Among other factors, the lack of vasculature and the fact that they rely on self-organization for their development (and therefore might lack critical external factors) limit the size of organoids to the millimeter scale as well as their full maturation⁹. In addition, all organoid models are not at the same stage of development; while for some organs, culture conditions are well-established and permit an accurate recapitulation of the *in vivo* counterpart, for some others, organoids only start to be established or do not even exist yet.

Overcoming these limitations and developing new, more robust and functional organoid models will provide us with more insights into complex biological processes and be transformative for the fields of tissue engineering and regenerative medicine⁹.

In this work, I aimed at addressing some of the aforementioned limitations by leveraging bioengineering approaches (Figure 1) to develop functional organoid models across different biological scales.

Aim 1: To control oncogenic mutations at the cellular level through optogenetics for studying tumor initiation and growth in a colon organoid-on-a-chip model

Organoids of the gastrointestinal tract are the canonical example of tissue-resident stem cell-derived organoids¹⁸. Their already well-established culture conditions permit the application of bioengineering approaches to obtain a tighter control over the organoid formation processes¹⁷. One such example is use of organ-on-chip technologies, leading to the generation of “organoid-on-a-chip^{19,20}”.

Here, we aimed at going one step further and engineering at the (single) cell level the response of organoid-on-a-chip to certain stimuli. We took advantage of the inducible *Apc^{fl/fl};Kras^{LSL-G12D/+};Trp53^{fl/f}* (AKP) colon organoids and developed a doxycycline-sensitive blue-light-regulated Cre system^{21,22} and Hübscher, Neumayer, Wernig 2017, unpublished to direct their recombination. The spatiotemporal control over the induction of oncogenic mutations obtained with this system allowed us to recapitulate the process of tumor initiation. We were then able to study tumor formation and growth in an unprecedented way, thanks to the possibility for live imaging and long-term culture provided by the colon-on-a-chip.

Aim 2: To develop a new type of organoids, thymic epithelial organoids, with preserved thymopoietic functionality ex vivo

For some organs, the mere development of organoids remains challenging. This is in particular true for immune system-related organs, despite their great importance for protecting us against diseases. Indeed, organoids are mostly derived from one single cell type, and lymphoid organs often rely on complicated interactions between immune and stromal cells for their development and function²³, rendering their modelling challenging.

Here, taking the thymus as example, I aimed at generating a new type of organoids. The endodermal origin of thymic epithelial cells²⁴, similar to the intestine, made them an excellent candidate for the development of functional organoids from one of the few remaining organs for which bona fide organoids do not yet exist. The thymus (and thymic epithelial cells) main function is to educate T cells to provide effective immune defenses against pathogens, immune surveillance of tumors, and also immune tolerance to self. Thus, I proved the functionality of thymic epithelial cells cultured as organoids by reaggregating them with T cell progenitors. I

then compared T cells that matured in vitro with T cells from the native thymus and show their resemblance. Finally, I transplanted the reaggregates in mice and demonstrated their ability to recruit new T cell progenitors, thereby recapitulating another important function of the native thymus.

Aim 3: To leverage bioprinting for guiding organoid self-organization for the generation of macroscale (multi)tissue constructs

Although some organoids already offer promising translational opportunities, they remain very small, round, and mostly only mimic one compartment of their native organ.

Here, we aimed at generating larger tissue constructs with a macroscopic shape resembling the native organ and integrating multiple cell types. We did that by exploring the possibility to guide organoid self-organization using a novel and easily applicable bioprinting setup based on a microscope with a motorized stage. We showed the potential of the approach mostly with gastrointestinal tract organoids. For example, we combined stomach and intestine or intestine and colon in one printed construct, and also demonstrated the functionality of the printed tubes by testing their response to different stimuli.

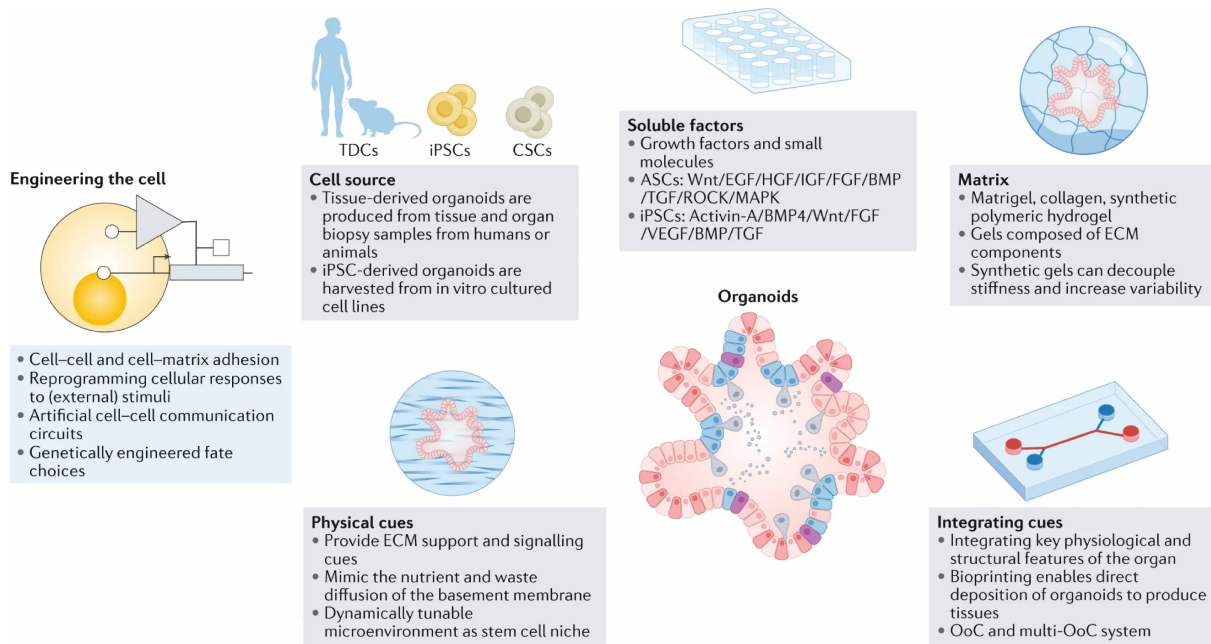


Figure 1 Engineering organoids. Bioengineering approaches can be applied at different levels. First, the initial cell source to derive organoids should be chosen. The cells themselves can be genetically engineered to respond to specific stimuli. The medium (including soluble factors) and matrix can be tuned to match the in vivo tissue, allow organoid development and mimic either physiological or pathological conditions. Integrating organoids with more complex methods including microfluidic chips and bioprinting permit a tighter control over organoid development, the formation of larger tissue constructs and longer-term culture. Modified from ^{11,12}.

Aim-specific background

For aim 1: To control oncogenic mutations at the cellular level through optogenetics for studying tumor initiation and growth in a colon organoid-on-a-chip model

Intestinal organoids were the first example of tissue-resident stem cell-derived organoids. Their establishment was possible thanks to the understanding of the anatomy and physiology of the intestine and to the identification of intestinal stem cells^{25–27}. The intestine is organized into crypt and villus structures, with stem cells located at the bottom of the crypts and more differentiated cell types towards the top of the villi. Crypts form a niche environment where stem cells are maintained thanks to different signals such as Wnt (or the Wnt agonist R-spondins), Epidermal growth factor (EGF) and bone morphogenic protein (BMP) inhibition by Noggin. Isolated crypts could be grown in medium containing these supplements when plated in Matrigel, which mimics the extracellular matrix. Remarkably, single Lgr5-positive stem cells could also be grown in the same culture conditions and formed small organoids with different cell types organized in a way that resembles the native intestine. Similar culture conditions were adopted to generate organoids from other parts of the gastrointestinal tract. Regarding the colon, the main differences are the absence of villus structures in vivo and a higher requirement for Wnt in the culture medium²⁸.

The relatively good understanding of mouse intestinal organoid culture requirements allowed the application of bioengineering approaches to decrease organoid variability, to have access to the apical side and to permit long-term culture without the need for passaging and with the possibility for imaging over time. These bioengineering approaches included for example patterned surfaces^{17,29,30} or a chip with a laser-ablated hydrogel³¹ mimicking the intestinal topology and developed in our lab¹⁹. The use of microfluidic chips with organoids instead of standard cell lines opened up many opportunities to study physiologically relevant processes in a controlled manner. Since then, our lab applied the same technology to generate organoid-on-a-chip models of different organs, one of the most logical follow-ups being the colon.

The gastrointestinal tract can be affected by many different diseases and the features of this new model make it applicable to study at least some of them¹⁹. One of the most important disease is cancer. Indeed, gastrointestinal tract cancers are cumulatively the most common cancer types, and among them colorectal cancer has the highest prevalence³². Colorectal cancers arise from a series of mutations in specific genes³³ such as *APC*, *KRAS*, *SMAD4* and *TP53* (Figure 2), that actually affect mostly the same pathways as the ones implicated in intestinal stem cell maintenance and organoid growth.

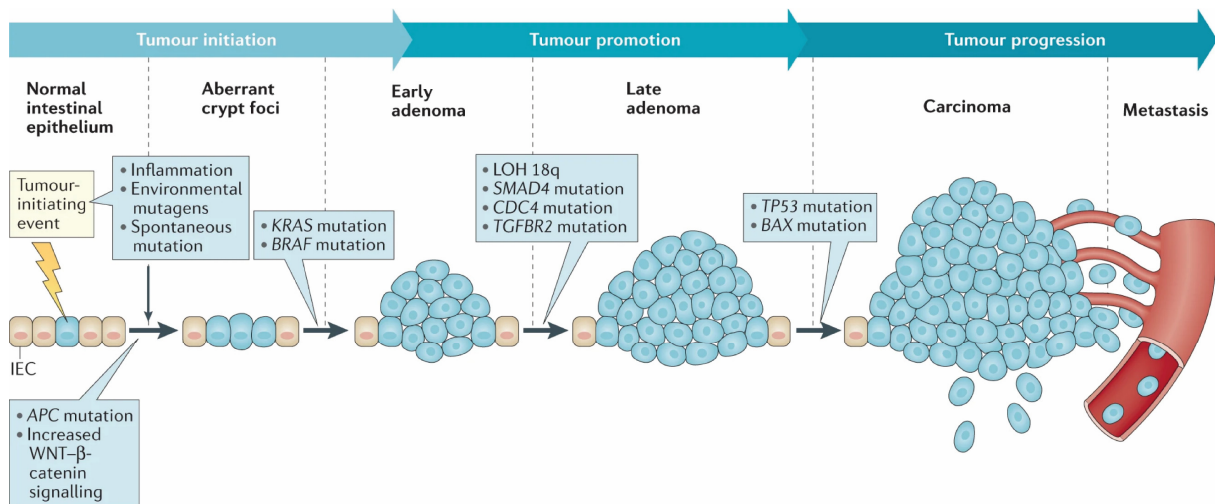


Figure 2 Mutations involved in colorectal cancer development. Of note, the pathways affected by the mutations are also the ones implicated in organoid growth. Adapted from¹⁵⁹

Traditionally, cancer has been studied with animal models, where either tumors are chemically induced, patient-derived cancer cells transplanted (xenograft), or cancer mutations genetically engineered³⁴. Regarding the latter, many different models exist, with genetic modifications allowing to investigate diverse aspects of the disease, such as tumor initiation and progression³⁴. However, once oncogenic mutations are induced, the tumor formation process remains a black-box until actual tumors can be observed. Moreover, despite the obvious advantage of modelling the disease at the organism level, animal studies are costly, relatively low-throughput, raise ethical questions and are under constant pressure to being reduced³⁵.

For cancer as well, organoids present an interesting intermediate between animal models and cell lines cultured in 2D. Two approaches allow to model cancer with organoids: deriving organoids from existing tumors, or genetically engineering organoids with mutations leading to tumor development³⁶. For the second approach, an alternative consists in isolating healthy organoids from mice bearing inducible mutations such as *Apc^{fl/fl};Kras^{LSL-G12D/+};Trp53^{fl/f}* (AKP), and inducing the mutations in vitro. In both cases, compared to organoids derived from established tumors, genetically engineered organoids present the advantage of allowing to model oncogenic recombination, tumor initiation and evolution³⁶. However, despite their higher observability, organoids are also not a perfect model. They need to be passaged relatively often due to the accumulation of shed dead cells, hence preventing their long-term monitoring. Moreover, many organoids do not display obvious differences between healthy and mutated tissue, and they do not form structures with pathophysiological resemblance to real tumors. Some of these limitations can however be alleviated by the use of the colon-on-a-chip introduced previously with cancer organoids.

Different methods exist to control inducible mutations such as the ones carried by AKP organoids/organoid-on-a-chip. The most common are based on chemically induced Cre recombinase expression, or imply directly adding Cre protein to the culture medium. They however present some drawbacks such as difficulties in removing the inducer and diffusion-based transport, preventing precise time- and space-resolved activation³⁷. One alternative for a more precise spatiotemporal control involves the use of optogenetic systems (i.e. genetically encoded light-responsive tools³⁷). Several such systems are available and present different characteristics in terms of gene expression (endogenous vs. exogenous), responding wavelength, luminous intensity required for activation, induction level, rapidity of activation, reversibility, need for an exogenous ligand, etc^{38,39}. Based on knowledge from previous work^{Hübscher, Neumayer, Wernig 2017, unpublished}, we focused on the system developed by Wang et al²¹ and further used by Sokolik et al²² (Figure 3) due to its high induction of gene expression and to the relatively low illumination intensity required for its activation compared to other systems³⁸.

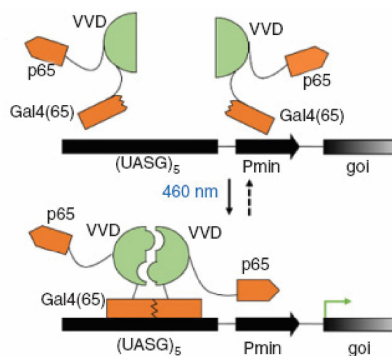


Figure 3 Optogenetic system for gene expression developed by Wang et al²¹. Blue light induces homodimerization of a construct, allowing its binding to a specific sequence located upstream of a minimal promoter. The construct acts as a transactivator and triggers expression of the downstream gene. More specifically, the construct is based on the GAL4-UASG system from yeast. Gal4 was modified to enable its binding to UASG only as a dimer, and fused to VVD, a protein that dimerizes in the presence of blue light. Upon light induction, VVD dimerizes, triggering the dimerization of GAL4, which binds to UASG. UASG is upstream of a minimal promoter and a transactivator (p65) has been fused to the construct. Therefore, when Gal4 binds to UASG, the transactivator comes in close proximity to the minimal promoter, which leads to the expression of the gene of interest (goi). Adapted from ³⁸.

This system is composed of two different vectors, one containing a UASG sequence, a minimal promoter and the gene of interest, and the other containing Gal4(65), VVD and p65 (so called GAVPO). This optogenetic system being sensitive to ambient light²¹, we previously modified it to add another level of control by cloning the GAVPO part under the control of a doxycycline-inducible promoter (TetO)^{Hübscher, Neumayer, Wernig 2017, unpublished}. For induction of oncogenic recombination, we used the gene encoding Cre recombinase as gene of interest. This system

thus can be applied to engineer organoids and organoid-on-a-chip at the cellular level to respond to blue light.

In the work presented in Chapter I, we therefore aimed at combining inducible *Apc^{fl/fl};Kras^{SL-G12D/+};Trp53^{fl/f}* (AKP) colorectal cancer organoids with 1) an optogenetic system to control oncogenic recombination at the cellular level in space and time 2) a microfluidic chip with apical side accessibility and allowing long-term observable culture. This model allowing for the first time the formation of pathophysiologically relevant tumors in vitro in an observable setting, we applied it to gain insights into tumor initiation and development. We additionally probed its applicability to functional studies, more specifically by testing the effects of environmental factors (such as bacterial metabolites, etc.) on tumor growth and its potential to predict the efficacy of new tumor-suppressive drugs.

For aim 2: To develop a new type of organoids, thymic epithelial organoids, with preserved thymopoietic functionality ex vivo

Perhaps because its location does not give many indications about its role, it took until 1961 for the thymus to be identified as the site of T cell development⁴⁰. As T cells are an essential cellular component of the adaptive immune system, thymic education of T cells plays a crucial role in protecting us against pathogens, in preventing tumor development and in avoiding autoimmune disorders.

At the gross anatomy level, the thymus is formed by two lobes, each divided into lobules. The lobules are further organized into a cortical (outer) and a medullary (inner) regions⁴¹. Histologically, the internal structure of the thymus is an intricate tridimensional meshwork of different microenvironments through which T cell progenitors undergo maturation by interacting with thymic stromal cells⁴². Among them, thymic epithelial cells (TECs) play the major role in mediating T cell development (Figure 4). Based on their anatomical location and on their molecular and functional characteristics, TECs are divided into cortical and medullary lineages (cTECs and mTECs, respectively)⁴³. cTECs are responsible for the first part of T cell development. They promote the homing of lymphoid progenitors into the thymus and commit them to the T cell lineage. After commitment, progenitors undergo T cell receptor (TCR) recombination, β -selection, a subsequent proliferation phase and recombination of the second TCR chain. During that time, they receive proliferation and survival signals from cTECs. cTECs then mediate the positive selection of developing T cells (so called thymocytes) expressing a functional TCR which binds with the right affinity to peptides presented on the major histocompatibility complex (MHC). After that, thymocytes migrate to the medulla, where mTECs mediate their terminal differentiation, including negative selection, which is important for the establishment of immunological self-tolerance and achieved through promiscuous expression of tissue-restricted antigens (TRAs). T cells that passed all the thymic selection processes fully mature and exit to the periphery to perform their function (as helper or cytotoxic T cells). In addition to the development of classical $\alpha\beta$ -T cells described here, alternative T cell lineages also arise in the thymus^{44,45}. These include $\gamma\delta$ T cells, innate natural killer T cells, mucosal-associated invariant T cells, intraepithelial lymphocytes, H2-M3-restricted T cells, CD1a, b or c-restricted T cells, MHC class Ib-restricted T cells and perhaps innate lymphoid cells⁴⁶.

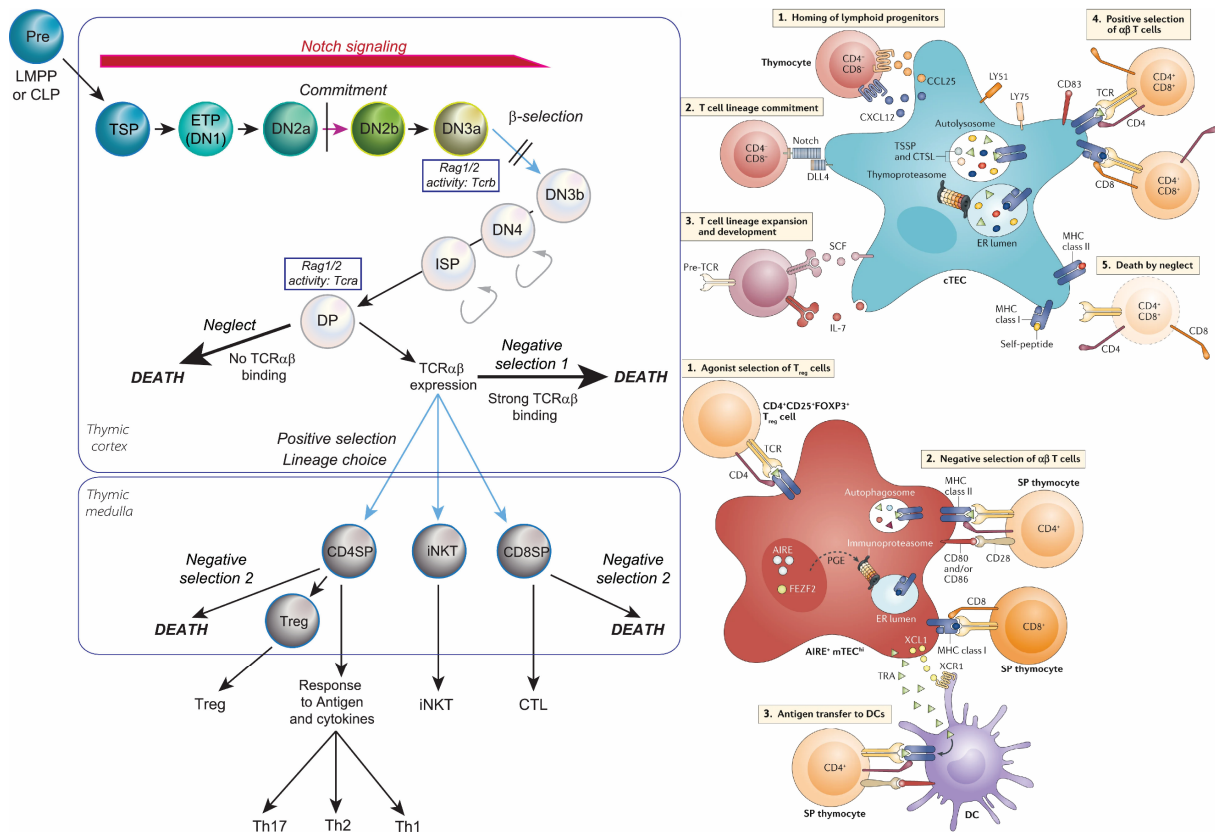


Figure 4 Classical ($\alpha\beta$) T cell developmental stages (in mice) and the role of thymic epithelial cells. Lymphoid progenitors entering the thymus are called thymus-settling progenitors (TSPs). The first stages of T cell development take place in the cortex. Early T cell precursors (ETPs) and the subsequent first stages of developing T cells do not express the CD4 and CD8 coreceptors (and thus are termed double negative, DN). T lineage commitment happens by interacting with cTECs, which express Notch ligands. After that, a first round of TCR recombination targeting the variable-diversity-joining (VDJ) regions of the β -chain takes place. Thymocytes experiencing signaling through a TCR complex containing TCR β are selected (β -selection) and undergo proliferation. Thymocytes then transiently upregulate CD8, and become CD4 and CD8 double positive (DP). A second round of VJ recombination targeting the TCR α -chain takes place at this stage. The fate of DP thymocytes is driven by their interactions with cTECs, which have a specific machinery to process peptides and present self-antigens on the MHC. If their TCR fails to interact with a peptide-MHC complex, thymocytes die by neglect. Too strong activation of their TCR (mainly by binding to peptides presented on the MHC of dendritic cells) can also lead to death through negative selection. Thymocytes bearing a TCR interacting with the right affinity with peptide-MHC (I or II) complexes are positively selected and directed to the CD8 or CD4 lineage, respectively. Positively selected thymocytes then migrate to the medulla and interact with mTECs. Specialized mTECs have the unique capacity to express many genes from which the expression is usually restricted to specific tissues. Thymocytes with strong TCR binding to self-antigens presented on the MHC of mTECs or of dendritic cells are either negatively selected or redirected to the regulatory T cell lineage, while thymocytes that escape negative selection can complete their maturation⁴⁷. Modified from ^{43,48}.

T cells require thymic epithelial cells to mature, but the opposite is equally true, as signals from thymocytes are also necessary for TEC development, differentiation (in particular of the medulla) and maintenance⁴⁹. In addition to this set of reciprocal interactions termed crosstalk, both thymocytes and TECs interact with other thymic stromal cells such as thymic

mesenchyme (cortical and medullary fibroblasts) and vasculature (endothelial cells and pericytes). These non-epithelial stromal cells are increasingly recognized as playing an important role in thymus organogenesis and T cell development⁵⁰. For instance, although the role of fibroblasts for TEC differentiation and expansion during organogenesis as well as for early T cell development were known for some time^{51,52}, their contribution to the induction of self-tolerance was only discovered recently⁵³. Finally, other immune cells including B cells, natural killer cells, macrophages, monocytes, and dendritic cells are also present in the thymus⁵⁴.

Recent sequencing efforts broadened our understanding of the thymus cellular composition and of the relationships between the different cell types^{54,55}. For TECs in particular, sequencing helped identifying many subpopulations that could not be differentiated by classical flow cytometry approaches (Figure 5)^{54,56–61}. An alignment of the cell types between the different studies and a nomenclature consensus are however currently still lacking in the field.

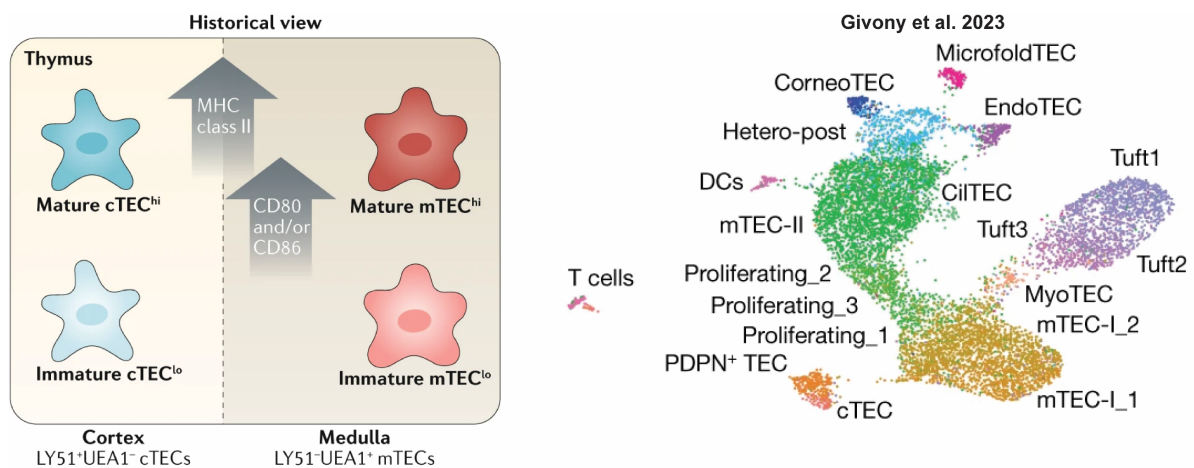


Figure 5 TEC subtypes, historically and based on a scRNAseq dataset published in 2023. By flow cytometry, TECs are isolated as EpCAM positive cells and divided into cTECs and mTECs based on their expression of Ly51 and their reactivity to UEA1. Subdivision between high and low phenotypes is based on MHCII and/or CD80/CD86 expression. Different studies involving scRNAseq permitted the identification of a broader diversity of TECs, especially of mTECs, with some subtypes specifically mimicking peripheral cell types within the thymus to induce self-tolerance. Modified from^{43,60}.

Specific single-cell RNA sequencing (scRNAseq) studies have also focused on thymus and TEC development^{62,63}, as well as on TEC deterioration in ageing^{64,65}. The thymus indeed undergoes large changes in cell type composition throughout the lifespan of an individual. During embryonic development, thymus organogenesis (reviewed in^{41,66–68}) occurs in the pharyngeal region⁶⁹. The thymic epithelial compartment is derived from the third pouch endoderm, which separates into a thymus and a parathyroid domains. At around E11.25 in mice, the thymic domain starts to express *Foxn1*, a transcription factor considered as master regulator of the TEC lineage⁷⁰. The third pharyngeal pouch is surrounded by neural crest cell-

derived mesenchymal cells that will then both form the thymic capsule and colonize the thymic epithelium, where they will become pericytes and medullary fibroblasts. Mesoderm-derived endothelial cells later also surround the thymic rudiment, and migrate into the epithelium to contribute to the vasculature^{50,71,72}. The entry of the first hematopoietic progenitors constituting the first wave of thymopoiesis is independent of the vasculature, which is only established around E15.5. After that, progenitors colonize the thymus from blood vessels located at the cortico-medullary junction. Different transcription factor networks such as *Eya1*, *Hoxa3*, *Pax1/9*, *Six1/4* and *Tbx1* and pathways families including Sonic hedgehog, Retinoic acid, BMP, Wnt and Fibroblast growth factor (FGF) are implicated in thymus organogenesis^{41,69}. However, despite many efforts and although *Six1* and *Foxn1* itself have been shown to regulate *Foxn1* expression⁷³, how to precisely interfere with the TEC master regulator remains unknown.

During development, both c- and mTECs differentiate from a bipotent progenitor with cTEC traits⁴³ and, as already mentioned, require crosstalk with thymocytes to complete their maturation. cTEC differentiation and heterogeneity are only beginning to be understood^{43,74,75}. However, cTECs subtypes are generally more similar to each other than in the case of mTECs, as scRNAseq studies keep identifying new mTEC subtypes and maturation trajectories. It is nonetheless admitted that Notch signaling promotes progenitor commitment to the mTEC lineage^{76,77} and that the differentiation of mTECs expressing TRAs is mediated by receptor activator of nuclear factor- κ B (RANK) signaling^{43,78}. Conversely, the existence and identity of a bipotent progenitor in the adult thymus remains debated^{43,79–81}, although recent scRNAseq studies have tried to solve this question^{63,82,83}. In particular, whether the putative progenitor can differentiate into functional TECs and why there seem to be an increase in cells with progenitor-like characteristics in aged mice remain to be understood^{64,83}.

Changes in cell type composition later in life are linked to thymic involution, a process in which the epithelial compartment is gradually replaced by adipose tissue and leading to a decrease in thymus size and in naïve T cell output^{84–87}. In addition to ageing, acute injuries such as radiation, chemotherapy, graft-versus-host disease, corticosteroids, sex hormones and infections also affect the thymus^{88,89}. Since impaired thymic function increases the risk of diseases, understanding and promoting thymic regeneration capabilities is of major interest. Current strategies are often based on recapitulating endogenous regenerative pathways⁹⁰ and imply IL7^{91,92}, IL22⁹³, IL23^{93,94}, IL33⁹⁵, RANKL⁹⁶, BMP4⁹⁷, VEGF⁹⁸ and FGF7 (KGF)⁹⁹. Sex hormone inhibition¹⁰⁰ and administration of growth hormone and ghrelin have also been shown to boost thymic function⁹⁰.

Alternative strategies to regenerate or enhance thymic function rely on in vitro systems producing T cells and TECs. These systems are also important to model diverse aspects of thymus biology and are complementary to animal models which, despite their importance,

present ethical concerns and only partially recapitulate human immune system physiology¹⁰¹. As highlighted again recently, thymus models should recreate the native features necessary to support the development of mature T cells with a functional, diverse and self-tolerant repertoire¹⁰¹. Since they are the main responsible for T cell maturation, TECs should be an integral part of such models. However, TECs quickly lose *Foxn1* expression and their thymopoietic ability in vitro if cultured independently of a complex 3D environment and of other cell types¹⁰². Therefore, the prevalent in vitro models remain fetal thymic organ cultures (FTOCs)^{103,104}, or reaggregate fetal thymic organ cultures (RFTOCs)^{105,106}, approaches where either the full thymic lobe is cultured, or it is dissociated and diverse thymic populations are combined and cultured as aggregate.

Since the exact mechanisms involved in TEC functionality loss are not fully understood, diverse alternative strategies have been developed to circumvent their use and engineer an in vitro thymus (Figure 6). Some employ OP9 or MS5 cell lines modified to express Notch ligands, in 2D and 3D culture settings, and allow to recapitulate T cell development to a certain extent^{107–109}. Instead of cells, other approaches use beads functionalized with Notch ligands¹¹⁰. However, in both cases, the absence of TECs prevents fully physiological T cell selection processes. Other efforts focused on obtaining TECs from embryonic and induced pluripotent stem cells^{111–119} or through direct reprogramming¹²⁰, but these cells largely rely on in vivo transplantation to reveal thymopoietic functionality. A recent study seems however to have succeeded in generating thymic reagggregates comprising mesenchyme, TECs and T cell progenitors all derived from pluripotent stem cells and capable of mediating T cell development¹²¹. Other approaches capitalize on bioengineering to help preserve TEC functionality¹²². These include decellularized native ECM^{123–126}, other ECM^{127–129}/synthetic hydrogel^{130–132} or inert scaffolds¹³³. However, here again the reconstituted thymi often need to be grafted in vivo to be able to mediate T cell maturation. Matrigel, the main ECM used for organoids, has also been applied to the thymus and was shown to support TEC colony formation^{80,134–136}. However, these cultures still required feeder layers (a method used to culture TECs in the long term inspired from keratinocyte cultures) and TEC functionality was not demonstrated.

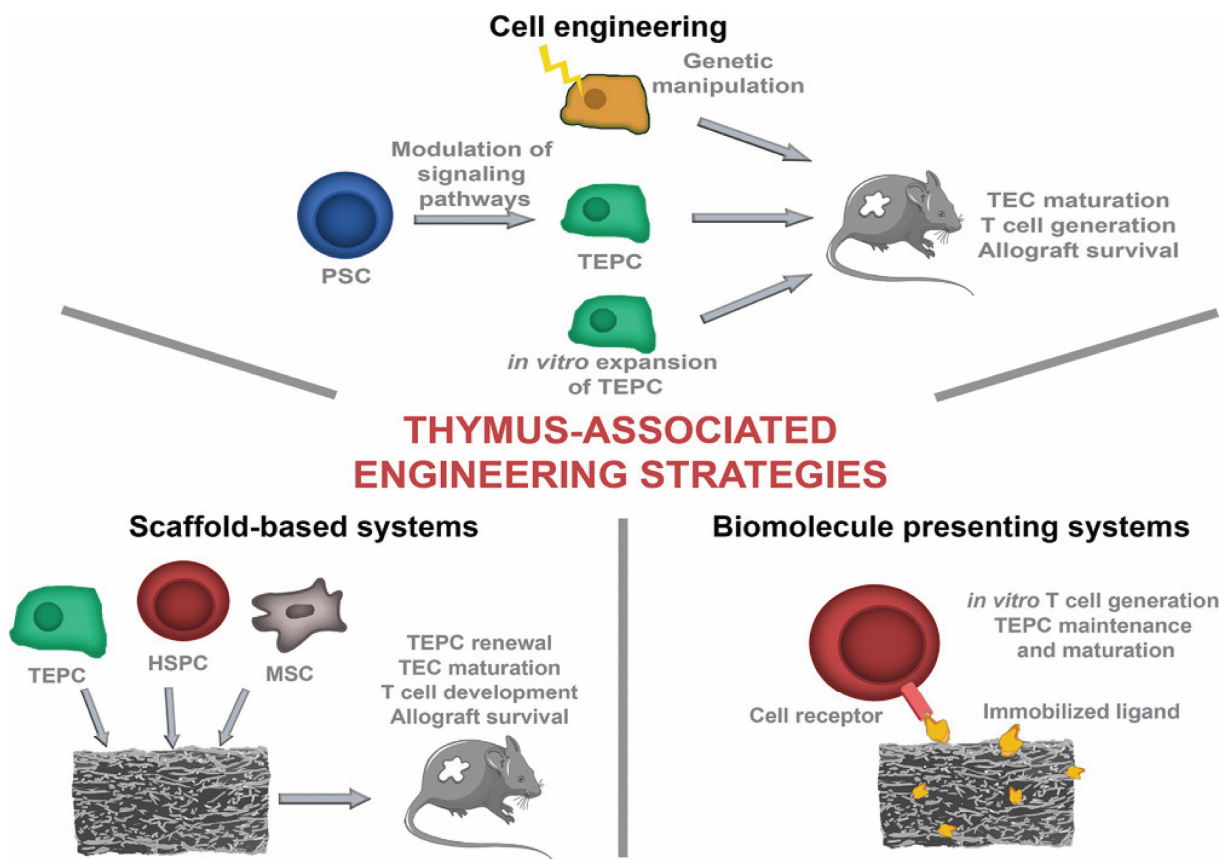


Figure 6 Strategies to engineer a thymus. One research axis leverages cell engineering to differentiate thymic epithelial progenitor cells (TEPCs) from pluripotent stem cells (PSCs) or via direct reprogramming approaches. Scaffold-based systems can be used to culture TEPCs, hematopoietic stem and progenitor cells (HSPCs) and mesenchymal stem cells (MSCs) in tissue-engineering approaches aiming at reconstituting thymic function. Ligands important for T cell development can also be presented either by cell lines or by functionalized substrates such as beads, plates, or scaffolds. Adapted from¹²².

In the work presented in Chapter II, I aimed at creating a new thymus model overcoming some of the aforementioned limitations. I leveraged the knowledge gained from other endoderm-derived organoid culture methods and develop thymic epithelial organoids. I started with embryonic TECs given their higher progenitor potential, and cultured them independently of other cell types in a defined medium supplemented with growth factors previously highlighted as important for TEC development and/or regeneration. In these conditions, I showed that the 3D structure provided by Matrigel was sufficient to maintain the functional ability of thymic epithelial organoids to mediate thymopoiesis. To do so, I reaggreated thymic epithelial cells cultured as organoids with T cell progenitors. I then compared T cell maturation processes happening *in vitro* and in the native thymus and showed their similarity. Finally, I demonstrated the ability of organoid-based thymic reaggregates to attract new T cell progenitors when transplanted under the kidney capsule of mice.

For aim 3: To leverage bioprinting for guiding organoid self-organization for the generation of macroscale (multi)tissue constructs

(Partially contributed to a publication in Nature Review Methods Primers [2021]

<https://doi.org/10.1038/s43586-021-00073-8>)

Although organoids are already applicable to basic and translational research, one of the long-term goals of the field is to generate transplantable tissue or organs. However, as previously mentioned, current organoid models are limited in terms of size and cell type composition.

Typical tissue engineering strategies rely on scaffolds, hydrogels and bioprinting approaches to generate larger tissue constructs and integrate multiple cell types. Bioprinting, “the use of computer-aided transfer processes for patterning and assembling living and non-living materials with a prescribed 2D or 3D organization in order to produce bioengineered structures^{137–139}, in particular gained substantial interest in the past few years. It presents several attractive features such as the possibility to print anatomical structures based on imaging data and the advantage to improve the construction of heterogeneous tissue structures with complex volume compared to other biofabrication techniques¹³⁹. Common bioprinting strategies are categorized as (micro)extrusion, laser-assisted, inkjet-based, light-based vat-polymerization and microfluidic bioprinting^{140,141}. Among those, the most popular is extrusion bioprinting, which relies on bioinks composed of cells and/or biomaterials mimicking the extracellular matrix¹⁴². These bioinks are then loaded into a printhead and extruded mechanically or pneumatically from a nozzle¹³⁹. However, classical application of extrusion bioprinting to cells still suffers compromises in terms of viability, complexity and functionality of the printed tissues¹⁴³.

Compared to trying to print high resolution tissue constructs, one interesting alternative consists in leveraging the ability of cells, and in particular of stem cells, to self-organize in presence of the correct environmental cues^{9,144}. Despite the seemingly low initial resolution of such printed constructs, their viability is indeed improved and overtime they approach the architecture of native tissues. Among the first examples applying this strategy was the bioprinting of multicellular spheroids. They were deposited onto/into different supports and matrices^{145–150}, with methods also applicable to organoids (Figure 7). The printed spheroids/organoids thereafter fused into larger constructs, but these were highly variable, just as standard organoids¹⁵¹. To overcome this issue, a solution consists in using a single cell suspension as bioink^{152,153}, for example of organoid-forming stem cells. This allows to print highly reproducible tissues¹⁵⁴.

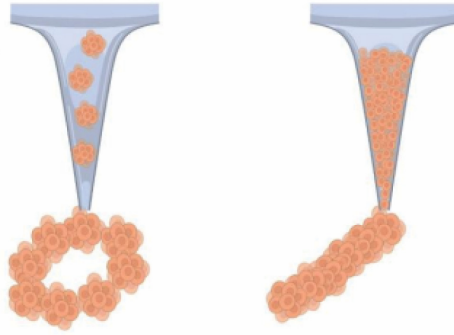


Figure 7 Bioprinting strategies using bioinks composed solely of cells. Left: printing of entire spheroids or organoids. Right: printing of single cells that can be obtained from organoids, and that fuse into homogeneous larger tissue constructs overtime. Adapted from¹³⁹

The formulation of such high-density cell-only bioinks is simplified compared to the use of biomaterials where rheological, biological, chemical, and mechanical characteristics can be tuned¹⁵⁵. However, the properties of the matrices where cells are deposited, and which act as physical and chemical support, play an important role in the development of the tissues^{156–158}. Moreover, the use of permissive matrices allows remodeling by the cells upon tissue growth. Matrices with self-healing properties also permits to modulate morphogenesis in space and time, for instance by depositing other cell types or signaling cues after the initial printing.

In the work presented in Chapter III, we combined a custom-built microscope-based extrusion bioprinting setup with organoid-forming single cells and organoid-supporting permissive matrices. This method was used to 1) generate reproducible centimeter-scale tissues, 2) add supporting cells to the main tissue, and 3) sequentially print different cells to mimic tissue/organ boundaries, here exemplified with the gastrointestinal tract. Thus, this novel bioprinting approach allowed us to combine different cell types to generate more complex and larger tissue constructs compared to standard organoids. We also demonstrated the physiological relevance of the printed tissues by testing their response to different chemical stimuli.

References

1. Ramalho-Santos, M. & Willenbring, H. On the Origin of the Term 'Stem Cell'. *Cell Stem Cell* 1, 35–38 (2007).
2. Becker, A. J., McCulloch, E. A. & Till, J. E. Cytological Demonstration of the Clonal Nature of Spleen Colonies Derived from Transplanted Mouse Marrow Cells. *Nature* 197, 452–454 (1963).
3. Evans, M. & Kaufman, M. Establishment in culture of pluripotential cells from mouse embryos. *Nature* 292, 154–156 (1981).
4. Takahashi, K. & Yamanaka, S. Induction of Pluripotent Stem Cells from Mouse Embryonic and Adult Fibroblast Cultures by Defined Factors. *Cell* 126, 663–676 (2006).
5. Lutolf, M. P., Gilbert, P. M. & Blau, H. M. Designing materials to direct stem-cell fate. *Nature* 462, (2009).
6. Rheinwald, J. G. & Green, H. Serial cultivation of strains of human epidermal keratinocytes: the formation of keratinizing colonies from single cells. *Cell* 6, 331–343 (1975).
7. Shao, X. *et al.* MatrisomeDB 2.0: 2023 updates to the ECM-protein knowledge database. *Nucleic Acids Res.* 51, D1519–D1530 (2023).
8. Rossi, G., Manfrin, A. & Lutolf, M. P. Progress and potential in organoid research. *Nat. Rev. Genet.* 19, 671–687 (2018).
9. Brassard, J. A. & Lutolf, M. P. Engineering Stem Cell Self-organization to Build Better Organoids. *Cell Stem Cell* 24, 860–876 (2019).
10. Li, M. L. *et al.* Influence of a reconstituted basement membrane and its components on casein gene expression and secretion in mouse mammary epithelial cells. *Proc. Natl. Acad. Sci. U. S. A.* 84, 136–140 (1987).
11. Zhao, Z. *et al.* Organoids. *Nat. Rev. Methods Prim.* 2, (2022).
12. Hofer, M. & Lutolf, M. P. Engineering organoids. *Nat. Rev. Mater.* 6, 402–420 (2021).
13. Serra, D. *et al.* Self-organization and symmetry breaking in intestinal organoid development. *Nature* 569, 66–72 (2019).
14. Li, M. & Izpisua Belmonte, J. C. Organoids — Preclinical Models of Human Disease. *N. Engl. J. Med.* 380, 569–579 (2019).
15. Mitropoulou, G. *et al.* Rectal organoid-guided CFTR modulator therapy restores lung function in a cystic fibrosis patient with the rare 1677delTA/R334W genotype. *Eur. Respir. J.* 60, (2022).
16. Bose, S., Clevers, H. & Shen, X. Promises and challenges of organoid-guided precision medicine. *Med* 2, 1011–1026 (2021).
17. Gjorevski, N. *et al.* Tissue geometry drives deterministic organoid patterning. *Science*. 375, (2022).
18. Sato, T. *et al.* Single Lgr5 stem cells build crypt-villus structures in vitro without a mesenchymal niche. *Nature* 459, 262–265 (2009).
19. Nikolaev, M. *et al.* Homeostatic mini-intestines through scaffold-guided organoid morphogenesis. *Nature* 585, 574–578 (2020).
20. Park, S. E., Georgescu, A. & Huh, D. Organoids-on-a-chip. *Science*. 364, 960–965 (2019).
21. Wang, X., Chen, X. & Yang, Y. Spatiotemporal control of gene expression by a light-switchable transgene system. *Nat. Methods* 9, 266–269 (2012).
22. Sokolik, C. *et al.* Transcription Factor Competition Allows Embryonic Stem Cells to Distinguish Authentic Signals from Noise. *Cell Syst.* 1, 117–129 (2015).
23. Anderson, G. & Jenkinson, E. J. Use of explant technology in the study of in vitro immune responses. *J. Immunol. Methods* 216, 155–163 (1998).
24. Gordon, J. *et al.* Functional evidence for a single endodermal origin for the thymic epithelium. *Am. J. Anat.* 5, 546–553 (2004).
25. Cheng, H. & Leblond, C. P. Origin, differentiation and renewal of the four main epithelial cell types in the mouse small intestine V. Unitarian theory of the origin of the four epithelial cell types. *Am. J. Anat.* 141, 537–561 (1974).

26. Potten, C. Extreme sensitivity of some intestinal crypt to X and gamma irradiation. *Nature* 269, 364–382 (1977).
27. Barker, N. *et al.* Identification of stem cells in small intestine and colon by marker gene Lgr5. *Nature* 449, 1003–1007 (2007).
28. Sato, T. *et al.* Long-term expansion of epithelial organoids from human colon, adenoma, adenocarcinoma, and Barrett's epithelium. *Gastroenterology* 141, 1762–1772 (2011).
29. Wang, Y., Ahmad, A. A., Sims, C. E., Magness, S. T. & Allbritton, N. L. In vitro generation of colonic epithelium from primary cells guided by microstructures. *Lab Chip* 14, 1622–1631 (2014).
30. Wang, Y. *et al.* A microengineered collagen scaffold for generating a polarized crypt-villus architecture of human small intestinal epithelium. *Biomaterials* 128, 44–55 (2017).
31. Brandenburg, N. & Lutolf, M. P. In Situ Patterning of Microfluidic Networks in 3D Cell-Laden Hydrogels. *Adv. Mater.* 7450–7456 (2016). doi:10.1002/adma.201601099
32. Jardim, S. R., de Souza, L. M. P. & de Souza, H. S. P. The Rise of Gastrointestinal Cancers as a Global Phenomenon: Unhealthy Behavior or Progress? *Int. J. Environ. Res. Public Health* 20, (2023).
33. Fearon, E. R. & Vogelstein, B. A genetic model of colorectal tumorigenesis. *Cell* 61, 759–767 (1990).
34. Bürtin, F., Mullins, C. S. & Linnebacher, M. Mouse models of colorectal cancer: Past, present and future perspectives. *World J. Gastroenterol.* 26, 1394–1426 (2020).
35. LeSavage, B. L., Suhar, R. A., Broguiere, N., Lutolf, M. P. & Heilshorn, S. C. Next-generation cancer organoids. *Nat. Mater.* 21, 143–159 (2022).
36. Lo, Y. H., Karlsson, K. & Kuo, C. J. Applications of organoids for cancer biology and precision medicine. *Nat. Cancer* 1, 761–773 (2020).
37. Taylor, J. L., Rohatgi, P., Spencer, H. T., Doyle, D. F. & Azizi, B. Characterization of a molecular switch system that regulates gene expression in mammalian cells through a small molecule. *BMC Biotechnol.* 10, (2010).
38. Müller, K., Naumann, S., Weber, W. & Zurbriggen, M. D. Optogenetics for gene expression in mammalian cells. *Biol. Chem.* 396, 145–152 (2015).
39. Wichert, N., Witt, M. & Scheper, T. Clinical applicability of optogenetic gene regulation. *Biotechnol. Bioeng.* 4168–4185 (2021). doi:10.1002/bit.27895
40. Miller, J. F. A. P. Immunological function of the thymus. *Lancet* 278, 748–749 (1961).
41. Gordon, J. & Manley, N. R. Mechanisms of thymus organogenesis and morphogenesis. *Development* 138, 3865–3878 (2011).
42. Manley, N. R., Richie, E. R., Blackburn, C. C., Condie, B. G. & Sage, J. Structure and function of the thymic microenvironment. *Front. Biosci.* 16, 2461–2477 (2011).
43. Kadouri, N., Nevo, S., Goldfarb, Y. & Abramson, J. Thymic epithelial cell heterogeneity: TEC by TEC. *Nat. Rev. Immunol.* 20, 239–253 (2020).
44. Winter, S. J. & Krueger, A. Development of unconventional T cells controlled by microRNA. *Front. Immunol.* 10, 1–12 (2019).
45. Mayassi, T., Barreiro, L. B., Rossjohn, J. & Jabri, B. A multilayered immune system through the lens of unconventional T cells. *Nature* 595, 501–510 (2021).
46. Shin, S. B. & McNagny, K. M. ILC-You in the Thymus: A Fresh Look at Innate Lymphoid Cell Development. *Front. Immunol.* 12, 1–12 (2021).
47. Takaba, H. & Takayanagi, H. The Mechanisms of T Cell Selection in the Thymus. *Trends Immunol.* 38, 805–816 (2017).
48. Rothenberg, E. V. Single-cell insights into the hematopoietic generation of T-lymphocyte precursors in mouse and human. *Exp. Hematol.* 95, 1–12 (2021).
49. van Ewijk, W., Shores, E. W. & Singer, A. Crosstalk in the mouse thymus. *Immunol. Today* 15, 214–217 (1994).
50. Nitta, T. & Takayanagi, H. Non-Epithelial Thymic Stromal Cells: Unsung Heroes in Thymus Organogenesis and T Cell Development. *Front. Immunol.* 11, 1–11 (2021).
51. Anderson, G., Anderson, K. L., Tchilian, E. Z., Owen, J. J. T. & Jenkinson, E. J. Fibroblast dependency during early thymocyte development maps to the CD25+ CD44+ stage and involves interactions with fibroblast matrix molecules. *Eur. J. Immunol.* 27,

- 1200–1206 (1997).
52. Shinohara, T. & Honjo, T. Epidermal growth factor can replace thymic mesenchyme in induction of embryonic thymus morphogenesis in vitro. *Eur. J. Immunol.* 26, 747–752 (1996).
 53. Nitta, T. *et al.* Fibroblasts as a source of self-antigens for central immune tolerance. *Nat. Immunol.* (2020). doi:10.1038/s41590-020-0756-8
 54. Park, J. E. *et al.* A cell atlas of human thymic development defines T cell repertoire formation. *Science.* 367, (2020).
 55. Steier, Z. *et al.* Single-cell multi-omic analysis of thymocyte development reveals drivers of CD4/CD8 lineage commitment. *Nat. im* 24, 1579–1590 (2023).
 56. Bautista, J. L. *et al.* Single-cell transcriptional profiling of human thymic stroma uncovers novel cellular heterogeneity in the thymic medulla. *Nat. Commun.* (2021). doi:10.1038/s41467-021-21346-6
 57. Klein, F. *et al.* Combined multidimensional single-cell protein and RNA profiling dissects the cellular and functional heterogeneity of thymic epithelial cells. *Nat. Commun.* 14, 4071 (2023).
 58. Wells, K. L. *et al.* Combined transient ablation and single-cell RNA-sequencing reveals the development of medullary thymic epithelial cells. 1–27 (2020).
 59. Michelson, D. A. *et al.* Thymic epithelial cells co-opt lineage-defining transcription factors to eliminate autoreactive T cells II II Article Thymic epithelial cells co-opt lineage-defining transcription factors to eliminate autoreactive T cells. *Cell* 185, 2542-2558.e18 (2022).
 60. Givony, T. *et al.* Thymic mimetic cells function beyond self-tolerance. *Nature* (2023). doi:10.1038/s41586-023-06512-8
 61. Miller, C. N. *et al.* Thymic tuft cells promote an IL-4-enriched medulla and shape thymocyte development. *Nature* 559, 627–631 (2018).
 62. Kernfeld, E. M. *et al.* A Single-Cell Transcriptomic Atlas of Thymus Organogenesis Resolves Cell Types and Developmental Maturation. *Immunity* 48, 1258-1270.e6 (2018).
 63. Gao, H. *et al.* The Lineage Differentiation and Dynamic Heterogeneity of Thymic Epithelial Cells During Thymus Organogenesis. *Front. Immunol.* 13, 1–24 (2022).
 64. Baran-Gale, J. *et al.* Ageing compromises mouse thymus function and remodels epithelial cell differentiation. *Elife* 9, 1–71 (2020).
 65. Kousa, A. I. *et al.* Age-related epithelial defects limit thymic function and regeneration. (2023).
 66. Blackburn, C. C. & Manley, N. R. DEVELOPING A NEW PARADIGM FOR THYMUS ORGANOGENESIS. 4, 278–289 (2004).
 67. Rodewald, H.-R. Thymus Organogenesis. *Annu. Rev. Immunol.* 26, 355–388 (2008).
 68. Farley, A. M. *et al.* Dynamics of thymus organogenesis and colonization in early human development. *Development* 140, 2015–2026 (2013).
 69. Nowell, C. S., Farley, A. M. & Blackburn, C. C. Thymus organogenesis and development of the thymic stroma. *Methods Mol. Biol.* 380, 125–162 (2007).
 70. Romano, R. *et al.* FOXP1: A Master Regulator Gene of Thymic Epithelial Development Program. *Front. Immunol.* 4, 187 (2013).
 71. Handel, A. E. *et al.* Developmental dynamics of the neural crest–mesenchymal axis in creating the thymic microenvironment. *Sci. Adv.* 8, 1–17 (2022).
 72. Nitta, T. Mesenchymal stromal cells in the thymus. *Inflamm. Regen.* 42, (2022).
 73. Kadouri, N. *et al.* Transcriptional regulation of the thymus master regulator Foxn1. (2022).
 74. Alawam, A. S., Anderson, G. & Lucas, B. Generation and Regeneration of Thymic Epithelial Cells. *Front. Immunol.* 11, 1–15 (2020).
 75. White, A. J. *et al.* Diversity in Cortical Thymic Epithelial Cells Occurs through Loss of a Foxn1-Dependent Gene Signature Driven by Stage-Specific Thymocyte Cross-Talk. *J. Immunol.* (2022). doi:10.4049/jimmunol.2200609
 76. Liu, D. *et al.* Canonical NOTCH signaling controls the early progenitor state and

- emergence of the medullary epithelial lineage in fetal thymus development. *Development* 1–46 (2020). doi:10.1101/600833
77. Li, J. *et al.* NOTCH1 signaling establishes the medullary thymic epithelial cell progenitor pool during mouse fetal development. *Dev.* 147, (2020).
 78. Cosway, E. J. *et al.* Redefining thymus medulla specialization for central tolerance. *J. Exp. Med.* 214, 3183–3195 (2017).
 79. Ulyanchenko, S. *et al.* Identification of a Bipotent Epithelial Progenitor Population in the Adult Thymus. *Cell Rep.* 14, 2819–2832 (2016).
 80. Wong, K. *et al.* Multilineage potential and self-renewal define an epithelial progenitor cell population in the adult thymus. *Cell Rep.* 8, 1198–1209 (2014).
 81. Ishikawa, T., Akiyama, N. & Akiyama, T. In Pursuit of Adult Progenitors of Thymic Epithelial Cells. 12, 1–8 (2021).
 82. Nusser, A. *et al.* Developmental dynamics of two bipotent thymic epithelial progenitor types. *Nature* 606, 165–171 (2022).
 83. Ragazzini, R. *et al.* Defining the identity and the niches of epithelial stem cells with highly pleiotropic multilineage potency in the human thymus. *Dev. Cell* 1–19 (2023). doi:10.1016/j.devcel.2023.08.017
 84. Palmer, S., Albergante, L., Blackburn, C. C. & Newman, T. J. Thymic involution and rising disease incidence with age. *Proc. Natl. Acad. Sci. U. S. A.* 115, 1883–1888 (2018).
 85. George, A. J. T. & Ritter, M. A. Thymic involution with ageing: Obsolescence or good housekeeping? *Immunol. Today* 17, 267–272 (1996).
 86. Murray, J. M. *et al.* Naive T cells are maintained by thymic output in early ages but by proliferation without phenotypic change after age twenty. *Immunol. Cell Biol.* 81, 487–495 (2003).
 87. Cowan, J. E., Takahama, Y., Bhandoola, A. & Ohigashi, I. Postnatal Involution and Counter-Involution of the Thymus. 11, 1–11 (2020).
 88. Chaudhry, M. S., Velardi, E., Dudakov, J. A. & van den Brink, M. R. M. Thymus: The next (re)generation. *Immunol. Rev.* 271, 56–71 (2016).
 89. Velardi, E., Tsai, J. J. & van den Brink, M. R. M. T cell regeneration after immunological injury. *Nat. Rev. Immunol.* 21, 277–291 (2021).
 90. Granadier, D., Iovino, L., Kinsella, S. & Dudakov, J. A. Dynamics of thymus function and T cell receptor repertoire breadth in health and disease. *Semin. Immunopathol.* 43, 119–134 (2021).
 91. Andrew, D. & Aspinall, R. IL-7 and Not Stem Cell Factor Reverses Both the Increase in Apoptosis and the Decline in Thymopoiesis Seen in Aged Mice 1. 2–8 (2001).
 92. Alpdogan, Ö. *et al.* IL-7 enhances peripheral T cell reconstitution after allogeneic hematopoietic stem cell transplantation. 112, 1095–1107 (2003).
 93. Dudakov, J. A. *et al.* Interleukin-22 drives endogenous thymic regeneration in mice. *Science.* 336, 91–95 (2012).
 94. Gerosa, F. *et al.* Differential regulation of interleukin 12 and interleukin 23 production in human dendritic cells. 205, 1447–1461 (2008).
 95. Cosway, E. J. *et al.* The alarmin IL33 orchestrates type 2 immune-mediated control of thymus regeneration. *Nat. Commun.* 14, 1–11 (2023).
 96. Lopes, N., Vachon, H., Marie, J. & Irla, M. Administration of RANKL boosts thymic regeneration upon bone marrow transplantation. 9, 835–851 (2017).
 97. Wertheimer, T. *et al.* Production of BMP4 by endothelial cells is crucial for endogenous thymic regeneration. *Sci. Immunol.* 3, (2018).
 98. Park, H. *et al.* Up-regulation of VEGF expression by NGF that enhances reparative angiogenesis during thymic regeneration in adult rat. 1773, 1462–1472 (2007).
 99. Alpdogan, Ö. *et al.* Keratinocyte growth factor (KGF) is required for postnatal thymic regeneration. 107, 2453–2460 (2006).
 100. Velardi, E. *et al.* Sex steroid blockade enhances thymopoiesis by modulating Notch signaling. 211, 2341–2349 (2014).
 101. Michaels, Y. S., Buchanan, C. F., Gjorevski, N. & Moisan, A. Bioengineering translational models of lymphoid tissues. *Nat. Rev. Bioeng.* (2023). doi:10.1038/s44222-

023-00101-0

102. Mohtashami, M. & Zúñiga-Pflücker, J. C. Cutting Edge: Three-Dimensional Architecture of the Thymus Is Required to Maintain Delta-Like Expression Necessary for Inducing T Cell Development. *J. Immunol.* 176, 730–734 (2006).
103. Auerbach, R. Morphogenetic interactions in the development of the mouse thymus gland. *Dev. Comp. Immunol.* 2, 271–284 (1960).
104. Owen, J. J. T. & Ritter, M. A. Tissue interaction in the development of thymus lymphocytes. *J. Exp. Med.* 129, 431–442 (1969).
105. Jenkinson, E. J., Anderson, G. & Owen, J. J. T. Studies on T cell maturation on defined thymic stromal cell populations in vitro. *J. Exp. Med.* 176, 845–853 (1992).
106. Anderson, G., Jenkinson, E. J., Moore, N. C. & Owen, J. J. T. MHC class II-positive epithelium and mesenchyme cells are both required for T-cell development in the thymus. *Nature* 362, 70–73 (1993).
107. Schmitt, T. M. & Zúñiga-Pflücker, J. C. Induction of T cell development from hematopoietic progenitor cells by delta-like-1 in vitro. *Immunity* 17, 749–756 (2002).
108. Seet, C. S. *et al.* Generation of mature T cells from human hematopoietic stem and progenitor cells in artificial thymic organoids. *Nat. Methods* 14, 521–530 (2017).
109. Montel-Hagen, A. *et al.* In Vitro Recapitulation of Murine Thymopoiesis from Single Hematopoietic Stem Cells. *Cell Rep.* 33, 108320 (2020).
110. Trotman-Grant, A. C. *et al.* DL4- μ beads induce T cell lineage differentiation from stem cells in a stromal cell-free system. *Nat. Commun.* 12, 1–11 (2021).
111. Parent, A. V. *et al.* Generation of functional thymic epithelium from human embryonic stem cells that supports host T cell development. *Cell Stem Cell* 13, 219–229 (2013).
112. Ramos, S. A. *et al.* Generation of functional human thymic cells from induced pluripotent stem cells. *J. Allergy Clin. Immunol.* 149, 767-781.e6 (2022).
113. Sun, X. *et al.* Directed differentiation of human embryonic stem cells into thymic epithelial progenitor-like cells reconstitutes the thymic microenvironment in vivo. *Cell Stem Cell* 13, 230–236 (2013).
114. Lai, L. & Jin, J. Generation of thymic epithelial cell progenitors by mouse embryonic stem cells. *Stem Cells* 27, 3012–3020 (2009).
115. Su, M. *et al.* Efficient in vitro generation of functional thymic epithelial progenitors from human embryonic stem cells. *Sci. Rep.* 5, 1–8 (2015).
116. Inami, Y. *et al.* Differentiation of induced pluripotent stem cells to thymic epithelial cells by phenotype. *Immunol. Cell Biol.* 89, 314–321 (2011).
117. Chhatta, A. R. *et al.* De novo generation of a functional human thymus from induced pluripotent stem cells. *J. Allergy Clin. Immunol.* (2019). doi:10.1016/j.jaci.2019.05.042
118. Okabe, M., Ito, S., Nishio, N., Tanaka, Y. & Isobe, K.-I. Thymic Epithelial Cells Induced from Pluripotent Stem Cells by a Three-Dimensional Spheroid Culture System Regenerates Functional T Cells in Nude Mice. *Cell. Reprogram.* 17, 368–375 (2015).
119. Isotani, A., Hatayama, H., Kaseda, K., Ikawa, M. & Okabe, M. Formation of a thymus from rat ES cells in xenogeneic nude mouse \leftrightarrow rat ES chimeras. *Genes to Cells* 16, 397–405 (2011).
120. Bredenkamp, N. *et al.* An organized and functional thymus generated from FOXP1-reprogrammed fibroblasts. *Nat. Cell Biol.* 16, 902–908 (2014).
121. Ramos, S. A. *et al.* Generation of functional thymic organoids from human pluripotent stem cells. *Stem cell reports* 18, 829–840 (2023).
122. Silva, C. S., Reis, R. L., Martins, A. & Neves, N. M. Recapitulation of Thymic Function by Tissue Engineering Strategies. *Adv. Healthc. Mater.* 10, (2021).
123. Hun, M. *et al.* Native thymic extracellular matrix improves in vivo thymic organoid T cell output, and drives in vitro thymic epithelial cell differentiation. *Biomaterials* 118, 1–15 (2016).
124. Campinoti, S. *et al.* Reconstitution of a functional human thymus by postnatal stromal progenitor cells and natural whole-organ scaffolds. *Nat. Commun.* 11, 6372 (2020).
125. Fan, Y. *et al.* Bioengineering Thymus Organoids to Restore Thymic Function and Induce Donor-Specific Immune Tolerance to Allografts. *Mol. Ther.* 23, 1262–1277 (2015).

126. Asnaghi, M. A. *et al.* Thymus Extracellular Matrix-Derived Scaffolds Support Graft-Resident Thymopoiesis and Long-Term In Vitro Culture of Adult Thymic Epithelial Cells. *Adv. Funct. Mater.* 31, 2010747 (2021).
127. Silva, C. S. *et al.* Fibronectin-Functionalized Fibrous Meshes as a Substrate to Support Cultures of Thymic Epithelial Cells. *Biomacromolecules* 21, 4771–4780 (2020).
128. Bortolomai, I. *et al.* Gene Modification and Three-Dimensional Scaffolds as Novel Tools to Allow the Use of Postnatal Thymic Epithelial Cells for Thymus Regeneration Approaches. 1107–1122 (2019). doi:10.1002/sctm.18-0218
129. Pinto, S. *et al.* An Organotypic Coculture Model Supporting Proliferation and Differentiation of Medullary Thymic Epithelial Cells and Promiscuous Gene Expression. (2013). doi:10.4049/jimmunol.1201843
130. Tajima, A. *et al.* Bioengineering mini functional thymic units with EAK16-II / EAKIIIH6 self-assembling hydrogel. *Clin. Immunol.* 160, 82–89 (2015).
131. Suraiya, A. B., Hun, M. L., Truong, V. X., Forsythe, J. S. & Chidgey, A. P. Gelatin-Based 3D Microgels for in Vitro T Lineage Cell Generation. *ACS Biomater. Sci. Eng.* 6, 2198–2208 (2020).
132. Zeleniak, A. *et al.* De novo construction of T cell compartment in humanized mice engrafted with iPSC-derived thymus organoids. *Nat. Methods* 19, 1306–1319 (2022).
133. Poznansky, M. C. *et al.* Efficient generation of human T cells from a tissue-engineered thymic organoid. *Nat. Biotechnol.* 18, 729–734 (2000).
134. Lepletier, A. *et al.* Interplay between Follistatin, Activin A, and BMP4 Signaling Regulates Postnatal Thymic Epithelial Progenitor Cell Differentiation during Aging. *Cell Rep.* 27, 3887-3901.e4 (2019).
135. Barsanti, M. *et al.* A novel Foxn1eGFP/+ mouse model identifies Bmp4-induced maintenance of Foxn1 expression and thymic epithelial progenitor populations. *Eur. J. Immunol.* 47, 291–304 (2017).
136. Meireles, C. *et al.* Thymic crosstalk restrains the pool of cortical thymic epithelial cells with progenitor properties. *Eur. J. Immunol.* 47, 958–969 (2017).
137. Guillemot, F., Mironov, V. & Nakamura, M. Bioprinting is coming of age : report from the International Conference on Bioprinting and Biofabrication in Bordeaux (3B ' 09). 2, 1–7 (2010).
138. Groll, J. *et al.* Biofabrication: reappraising the definition of an evolving field. 8, (2016).
139. Zhang, Y. S. *et al.* 3D extrusion bioprinting. *Nat. Rev. Methods Prim.* 1, (2021).
140. Jo, Y., Hwang, D. G., Kim, M., Yong, U. & Jang, J. Bioprinting-assisted tissue assembly to generate organ substitutes at scale. *Trends Biotechnol.* 41, 93–105 (2023).
141. Levato, R. *et al.* Light-based vat-polymerization bioprinting. *Nat. Rev. Methods Prim.* 3, 47 (2023).
142. Daly, A. C., Prendergast, M. E., Hughes, A. J. & Burdick, J. A. Bioprinting for the Biologist. *Cell* 184, 18–32 (2021).
143. Malekpour, A. & Chen, X. Printability and Cell Viability in Extrusion-Based Bioprinting from Experimental , Computational , and Machine Learning Views. (2022).
144. Jakab, K. *et al.* Tissue Engineering by Self-Assembly of Cells Printed into Topologically Defined Structures. 14, (2008).
145. Mironov, V. *et al.* Biomaterials Organ printing : Tissue spheroids as building blocks q. *Biomaterials* 30, 2164–2174 (2009).
146. Norotte, C., Marga, F. S., Niklason, L. E. & Forgacs, G. Scaffold-free vascular tissue engineering using bioprinting. *Biomaterials* 30, 5910–5917 (2009).
147. Ayan, B. *et al.* Aspiration-assisted bioprinting for precise positioning of biologics. *Sci. Adv.* 6, 1–17 (2020).
148. Moldovan, N., Hibino, N. & Nakayama, K. Principles of the Kenzan Method for Robotic Cell Spheroid-Based Three-Dimensional Bioprinting. 23, (2017).
149. Daly, A. C., Davidson, M. D. & Burdick, J. A. 3D bioprinting of high cell-density heterogeneous tissue models through spheroid fusion within self- healing hydrogels. *Nat. Commun.* 1–13 doi:10.1038/s41467-021-21029-2
150. Skylar-scott, M. A. *et al.* Biomanufacturing of organ-specific tissues with high cellular

- density and embedded vascular channels. (2019).
151. Brassard, J. A., Nikolaev, M., Hübscher, T., Hofer, M. & Lutolf, M. P. Recapitulating macro-scale tissue self-organization through organoid bioprinting. *Nat. Mater.* 20, 22–29 (2021).
 152. Yu, Y. *et al.* Three-dimensional bioprinting using self-assembling scalable scaffold-free “tissue strands” as a new bioink. *Sci. Rep.* 6, (2016).
 153. Jeon, O., Lee, B. & Alsberg, E. Individual cell-only bioink and photocurable supporting medium for 3D printing and generation of engineered tissues with complex geometries. *Mater. Horizons* 6, 1625–1631 (2019).
 154. Lawlor, K. T. *et al.* Cellular extrusion bioprinting improves kidney organoid reproducibility and conformation. *Nat. Mater.* 20, 260–271 (2021).
 155. Gungor-Ozkerim, P. S., Inci, I., Zhang, Y. S., Khademhosseini, A. & Dokmeci, M. R. Bioinks for 3D bioprinting: an overview. *Biomater. Sci.* 6, 915–946 (2018).
 156. Gjorevski, N. *et al.* Designer matrices for intestinal stem cell and organoid culture. *Nature* 539, 560–564 (2016).
 157. Chrisnandy, A., Blondel, D., Rezakhani, S., Broguiere, N. & Lutolf, M. P. Synthetic dynamic hydrogels promote degradation-independent in vitro organogenesis. 21, (2022).
 158. Viola, J. M. *et al.* Guiding Cell Network Assembly using Shape-Morphing Hydrogels. 2002195, 1–9 (2020).
 159. Schmitt, M. & Greten, F. R. The inflammatory pathogenesis of colorectal cancer. *Nat. Rev. Immunol.* 21, 653–667 (2021).

**Chapter I – Optogenetic control over oncogenic mutations
at the cellular level for studying tumor initiation and growth
in a colon organoid-on-a-chip model**

Spatiotemporally resolved ex vivo colorectal cancer development in engineered mini-colons

L. Francisco Lorenzo-Martín^{1*}, Tania Hübscher^{1*}, Nicolas Broguiere¹, Amber D. Bowler^{2,3}, Jakob Langer¹, Lucie Tillard¹, Mikhail Nikolaev⁴, Freddy Radtke^{2,3}, and Matthias P. Lutolf^{1,4#}

¹Laboratory of Stem Cell Bioengineering, Institute of Bioengineering, School of Life Sciences and School of Engineering, Ecole Polytechnique Fédérale de Lausanne (EPFL), Lausanne 1015, Vaud, Switzerland.

²Swiss Institute for Experimental Cancer Research (ISREC), School of Life Sciences, Ecole Polytechnique Fédérale de Lausanne (EPFL), Lausanne 1015, Vaud, Switzerland.

³Swiss Cancer Center Lemman (SCCL), Lausanne 1015, Vaud, Switzerland

⁴Roche Institute for Human Biology (IHB), Roche Pharma Research and Early Development, Roche Innovation Center Basel, Basel 4058, Switzerland

* These authors contributed equally: L. Francisco Lorenzo-Martín, Tania Hübscher.

Corresponding author: matthias.lutolf@epfl.ch

Manuscript in revision in Nature

Abstract

Three-dimensional organoid culture technologies have revolutionized cancer research by allowing more realistic and scalable reproductions of both tumor and microenvironmental structures¹⁻³. This has enabled better modelling of low-complexity cancer cell behaviors that occur over relatively short periods of time⁴. However, available organoid systems do not capture the intricate evolutionary process of cancer development in terms of tissue architecture, cell diversity, homeostasis, and lifespan. Consequently, oncogenesis and tumor formation studies are not possible in vitro and instead require the extensive use of animal models, which provide limited spatiotemporal resolution of cellular dynamics and come at a heavy cost in resources and animal lives. Here we developed topobiologically complex mini-colons able to undergo tumorigenesis ex vivo by integrating microfabrication, optogenetic, and tissue engineering approaches. With this system, tumorigenic transformation can be spatiotemporally controlled by directing oncogenic activation through blue-light exposure, and emergent colon tumors can be tracked in real-time with single-cell resolution for several weeks without breaking the culture. These induced mini-colons display rich intra- and inter-tumoral diversity and recapitulate key pathophysiological hallmarks displayed by colorectal tumors in vivo. By fine-tuning cell-intrinsic and -extrinsic parameters, mini-colons can be leveraged to unveil tumorigenic determinants, including dietary patterns, microbiota-derived metabolites, and pharmacological therapies. As a whole, our work paves the way for animal-free cancer initiation research.

Article

Cancer arises through the accumulation of genetic lesions that confer unrestrained cell growth potential. Over the past 70 years, both two- (2D) and three-dimensional (3D) *in vitro* culture models have been developed to make simplified, animal-free versions of cancers readily available for research⁴. These models successfully portray and dissect a wide range of relatively simple cancer cell behaviors, such as proliferation, motility, invasiveness, survival, cell-cell and cell-stroma interactions, and drug responses, among others^{1,2,4}. However, modelling more complex processes that involve multiple cell (sub)types and tissue-level organization remains a challenge, as is the case for cancer initiation.

The cellular transition from healthy to cancerous is an intricate evolutionary process that is still largely obscure due to the insufficient topobiological complexity of the available *in vitro* cell culture systems, which precludes *de novo* tumor generation and the establishment of pathophysiologically relevant tumorigenic models^{5,6}. Even the current “gold standard” organoid-based 3D models, which are often postulated as a bridge between *in vitro* and *in vivo*^{1,3,7}, are too simplified for modeling cancer development *ex vivo*. This is mostly due to their *i)* closed cystic structure instead of an *in vivo*-like apically open architecture⁸, *ii)* short lifespan that requires breaking up the culture every few days for passaging⁹, *iii)* lack of topobiological stability and consistency because of their stochastic growth in 3D matrices⁸, and *iv)* inability to generate hybrid tissues composed of healthy and cancer cells in a balanced and integrated manner¹⁰. Various “next generation” approaches such as bioprinting and microfabrication technologies have been recently implemented to partially address some of these issues^{11,12}, however, none have been able to fully recreate intra- and inter-tumor complexity. Consequently, cancer research is still inevitably bound to animal experimentation, which provides a pathophysiologically relevant setting, but forbids high-resolution and real-time analyses of cellular dynamics during oncogenesis. In addition, these models are economically and ethically costly. Therefore, while there is the widespread consensus that animal usage in research should be reduced, replaced, and refined (the 3Rs¹³), this commitment is severely hindered by the insufficient physiological complexity displayed by classical *in vitro* systems.

Here, we postulated that a 3D system able to solve the existing limitations of *in vitro* cultures could be engineered by leveraging scaffold-guided organoid morphogenesis and optogenetics. Specifically, we developed miniature colon tissues where cells could *i)* be cultured for long durations (several weeks) without the need for breaking the culture through passaging, *ii)* reproduce the stem-differentiated cell patterning axis in a stable and anatomically relevant topology, *iii)* be easily mutated and tracked in a spatiotemporally controlled manner, and *iv)* create a biomechanically dynamic system that allows for tumor emergence while preserving

the integrity of the surrounding healthy tissue. These features permit the development of biologically-complex tumors *ex vivo*, bridging the gap between *in vitro* and *in vivo* models by providing a high-resolution animal-free system able to dissect the molecular factors orchestrating cancer initiation.

Spatiotemporally regulated *de novo* tumorigenesis in mini-colons

We focused on colorectal cancer (CRC) since it is one of the most prominent cancer types worldwide and its malignant transformation can be readily engineered genetically^{14,15}. To first achieve spatiotemporal control of oncogenic DNA recombination, we developed a doxycycline-sensitive blue-light-regulated Cre system (referred to as “OptoCre”), which we then introduced into inducible *Apc*^{fl/fl};*Kras*^{LSL-G12D/+};*Trp53*^{fl/fl} (“AKP”) healthy colon organoids (Fig. S1a-c). A fluorescent Cre reporter was also incorporated to track cells that have undergone oncogenic recombination (Fig. S1b,c). We initially tested the system in conventional organoid cultures, where OptoCre efficiently induced recombination in the presence of blue light and doxycycline (Fig. S1d,e). Dosage optimization prevented unwanted activation by coupling high efficiency with low leakiness (~1.6%) (Fig. S1d,e). To confirm successful oncogenic transformation, we removed growth factors (EGF, Noggin, R-spondin, Wnt3a) from the organoid medium and observed that only cells with an activated OptoCre were able to grow, a well-known hallmark of mutated AKP colon organoids¹⁶ (Fig. S1f). The presence of the expected mutations in the *Apc*, *Kras* and *Trp53* loci was confirmed by PCR and exome sequencing (see below, Fig. S2g,h).

Based on previous evidence that small intestine cells can form stable tube-shaped epithelia through scaffold-guided organoid morphogenesis in microfluidic devices⁹, we next aimed at establishing a “mini-colon” constituted by OptoCre-AKP cells. By seeding colon cell suspensions in hydrogel-patterned microfluidic devices, we generated single-layered colonic epithelia spatially arranged into crypt- and lumen-like domains (Fig. S2a). This spatial arrangement recapitulated the spatial distribution found *in vivo*, with stem and progenitor (Sox9⁺) cells located at the bottom of the crypt domains and more differentiated colonocytes (Fabp1⁺) located in the upper crypt and lumen areas (Fig. S2b)^{17,18}. Unlike conventional colon organoids, the lumen of these mini-colons was readily perfusable with fresh medium, allowing the removal of cell debris and extending their lifespan to several weeks without the need for passaging or tissue disruption (Fig. S2a).

Once the healthy mini-colon system was established, we explored its potential to capture tumor biology by inducing oncogenic recombination through blue-light illumination (Fig. 1a). To mimic the scenario found *in vivo*, we fine-tuned OptoCre activation to mutate only a small number of

cells (<0.5% of the total population). Because of the stability and defined topology of the mini-colon, we easily detected the acquisition of AKP mutations at the single-cell level (GFP⁺ cells) and tracked their evolution over time (Fig. S2c,d). This revealed that cell death is one of the earliest responses to oncogenic recombination, as around ~60% of the mutated colon cells underwent apoptosis in the following 48 hours (Supplementary Video 1). This response is a well-described “fail-safe” mechanism that protects healthy epithelia from tumor development¹⁹, thus showing that homeostatic responses are preserved in the mini-colon. Nevertheless, some mutated cells escaped apoptosis and, after a quiescent period (24–72 hours), started dividing at an accelerated pace (Fig. S2d). In conventional organoid cultures, these fast-proliferating mutated cells did not lead to any overt cellular rearrangements (Fig. 1b), whereas in the mini-colon system they developed neoplastic structures over 5–10 days (Fig. 1b). Furthermore, these mini-colon neoplasias evolved from polyp-like to full-blown tumors, recapitulating in vivo tumor development (Fig. 1b,c, Supplementary Videos 2,3). Histopathological analyses revealed that mini-colon tumors were not formed by the stochastic aggregation of undifferentiated cells, but rather displayed the histological organization characteristic of tubular adenomas (Fig. S2e). More importantly, immunostaining showed that these tumors stemmed from CD44^{high} cells – a bona fide marker for cancer stem cells in vivo²⁰ – at the base of the epithelium (Figs. 1d, S2f; Supplementary Video 4). Additionally, the bulk of the tumors was composed of cells with different degrees of differentiation, as revealed by the down- and upregulation of CD44 and Fabp1, respectively (Fig. 1d, Supplementary Video 5). This indicated the existence of intratumor heterogeneity in the mini-colon, further resembling the in vivo scenario²¹.

We confirmed through PCR and exome sequencing that tumor development in the mini-colon was directly associated with the expected mutations in *Apc*, *Kras*, and *Trp53* loci (Fig. S2g,h). In line with this, using an organoid line with reduced mutational burden (*Apc*^{fl/fl};*Kras*^{LSL-G12D/+}) produced longer latencies in tumor development (Fig. 1e), demonstrating that mini-colon tumorigenesis can be modulated by the number of oncogenic driver mutations. Collectively, these data show that the mini-colon system allows spatiotemporally controlled in vitro modelling of CRC tumorigenesis with an unprecedented degree of topobiological complexity.

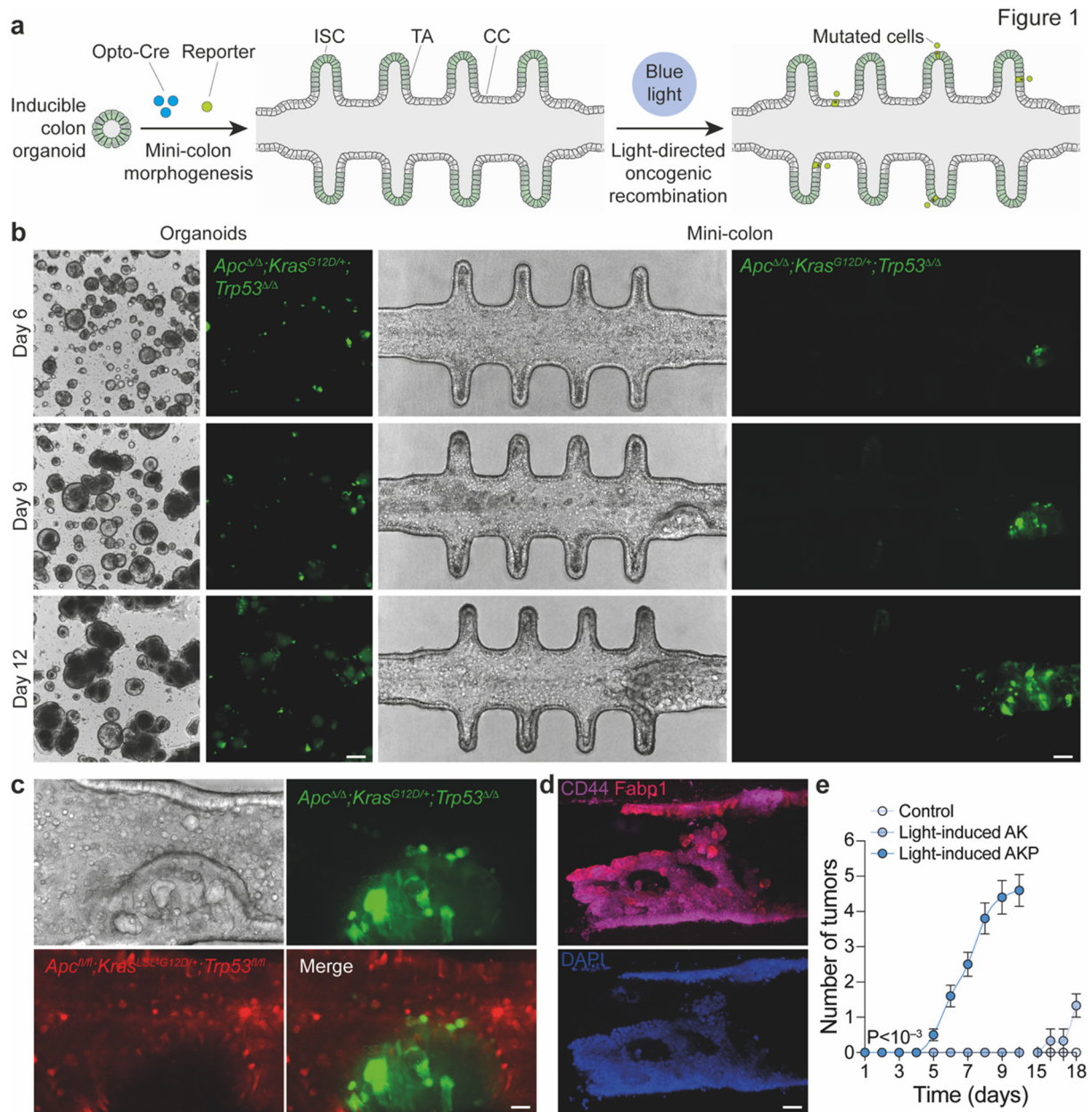


Figure 1 Spatiotemporally regulated de novo tumorigenesis in mini-colons. **a**, Schematic of the experimental workflow followed to induce tumorigenesis in mini-colons. **b**, Brightfield and fluorescence images of time-course tumorigenesis experiments in conventional organoids and mini-colons. Fluorescence signal indicates oncogenic recombination. Scale bars, 200 μm (organoids) and 75 μm (mini-colons). **c**, Brightfield and fluorescence close-up images of a mini-colon tumor. Red and green signals correspond to healthy and mutated cells, respectively. Scale bar, 25 μm. **d**, Immunofluorescence images of a mini-colon tumor showing the presence of CD44 (top, magenta), Fabp1 (top, red), and nuclei (bottom, blue). Scale bar, 35 μm. **e**, Multiplicity of tumors emerged in mini-colons of the indicated genotypes upon light-mediated oncogenic induction. P < 0.0001 (two-way ANOVA and Sidak's multiple comparisons test; n = 5, 3, and 10 for control, light-induced AK, and light-induced AKP mini-colons, respectively). Data represent mean ± SEM. ISC, intestinal stem cell; TA, transit-amplifying cell; CC, colonocyte.

Mini-colons display context-dependent tumorigenic plasticity

Careful examination of induced mini-colons revealed consistent morphological differences among tumors according to their initiation site, with prominent dense or cystic internal structures arising from the crypt and the luminal epithelium, respectively (see below, Fig. 2b, top panel). Since mini-colons comprise different types of cells along the crypt-lumen axis (Fig. S2b), we leveraged the spatial resolution provided by OptoCre to investigate whether the initiating cell niche conditioned the morphological and functional features of nascent tumors. To spatially control AKP mutagenesis, we coupled the mini-colon to a photomask restricting blue-light exposure to specific regions of the colonic epithelium (Fig. 2a), which provided low off-target recombination rates (~8.5%) (Figs. 2b,c, S3a). Here again, dense and cystic tumors developed when crypt and lumen epithelia, respectively, were mutationally targeted by blue light (Fig. 2b). To confirm this was associated with the differentiation status of the tumor-initiating cell, we cultured mini-colons in either low- or high-differentiation medium before oncogenic induction to shift the proportions of (un)differentiated cells. Low-differentiation conditions produced mini-colons with thicker epithelia, early tumor development, and a reduced fraction of cystic tumors (Fig. 2d, Fig. S3b,c). Conversely, high-differentiation conditions produced mini-colons with thinner epithelia, delayed tumor formation, and increased cystic tumor frequency (Fig. 2d, Fig. S3b,c). These results indicate that the different environments of the mini-colon can shape tumor fate.

To evaluate the functional repercussions of the tumor-initiating niche, we isolated cancer cells from mini-colons enriched in either crypt- or lumen-derived tumors and established organoid cell lines (termed “mini-colon AKP”) (Fig. 2e). As a control, we generated AKP mutant organoids by shining blue light on inducible organoids and kept these mutants in parallel with their mini-colon equivalents, doing the required passages upon confluency (termed “organoid AKP”) (Fig. 2e). We also established organoid cultures from AKP colon tumors extracted from tamoxifen-treated *Cdx2-CreERT2* AKP mice (termed “in vivo AKP”) (Fig. 2e). Notably, unlike in mini-colons, none of these three types of mutant AKP lines were morphological distinguishable from healthy non-mutated cells when cultured as organoids (Figs. 1b and S3d). When we cultured these organoids in basal medium depleted of growth factors (BM, see Methods), both “in vivo” and crypt tumor-derived “mini-colon AKP” organoids preserved their proliferative potential (Fig. 2f,g). Conversely, “organoid” and lumen tumor-enriched “mini-colon AKP” lines displayed significantly reduced proliferation rates (Fig. 2f,g). This was not due to intrinsic cycling defects in any of the organoid lines tested, as these differences were not observed in standard cancer organoid medium (BMGF, see Methods) (Fig. S3e). As expected, healthy organoids did not grow in any of these conditions (Figs. 2f,g, S3e). Collectively, these results show that there are context-dependent factors aside from the founding AKP mutations

that condition the growth potential of AKP cells. They also indicate that the cells derived from mini-colon crypt tumors recapitulate the behavior of in vivo CRC cells more faithfully than conventional organoids.

To investigate the molecular programs underpinning these observations, we profiled the transcriptome of the different AKP lines by RNA sequencing. We first characterized the differences between the two AKP lines derived from conventional systems, “in vivo” and “organoid AKP” cells, which also had the biggest disparity in growth potential (Fig. 2g). Similarly to our previous experiments, “in vivo AKP” cells upregulated many genes involved in canonical cancer pathways and the promotion of cell growth (Fig. S3f,g). Conversely, these cells downregulated genes associated with cell differentiation, patterning, and transcription regulation (Fig. S3f,g). To evaluate whether “mini-colon AKP” cells recapitulated this “in vivo AKP” transcriptional signature, we performed single-sample GSEA across all cell lines. Here, most “mini-colon AKP” lines outscored their “organoid AKP” counterparts, especially those derived from crypt tumors (Fig. S3h). To investigate the transcriptional divergence between crypt- and lumen-enriched “mini-colon AKP” cells, we compared the lines with the highest (#v, crypt-enriched) and lowest (#i, lumen-enriched) “in vivo AKP” signature score (Fig. S3h). These analyses revealed that crypt-derived “mini-colon AKP” cells upregulated genes involved in Wnt signaling, stem cell pluripotency, lipid metabolism, and other pathways involved in cancer (Fig. S3i). These findings are well aligned with the growth potential of these cells upon growth factor deprivation (Fig. 2g). Taken together, these data indicate that the mini-colon is a plastic system where context-dependent factors can drive different functional features in CRC cells.

Figure 2

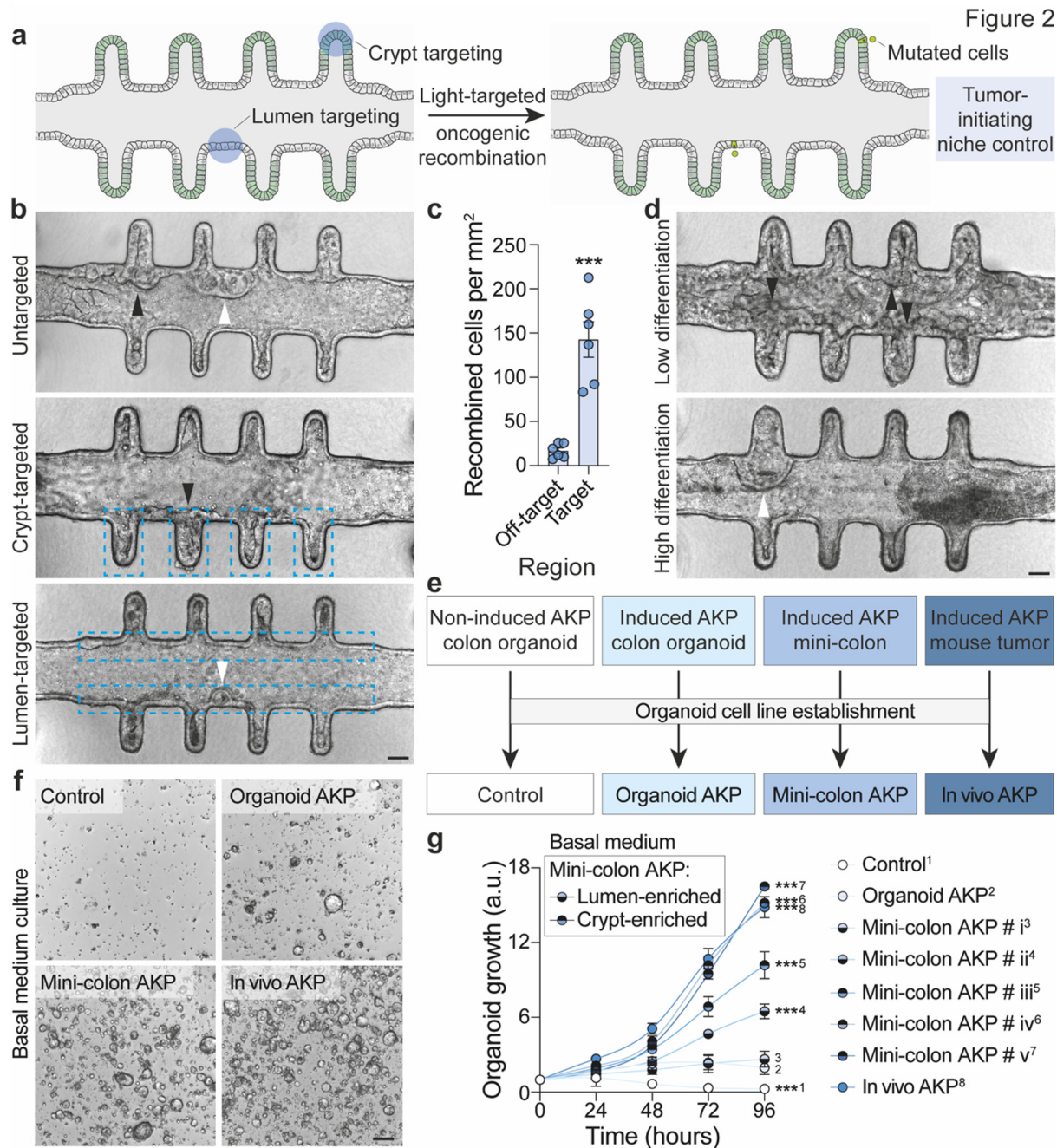


Figure 2 Mini-colons display context-dependent tumorigenic plasticity. **a**, Schematic of the experimental workflow followed to spatiotemporally target tumorigenesis in mini-colons. **b**, Brightfield images of mini-colons that have undergone untargeted (top), crypt-targeted (middle), and lumen-targeted (bottom) tumorigenesis. Targeted areas are delimited with a dashed blue line. Black and white arrowheads indicate tumors with compact and cystic morphologies, respectively. Scale bar, 75 μm . **c**, Oncogenic recombination efficiency in targeted and off-target areas in mini-colons. *** $P < 0.001$ (two-tailed t -test; $n = 6$ per condition). Each point represents one mini-colon. **d**, Brightfield images of induced mini-colons cultured in low- (top, WENRNI) and high-differentiation (bottom, ENR) conditions. Black and white arrowheads indicate tumors with compact and cystic morphologies, respectively. Scale bar, 75 μm . **e**, Schematic of the different colon organoid lines generated in this work. **f**, Brightfield images of the indicated colon organoid lines cultured for 2 days in basal medium. Scale bar, 200 μm . **g**, Metabolic activity (measured using resazurin) of the indicated colon organoid lines cultured in basal medium for the indicated time. Numeric labeling (1-8) is used to facilitate cell line identification. *** $P < 0.001$ (two-way ANOVA and Sidak's multiple comparisons test; $n = 3$ for each line). In **c** and **g**, data represent mean \pm SEM.

Mini-colons support intra- and inter-tumor heterogeneity

We hypothesized that the diversity observed in tumor morphology and growth potential reflected clonally and molecularly distinct tumor types formed within the mini-colon. To validate this idea, we performed single-cell transcriptomic profiling of tumor-bearing mini-colons incorporating a genetic cell barcoding system²² to preserve clonal information (Fig. 3a). Based on bona fide transcriptional markers, mini-colons comprised eight major cell types that were segregated into undifferentiated, absorptive, and secretory lineages (Fig. 3b). Undifferentiated (*Krt20*⁻) cells included stem (*Lgr5*⁺), actively proliferating (*Mki67*⁺), and progenitor (*Sox9*⁺, *Cd44*⁺) cells (Figs. 3b,c, S4a). Mature (*Krt20*⁺) absorptive colonocytes constituted the largest fraction of the mini-colon, and included bottom, middle, and top colonocytes based on zonation markers²³ (*Aldob*, *Iqgap2*, *Ctca4a*, etc.) (Figs. 3b,c, S4a). Mucus-producing goblet cells (*Muc2*⁺) and hormone-releasing enteroendocrine cells (*Neurod1*⁺) constituted the secretory compartment (Figs. 3b,c, S4a). Collectively, this diverse in vivo-like cell composition indicates that mini-colons provide a physiologically relevant context for conducting oncogenesis studies.

To unveil the clonal identities across the mini-colon, we compared the genetic barcodes among cells and detected 83 clonal populations. We then discarded small (<5 cells) clones and identified cells containing reads corresponding to the mutated versions of *Apc* and *Trp53* (Fig. S4b,c). These bona fide tumor cells distinguished tumor clonal populations (18 classified) from healthy counterparts (16 classified) (see Methods for details) (Fig. S4d). On average, healthy clonal populations consisted of ~18% undifferentiated cells, which gave rise to the remaining ~82% of absorptive colonocytes and secretory cells (Fig. 3d,e). Conversely, mini-colon tumors were mostly formed by undifferentiated cells (~92%), with sparsely present colonocytes and secretory cells (Fig. 3d,e). Tumor cells also formed larger clonal populations than healthy counterparts (Fig. 3f). These cell proportions are well aligned with the ones commonly observed in vivo^{24,25}.

Analyses of the internal structure of single clonal tumors showed that they comprised a non-homogeneous collection of cells with different proliferation, differentiation, and stemness markers (Fig. S5a). Such intra-tumor heterogeneity reflects the complexity of mini-colon tumors, in line with our immunostaining data (Fig. 1d). To investigate the mechanisms orchestrating cancer stemness and tumor development, we analyzed the transcriptional differences between differentiated (*Krt20*⁺, *Apoc2*⁺, *Fabp2*⁺) and stem (*Lgr5*⁺, *Cd44*⁺, *Sox9*⁺) cancer cells within tumors. We found that *Gpx2*, a glutathione peroxidase recently linked to CRC malignant transformation²⁴, strongly correlates with the stemness potential of mini-colon cancer cells (Fig. 3g).

To explore whether mini-colons could produce different types of tumors, we then compared the transcriptional profiles of the different tumor clones. Even though all tumor-initiating cells

carried the same founding AKP mutations and shared many molecular features, we found clear diversity across mini-colon tumors (Fig. S5b). For instance, the expression of the interleukin *Il1a* and leukocyte peptidase inhibitor *Sipi* revealed the presence of tumors with an inflammatory-like profile (Figs. 3h,i, S5c). *Cdkn2a* (coding for tumor suppressors p14 and p16) and *Prdm16* were exclusively expressed by actively proliferating tumors able to escape the cell cycle arrest mediated by these genes (Figs. 3h,i, S5c). *Aqp5*, an aquaporin inductor of gastric and colon carcinogenesis²⁶, marked specific tumors able to produce the oncogenesis-promoting fibroblast growth factor Fgf13 (Fig. S5b,c). Together with other markers (Fig. S5b,c), these data indicate that a variety of tumor subtypes can be generated in the mini-colon, arguably due to tumor niche-intrinsic and/or environmental factors. This likely accounts for the observed differences among “mini-colon AKP” cell lines (Figs. 2g, S3h,i), since they show uneven enrichments in signatures from different types of tumors (Fig. S5d). Collectively, these findings demonstrate that the mini-colon is a complex cellular ecosystem that recreates both healthy and cancer cell diversity.

Figure 3

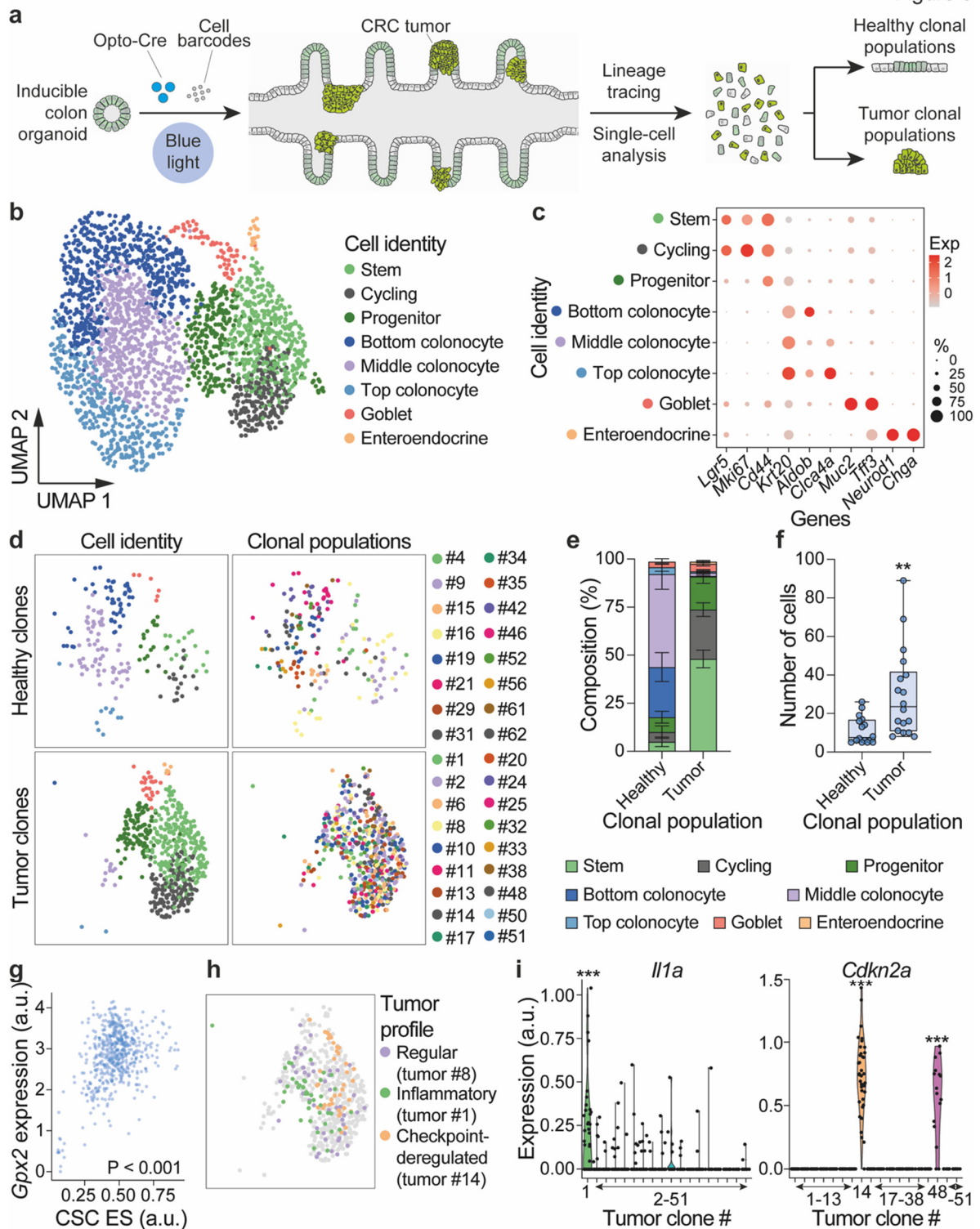


Figure 3 Mini-colons support intra- and inter-tumor heterogeneity. **a**, Schematic of the experimental workflow followed for single-cell and lineage tracing analysis of mini-colons. **b**, Unsupervised UMAP clustering of the main cell types in mini-colons 7 days after tumorigenic induction. **c**, Expression of representative cell-type specific markers in the different cell populations comprising mini-colons. **d**, Unsupervised clustering (UMAP) of healthy (top) and tumor (bottom) clonal populations in mini-colons. The cell type (left, legend as panel b) and clonal identity (right) are indicated. **e**, Relative cell-type abundance in healthy and tumor mini-colon clonal populations. Data represent mean \pm SEM. $n = 16$ and 18 for healthy and tumor clones, respectively. **f**, Healthy and tumor mini-colon clonal population sizes.

** $P < 0.01$ (two-tailed Mann Whitney test; $n = 16$ and 18 for healthy and tumor clones, respectively). Boxes indicate the median and the first and third quartiles. Each point represents one clonal population. **g**, Correlation between *Gpx2* expression and cancer stem cell transcriptional signature enrichment (*CD44*, *Lgr5*, *Sox9*). $P < 10^{-5}$ (Pearson correlation coefficient test; $n = 540$). Each point represents one cell. **h**, UMAP plot showing the distribution of cells belonging to different types of tumors. **i**, Expression of the indicated genes in the indicated tumor clones. *** $P < 0.001$ (Wilcoxon rank-sum test; $n = 540$). Each point represents one cell. CSC, cancer stem cell; ES, enrichment score.

Mini-colons allow physiologically relevant screening of tumorigenic factors

The longevity, experimental flexibility, and tumor formation dynamics of mini-colons provides an unparalleled in vitro setup for conducting tumorigenesis assays. We thus next used mini-colons as screening tools for identifying molecules with a prominent role in tumor development. Since our scRNAseq analyses revealed *Gpx2* overexpression in cancer stem cells (Fig. 3g), we validated its functional relevance by adding the glutathione peroxidase inhibitor tiopronin²⁷ to the basal medium reservoirs of mini-colons right after blue–light-induced AKP mutagenesis (Fig. 4a). Basal application of the drug provides ubiquitous exposure on the mini-colon basolateral domain, mimicking a systemic therapy model (Fig. 4a). By the time control mini-colons developed full-blown tumors, tiopronin-treated counterparts were largely tumor-free with a healthy colonic epithelium (Fig. 4b,c). Together with reduced tumor development kinetics, tiopronin also decreased tumor burden in the longer term (Fig. 4c). These experiments suggest that *Gpx2* activity is exploited by cancer stem cells to drive tumor initiation, shedding light on some questions concerning this protein recently raised by a large-scale single-cell RNA-Seq characterization of human CRC tumors²⁴. Importantly, mini-colons were instrumental for this finding, since conventional organoid cultures could not reveal differences in tumor-forming capabilities, only in proliferation rates (Fig. S6a).

Colon tumorigenesis in vivo is heavily modulated by a myriad of environmental molecules, such as the metabolites produced by colon-residing microbiota²⁸, that continuously contact the luminal side of colonocytes. The impact of these molecules cannot be faithfully evaluated in conventional organoid cultures, as their lumen is not accessible. Since mini-colons address this limitation, we validated whether they could model the role of bacterial metabolites whose tumorigenic function has been corroborated in vivo. To that end, we administered specific metabolites exclusively in the luminal side of healthy mini-colons and, after a conditioning period of 2 days, induced oncogenic recombination (Fig. 4d). When luminally exposed to deoxycholic acid, a bona fide tumor-promoting metabolite^{28,29}, mini-colons developed tumors with fast kinetics and high multiplicity (Fig. 4e,f). Conversely, both tumor-suppressive butyrate^{28,30} and β -hydroxybutyrate³¹ slowed tumor development and reduced multiplicity (Fig. 4e,f). These results demonstrate that mini-colons faithfully recapitulate the in vivo

pathophysiological responses to bacterial metabolites, whereas conventional organoid cultures did not provide informative data on the tumorigenic relevance (Fig. 4e).

Dietary components also constitute a relevant source of luminal factors conditioning colon tumorigenesis³². Therefore, we performed analogous experiments modeling diets with different caloric contents (Fig. 4d). These revealed that calorie restriction in the luminal space effectively reduced tumor burden when compared to calorie-enriched medium (Figs. 4g, S6b), in line with *in vivo* evidence³³. To show the relevance of luminal accessibility, we placed the same amount of dietary medium in the basal medium reservoirs instead of the luminal space (Fig. S6c). Here, no differences were observed between the two dietary patterns (Fig. S6d,e), thus indicating that an accessible lumen – a forbidden feature in conventional organoids – is decisive for the physiologically relevant modelling of colon biology. Collectively, these findings demonstrate that the mini-colon is a versatile tool that allows faithful *in vitro* recapitulation of CRC tumorigenesis and its environmental determinants.

Figure 4

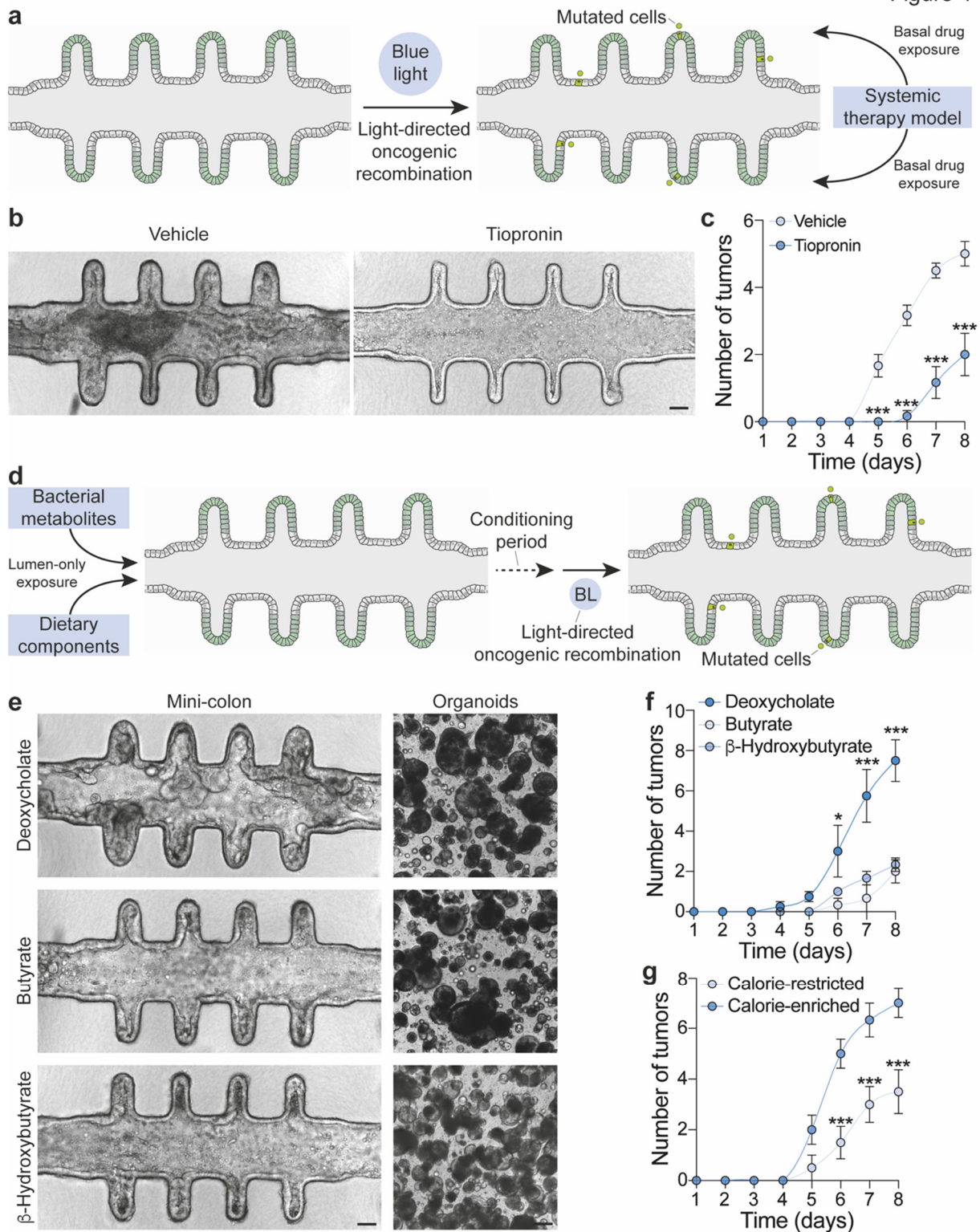


Figure 4 Mini-colons allow physiologically relevant screening of tumorigenic factors. **a**, Schematic of the experimental workflow followed for systemic therapy modeling in mini-colons. **b**, Brightfield images of mini-colons treated with vehicle (left) or tiopronin (right) after tumorigenic recombination. Images correspond to 6 days after induction. Scale bar, 75 μ m. **c**, Multiplicity of tumors emerged in mini-colons treated with the indicated compound upon oncogenic induction. ***P < 0.001 (two-way ANOVA and Sidak's multiple comparisons test; n = 6 for each condition). **d**, Schematic of the experimental workflow followed for microbiota and dietary pattern modeling in mini-colons. **e**, Brightfield images of mini-colons (left) and conventional organoids (right) treated with the indicated microbiota-

derived metabolites. Images correspond to 7 days after tumorigenic induction. Scale bars, 75 μm (mini-colons), 200 μm (organoids). **f**, Multiplicity of tumors emerged in mini-colons treated with the indicated microbiota-derived metabolites. * $P < 0.05$, *** $P < 0.001$ (two-way ANOVA and Sidak's multiple comparisons test; $n = 4, 3$, and 3 for deoxycholate, butyrate, and β -hydroxybutyrate, respectively). **g**, Multiplicity of tumors emerged in mini-colons treated with the indicated dietary patterns. *** $P < 0.001$ (two-way ANOVA and Sidak's multiple comparisons test; $n = 4$ and 3 for calorie-restricted and -enriched diets, respectively). In **c**, **f** and **g**, data represent mean \pm SEM. BL, blue light.

Here we show that the mini-colon model shifts the paradigm of cancer initiation research, allowing ex vivo tumorigenesis with unparalleled pathophysiological intricacy. Coupled with spatiotemporal control of oncogenesis, real-time single cell resolution, and broad experimental flexibility, this system opens new perspectives for animal-free screening of cellular and molecular determinants of cancer development. Supporting this, mini-colons faithfully reflect in vivo-like responses to microbiota-derived metabolites, whereas conventional organoids provide much coarser data³¹. Likewise, our model can help predict the efficacy of tumor-suppressive drugs not yet validated in vivo, as illustrated by the finding that glutathione peroxidase inhibition abrogates tumor development, in line with existing evidence on the implication of Gpx2 in CRC^{24,34}. Importantly, mini-colon complexity can be readily enhanced by including stromal and immune cells in the surrounding biomimetic extracellular matrix. Current lines of work have also proved that this model can be applied to patient-derived colorectal cancer specimens. Lastly, we anticipate that by adapting its biomechanical properties, topology, and culture conditions, it will be possible to expand the system to other prominent epithelial cancer types, such as lung, breast, or prostate, bringing a groundbreaking experimental resource to multiple fields.

References

1. Drost, J. & Clevers, H. Organoids in cancer research. *Nat Rev Cancer* **18**, 407-418 (2018).
2. Rodrigues, J., Heinrich, M. A., Teixeira, L. M. & Prakash, J. 3D In Vitro Model (R)evolution: Unveiling Tumor-Stroma Interactions. *Trends Cancer* **7**, 249-264 (2021).
3. Tuveson, D. & Clevers, H. Cancer modeling meets human organoid technology. *Science* **364**, 952-955 (2019).
4. Katt, M. E., Placone, A. L., Wong, A. D., Xu, Z. S. & Searson, P. C. In Vitro Tumor Models: Advantages, Disadvantages, Variables, and Selecting the Right Platform. *Front Bioeng Biotechnol* **4**, 12 (2016).
5. Lee-Six, H. *et al.* The landscape of somatic mutation in normal colorectal epithelial cells. *Nature* **574**, 532-537 (2019).
6. Vendramin, R., Litchfield, K. & Swanton, C. Cancer evolution: Darwin and beyond. *EMBO J* **40**, e108389 (2021).
7. Kim, J., Koo, B. K. & Knoblich, J. A. Human organoids: model systems for human biology and medicine. *Nat Rev Mol Cell Biol* **21**, 571-584 (2020).
8. Sato, T. *et al.* Single Lgr5 stem cells build crypt-villus structures in vitro without a mesenchymal niche. *Nature* **459**, 262-265 (2009).
9. Nikolaev, M. *et al.* Homeostatic mini-intestines through scaffold-guided organoid morphogenesis. *Nature* **585**, 574-578 (2020).
10. Krotenberg Garcia, A. *et al.* Active elimination of intestinal cells drives oncogenic growth in organoids. *Cell Rep* **36**, 109307 (2021).
11. Liu, X. *et al.* Tumor-on-a-chip: from bioinspired design to biomedical application. *Microsyst Nanoeng* **7**, 50 (2021).
12. Augustine, R. *et al.* 3D Bioprinted cancer models: Revolutionizing personalized cancer therapy. *Transl Oncol* **14**, 101015 (2021).
13. Hubrecht, R. C. & Carter, E. The 3Rs and Humane Experimental Technique: Implementing Change. *Animals (Basel)* **9** (2019).
14. Keum, N. & Giovannucci, E. Global burden of colorectal cancer: emerging trends, risk factors and prevention strategies. *Nat Rev Gastroenterol Hepatol* **16**, 713-732 (2019).
15. Bürtin, F., Mullins, C. S. & Linnebacher, M. Mouse models of colorectal cancer: Past, present and future perspectives. *World J Gastroenterol* **26**, 1394-1426 (2020).
16. Drost, J. *et al.* Sequential cancer mutations in cultured human intestinal stem cells. *Nature* **521**, 43-47 (2015).
17. Gehart, H. & Clevers, H. Tales from the crypt: new insights into intestinal stem cells. *Nat Rev Gastroenterol Hepatol* **16**, 19-34 (2019).
18. Levy, E. *et al.* Localization, function and regulation of the two intestinal fatty acid-binding protein types. *Histochem Cell Biol* **132**, 351-367 (2009).
19. Shortt, J. & Johnstone, R. W. Oncogenes in cell survival and cell death. *Cold Spring Harb Perspect Biol* **4** (2012).
20. Du, L. *et al.* CD44 is of functional importance for colorectal cancer stem cells. *Clin Cancer Res* **14**, 6751-6760 (2008).
21. Fleming, M., Ravula, S., Tatishchev, S. F. & Wang, H. L. Colorectal carcinoma: Pathologic aspects. *J Gastrointest Oncol* **3**, 153-173 (2012).
22. Bidy, B. A. *et al.* Single-cell mapping of lineage and identity in direct reprogramming. *Nature* **564**, 219-224 (2018).
23. Moor, A. E. *et al.* Spatial Reconstruction of Single Enterocytes Uncovers Broad Zonation along the Intestinal Villus Axis. *Cell* **175**, 1156-1167.e1115 (2018).
24. Becker, W. R. *et al.* Single-cell analyses define a continuum of cell state and composition changes in the malignant transformation of polyps to colorectal cancer. *Nat Genet* **54**, 985-995 (2022).
25. Snippert, H. J. *et al.* Intestinal crypt homeostasis results from neutral competition between symmetrically dividing Lgr5 stem cells. *Cell* **143**, 134-144 (2010).

26. Kang, S. K. *et al.* Role of human aquaporin 5 in colorectal carcinogenesis. *Am J Pathol* **173**, 518-525 (2008).
27. Hall, M. D. *et al.* Inhibition of glutathione peroxidase mediates the collateral sensitivity of multidrug-resistant cells to tiopronin. *J Biol Chem* **289**, 21473-21489 (2014).
28. Louis, P., Hold, G. L. & Flint, H. J. The gut microbiota, bacterial metabolites and colorectal cancer. *Nat Rev Microbiol* **12**, 661-672 (2014).
29. Bernstein, C. *et al.* Carcinogenicity of deoxycholate, a secondary bile acid. *Arch Toxicol* **85**, 863-871 (2011).
30. Wu, X. *et al.* Effects of the intestinal microbial metabolite butyrate on the development of colorectal cancer. *J Cancer* **9**, 2510-2517 (2018).
31. Dmitrieva-Posocco, O. *et al.* β -Hydroxybutyrate suppresses colorectal cancer. *Nature* **605**, 160-165 (2022).
32. Veettil, S. K. *et al.* Role of Diet in Colorectal Cancer Incidence: Umbrella Review of Meta-analyses of Prospective Observational Studies. *JAMA Netw Open* **4**, e2037341 (2021).
33. Castejón, M. *et al.* Energy Restriction and Colorectal Cancer: A Call for Additional Research. *Nutrients* **12** (2020).
34. Emmink, B. L. *et al.* GPx2 suppression of H₂O₂ stress links the formation of differentiated tumor mass to metastatic capacity in colorectal cancer. *Cancer Res* **74**, 6717-6730 (2014).
35. Wang, X., Chen, X. & Yang, Y. Spatiotemporal control of gene expression by a light-switchable transgene system. *Nat Methods* **9**, 266-269 (2012).
36. Sokolik, C. *et al.* Transcription factor competition allows embryonic stem cells to distinguish authentic signals from noise. *Cell Syst* **1**, 117-129 (2015).
37. Dobin, A. *et al.* STAR: ultrafast universal RNA-seq aligner. *Bioinformatics* **29**, 15-21 (2013).
38. Robinson, M. D., McCarthy, D. J. & Smyth, G. K. edgeR: a Bioconductor package for differential expression analysis of digital gene expression data. *Bioinformatics* **26**, 139-140 (2010).
39. Robinson, M. D. & Oshlack, A. A scaling normalization method for differential expression analysis of RNA-seq data. *Genome Biol* **11**, R25 (2010).
40. Law, C. W., Chen, Y., Shi, W. & Smyth, G. K. voom: Precision weights unlock linear model analysis tools for RNA-seq read counts. *Genome Biol* **15**, R29 (2014).
41. Reiner, A., Yekutieli, D. & Benjamini, Y. Identifying differentially expressed genes using false discovery rate controlling procedures. *Bioinformatics* **19**, 368-375 (2003).
42. Subramanian, A. *et al.* Gene set enrichment analysis: a knowledge-based approach for interpreting genome-wide expression profiles. *Proc Natl Acad Sci U S A* **102**, 15545-15550 (2005).
43. Dennis, G. *et al.* DAVID: Database for Annotation, Visualization, and Integrated Discovery. *Genome Biol* **4**, P3 (2003).
44. Walter, W., Sánchez-Cabo, F. & Ricote, M. GOplot: an R package for visually combining expression data with functional analysis. *Bioinformatics* **31**, 2912-2914 (2015).
45. Zheng, G. X. *et al.* Massively parallel digital transcriptional profiling of single cells. *Nat Commun* **8**, 14049 (2017).
46. Kong, W. *et al.* CellTagging: combinatorial indexing to simultaneously map lineage and identity at single-cell resolution. *Nat Protoc* **15**, 750-772 (2020).
47. Hao, Y. *et al.* Integrated analysis of multimodal single-cell data. *Cell* **184**, 3573-3587.e3529 (2021).

Acknowledgements

We thank Prof. M. Thomson for the original light-inducible plasmids; Prof. M. Wernig and Dr. G. Neumayer for the initial idea and work on the doxycycline- and light-inducible system; Dr. C. Baur for discussing, designing, and building the custom illumination device; A. Chrisnandy for assistance on photomask fabrication; O. Mitrofanova and Y. Tinguely for assistance on microdevice fabrication; Dr. D. Dutta and Dr. S. Li for inputs on organoid work; and J. Pr ebandier for administrative assistance. We acknowledge support from the following EPFL core facilities: CMI, PTBTG, HCF, BIOP, FCCF, BSF, and GECF. This work was funded by the Swiss Cancer League (KFS-5103-08-2020), the Personalized Health and Related Technologies (PHRT) Initiative from the ETH Board, and EPFL.

Author contributions

L.F.L.-M. conceived the study, designed experiments, carried out the experimental and bioinformatic work, analyzed the data, performed artwork design, and wrote the manuscript. T.H. generated the OptoCre module and blue light-associated systems, designed experiments, carried out experimental work, and analyzed data. N.B. carried out bioinformatic work and analyzed data. A.B. performed mouse-related work and isolated primary cells. J.L. produced the microfluidic devices, optimized hydrogel patterning, and generated mini-colon histological sections. L.T. carried out experimental work. M.N. designed and developed the first mini-gut system. F.R. helped to conceive the work. M.P.L. conceived the work, designed experiments, and editing the manuscript.

Extended data figures and supplementary videos

Figure S1

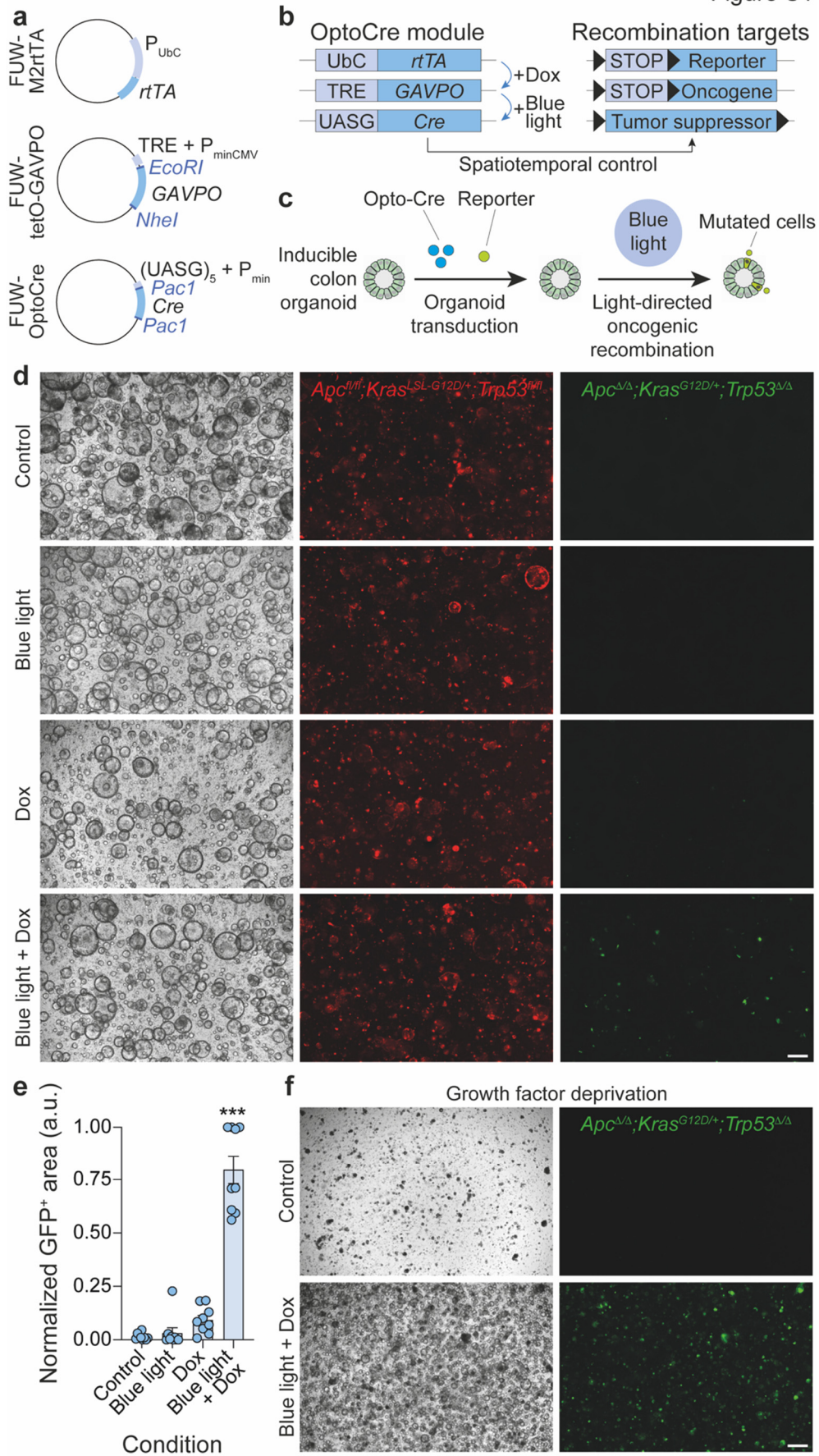


Figure S1 Generation of blue–light-inducible AKP colon organoids. **a**, Schematic of the plasmids comprising the OptoCre module. The promoter, gene, and restriction sites used to generate the plasmids are indicated. **b**, Schematic of the integration of the different genetic elements that allow spatiotemporal control of oncogenic recombination in colon organoids. **c**, Schematic of the experimental workflow used to test and optimize the OptoCre system. **d**, Brightfield and fluorescence images of OptoCre-carrying inducible colon organoids exposed to the indicated conditions. Red and green signals correspond to healthy and mutated cells, respectively. Images were taken 48 hours after induction. Scale bar, 200 μm . **e**, Recombination efficiency in inducible colon organoid exposed to the conditions indicated in panel d. *** $P < 0.001$ (Kruskal-Wallis and Dunn's multiple comparisons test; $n = 9$ for each condition). Each point represents one well of organoids. Data represent mean \pm SEM. **f**, Brightfield and fluorescence images of inducible colon organoids exposed to control (top) and activation (bottom) conditions, dissociated into single cells and replated in the absence of growth factors (BMGF medium). Green signal corresponds to mutated cells. Images were taken 24 hours after replating. Scale bar, 200 μm .

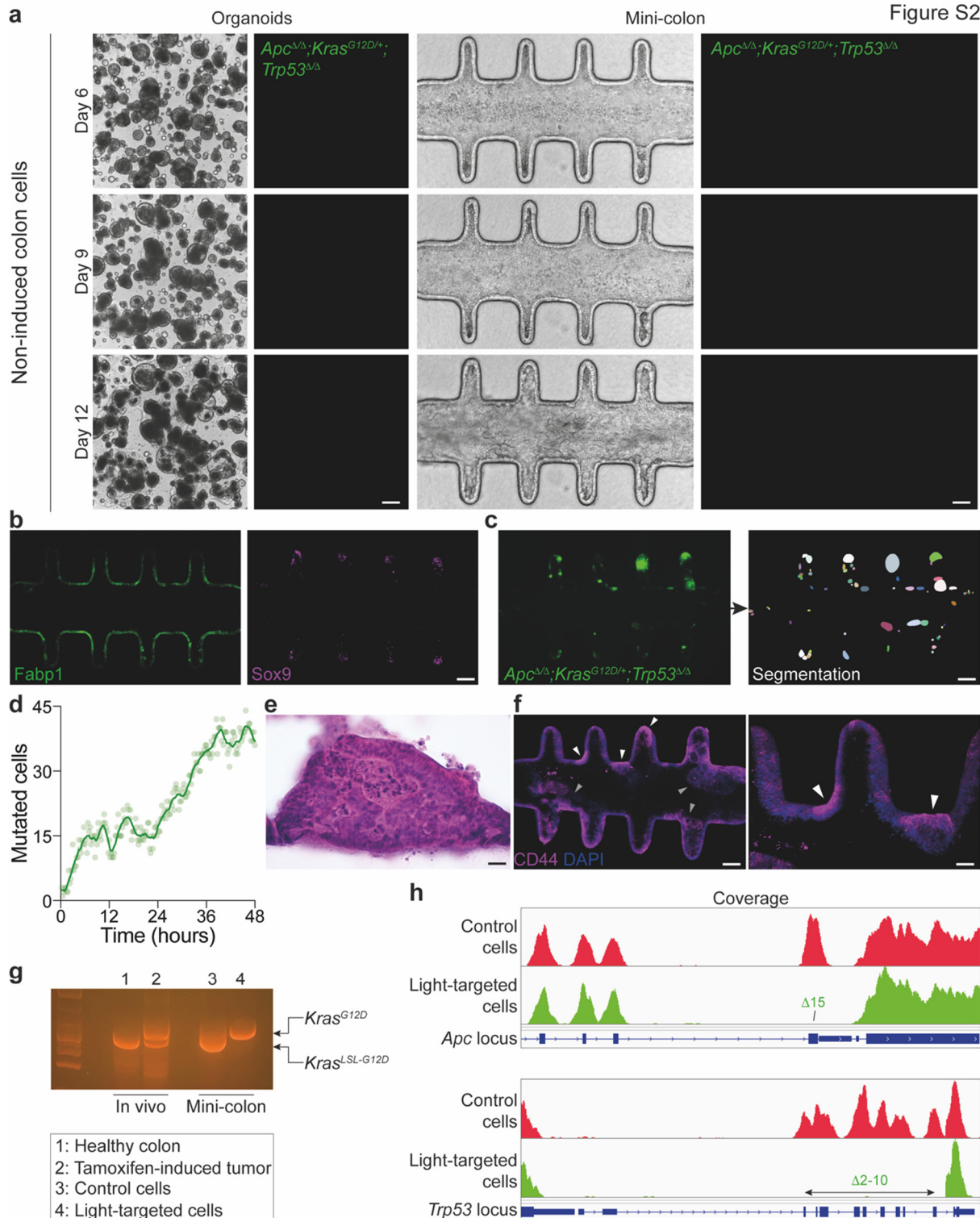


Figure S2 Oncogenic mutations in mini-colons produce complex tumor structures. **a**, Time-course brightfield and fluorescence images of non-induced healthy colon cells grown as conventional organoids and mini-colons. Absence of fluorescence signal indicates absence of oncogenic recombination. Scale bars, 200 μm (organoids) and 75 μm (mini-colons). **b**, Immunofluorescence images showing the expression of Fabp1 (left, green), and Sox9 (right, magenta) in healthy mini-colons cultured for 7 days. Scale bar, 100 μm . **c**, Fluorescence image (left) showing the presence of mutated cells 36 hours after the blue-light-mediated induction of a mini-colon. The segmentation of each mutated cell is shown (right). Scale bar, 120 μm . **d**, Evolution of the number of mutated cells in an inducible mini-colon after blue-light-mediated activation. Each dot represents a measurement every 15 minutes. The

2nd order smoothing of the data is shown. **e**, Hematoxylin and eosin staining of a mini-colon tumor section. Scale bar, 25 μm . **f**, Low- (left) and high-magnification (right) immunofluorescence images showing the presence of CD44 (magenta) and nuclei (blue) in a tumor-bearing mini-colon. White and grey arrowheads indicate early and advanced tumorigenic events, respectively. Scale bars, 120 μm (left) and 50 μm (right). **g**, Electrophoretic separation of PCR-amplified KRAS^{L^{SL}} locus in the indicated samples. See Methods for more details on PCR design. **h**, Whole exome sequencing coverage in the indicated loci and cells. Missing exons in recombined cells are indicated.

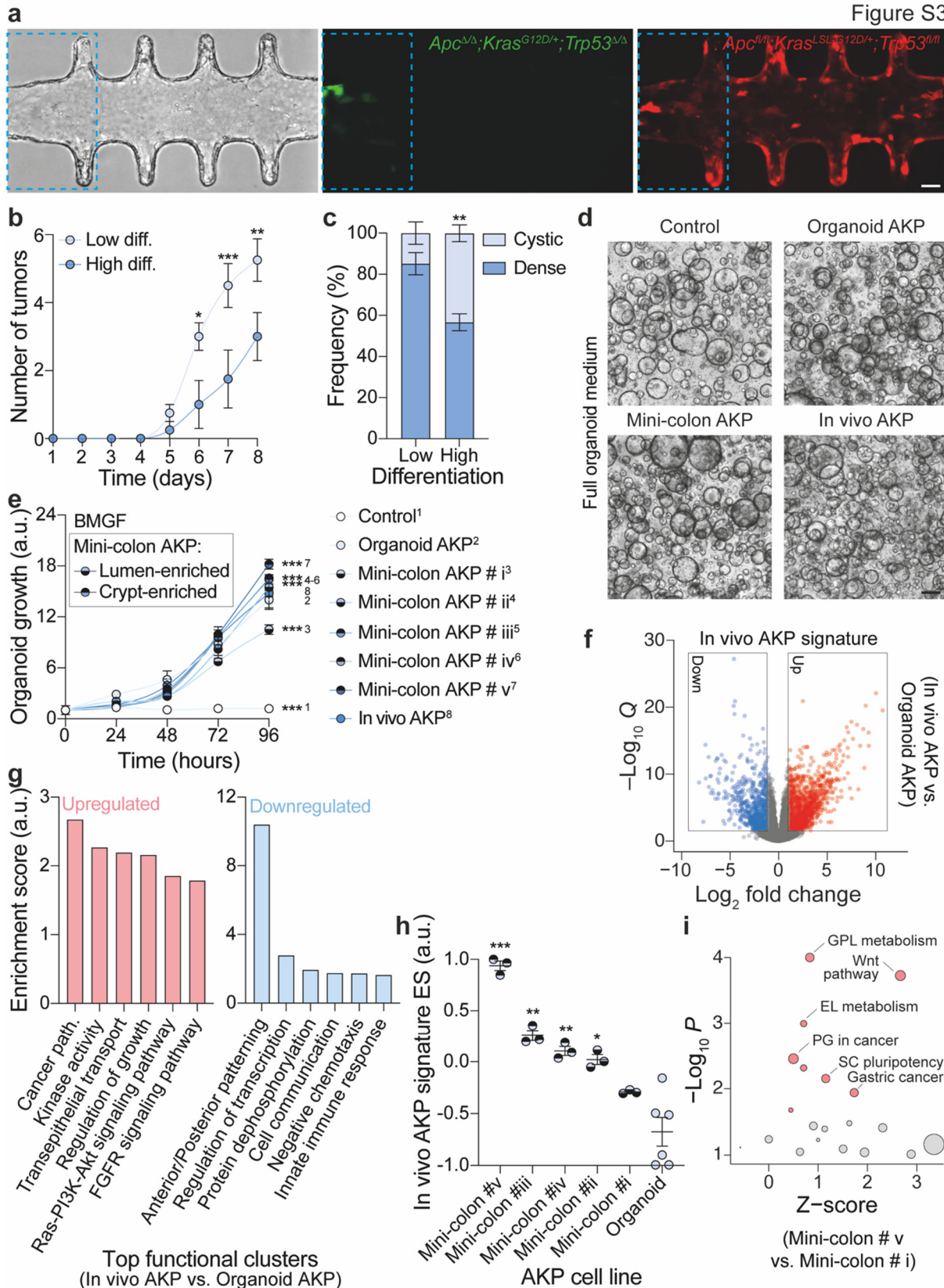


Figure S3 Mini-colon tumors display in vivo-like functional and transcriptional features. **a**, Brightfield and fluorescence images of a mini-colon where blue light exposure has been targeted to a specific area (dashed blue line). Red and green signals correspond to healthy and mutated cells, respectively. Images were taken 36 hours after induction. Scale bar, 75 μ m. **b**, Multiplicity of tumors emerged in mini-colons cultured in the indicated conditions. *P < 0.05, **P < 0.01, ***P < 0.001 (two-

way ANOVA and Sidak's multiple comparisons test; n = 4 for each condition). **c**, Distribution of tumor morphologies in mini-colons cultured in the indicated conditions. **P < 0.01 (two-way ANOVA and Sidak's multiple comparisons test; n = 4 for each condition). **d**, Brightfield images of the indicated colon organoid lines cultured for 3 days in full organoid medium. Scale bar, 200 μ m. **e**, Metabolic activity (measured using resazurin) of the indicated colon organoid lines cultured in BMGF medium for the indicated time. Numeric labeling (1-8) is used to facilitate cell line identification. ***P < 0.001 (two-way ANOVA and Sidak's multiple comparisons test; n = 3 for each line). **f**, Volcano plot of the differentially expressed genes between "in vivo" and "organoid AKP" cell lines. **g**, Top enriched functional clusters in the differentially expressed genes identified in panel f. **h**, Enrichment of the "in vivo AKP" transcriptional signature identified in panel f across the different "mini-colon" and "organoid AKP" lines. *P < 0.05, **P < 0.01, ***P < 0.001 (Brown-Forsythe ANOVA and Dunnett's T3 multiple comparisons test, n = 3 for each line). Each dot represents one culture. **i**, Main enriched functional terms in the differentially expressed genes between "mini-colon AKP" lines # i and # v. Significant terms are highlighted in red. In **b**, **c**, **e**, and **h**, data represent mean \pm SEM. GPL, glycerophospholipid; EL, ether lipid; PG, proteoglycans; SC, stem cell.

Figure S4

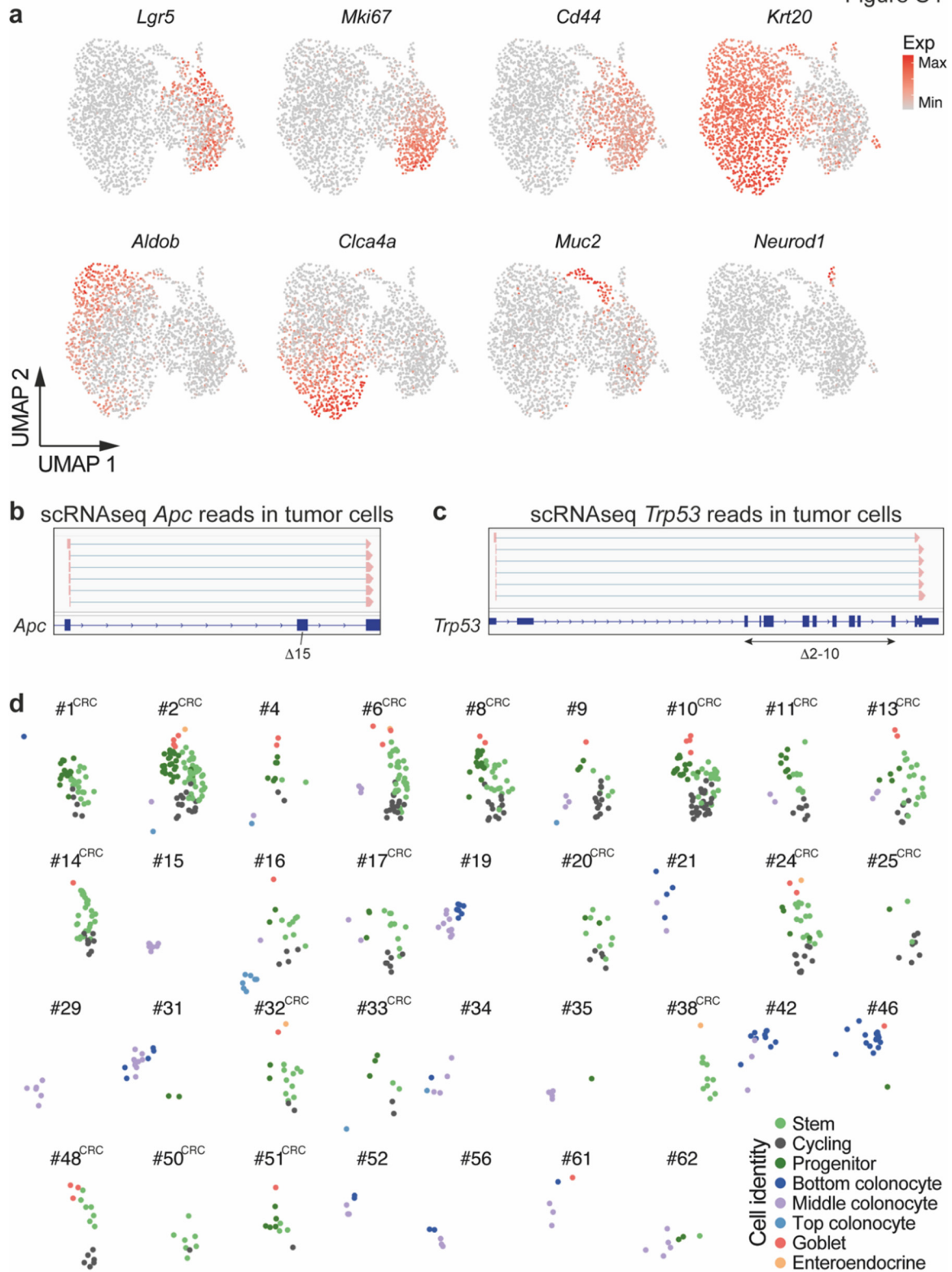


Figure S4 Mini-colons comprise a complex cellular ecosystem. **a**, Expression distribution of cell-type-specific markers across mini-colon cells. Cell-type labels can be found in Fig. 3b. **b**, Examples of single-cell RNA reads capturing exon-exon junctions that reveal the expected oncogenic recombination in *Apc*. **c**, Examples of single-cell RNA reads capturing exon-exon junctions that reveal the expected oncogenic recombination in *Trp53*. **d**, Unsupervised UMAP clustering of the main cell types found in each of the healthy and tumor clonal populations found within the mini-colon. Tumor clones carry the “CRC” label. UMAP structure corresponds to the one shown in Fig. 3b.

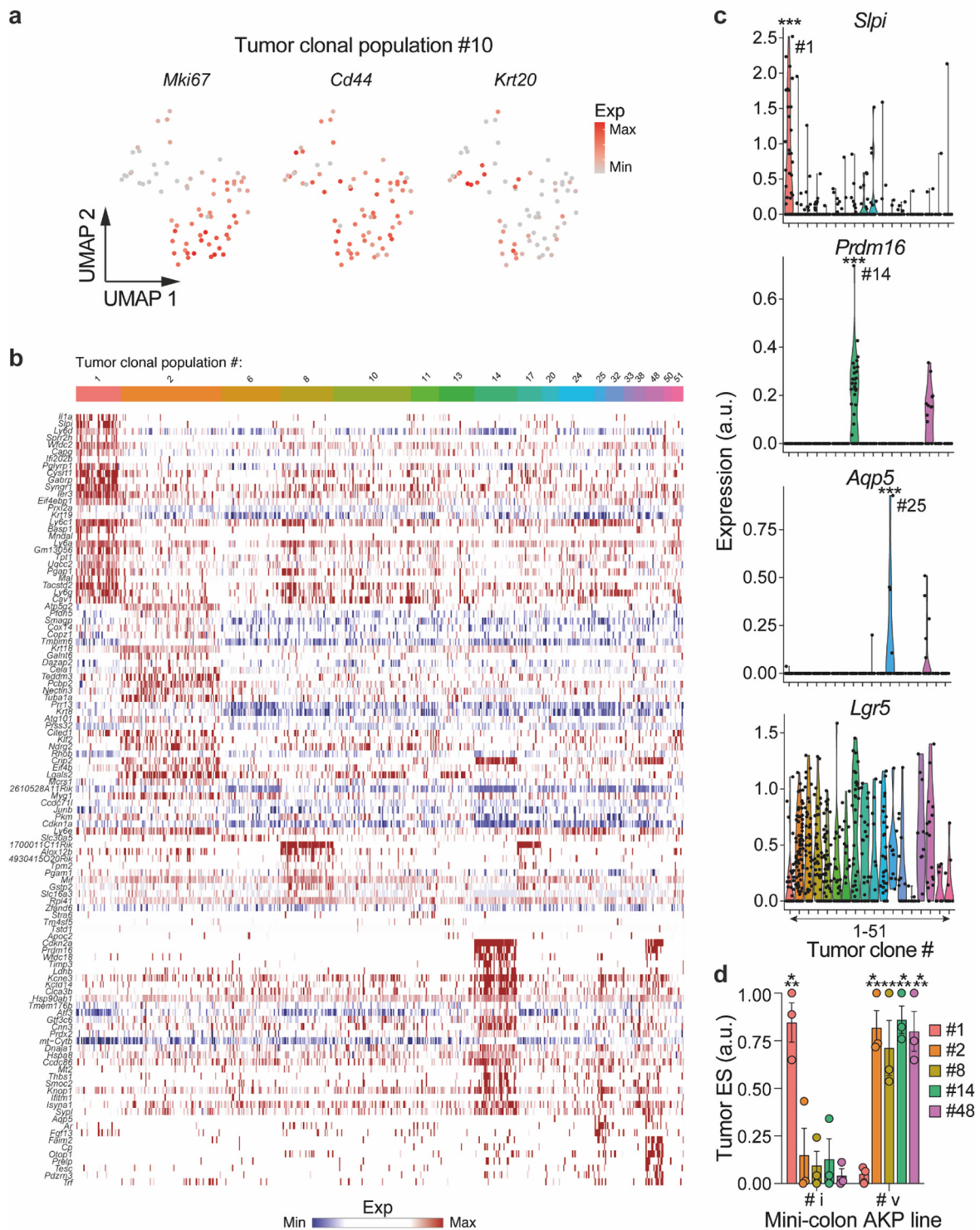


Figure S5 Mini-colons display intra- and inter-tumor diversity. **a**, Expression distribution of proliferation (Mki67), stemness (Cd44), and differentiation (Krt20) markers within a single clonal tumor population. **b**, Heatmap of the genes showing the strongest ($P < 10^{-5}$) differential expression across mini-colon tumors. The tumor clonal population is indicated on top. **c**, Expression of the indicated genes in the indicated tumor clones. *** $P < 0.001$ (Wilcoxon rank-sum test; $n = 540$). Each point represents one cell. **d**, Enrichment of the indicated tumor transcriptional signatures identified in panel b in the indicated “mini-colon AKP” lines. ** $P < 0.01$, *** $P < 0.001$ (two-way ANOVA and Sidak’s multiple comparisons test; $n = 3$ for each line). Each dot represents one culture. Data represent mean \pm SEM. ES, enrichment score; Exp, expression.

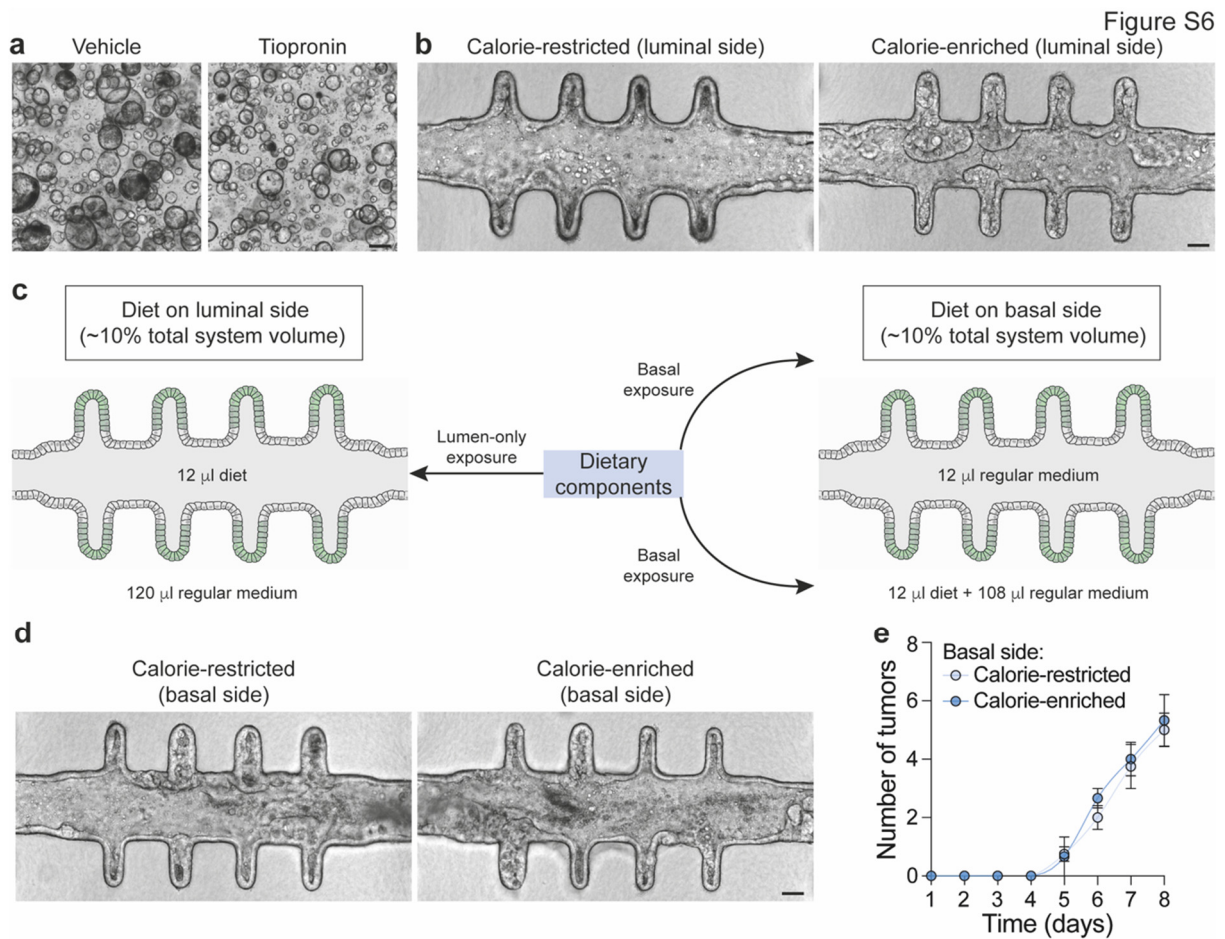


Figure S6 Mini-colons provide experimental flexibility and resolution to tumorigenic studies. **a**, Brightfield images of colon organoids treated with vehicle (left) or tiopronin (right) after tumorigenic recombination. Images correspond to 3 days after induction. Scale bar, 200 μ m. **b**, Brightfield images of mini-colons treated with the indicated diets according to the experimental setup displayed in Fig. 4d and in panel c (left). Images correspond to 6 days after tumorigenic induction. Scale bar, 75 μ m. **c**, Schematic of the experimental setup used to evaluate the relevance of luminal access in tumorigenic studies. **d**, Brightfield images of mini-colons treated with the indicated diets according to experimental setup displayed in panel c (right). Images correspond to 6 days after tumorigenic induction. Scale bar, 75 μ m. **e**, Multiplicity of tumors emerged in mini-colons treated with the indicated diets according to experimental setup displayed in panel c (right). Differences are not significant (two-way ANOVA and Sidak's multiple comparisons test; $n = 4$ and 3 for calorie-restricted and -enriched diets, respectively). Data represent mean \pm SEM

[Supplementary video 1](#)

https://drive.google.com/file/d/1_kWSMTmvBjO9GY7WZzjdBFgfRiXkIYJ-/view?usp=sharing

Early response to oncogenic activation within a mini-colon. 46-hour time-lapse video of mutated cells in a mini-colon 24 hours after oncogenic recombination.

[Supplementary video 2](#)

https://drive.google.com/file/d/1nhbk_67KHhbpVAuuZRrUhMAqPuUgdo_/view?usp=drive_link

Hyperplasia and early tumor development in a mini-colon. 36-hour time-lapse video of a mini-colon with multiple tumor-initiating events 5 days after oncogenic recombination.

[Supplementary video 3](#)

<https://drive.google.com/file/d/1m7WJAqJc6QHNH9932jKZt2GBfpjhijFb/view?usp=sharing>

Ex vivo tumor development in a mini-colon. 38-hour time-lapse video of tumor development in a mini colon 9 days after oncogenic recombination.

[Supplementary video 4](#)

https://drive.google.com/file/d/1eyOTv7J_szoqg4kwniOtNXWefvdqG5q1/view?usp=sharing

Cancer stem cells initiate tumor development in mini-colons. 3D visualization of cancer stem cell marker CD44 overexpression in early tumorigenic sites.

[Supplementary video 5](#)

<https://drive.google.com/file/d/1zeIGZExBpzigDYqnN5uoGwHI1SG0iw2sr/view?usp=sharing>

Intra-tumor complexity in mini-colons. 3D visualization of CD44 (cancer stem cell marker) and Fabp1 (mature colonocyte marker) expression in mini-colon tumors and epithelium.

Methods

Mice

Apcfl/fl mice (a kind gift from Tatiana Petrova, University of Lausanne, Switzerland) were crossed to Cdx2-CreERT2 mice (The Jackson Laboratory, Charles River, L'Arbresle, France). Apcfl/fl Cdx2-CreERT2 mice were then crossed with KrasLSL-G12D/+;Trp53fl/fl mice (a kind gift from Etienne Meylan, Ecole Polytechnique Fédérale de Lausanne, Switzerland) to generate Apcfl/fl;KrasLSL-G12D/+;Trp53fl/fl Cdx2-CreERT2 mice (termed AKP). AKP mice were then back-crossed with C57BL6/J (The Jackson Laboratory, Charles River, L'Arbresle, France) to generate Apcfl/fl;KrasLSL-G12D/+ Cdx2-CreERT2 mice (termed AK).

To induce tumorigenesis *in vivo*, CreERT2 recombinase was activated at an age of 8–10 weeks by a single intraperitoneal injection of 18 mg kg⁻¹ tamoxifen (Sigma, Catalog No. T5648) in sunflower oil. Tumors were allowed to develop for 6 weeks, then the mice were sacrificed for tissue and cell isolation. All animal work was conducted in accordance with Swiss national guidelines, reviewed and approved by the Service Veterinaire Cantonal of Etat de Vaud, license numbers VD3035.1 and VD3823. Mice were kept in the animal facility under EPFL animal care regulations. They were housed in individual cages at 23°C ± 1°C with a 12-h light/dark cycle. All animals were supplied with food and water *ad libitum*.

OptoCre module plasmid generation

The OptoCre module was designed by integrating the following constructs: i) FUW-M2rtTA, which constitutively expresses the reverse tetracycline transactivator (rtTA); ii) FUW-tetO-GAVPO, which expresses the light-switchable trans-activator GAVPO upon rtTA binding in the presence of doxycycline; and iii) FUW-OptoCre, which expresses Cre recombinase upon GAVPO binding in the presence of blue light (Fig. S1a). FUW-M2rtTA was purchased from Addgene (Catalog No. 20342). Vectors containing GAVPO and the GAVPO-binding promoter (UASG)5-Pmin, first developed by Wang et al.³⁵, were a kind gift from Dr. Matt Thomson³⁶. For FUW-tetO-GAVPO generation, GAVPO was subcloned into the doxycycline-responsive FUW-TetO backbone (Wernig Lab, Stanford) using the EcoRI and NheI restriction sites (Fig. S1a). For FUW-OptoCre generation, (UASG)5-Pmin was inserted into the FUW-TetO backbone from which the TetO promoter had been removed (Wernig Lab, Stanford) using the BstBI and BamHI restriction sites. We then introduced the Cre recombinase (Addgene, Catalog No. 25997) downstream of (UASG)5-Pmin using the Pac1 restriction sites (Fig. S1a).

Isolation of colon cells

Healthy colon or tumor pieces were finely chopped using a scalpel and transferred to a gentle-MACS C-tube (Miltenyi, Catalog No. 130-093-237) containing 4 ml of digestion media (RPMI [Thermo Fisher Scientific, Catalog No. 22400089], 1 mg ml⁻¹ Collagenase Type IV [Life Technologies, Catalog No. 9001-12-1], 0.5 mg ml⁻¹ Dispase II [Life Technologies, Catalog No. 17105041], and 10 µg ml⁻¹ DNase I [Applichem, Catalog No. A3778]). Tissues were then digested using the 37C_m_TDK_1 program on the gentle-MACS Octo Dissociator with heaters (Miltenyi). After the program was complete, the cell suspension was passed through a 70-µm strainer (Corning, Catalog No. 431751) and centrifugated at 400 g for 5 min.

Colon organoid culture

Colon cells were embedded in growth-factor-reduced Matrigel (Corning, Catalog No. 356231) (~2 × 10⁴ cells per 20 µL dome) and cultured in Advanced DMEM/F-12 (Thermo Fisher Scientific, Catalog No. 12634028) supplemented with 1× GlutaMAX (Thermo Fisher Scientific, Catalog No. 35050038), 10 mM HEPES (Thermo Fisher Scientific, Catalog No. 15630056), 100 µg ml⁻¹ penicillin–streptomycin (Thermo Fisher Scientific, Catalog No. 15140122), 1× B-27 supplement (Thermo Fisher Scientific, Catalog No. 17504001), 1× N2 supplement (Thermo Fisher Scientific, Catalog No. 17502001), 1 mM N-acetylcysteine (Sigma-Aldrich, Catalog No. A9165), 50 µg ml⁻¹ Primocin (InvivoGen, Catalog No. ant-pm-2), 50 ng ml⁻¹ EGF (Peprotech, Catalog No. 315-09), 100 ng ml⁻¹ Noggin (produced at EPFL Protein Production and Structure Core Facility), 500 ng ml⁻¹ R-spondin (produced at EPFL Protein Production and Structure Core Facility), 50 ng ml⁻¹ Wnt3a (Time Bioscience, Catalog No. rmW3aL-010), 10 mM Nicotinamide (Calbiochem, Catalog No. 481907), and 2.5 µM Thiazovivin (Stemgen, Catalog No. AMS.04-0017). This full medium is termed “WENRNI”. The base version of this medium without EGF, Noggin, R-spondin, Wnt3a, and nicotinamide is referred to as “BMGF” and was used for the expansion of colon tumor organoids since they do not require the additional growth factors. The base version of BMGF without B-27, N2, and N-acetylcysteine is termed “BM” or basal medium, and was used for growth-factor deprivation experiments. A detailed protocol describing organoid culture can be found elsewhere⁹. Cells were tested for mycoplasma before cryopreservation and in randomized routine checks using the MycoAlert PLUS Mycoplasma Detection Kit (Lonza, Catalog No. LT07-705).

Generation of light-inducible cells

Lentiviral particles carrying the three components of the OptoCre module (see above and in Fig. S1b) and a Cre recombination reporter were produced at the EPFL Gene Therapy Platform

by transfecting HEK293 cells with each plasmid of the OptoCre module and pLV-CMV-LoxP-DsRed-LoxP-eGFP (Addgene, Catalog No. 65726) plasmids. Lentivirus-containing supernatants were collected and concentrated by centrifugation (1,500 g for 1 hour at 4°C). Lentiviral titration was performed using a p24-antigen ELISA (ZeptoMetrix, Catalog No. 0801111). For transduction, colon organoids (~2 × 10⁵ cells) were dissociated into single cells by incubating in TrypLE Express Enzyme (Thermo Fisher Scientific, Catalog No. 12605028) at 37°C for 5 min. Cells were then washed with basal medium supplemented with 10% fetal bovine serum (FBS) (Thermo Fisher Scientific, Catalog No. 10500064) and resuspended in WENRNi medium containing 8 µg ml⁻¹ polybrene (Sigma-Aldrich, Catalog No. TR-1003-G) and the following amounts of viral particles: ~10 ng of p24 FUW-M2rtTA ml⁻¹, ~80 ng of p24 FUW-tetO-GAVPO ml⁻¹, ~80 ng of p24 FUW-OptoCre ml⁻¹, and ~1000 ng of p24 CMV-LoxP-DsRed-LoxP-eGFP ml⁻¹. These cells were plated in a 24-well plate, centrifuged at 600 g for 60 min at room temperature, and incubated for 6 hours at 37°C. After incubation, the cells were collected, spun down, plated in 20 µL Matrigel domes in a 24-well plate and cultured in WENRNi medium. Cells expressing the Cre recombination reporter were selected by supplementing WENRNi medium with 8 µg ml⁻¹ puromycin (InvivoGen, Catalog No. ant-pr-1).

Light-mediated oncogenic recombination

The OptoCre module requires i) doxycycline to induce rtTA-mediated GAVPO expression and ii) blue light to induce GAVPO-mediated Cre recombinase expression (Fig. S1a,b). At the desired time of oncogenic induction, 2 µg ml⁻¹ doxycycline hydrochloride (Sigma-Aldrich, Catalog No. D3072) was added to the culture medium of either the organoids or mini-colons. Light induction was then performed using a custom-made LightBox built by Baur SA and the Instant Lab at EPFL. The LightBox consisted of an Acqua A5 System (Acme Systems) that could be remotely parametrized using a custom-made web-based application. Communication between the Acqua A5 System and the microcontroller (PJRC, Teensy 3.2) was done through Blockly programming, which allowed for control of the LED drivers (Sparkfun, PicoDuck). The LEDs (Cree LEDs, XLamp® XP-C Blue LEDs) were placed into a custom multilayer 24-well plate-holder made of black anodized aluminum and polyphenylsulfone; the height was optimized for homogeneous light distribution within each well. The entire LightBox, plate-holder, LEDs, and cables were made to be placed in the incubator (watertight and heat-resistant). Diffusive elements (Luminit, Light Shaping Diffuser 80°) were used to render the illumination more homogeneous inside each well. The intensity of the blue light (450–465 nm, peak at 455 nm) was optimized, set to 100 µW cm⁻², and shined on the cells for 3 hours. After blue-light exposure, doxycycline was removed by washing the cultures with fresh medium. In experiments targeting the light to specific regions of the mini-colon, work was carried out in the

dark using a near infrared light (Therabulb, NIR-A) to prevent leaky Cre expression. Light-targeting was performed using a photomask that was adapted to the dimensions of the mini-colon and that was created from a photoresist and chrome-coated standard 5×5-inch silica plate (Nanofilm) with an automated machine (VPG200 Heidelberg Instrument, 2.0 μm resolution). Once the exposed photoresist was developed, the chrome layer was wet-etched, and the remaining photoresist was stripped with a mask processor (Hamatech HMR900)⁹.

Microdevice design, fabrication, and loading

The microfluidic device used for mini-colon cultures was designed and fabricated as previously described⁹. It was composed of three main compartments: i) a hydrogel chamber for cell growth in the center, ii) two basal medium reservoirs flanking the hydrogel compartment, and iii) inlet and outlet channels for luminal perfusion⁹. An extracellular matrix containing 80% (v/v) type I collagen (5 mg ml⁻¹, Reprocell, Catalog No. KKN-IAC-50) and 20% (v/v) growth-factor-reduced Matrigel was loaded into the hydrogel compartment. The microchannels constituting the mini-colon architecture within the hydrogel were ablated using a nanosecond laser system (1-ns pulses, 100-Hz frequency, 355 nm; PALM Micro-Beam laser microdissection system, Zeiss). The dimensions of the mini-colon architecture can be found in Nikolaev et al.⁹

Mini-colon culture, development, and tumorigenesis

Colon organoids were dissociated into single cells by incubating in TrypLE Express Enzyme for 5 min at 37°C followed by vigorous pipetting. This cell suspension was washed in 5 volumes of Advanced DMEM/F-12 supplemented with 10% FBS and passed through 40-μm cell strainers (Corning, Catalog No. 431750). After centrifugation at 400 g for 5 min, cells were resuspended in WENRNi medium at ~10⁶ cells per ml. The mini-colon luminal microchannel was filled with 10 μL of this cell suspension. Cells were allowed to settle down in the mini-colon crypt-shaped cavities for 5 min, and the leftover unadhered cells were washed out from the microchannel by medium perfusion. The basal medium reservoirs were filled with 100 μL of WENRNi. Unless otherwise indicated, once the healthy colonic epithelium was fully formed (~2 days after seeding), the medium in the luminal channel was switched to BM, while WENRNi was kept in the basal medium reservoirs. This gradient of growth factor from basal medium reservoirs to luminal space favors colonocyte differentiation across the crypt-lumen axis. For low-differentiation conditions of the differentiation experiments, WENRNi was kept in both the lumen and basal medium reservoirs. Conversely, high-differentiation mini-colons were cultured in WENRNi medium without Wnt3a and nicotinamide (termed “ENR”). Unless otherwise stated, once the colonic epithelium was fully formed, oncogenic induction in the mini-colons was

performed as stated above. Where indicated, tiopronin (5 mM, Selleckchem, Catalog No. S2062) was added to the basal medium reservoirs after oncogenic induction and replenished with every medium change. In all cases, the mini-colons were incubated at 37°C in 5% CO₂ humidified air, with daily luminal perfusions and media changes every other day.

Mini-colon whole-mount immunofluorescence staining

Mini-colons were rinsed with phosphate buffered saline (PBS) and fixed in 4% paraformaldehyde (Thermo Fisher Scientific, Catalog No. 15434389) overnight at 4°C. After rinsing with PBS, the hydrogels were extracted from the PDMS scaffold using a scalpel, placed in a 48-well plate, permeabilized with 0.1% Tween-20 (Sigma-Aldrich, Catalog No. P9416) in PBS (10 min at 4°C) and blocked in 2 mg ml⁻¹ bovine serum albumin (BSA) (Sigma-Aldrich, Catalog No. A3059) in PBS containing 0.1% Triton X-100 (Sigma-Aldrich, Catalog No. T8787) (termed “blocking buffer”) for at least 45 min at 4°C. The samples were subsequently incubated overnight at 4 °C in blocking buffer with the corresponding following primary antibodies: CD44 (1:200; Abcam, Catalog No. ab157107), Fabp1 (1:100; R&D systems, Catalog No. AF1565), and Sox9 (1:200; Abcam, Catalog No. ab185966). After 3 washes in blocking buffer for a total of 6 h at room temperature, the samples were incubated overnight at 4°C in blocking buffer with the following corresponding secondary antibodies: Alexa Fluor 488 anti-goat (1:400, Thermo Fisher Scientific, Catalog No. A-11055) and Alexa Fluor 647 anti-rabbit (1:400, Thermo Fisher Scientific, Catalog No. A-31573). After 3 washes in blocking buffer for a total of 6 h at room temperature, the samples were incubated with DAPI (1 µg ml⁻¹; Tocris Bioscience, Catalog No. 5748) for 10 min at room temperature in blocking buffer. Before imaging, the hydrogels were mounted onto 35 mm glass bottom dishes (Ibidi, Catalog No. 81218-200) in Fluoromount-G (SouthernBiotech, Catalog No. 0100-01).

Mini-colon sectioning and histochemistry

Mini-colons were fixed and extracted from the PDMS scaffold as indicated above and were prepared for cryosectioning by incubating in 30% (W/V) sucrose (Sigma-Aldrich, Catalog No. S1888) in PBS until the sample sank. Subsequently, samples were incubated for 12 hours in a mixture of Cryomatrix (EpreDia, Catalog No. 6769006) and 30% sucrose (mixing ratio 50/50) followed by a 12-hour incubation in pure Cryomatrix. The samples were then embedded in a tissue mold, frozen on dry ice, and cut into 40 µm-thick sections at -20°C using a CM3050S cryostat (Leica). Hematoxylin and eosin staining was performed at the EPFL Histology Core Facility using a Ventana Discovery Ultra automated slide preparation system (Roche).

Microscopy and image analysis

Brightfield and fluorescent imaging of living organoids and mini-colons was performed using a Nikon Eclipse Ti2 inverted microscope with 4×/0.13 NA, 10×/0.30 NA, and 40×/0.3 NA air objectives and a DS-Qi2 camera (Nikon Corporation). Time lapses were taken in a Nikon Eclipse Ti inverted microscope system equipped with 4×/0.20 NA and 10×/0.30 NA air objectives and DS-Qi2 (Nikon Corporation) and Andor iXon Ultra 888 (Oxford Instruments) cameras. Both systems were controlled using the NIS-Elements AR software (Nikon Corporation). The extended depth of field (EDF) of brightfield images was calculated using a built-in NIS-Elements function. Fluorescent confocal imaging of fixed mini-colons was performed using a Leica SP8 STED 3X inverted microscope system equipped with a 10×/0.30 NA air and 25×/0.95 NA water objectives, 405 nm diode, and supercontinuum 470–670 nm lasers, and the system was controlled by the Leica LAS-X software (Leica microsystems). Histological sections were imaged using a Leica DM5500 upright microscope with 10×/0.30 NA and 20×/0.75 NA air objectives, a 40×/1.0 NA oil objective, a DMC 2900 Color camera, and the system was controlled by the Leica LAS-X software (Leica microsystems). Image processing was performed using standard contrast- and intensity-level adjustments in ImageJ (NIH). For oncogenic recombination analyses, the GFP positive area was measured from 16-bit EDF images by subtracting the background, sharpening images, and applying a signal threshold and a mask. The ratio between GFP-positive and total organoid area was used for analyses. Recombined cells were segmented using StarDist with the default parameters (<https://github.com/stardist>) on the GFP channel of mini-colon images. Cell debris was discarded from segmentation analyses by setting an empirically established size threshold. For tumor quantification in the mini-colon, neoplastic structures with at least 3 times the thickness of the surrounding healthy epithelium were considered as tumors. Videos of immunostainings were rendered using Imaris (Oxford Instruments).

Mini-colon cell line derivation

Mini-colon-containing hydrogels were extracted from their microfluidic devices with a scalpel as indicated above and incubated with 0.1% (W/V) collagenase I (Thermo Fisher Scientific, Catalog No. 17100-017) at 37°C for 10 min. Once the hydrogel was fully digested, the mini-colon was washed with PBS and digested with TrypLE Express Enzyme for 5 min at 37°C. The resulting cell suspension was washed with Advanced DMEM/F-12 supplemented with 10% FBS, pelleted, embedded in Matrigel, and cultured as indicated above for regular colon organoids.

Mutational screening in colon organoids

Genomic DNA was isolated from colon cells using the PureLink Genomic DNA Mini Kit (Thermo Fisher Scientific, Catalog No. K182001) according to the manufacturer's instructions. Recombination of the LSL (LoxP-Stop-LoxP) cassette controlling KrasG12D expression was confirmed by PCR using the protocol and oligos described by the Tyler Jacks laboratory (jacks-lab.mit.edu, Kras G12D Conditional PCR). Apc and Trp53 recombinations were confirmed through exome sequencing performed at BGI Genomics (Hong Kong) at 100× coverage using DNBSAQ sequencing technology. DNA reads were mapped to the mouse GRCm39 genome assembly using BWA-MEM (v0.7.17), filtered using samtools (v1.9) and visualized using IGV (Integrative Genomics Viewer, Broad Institute, v2.12.3).

Organoid proliferation assays

Single-cell suspensions of colon cells were generated as indicated above and embedded in 10 µl Matrigel domes at ~104 cells/dome in a 48-well plate. For each of the following 4 days, 220 µM resazurin (Sigma-Aldrich, Catalog No. R7017) was added to the culture medium and incubated for 4 hours at 37°C. Afterwards, the resazurin-containing medium was collected and replaced by regular medium. Organoid proliferation was estimated by measuring the reduction of resazurin to fluorescent resorufin in the medium each day using a Tecan Infinite F500 microplate reader (Tecan) with 560 nm excitation and 590 nm emission filters.

Organoid RNA extraction and bulk transcriptome profiling

Organoids were cultured for 3 days as indicated above and starved for 24 hours in BM to evaluate the growth-factor dependence. Cells were collected using TrypLE Express Enzyme as indicated above and lysed in RLT buffer (QIAGEN, Catalog No. 74004), and the RNA was extracted using the QIAGEN RNeasy Micro Kit (QIAGEN, Catalog No. 74004) according to the manufacturer's instructions. Purified RNA was quality checked using a TapeStation 4200 (Agilent), and 500 ng were used for QuantSeq 3' mRNA-Seq library construction according to the manufacturer's instructions (Lexogen, Catalog No. 015.96). Libraries were quality checked using a Fragment Analyzer (Agilent) and were sequenced in a NextSeq 500 (Illumina) using NextSeq v2.5 chemistry with Illumina protocol #15048776. Reads were aligned to the mouse genome (GRCm39) using star (version 2.7.0e)37. R (version 4.1.2) was used to perform the differential expression analyses. Count values were imported and processed using edgeR38. Expression values were normalized using the trimmed mean of M values (TMM) method39 and lowly-expressed genes (< 1 counts per million) were filtered out. Differentially expressed genes were identified using linear models (Limma-Voom)40, and P values were adjusted for

multiple comparisons by applying the Benjamini-Hochberg correction method⁴¹. Volcano plots were generated using EnhancedVolcano (github.com/kevinblighe/EnhancedVolcano). The “in vivo” AKP signature was established from the differentially expressed genes between “in vivo” and “organoid” AKP lines with a log₂ fold change of at least |2|. To evaluate the enrichment of the “in vivo” AKP gene expression program across samples, the enrichment scores for both the upregulated and downregulated signatures were calculated using single-sample GSEA⁴². The difference between the two normalized enrichment scores yielded the fit score. Functional annotation was performed using DAVID⁴³. GOplot⁴⁴ was used for the integration of expression and functional annotation data.

Single-cell transcriptome profiling and lineage tracing

Lineage tracing was performed using the “CellTag” system²² (V1 pooled barcode library, Addgene, Catalog No. 115643-LVC). Briefly, we co-transduced inducible colon organoids with the CellTag barcode library (MOI ~ 5) and the OptoCre module as indicated above. These cells were then introduced and induced in the mini-colon system as indicated before. After 7 days in the system and when mini-colon tumors were clearly visible, we extracted the cells from mini-colons as indicated above. After pooling and filtering (40 μm) the cell suspensions from two mini-colons, the single-cell sequencing library was constructed using 10× Genomics Chromium 3’ reagents v3.1 according to the manufacturer’s instructions (10× Genomics, Catalog No. PN-1000269, PN-1000127, PN-1000215). Sequencing was done using NovaSeq 6000 v1.5 reagents (Illumina protocol #1000000106351 v03) for around 100,000 reads per cell. The reads were aligned using Cell Ranger v6.1.245 to the mouse genome (mm10) carrying artificial chromosomes for both GFP and CellTag UTR genes, as recommended by CellTag developers for facilitating barcode identification⁴⁶. Raw count matrices were imported into R and analyzed using Seurat v4.2.047. Dead cells were discarded on the basis of the number of detected genes (less than 3,000) and the percentage of mitochondrial genes (more than 20%), leading to 2,429 cells after filtering. The data were log-normalized and scaled, and dimensionality reduction was conducted using UMAP with 10 dimensions. Louvain clustering yielded 17 clusters that were merged and named on the basis of canonical cell type markers. Stem, cycling, progenitor, goblet, and enteroendocrine cell scoring was based on published signatures in mini-intestines and in vivo⁹. Gene sets highlighting bottom, middle, and top colonocytes were taken from enterocyte zonation studies²³. Cancer stemness was scored based on the expression of Lgr5, Cd44, and Sox9. Signature scoring was carried out using burgertools (github.com/nbroguiere/burgertools). Visual representations of the data were generated using Seurat internal functions. For lineage-tracing analyses, CellTag detection, quantification, and clone calling were performed as indicated by CellTag developers⁴⁶,

excluding cells expressing fewer than 2 or more than 30 CellTags. After filtering, 83 clonal populations were identified, from which only those with a minimum size of 5 cells were considered for further analyses. To identify clonal populations belonging to tumor cells, we looked for cells expressing transcripts carrying the genetically engineered Apc and Trp53 mutations, i.e., deletions of exons 15 and 2–10, respectively (Figs. S2h, S4b,c). Note that this approach could not be carried out for Kras, as the mutation is also present in the transcripts from WT cells (but not expressed). Since scRNA-Seq technology provides low coverage on exon junctions and therefore the presence of mutations can only be assessed in a small fraction of cells, we used both the cell-type composition and size distributions of bona-fide mutationally confirmed tumor clonal populations to classify the rest of clones. Those falling within plus or minus two standard deviations of the mean cell composition and size of bona-fide tumors were classified as tumor clonal populations. Healthy clones were defined as those with clearly distinct (outside the aforementioned range) cell type composition and the same upper limit size as was observed for tumor clones. After filtering and classification, 16 healthy and 18 tumor clonal populations were obtained and used for further analyses (Fig. S4d). To define the most robust tumor–clone-specific markers, the gene expression from cells in each clone was compared to that from cells in each other clone using the Wilcoxon rank-sum test. We considered only the positive markers and selected those with adjusted P values < 10⁻⁵. The enrichment of these markers in specific bulk RNAseq datasets was carried out through single-sample GSEA as indicated above. For more information, see “Data availability” and “Code availability”.

Microbiota and diet modeling

Inducible mini-colons were generated as indicated above. Once the epithelium was formed and before oncogenic induction, mini-colons were subjected to a conditioning period of 2 days in which luminal medium was i) supplemented with 50 μ M deoxycholate (Sigma-Aldrich, Catalog No. D2510), 50 μ M butyrate (Sigma-Aldrich, Catalog No. B5887), or 5 mM α -hydroxybutyrate (Sigma-Aldrich, Catalog No. 54965); or ii) replaced by MEM α (calorie-restricted condition, Thermo Fisher Scientific, Catalog No. 22561-021) or Advanced DMEM/F12 supplemented with 30 μ M palmitic acid (calorie-enriched condition, Sigma, Catalog No. P0500). The same concentrations were used in organoid control experiments, but these were added to the full culture medium as the luminal compartment is not accessible in organoids. To assess the relevance of luminal exposure to these factors in the mini-colon, the same total amounts were added in the basal medium reservoirs instead of the luminal channel. In all cases, after conditioning, oncogenic recombination was performed and the mini-colon

was cultured as indicated above. The different medium compositions were replenished every day during luminal perfusion.

Statistics

The number of biological replicates (n), the type of statistical tests performed, and the statistical significance are indicated for each experiment either in the figure legend or in the main text. Data normality and equality of variances were analyzed with Shapiro-Wilk and Bartlett's tests, respectively. Parametric distributions were analyzed using the Student's t-test (when comparing two experimental groups) or ANOVA followed by either Dunnett's (when comparing more than two experimental groups with a single control group) or Tukey's HSD test (when comparing more than two experimental groups with every other group). Nonparametric distributions were analyzed using either Mann-Whitney (for comparisons of two experimental groups) or the Kruskal-Wallis followed by Dunn's (for comparisons of three or more than three experimental groups) tests. Sidak's multiple comparison test was used when comparing different sets of means. The chi-squared test was used to determine the significance of the differences between expected and observed frequencies. In all cases, values were considered significant when $P \leq 0.05$. Data obtained are given as the mean \pm the standard error of the mean (SEM).

Data Availability

Bulk and single-cell RNAseq data reported in this paper have been deposited in the Gene Expression Omnibus (GEO) public repository under the accession numbers GSE221159 and GSE221162, respectively.

Code Availability

All code used for image, bulk RNAseq, and single-cell RNAseq analyses is available upon request.

**Chapter II – Development of a new type of organoids,
thymic epithelial organoids, with preserved thymopoietic
functionality ex vivo**

Thymic epithelial organoids mediate T cell maturation in vitro

Tania Hübscher¹, L. Francisco Lorenzo-Martín¹, Thomas Barthlott², Lucie Tillard¹, Jakob J. Langer¹, Paul Rouse³, C. Clare Blackburn³, Georg Holländer^{2,4,5} and Matthias P. Lutolf^{1,7,*}

¹ Laboratory of Stem Cell Bioengineering, Institute of Bioengineering, School of Life Sciences and School of Engineering, École Polytechnique Fédérale de Lausanne (EPFL), Lausanne, Switzerland

² Department of Biomedicine, University of Basel, Basel, Switzerland

³ Centre for Regeneration, Institute for Repair and Regeneration, School of Biological Sciences, University of Edinburgh, Edinburgh, UK

⁴ Department of Paediatrics and Institute of Developmental and Regenerative Medicine, University of Oxford, Oxford, UK

⁵ Pediatric Immunology, Department of Biomedicine, University of Basel and University Children's Hospital Basel, Basel, Switzerland

⁶ Department of Biosystems Science and Engineering, Eidgenössische Technische Hochschule Zürich (ETHZ), Basel, Switzerland

⁷ Institute of Human Biology (IHB), Pharma Research and Early Development, Roche Innovation Center Basel, Basel, Switzerland

*Corresponding author. Email: matthias.lutolf@epfl.ch

Manuscript submitted

Abstract

Although the advent of organoids opened unprecedented perspectives for basic and translational research, immune system-related organoids remain largely underdeveloped. Here we established organoids from the thymus, the lymphoid organ responsible for T cell development. We identified conditions enabling thymic epithelial progenitor cell proliferation and development into organoids with in vivo-like transcriptional profiles and diverse cell populations. Contrary to two-dimensional cultures, thymic epithelial organoids maintained thymus functionality in vitro and mediated physiological T cell development upon reaggregation with T cell progenitors. The reaggregates showed in vivo-like epithelial diversity and ability to attract T cell progenitors. Thymic epithelial organoids provide new opportunities to study TEC biology and T cell development in vitro, pave the way for future thymic regeneration strategies and are the first organoids originating from the stromal compartment of a lymphoid organ.

One-sentence summary: Establishment of organoids from the epithelial cells of the thymus which resemble their in vivo counterpart and have thymopoietic ability.

Article

Over the past two decades, organoids have revolutionized the field of stem cell biology. Recapitulating key elements of the architecture, multicellularity, or function of their native organs on a smaller scale (1), organoids have opened up unprecedented opportunities for personalized medicine. These three-dimensional (3D) structures derived from stem or progenitor cells have been established from a wide variety of organs, particularly of the endodermal lineage (1). However, despite the availability of organotypic cultures (e.g. tissue explants (2, 3) and reagggregates (4–6)) or engineering methods (7) (e.g. scaffolds (8–14), and organ-on-a-chip (15)), bona fide immune system-related organoids are considerably underdeveloped. Modelling lymphoid organs is indeed particularly challenging, largely due to the intricate crosstalk between immune and stromal cells required for organ development and function (3).

One essential organ for adaptive immunity is the thymus as it functions as the site of T cell development. In the thymus, T cell progenitors undergo lineage commitment and various selection processes to ensure the formation of a diverse, functional, and self-tolerant T cell repertoire, essential for effective immune protection. The instruction of the developing T cells (termed thymocytes) is mostly mediated by thymic epithelial cells (TECs). These stromal cells originate from the pharyngeal endoderm and can be subdivided into cortical and medullary lineages, which mediate successive stages of T cell development.

The essential thymopoietic ability of TECs is however mostly lost in vitro, as traditional two-dimensional (2D) cultures fail to maintain their functionality (3, 16, 17). Alternative approaches employing OP9 or MS5 cell lines have been developed to circumvent this limitation and study T cell-development in vitro (18, 19), but the absence of TECs still prevents physiological modelling of T cell selection processes. Other efforts focused on obtaining TECs from pluripotent stem cells (20–23) or through direct reprogramming (24), but these cells largely rely on in vivo grafting to reveal thymopoietic functionality. It was also shown that TECs can form colonies in Matrigel, but these cultures still require feeder cells and their functionality was not demonstrated (25–27). Thus, currently the only existing way to preserve TEC functionality in vitro is through (reaggregate) thymic organ cultures, which are organotypic 3D cultures containing different cell types.

Here, in light of what has been achieved for other endoderm-derived epithelia, we postulated that TECs could be grown independently of other cell types as 3D organoids in an extracellular matrix-based hydrogel. We identified culture conditions allowing TECs to form organoids mirroring to some extent the native tissue, and proved their functionality through their ability to mediate T cell development upon reaggregation with T cell progenitors. This work establishes the first thymic epithelial organoids with in vitro thymopoietic ability and is generally the first demonstration of organoids originating from the stromal compartment of a lymphoid organ.

Thymic epithelial cells grow and maintain marker expression in defined organoid culture conditions

To establish thymic epithelial organoids, we followed the approach used for other endodermal organs, which included dissociating the tissue, sorting the cells of interest, and seeding them in a basement membrane-rich hydrogel (Matrigel) (Fig. 1A and fig. S1A). Since organoids mostly develop from stem or progenitor cells, we focused on the embryonic thymus due to its higher abundance of thymic epithelial progenitor cells compared to the adult organ (28, 29). Although previous attempts to culture TECs often used serum-containing medium (13, 25, 30), we opted for defined organoid basal medium and investigated factors that could promote TEC growth. We hypothesized that mesenchyme-derived factors that have been shown to influence TEC populations both in vivo and in vitro (31–34) could also be important for TEC growth in organoid cultures. Among these factors, we found FGF7 of particular interest, as it has recently been shown to sustain the expansion of thymic microenvironments without exhausting the epithelial progenitor pools in vivo (35). Using E16.5 embryonic thymi, we showed that while sorted TECs failed to grow in organoid basal medium, adding FGF7 to the culture supported organoid formation (Fig. 1, B and C). To monitor organoid development, we performed time-lapse imaging from the time of seeding (Fig. 1D and movie S1) and found that most organoids were derived from single cells with stem/progenitor properties.

Immunostaining confirmed that organoids were generated by thymus-derived EpCAM-positive cells (Fig. 1E). Single cells formed small organoids in which a large majority of cells were positive for Ki67 after 3 days (Fig. 1F), and both proliferating and non-proliferating cells were present 4 days later (fig. S1B). To investigate whether these cell populations could recapitulate TEC diversity, including cortical and medullary types (cTECs and mTECs), we stained organoids for the cTEC marker Keratin 8 (KRT8) as well as for Keratin 5 (KRT5) and with UEA1 lectin as mTEC markers. Overall, our TEC culture system demonstrated a canonical feature of organoids in the emergence of different cell types, with varying degrees of KRT5 expression (Fig. 1G) and the presence of both KRT8-positive and UEA1-reactive populations (fig. S1C).

In addition, at least some organoids were positive for MHCII (Fig. 1H), an important marker of TEC functionality required for the development of CD4+ T cells (28). TEC differentiation, function and maintenance being critically dependent on the transcription factor *Foxn1* (36), we further sought to detect transcripts for this master regulator using RNAscope. Unlike in standard 2D cultures where it is highly downregulated (16, 17), a clear *Foxn1* expression could be observed in organoids (Fig. 1I).

To benchmark thymic epithelial organoids against standard 2D culture, we performed bulk RNA sequencing. Unsupervised hierarchical clustering showed the higher transcriptional similarity of thymic epithelial organoids to freshly extracted TECs (in vivo) than to 2D-cultured TECs (Fig. 1J, left). Similarly, a differential expression analysis showed that the expression levels of some key TEC genes, including *Foxn1*, *Dll4* and *Psmb11*, were more similar between in vivo TECs and thymic epithelial organoids compared to 2D-cultured TECs (Fig. 1J, right). Conversely, *Il7* and *Cdh1* were maintained in 2D culture as previously reported (16), and *Ly6a* (a marker of specific TEC subpopulations (37)) was upregulated. Lastly, gene set enrichment analysis performed on organoids at different time points confirmed the proliferation peak observed with staining (fig. S1D).

Collectively, these findings show that the defined culture conditions identified herein allow TECs (i) to grow independently of other cell types (ii) to form organoids containing diverse cell populations and that are transcriptionally similar to in vivo TECs.

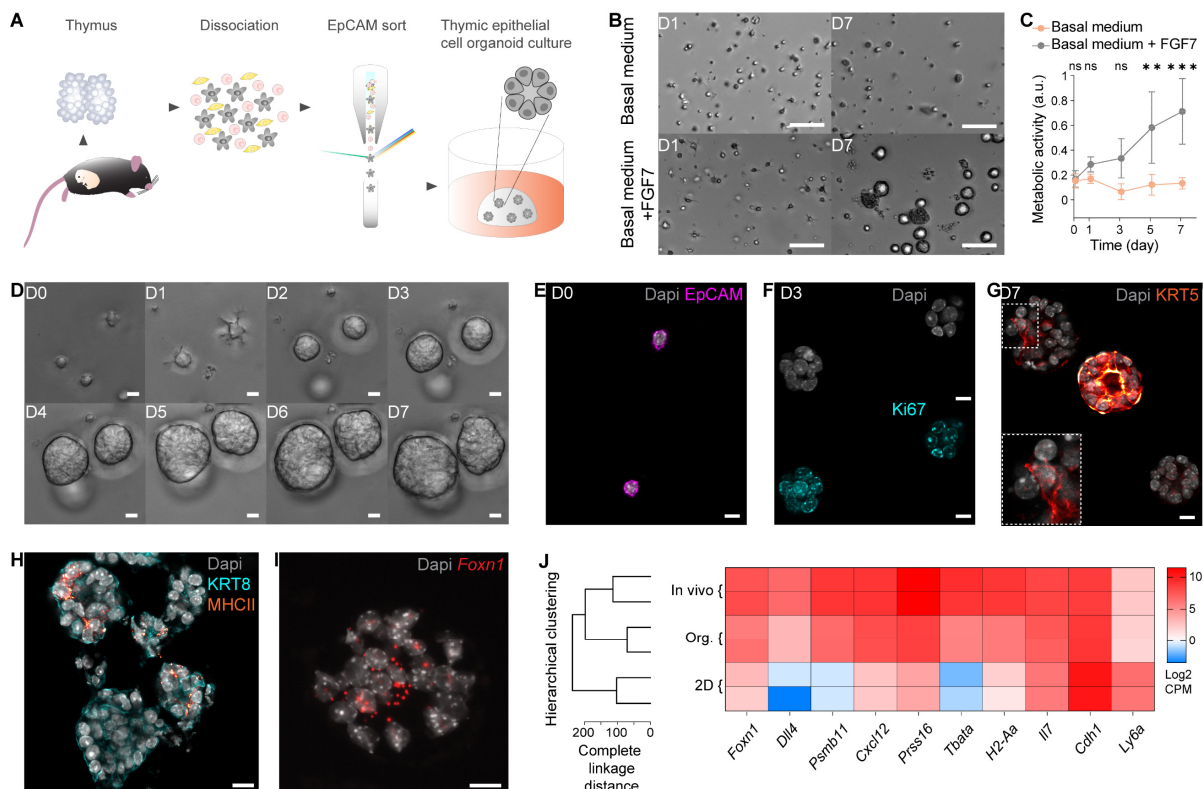


Fig. 1. Thymic epithelial cells grow and maintain marker expression in defined organoid culture conditions. (A) Schematic of the experimental workflow to isolate, select and culture thymic epithelial cells (TECs) to obtain organoids. (B) Brightfield images of TECs in organoid culture conditions one day (D1) and one week (D7) after seeding, in organoid basal medium and in organoid basal medium supplemented with FGF7. Scale bars, 100µm. (C) Metabolic activity (measured using resazurin) of TECs cultured in organoid basal medium and in organoid basal medium with FGF7. **: P = 0.0047, ***: P = 0.0005, ns: P > 0.05 (two-way ANOVA; n = 15 per condition, from 3 mice). Data represent mean ± standard deviation (SD). (D) One-week time course showing close up brightfield images of sorted TECs from single cells to multicellular organoids. Scale bars, 10µm. (E) Immunofluorescence image of individual EpCAM-positive (magenta) TECs immediately after seeding (D0) with nuclei counterstained using Dapi (grey). Scale bar, 10µm. (F) Immunofluorescence images of organoids three days after seeding demonstrating that cells undergo proliferation (Ki67 [cyan], Dapi stains nuclei [grey]). Scale bars, 10µm. (G) Immunofluorescence image of organoids showing different cell populations after one week in culture, here with medullary cells (KRT5 [red hot]) present in different patterns. Dapi counterstains nuclei (grey). Scale bar, 10µm. (H) Immunofluorescence image of D7 organoids highlighting MHCII expression (orange) with KRT8 (cyan) and nuclei counterstained using Dapi (grey). Scale bar, 10µm. (I) RNAscope image of organoid at D7 showing *Foxn1* expression (red) with nuclei counterstained using Spectral Dapi (grey). Scale bar, 10µm. (J) Gene expression profiling. Left: Hierarchical clustering (using hclust) showing clustering of thymic epithelial organoids (Org.) with freshly extracted TECs (In vivo) and not TECs cultured in 2D (2D). Metrics is complete linkage distance. Right: Heatmap displaying key TEC genes as well as *Cdh1* and *Ly6a* expression for the same three conditions. n = 2 mice per condition.

TECs cultured as organoids show in vitro functionality when reaggregated with T cell progenitors

To test the functionality of thymic epithelial organoids (i.e. their ability to mediate T cell development), we recapitulated the well-known reaggregate fetal thymic organ culture (RFTOC) approach, wherein selected thymic cell populations are reaggregated together and cultured at the air-liquid interface (4, 38). To do so, we dissociated TECs cultured as organoids and reaggregated them with an EpCAM-depleted single cell suspension obtained from E13.5 thymi. We performed EpCAM-depletion in order to keep the mesenchymal cells, which have been proven critical for T cell development (38). We used E13.5 embryonic thymi as source of T cell precursors because they contain thymocytes at the earliest stages of development, prior to the expression of CD4 and CD8 (thus referred to as double negative, DN) (fig. S2A). This allows to easily monitor whether T cell development happens in RFTOCs. To increase cell number and facilitate handling, mouse embryonic fibroblasts (MEFs) were also added, as done previously (39). We termed the RFTOCs formed with TECs from the organoid cultures organoid RFTOCs (ORFTOCs) (Fig. 2A).

After 6 days in culture, ORFTOCs were dissociated and analyzed by flow cytometry (fig. S2B). At this point, thymocytes expressing both CD4 and CD8 (termed double positive, DP) and constituting a developmental stage following the DN phenotype could be readily detected (Fig. 2, B and C), indicating that organoid-derived TECs mediated physiological progression of

thymocyte maturation. Notably, T cell development was similar to that observed in cultured intact thymic lobes (i.e. fetal thymic organ culture, FTOC) (Fig. 2, C and D, and fig. S2C). Conversely, reaggregating only the EpCAM-depleted fraction of E13.5 lobes and MEFs did not yield DP thymocytes (Fig. 2, C and D, and fig. S2D), demonstrating that organoid-derived TECs are necessary for T cell development in ORFTOCs. Lastly, reaggregates with only organoid-derived TECs and MEFs served as negative control and did not produce immune (CD45+) cells (Fig. 2E). To corroborate our findings, we reaggregated organoid-derived TECs with the earliest DN subpopulation (DN1) sorted from adult mice and MEFs, and could also observe thymocyte development (fig. S2E). The developmental kinetics was however faster in ORFTOCs containing E13.5-derived cells, as expected for first wave early T cell precursors (40).

Extending ORFTOC culture period from 6 to 13 days allowed thymocyte maturation to progress further, as an increased proportion of cells expressed the $\alpha\beta$ T cell receptor complex (TCR) (fig. S2F and Fig. 2F), and differentiated into the separate lineages of CD4+ and CD8+ single positive (SP) thymocyte, respectively (fig. S2F). FTOCs were again used as reference (fig. S2G) and demonstrated a comparable frequency of mature SP cells (fig. S2H).

As expected for functional TECs, ORFTOCs were positive for *Foxn1* (Fig. 2G). Morphologically, ORFTOCs also presented similarities to FTOCs, here highlighted by KRT8 and MHCII staining (Fig. 2H). UEA1 reactivity identified sparse medullary cells throughout ORFTOCs (Fig 2, I and J), and CD3 ϵ staining confirmed the presence of T cells in between EpCAM-positive epithelial cells (Fig. 2J).

In summary, we demonstrated that thymic epithelial organoids maintain their functionality and, when reaggregated with T cell progenitors, mediate T cell development similarly to intact thymic lobe cultures.

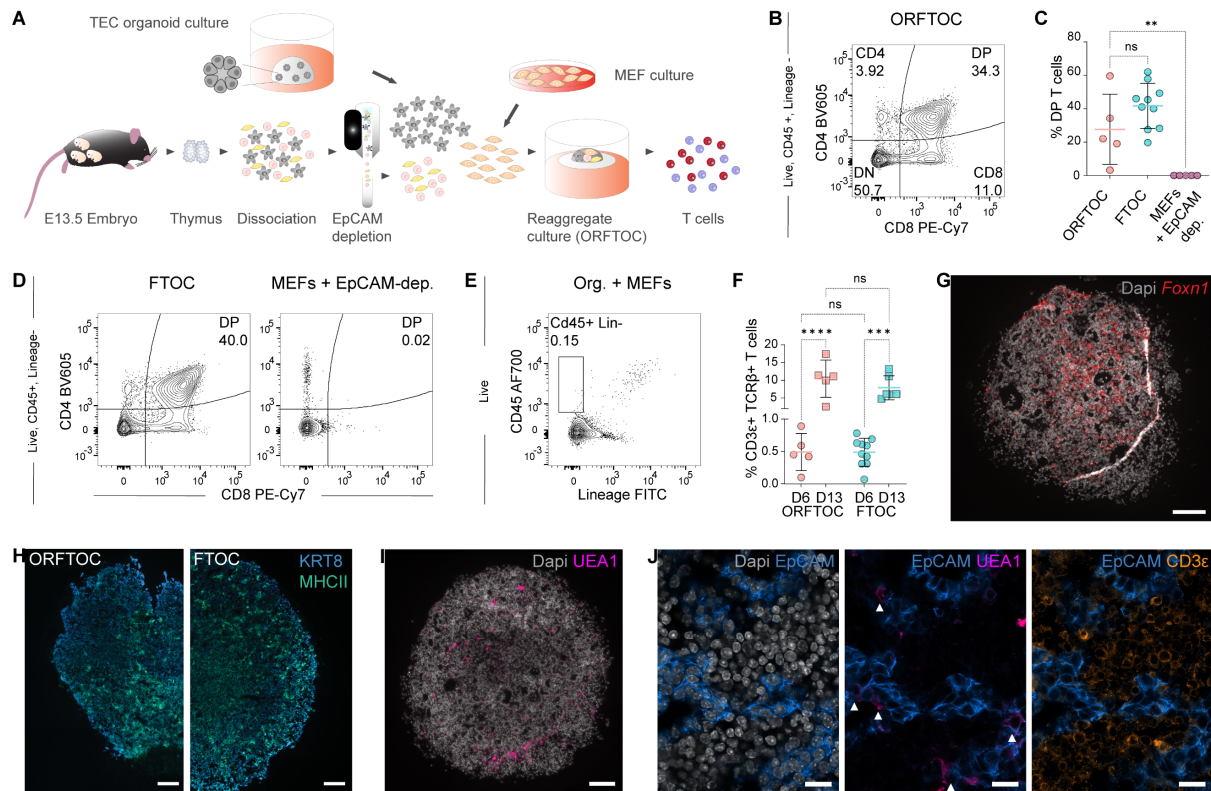


Fig. 2. TECs cultured as organoids show in vitro functionality when reaggregated with T cell progenitors. (A) Schematic of the experimental workflow to generate Organoid Reaggregate Fetal Thymic Organ Cultures (ORFTOCs) and analyze T cell development. (B) Flow cytometry plot showing T cell development in ORFTOCs. Gating strategy is indicated on the left. (C) Frequency of double positive (DP) thymocytes after 6 days in ORFTOCs and controls (fetal thymic organ cultures [FTOCs] and reaggregates containing only mouse embryonic fibroblasts [MEFs] and the EpCAM-depleted cells from thymic lobes). **: $P = 0.0081$, ns: $P > 0.05$ (Mood's median test with P-values adjusted with the false-discovery rate method; $n = 5, 10$ and 5 for ORFTOC, FTOC and MEFs + EpCAM-depleted cells, respectively, from 5 independent experiments). Graph represents individual datapoints with mean \pm SD. (D) Flow cytometry plots showing T cell development in controls (FTOCs [left] and MEFs + EpCAM-depleted cells reaggregates [right]). Gating strategy is indicated on the left. (E) Flow cytometry plot showing the absence of a CD45+ Lineage- population in control reaggregates containing only TECs cultured as organoids and MEFs. Gating strategy is indicated on the left. (F) Frequency of CD3 ϵ -positive, T cell receptor beta (TCR β)-positive cells in ORFTOCs and FTOCs at day 6 and 13. ***: $P = 0.0002$, ****: $P < 0.0001$, ns: $P > 0.05$ (one-way ANOVA with Tukey's multiple comparisons test; $n = 5, 5, 10$ and 6 for ORFTOC at day 6, 13 and FTOC at day 6, 13, respectively, from 5 independent experiments). Graph represents individual datapoints with mean \pm SD. (G) RNAscope image of D13 ORFTOC section highlighting *Foxn1* expression (red) with nuclei counterstained using Spectral dapi (grey). Scale bar, 100 μ m. (H) Immunofluorescence images of D13 ORFTOC (left) and FTOC (right) sections showing KRT8 (blue) and MHCII staining (green). Scale bar, 100 μ m. (I) Immunofluorescence image of D13 ORFTOC section demonstrating the presence of medullary cells (UEA1-reactivity [magenta]). Dapi counterstains nuclei (grey). Scale bar, 100 μ m. (J) Zoomed immunofluorescence images of ORFTOC section showing epithelial cells (EpCAM [blue]) and nuclei (dapi [grey]) (left), medullary cells (UEA1-reactivity [bright pink]) co-staining with epithelial cells (middle), and T cells (CD3 ϵ [amber]) in-between epithelial cells (right). Scale bars, 100 μ m.

ORFTOCs recapitulate in vivo-like TEC and T cell populations diversity and physiological T cell development

To further characterize the cell types in ORFTOCs, we profiled them and FTOC controls through single cell RNA sequencing (Fig. 3a). This analysis revealed three main clusters corresponding to the epithelial, immune, and mesenchymal compartments of ORFTOCs (Fig 3B). Unsupervised clustering identified 7 main clusters of epithelial cells (fig. S3A), which we annotated according to in vivo datasets (29, 35, 41–44): ‘early cTECs’, ‘cTECs’, ‘early mTECs’, ‘pre-Aire mTECs’, ‘Aire and Spink5 mTECs’, ‘tuft-like mTECs’, and ‘adult bipotent progenitor-like’ (fig. S3B). For the immune cells, clusters covered the main T cell developmental stages defined in vivo (40, 43, 45–48), spanning from progenitors to mature T cells (fig. S3, C and D). Both ORFTOCs and FTOCs contributed to all subpopulations (Fig. 3, C and D), suggesting that ORFTOCs faithfully recapitulate the different cell types present in FTOC controls. The biggest differences were observed for clusters representing cTECs and early stages of T cell development: (i) more ‘early cTECs’ were present in FTOCs and (ii) more ‘cTECs’ and ‘thymus-seeding progenitor (TSP) to DN early 1’ and ‘TSP to DN early 2’ cells were present in ORFTOCs.

To compare our in vitro populations with the in vivo thymus, we aligned our clusters to the mouse dataset of the reference atlas by Park et al. (43) (Fig. 3, E and F). We found strong overlap in most epithelial cell types (Fig. 3E), with the cTECs aligning together and most in vitro mTEC clusters matching their in vivo counterparts. However, the ‘adult bipotent progenitor-like’ cluster was smaller in vivo compared to in vitro. Immune clusters from our dataset also matched clusters defined for in vivo populations (Fig. 3F), especially from the ‘DP blast’/‘DP (P)’ stage onwards and, most importantly, for the CD4 and CD8 stages (mature T cells).

Besides gene expression, we also studied in vitro TCR recombination dynamics through V(D)J sequencing, allowing us to map productive T cells bearing both TCR chains on the immune UMAP (Fig. 3G). The quantification of productive chains presenting all V(D)J regions showed that TRB and TRA chain recombinations were mostly achieved prior to and at the DP stage, respectively (Fig. 3H), similarly to the Park dataset (43). In addition, thymocytes underwent proliferation (marked by high *Cdk1* expression) in between the recombination stages (marked by high *Rag1* and *Rag2* expression) (Fig. 3I), which also aligns with in vivo data (40, 43).

Taken together, these results show the transcriptional similarity of ORFTOCs to FTOCs and that ORFTOCs preserve in vivo-like TEC diversity and T cell development.

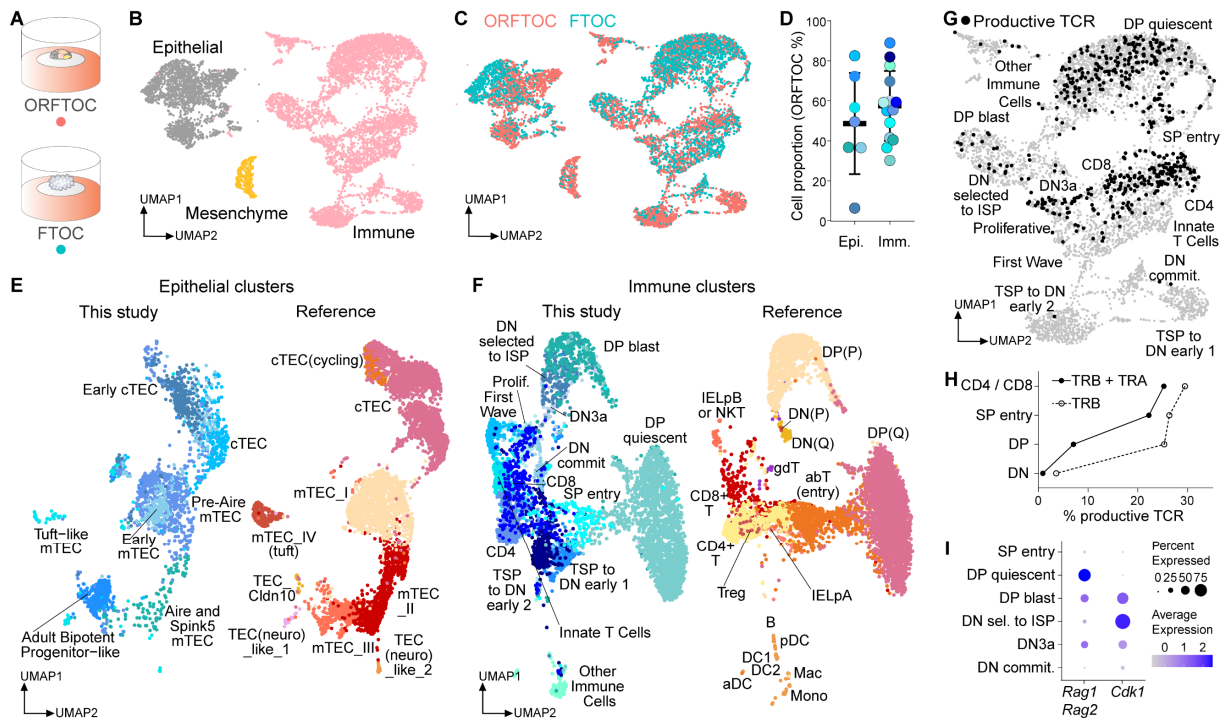


Fig. 3. ORFTOCs recapitulate in vivo-like TEC and T cell populations diversity and physiological T cell-development. (A) Schematic of the conditions used for ORFTOC and FTOC single-cell RNA sequencing with hashtag antibodies (HTOs). (B) Uniform Manifold Approximation and Projection (UMAP) showing 3 main clusters corresponding to the main input populations (epithelial, immune and mesenchymal cells). (C) UMAP displaying ORFTOC and FTOC cells distribution in the different clusters. (D) Dot plot representing ORFTOC proportion for each cluster (dot) within the epithelial or immune main populations, as well as mean ORFTOC proportion and standard deviation. Dot colors are matching clusters colors (fig. S3, A and C). No outliers within epithelial or immune compartments were identified by Grubbs test. (E - F) UMAPs showing the integration of the epithelial (E) and immune (F) clusters identified in this study (left) with the mouse dataset of the reference atlas by Park et al. (43) (right). (G) UMAP of the immune cluster (grey), highlighting cells identified as productive and bearing both TCR chains (black). (H) Frequency of productive cells with rearranged TRB or both TRA and TRB chains for the main thymocyte developmental stages. (I) Dot plot representing the frequency of cells and the expression level of the recombination enzymes *Rag1* and *Rag2* as well as of the cyclin protein *Cdk1* during the recombination and proliferation stages of thymocyte development.

cTEC: cortical TECs, mTEC: medullary TECs, DN: double negative, ISP: intermediate single positive, Prolif: proliferative, commit: commitment, TSP: thymus-seeding progenitors, DP: double positive, (P): proliferative, (Q): quiescent, IELpB: intestinal intraepithelial lymphocytes precursor B, NKT: natural killer T, IELpA: intestinal intraepithelial lymphocytes precursor A, DC: dendritic cells, pDC: plasmacytoid dendritic cells, aDC; activated dendritic cells, Mac: macrophages Mono: monocytes, sel: selected.

ORFTOCs show thymus-like ability to attract new T cell progenitors and improved epithelial organization upon in vivo grafting

The thymus continuously attracts bone marrow-derived hematopoietic precursors and commits them to the T cell lineage (49, 50). To test whether ORFTOCs retain this crucial capacity, we transplanted them under the kidney capsule of syngeneic CD45.1 recipient mice (Fig. 4A). After 5 weeks, all grafts developed into sizeable thymus-like tissues (4/4 ORFTOCs [Fig. 4B],

4/4 FTOC controls). Using flow cytometric analyses (fig. S4A), we identified all major thymocyte populations (DN, DP, CD4, CD8) in ORFTOC grafts (Fig. 4C), and their proportions were comparable to FTOC control grafts and control thymi (Fig. 4D). This result demonstrated that normal $\alpha\beta$ -TCR T cell lineage maturation was supported in ORFTOC grafts. A further detailed analysis (fig. S4, B to D) detected thymocytes at the DN3 to DN4 transition at the time of ORFTOC graft retrieval. This stage indicates successful β -selection (40), thus demonstrating ORFTOC graft ability to continuously attract and select blood-borne T cell progenitors (fig. S4, B to D). Finally, the presence of CD45.1+ mature thymocytes (classified as M1 [CD24+ CD69+] and M2 [CD24+ CD69-], respectively [Fig. 4E and fig. S4E]) and of regulatory T cells (Fig. 4F and fig. S4F) showed ORFTOC graft capacity to generate mature CD4 and CD8 T cells, impose their post-selection maturation and select T cells with a regulatory phenotype.

Histological staining showed that ORFTOC grafts, similar to FTOC grafts, displayed the characteristic differences in cellular densities between cortical and medullary areas seen in the native thymus (51) (fig. S4G and Fig. 4G). Immunostaining confirmed the presence of medullary areas (positive for KRT5 and reactive to UEA1) containing Aire-positive cells (Fig. 4G). These medullary areas were larger compared to the sparse medullary cells observed after in vitro culture only (Fig. 2I), likely due to continuous seeding with new T cell progenitors and prolonged crosstalk with immune cells (52).

In conclusion, kidney capsule transplants showed that organoid-derived TECs in ORFTOCs have the (i) capacity to mature and reach an organization resembling the native thymus and (ii) long-term ability to attract T cell progenitors and mediate physiological T cell development.

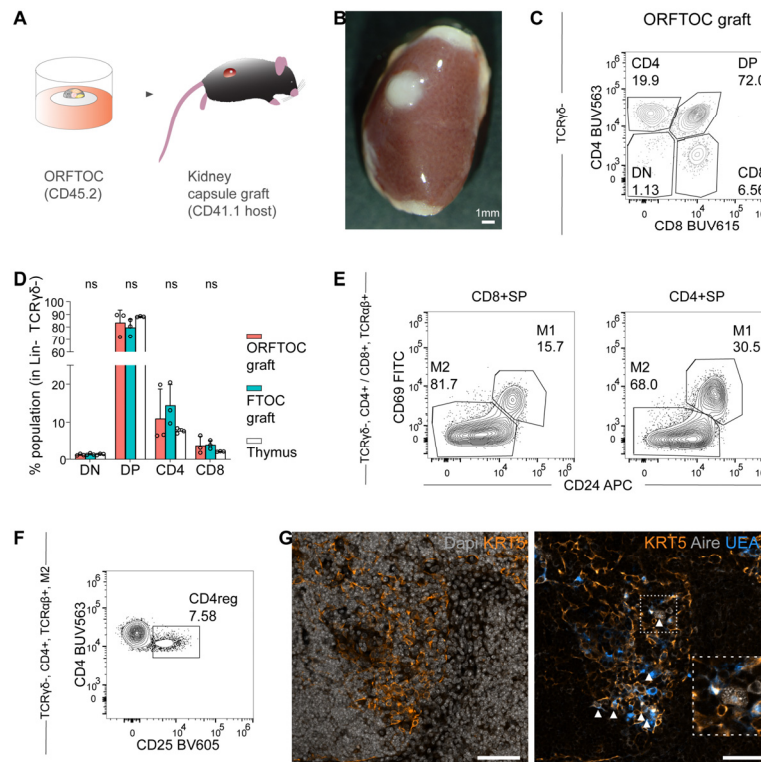


Fig. 4. ORFTOCs show thymus-like ability to attract new T cell progenitors and improved epithelial organization upon in vivo grafting. (A) Schematic representing the experimental design for the grafting of ORFTOCs under the kidney capsule. (B) Widefield image of an ORFTOC graft retrieved after 5 weeks. Scale bar, 1mm. (C) Flow cytometry plot showing host thymocyte development in ORFTOC grafts. Gating strategy is indicated on the left. (D) Relative frequency of the major thymocyte subpopulations in ORFTOC grafts, in control FTOC grafts and thymi. ns: $P > 0.05$ (one-way ANOVA for each subpopulation between conditions; $n = 3$ grafts/mice for each condition). Bar graph represents mean \pm SD and individual datapoints. (E) Flow cytometry plots showing the presence of two separate post-selection stages (defined by the expression of CD24 and CD69) within the CD8 and CD4 single positive (SP) populations in ORFTOC grafts. Gating strategy is indicated on the left. (F) Flow cytometry plot showing the presence of CD4 regulatory T cells (CD4reg, defined by CD45 and CD25 expression) in ORFTOC grafts. Gating strategy is indicated on the left. (G) Immunofluorescence images of ORFTOC graft section. Left: medullary cells (KRT5 [amber]) are present in the less dense area (Dapi [grey]). Right: UEA1-reactive (azure) and Aire-positive cells (grey, highlighted with arrowhead) are also present in the medullary region. Scale bars, 100 μ m.

In this study, we showed that stromal cells of a lymphoid organ, namely epithelial cells of the thymus, can be cultured as organoids similarly to cells from other endoderm-derived organs. We established TEC-specific culture conditions, characterized the organoids, and demonstrated their superiority in maintaining TEC marker expression compared to conventional 2D cultures. Reaggregating TECs from organoid cultures with T cell progenitors proved their functionality and ability to mediate T cell development. TEC and T cell populations in reaggregates resembled the native cell types, and T cell maturation was recapitulated in a physiological manner. Finally, kidney capsule transplants demonstrated the long-term

capability of organoid reagggregates to attract new T cell progenitors and mediate their entire development.

Overall, this work presents the first method to culture TECs independently of other cell types in a way that maintains their thymopoietic ability. Although thymic epithelial organoids recapitulate many key organoid features such as cell population diversity and possibility to be expanded and passaged, maintaining their functionality in the long term remains challenging. This is probably linked to some niche factors missing in the current relatively minimal culture conditions, which over time either generally prevent functionality to be maintained or enrich for specific subsets that might lack functionality (41). Future work including single-cell transcriptomics analysis of the organoids will most likely help identify yet unexplored but necessary niche factors.

Still, thymic epithelial organoids open up new opportunities to study T cell development in vitro in a physiological manner and gain new insights into TEC biology. As TECs undergo deterioration during aging and different medical conditions, the development of the current and future culture conditions might also pave the way for novel thymus regeneration strategies. Finally, to the best of our knowledge, this is the first work to generate bona fide organoids from the stromal compartment of a lymphoid organ.

References

1. G. Rossi, A. Manfrin, M. P. Lutolf, Progress and potential in organoid research. *Nat. Rev. Genet.* **19**, 671–687 (2018). doi:10.1038/s41576-018-0051-9.
2. J. J. T. Owen, M. A. Ritter, TISSUE INTERACTION IN THE DEVELOPMENT OF THYMUS LYMPHOCYTES. *J. Exp. Med.* **129**, 431–442 (1969). doi:10.1084/jem.129.2.431.
3. G. Anderson, E. J. Jenkinson, Use of explant technology in the study of in vitro immune responses. *J. Immunol. Methods.* **216**, 155–163 (1998). doi:10.1016/S0022-1759(98)00076-3.
4. E. J. Jenkinson, G. Anderson, J. J. T. Owen, Studies on T cell maturation on defined thymic stromal cell populations in vitro. *J. Exp. Med.* **176**, 845–853 (1992). doi:10.1084/jem.176.3.845.
5. S. Giger, M. Hofer, M. Miljkovic-Licina, S. Hoehnel, N. Brandenberg, R. Guiet, M. Ehrbar, E. Kleiner, K. Gegenschatz-Schmid, T. Matthes, M. P. Lutolf, Microarrayed human bone marrow organoids for modeling blood stem cell dynamics. *APL Bioeng.* **6** (2022). doi:10.1063/5.0092860.
6. L. E. Wagar, A. Salahudeen, C. M. Constantz, B. S. Wendel, M. M. Lyons, V. Mallajosyula, L. P. Jatt, J. Z. Adamska, L. K. Blum, N. Gupta, K. J. L. Jackson, F. Yang, K. Röltgen, K. M. Roskin, K. M. Blaine, K. D. Meister, I. N. Ahmad, M. Cortese, E. G. Dora, S. N. Tucker, A. I. Sperling, A. Jain, D. H. Davies, P. L. Felgner, G. B. Hammer, P. S. Kim, W. H. Robinson, S. D. Boyd, C. J. Kuo, M. M. Davis, Modeling human adaptive immune responses with tonsil organoids. *Nat. Med.* **27**, 125–135 (2021). doi:10.1038/s41591-020-01145-0.
7. S. Kim, S. B. Shah, P. L. Graney, A. Singh, Multiscale engineering of immune cells and lymphoid organs. *Nat. Rev. Mater.* **4**, 355–378 (2019). doi:10.1038/s41578-019-0100-9.
8. P. E. Bourguine, T. Klein, A. M. Paczulla, T. Shimizu, L. Kunz, K. D. Kokkaliaris, D. L. Coutu, C. Lengerke, R. Skoda, T. Schroeder, I. Martin, In vitro biomimetic engineering of a human hematopoietic niche with functional properties. *Proc. Natl. Acad. Sci. U. S. A.* **115**, E5688–E5695 (2018). doi:10.1073/pnas.1805440115.
9. M. C. Poznansky, R. H. Evans, R. B. Foxall, I. T. Olszak, A. H. Piascik, K. E. Hartman, C. Brander, T. H. Meyer, M. J. Pykett, K. T. Chabner, S. A. Kalams, M. Rosenzweig, D. T. Scadden, Efficient generation of human T cells from a tissue-engineered thymic organoid. *Nat. Biotechnol.* **18**, 729–734 (2000). doi:10.1038/77288.
10. M. A. Asnaghi, T. Barthlott, F. Gullotta, V. Strusi, A. Amovilli, K. Hafen, G. Srivastava, P. Oertle, R. Toni, D. Wendt, G. A. Holländer, I. Martin, Thymus Extracellular Matrix-Derived Scaffolds Support Graft-Resident Thymopoiesis and Long-Term In Vitro Culture of Adult Thymic Epithelial Cells. *Adv. Funct. Mater.* **31**, 2010747 (2021). doi:10.1002/adfm.202010747.
11. M. Hun, J. Ramshaw, A. P. Chidgey, M. Barsanti, K. Wong, J. Werkmeister, Native thymic extracellular matrix improves in vivo thymic organoid T cell output, and drives in vitro thymic epithelial cell differentiation. *Biomaterials.* **118**, 1–15 (2016). doi:10.1016/j.biomaterials.2016.11.054.
12. Y. Fan, A. Tajima, S. K. Goh, X. Geng, G. Gualtierotti, M. Grupillo, A. Coppola, S. Bertera, W. A. Rudert, I. Banerjee, R. Bottino, M. Trucco, Bioengineering Thymus Organoids to Restore Thymic Function and Induce Donor-Specific Immune Tolerance to Allografts. *Mol. Ther.* **23**, 1262–1277 (2015). doi:10.1038/mt.2015.77.
13. S. Campinoti, A. Gjinovci, R. Ragazzini, L. Zanieri, L. Ariza-McNaughton, M. Catucci, S. Boeing, J. E. Park, J. C. Hutchinson, M. Muñoz-Ruiz, P. G. Manti, G. Voza, C. E. Villa, D. E. Phylactopoulos, C. Maurer, G. Testa, H. J. Stauss, S. A. Teichmann, N. J. Sebire, A. C. Hayday, D. Bonnet, P. Bonfanti, Reconstitution of a functional human thymus by postnatal stromal progenitor cells and natural whole-organ scaffolds. *Nat. Commun.* **11**, 6372 (2020). doi:10.1038/s41467-020-20082-7.

14. A. Purwada, A. Singh, Immuno-engineered organoids for regulating the kinetics of B-cell development and antibody production. *Nat. Protoc.* **12**, 168–182 (2017). doi:10.1038/nprot.2016.157.
15. G. Goyal, P. Prabhala, G. Mahajan, B. Bausk, T. Gilboa, L. Xie, Y. Zhai, R. Lazarovits, A. Mansour, M. S. Kim, A. Patil, D. Curran, J. M. Long, S. Sharma, A. Junaid, L. Cohen, T. C. Ferrante, O. Levy, R. Prantil-Baun, D. R. Walt, D. E. Ingber, Ectopic Lymphoid Follicle Formation and Human Seasonal Influenza Vaccination Responses Recapitulated in an Organ-on-a-Chip. *Adv. Sci.* **9**, 1–15 (2022). doi:10.1002/advs.202103241.
16. K. L. Anderson, N. C. Moore, D. E. J. McLoughlin, E. J. Jenkinson, J. J. T. Owen, Studies on thymic epithelial cells in vitro. *Dev. Comp. Immunol.* **22**, 367–377 (1998). doi:10.1016/S0145-305X(98)00011-1.
17. M. Mohtashami, J. C. Zúñiga-Pflücker, Cutting Edge: Three-Dimensional Architecture of the Thymus Is Required to Maintain Delta-Like Expression Necessary for Inducing T Cell Development. *J. Immunol.* **176**, 730–734 (2006). doi:10.4049/jimmunol.176.2.730.
18. C. S. Seet, C. He, M. T. Bethune, S. Li, B. Chick, E. H. Gschwend, Y. Zhu, K. Kim, D. B. Kohn, D. Baltimore, G. M. Crooks, A. Montel-Hagen, Generation of mature T cells from human hematopoietic stem and progenitor cells in artificial thymic organoids. *Nat. Methods.* **14**, 521–530 (2017). doi:10.1038/nmeth.4237.
19. A. Montel-Hagen, V. Sun, D. Casero, S. Tsai, A. Zampieri, N. Jackson, S. Li, S. Lopez, Y. Zhu, B. Chick, C. He, S. C. de Barros, C. S. Seet, G. M. Crooks, In Vitro Recapitulation of Murine Thymopoiesis from Single Hematopoietic Stem Cells. *Cell Rep.* **33**, 108320 (2020). doi:10.1016/j.celrep.2020.108320.
20. A. V. Parent, H. A. Russ, I. S. Khan, T. N. Laflam, T. C. Metzger, M. S. Anderson, M. Hebrok, Generation of functional thymic epithelium from human embryonic stem cells that supports host T cell development. *Cell Stem Cell.* **13**, 219–229 (2013). doi:10.1016/j.stem.2013.04.004.
21. S. A. Ramos, J. J. Morton, P. Yadav, B. Reed, S. I. Alizadeh, A. H. Shilleh, L. Perrenoud, J. Jagers, J. Kappler, A. Jimeno, H. A. Russ, Generation of functional human thymic cells from induced pluripotent stem cells. *J. Allergy Clin. Immunol.* **149**, 767-781.e6 (2022). doi:10.1016/j.jaci.2021.07.021.
22. X. Sun, J. Xu, H. Lu, W. Liu, Z. Miao, X. Sui, H. Liu, L. Su, W. Du, Q. He, F. Chen, Y. Shi, H. Deng, Directed differentiation of human embryonic stem cells into thymic epithelial progenitor-like cells reconstitutes the thymic microenvironment in vivo. *Cell Stem Cell.* **13**, 230–236 (2013). doi:10.1016/j.stem.2013.06.014.
23. L. Lai, J. Jin, Generation of thymic epithelial cell progenitors by mouse embryonic stem cells. *Stem Cells.* **27**, 3012–3020 (2009). doi:10.1002/stem.238.
24. N. Bredenkamp, S. Ulyanchenko, K. E. O'Neill, N. R. Manley, H. J. Vaidya, C. C. Blackburn, An organized and functional thymus generated from FOXP1-reprogrammed fibroblasts. *Nat. Cell Biol.* **16**, 902–908 (2014). doi:10.1038/ncb3023.
25. K. Wong, N. L. Lister, M. Barsanti, J. M. C. Lim, M. V. Hammett, D. M. Khong, C. Siatskas, D. H. D. Gray, R. L. Boyd, A. P. Chidgey, Multilineage potential and self-renewal define an epithelial progenitor cell population in the adult thymus. *Cell Rep.* **8**, 1198–1209 (2014). doi:10.1016/j.celrep.2014.07.029.
26. A. Lepletier, M. L. Hun, M. V. Hammett, K. Wong, H. Naeem, M. Hedger, K. Loveland, A. P. Chidgey, Interplay between Follistatin, Activin A, and BMP4 Signaling Regulates Postnatal Thymic Epithelial Progenitor Cell Differentiation during Aging. *Cell Rep.* **27**, 3887-3901.e4 (2019). doi:10.1016/j.celrep.2019.05.045.
27. C. Meireles, A. R. Ribeiro, R. D. Pinto, C. Leitão, P. M. Rodrigues, N. L. Alves, Thymic crosstalk restrains the pool of cortical thymic epithelial cells with progenitor properties. *Eur. J. Immunol.* **47**, 958–969 (2017). doi:10.1002/eji.201746922.
28. N. Kadouri, S. Nevo, Y. Goldfarb, J. Abramson, Thymic epithelial cell heterogeneity: TEC by TEC. *Nat. Rev. Immunol.* **20**, 239–253 (2020). doi:10.1038/s41577-019-0238-0.
29. J. Baran-Gale, M. D. Morgan, S. Maio, F. Dhalla, I. Calvo-Asensio, M. E. Deadman, A.

- E. Handel, A. Maynard, S. Chen, F. Green, R. V. Sit, N. F. Neff, S. Darmanis, W. Tan, A. P. May, J. C. Marioni, C. P. Ponting, G. A. Holländer, Ageing compromises mouse thymus function and remodels epithelial cell differentiation. *Elife*. **9**, 1–71 (2020). doi:10.7554/ELIFE.56221.
30. P. Bonfanti, S. Claudinot, A. W. Amici, A. Farley, C. C. Blackburn, Y. Barrandon, Microenvironmental reprogramming of thymic epithelial cells to skin multipotent stem cells. *Nature*. **466**, 978–982 (2010). doi:10.1038/nature09269.
 31. A. S. Alawam, G. Anderson, B. Lucas, Generation and Regeneration of Thymic Epithelial Cells. *Front. Immunol.* **11**, 1–15 (2020). doi:10.3389/fimmu.2020.00858.
 32. K. D. James, W. E. Jenkinson, G. Anderson, Non-Epithelial Stromal Cells in Thymus Development and Function. *Front. Immunol.* **12**, 1–13 (2021). doi:10.3389/fimmu.2021.634367.
 33. M. S. Chaudhry, E. Velardi, J. A. Dudakov, M. R. M. van den Brink, Thymus: The next (re)generation. *Immunol. Rev.* **271**, 56–71 (2016). doi:10.1111/imr.12418.
 34. T. Boehm, J. B. Swann, Thymus involution and regeneration: Two sides of the same coin? *Nat. Rev. Immunol.* **13**, 831–838 (2013). doi:10.1038/nri3534.
 35. A. Nusser, Sagar, J. B. Swann, B. Krauth, D. Diekhoff, L. Calderon, C. Happe, D. Grün, T. Boehm, Developmental dynamics of two bipotent thymic epithelial progenitor types. *Nature*. **606**, 165–171 (2022). doi:10.1038/s41586-022-04752-8.
 36. S. Žuklys, A. Handel, S. Zhanybekova, F. Govani, M. Keller, S. Maio, C. E Mayer, H. Ying Teh, K. Hafen, G. Gallone, T. Barthlott, C. P. Ponting, G. A. Holländer, Foxn1 regulates key target genes essential for T cell development in postnatal thymic epithelial cells. *Nat. Immunol.* **17**, 1206–1215 (2016). doi:10.1038/ni.3537.
 37. F. Klein, C. Veiga-Villauriz, A. Börsch, S. Maio, S. Palmer, F. Dhalla, A. E. Handel, S. Zuklys, I. Calvo-Asensio, L. Musette, M. E. Deadman, A. J. White, B. Lucas, G. Anderson, G. A. Holländer, Combined multidimensional single-cell protein and RNA profiling dissects the cellular and functional heterogeneity of thymic epithelial cells. *Nat. Commun.* **14**, 4071 (2023). doi:10.1038/s41467-023-39722-9.
 38. G. Anderson, E. J. Jenkinson, N. C. Moore, J. J. T. Owen, MHC class II-positive epithelium and mesenchyme cells are both required for T cell development in the thymus. *Nature*. **362**, 70–73 (1993). doi:10.1038/362070a0.
 39. J. M. Sheridan, S. Taoudi, A. Medvinsky, C. C. Blackburn, A Novel Method for the Generation of Reaggregated Organotypic Cultures That Permits Juxtaposition of Defined Cell Populations. *Genesis*. **351**, 346–351 (2009). doi:10.1002/dvg.20505.
 40. E. V. Rothenberg, Single-cell insights into the hematopoietic generation of T-lymphocyte precursors in mouse and human. *Exp. Hematol.* **95**, 1–12 (2021). doi:10.1016/j.exphem.2020.12.005.
 41. H. Gao, M. Cao, K. Deng, Y. Yang, J. Song, M. Ni, C. Xie, W. Fan, C. Ou, D. Huang, L. Lin, L. Liu, Y. Li, H. Sun, X. Cheng, J. Wu, C. Xia, X. Deng, L. Mou, P. Chen, The Lineage Differentiation and Dynamic Heterogeneity of Thymic Epithelial Cells During Thymus Organogenesis. *Front. Immunol.* **13**, 1–24 (2022). doi:10.3389/fimmu.2022.805451.
 42. C. Bornstein, S. Nevo, A. Giladi, N. Kadouri, M. Pouzolles, F. Gerbe, E. David, A. Machado, A. Chuprin, B. Tóth, O. Goldberg, S. Itzkovitz, N. Taylor, P. Jay, V. S. Zimmermann, J. Abramson, I. Amit, Single-cell mapping of the thymic stroma identifies IL-25-producing tuft epithelial cells. *Nature*. **559**, 622–626 (2018). doi:10.1038/s41586-018-0346-1.
 43. J. E. Park, R. A. Botting, C. D. Conde, D. M. Popescu, M. Lavaert, D. J. Kunz, I. Goh, E. Stephenson, R. Ragazzini, E. Tuck, A. Wilbrey-Clark, K. Roberts, V. R. Kedlian, J. R. Ferdinand, X. He, S. Webb, D. Maunder, N. Vandamme, K. T. Mahbubani, K. Polanski, L. Mamanova, L. Bolt, D. Crossland, F. De Rita, A. Fuller, A. Filby, G. Reynolds, D. Dixon, K. Saeb-Parsy, S. Lisgo, D. Henderson, R. Vento-Tormo, O. A. Bayraktar, R. A. Barker, K. B. Meyer, Y. Saeys, P. Bonfanti, S. Behjati, M. R. Clatworthy, T. Taghon, M. Haniffa, S. A. Teichmann, A cell atlas of human thymic development defines T cell repertoire formation. *Science*. **367** (2020), doi:10.1126/science.aay3224.

- doi:10.1126/science.aay3224.
44. J. L. Bautista, N. T. Cramer, C. N. Miller, J. Chavez, D. I. Berrios, L. E. Byrnes, J. Germino, V. Ntranos, J. B. Sneddon, T. D. Burt, J. M. Gardner, C. J. Ye, M. S. Anderson, A. V Parent, Single-cell transcriptional profiling of human thymic stroma uncovers novel cellular heterogeneity in the thymic medulla. *Nat. Commun.* (2021), doi:10.1038/s41467-021-21346-6. doi:10.1038/s41467-021-21346-6.
 45. M. Cordes, K. Canté-Barrett, E. B. van den Akker, F. A. Moretti, S. M. Kiełbasa, S. A. Vloemans, L. Garcia-Perez, C. Teodosio, J. J. M. van Dongen, K. Pike-Overzet, M. J. T. Reinders, F. J. T. Staal, Single-cell immune profiling reveals thymus-seeding populations, T cell commitment, and multilineage development in the human thymus. *Sci. Immunol.* **7** (2022). doi:10.1126/sciimmunol.ade0182.
 46. M. Mingueneau, T. Kreslavsky, D. Gray, T. Heng, R. Cruse, J. Ericson, S. Bendall, M. H. Spitzer, G. P. Nolan, K. Kobayashi, H. Von Boehmer, D. Mathis, C. Benoist, A. J. Best, J. Knell, A. Goldrath, D. Koller, T. Shay, A. Regev, N. Cohen, P. Brennan, M. Brenner, F. Kim, T. N. Rao, A. Wagers, K. Rothamel, A. Ortiz-Lopez, N. A. Bezman, J. C. Sun, G. Min-Oo, C. C. Kim, L. L. Lanier, J. Miller, B. Brown, M. Merad, E. L. Gautier, C. Jakubzick, G. J. Randolph, P. Monach, D. A. Blair, M. L. Dustin, S. A. Shinton, R. R. Hardy, D. Laidlaw, J. Collins, R. Gazit, D. J. Rossi, N. Malhotra, K. Sylvia, J. Kang, A. Fletcher, K. Elpek, A. Bellemare-Pelletier, D. Malhotra, S. Turley, The transcriptional landscape of $\alpha\beta$ T cell differentiation. *Nat. Immunol.* **14**, 619–632 (2013). doi:10.1038/ni.2590.
 47. W. Zhou, M. A. Yui, B. A. Williams, J. Yun, B. J. Wold, L. Cai, E. V Rothenberg, W. Zhou, M. A. Yui, B. A. Williams, J. Yun, B. J. Wold, L. Cai, E. V Rothenberg, Single-Cell Analysis Reveals Regulatory Gene Expression Dynamics Leading to Lineage Commitment in Early T Cell Development Article Single-Cell Analysis Reveals Regulatory Gene Expression Dynamics Leading to Lineage Commitment in Early T Cell Development. *Cell Syst.* **9**, 321–337.e9 (2019). doi:10.1016/j.cels.2019.09.008.
 48. T. C. Luis, S. Luc, T. Mizukami, H. Boukarabila, S. Thongjuea, P. S. Woll, E. Azzoni, A. Giustacchini, M. Lutteropp, T. Bouriez-Jones, H. Vaidya, A. J. Mead, D. Atkinson, C. Böiers, J. Carrelha, I. C. MacAulay, R. Patient, F. Geissmann, C. Nerlov, R. Sandberg, M. F. T. R. De Bruijn, C. C. Blackburn, I. Godin, S. E. W. Jacobsen, Initial seeding of the embryonic thymus by immune-restricted lympho-myeloid progenitors. *Nat. Immunol.* **17**, 1424–1435 (2016). doi:10.1038/ni.3576.
 49. M. Lavaert, K. L. Liang, N. Vandamme, J. E. Park, J. Roels, M. S. Kowalczyk, B. Li, O. Ashenberg, M. Tabaka, D. Dionne, T. L. Tickle, M. Slyper, O. Rozenblatt-Rosen, B. Vandekerckhove, G. Leclercq, A. Regev, P. Van Vlierberghe, M. Guillems, S. A. Teichmann, Y. Saeys, T. Taghon, Integrated scRNA-Seq Identifies Human Postnatal Thymus Seeding Progenitors and Regulatory Dynamics of Differentiating Immature Thymocytes. *Immunity.* **52**, 1088–1104.e6 (2020). doi:10.1016/j.immuni.2020.03.019.
 50. A. Y. Lai, M. Kondo, Identification of a bone marrow precursor of the earliest thymocytes in adult mouse. *Proc. Natl. Acad. Sci. U. S. A.* **104**, 6311–6316 (2007). doi:10.1073/pnas.0609608104.
 51. J. Gordon, N. R. Manley, Mechanisms of thymus organogenesis and morphogenesis. *Development.* **138**, 3865–3878 (2011). doi:10.1242/dev.059998.
 52. M. Irla, G. Hollander, W. Reith, Control of central self-tolerance induction by autoreactive CD4+ thymocytes. *Trends Immunol.* **31**, 71–79 (2010). doi:10.1016/j.it.2009.11.002.
 53. M. D. Robinson, D. J. McCarthy, G. K. Smyth, edgeR: a Bioconductor package for differential expression analysis of digital gene expression data. *Bioinformatics.* **26**, 139–140 (2010). doi:10.1093/bioinformatics/btp616.
 54. G. K. Smyth, M. E. Ritchie, C. W. Law, M. Alhamdoosh, S. Su, X. Dong, L. Tian, RNA-seq analysis is easy as 1-2-3 with limma, Glimma and edgeR. *F1000Research.* **5** (2018). doi:10.12688/f1000research.9005.3.
 55. A. Reiner, D. Yekutieli, Y. Benjamini, Identifying differentially expressed genes using false discovery rate controlling procedures. *Bioinformatics.* **19**, 368–375 (2003). doi:10.1093/bioinformatics/btf877.

56. F. Murtagh, *Multivariate Data Analysis with Fortran, C and Java Code* (1987).
57. A. Subramanian, P. Tamayo, V. K. Mootha, S. Mukherjee, B. L. Ebert, M. A. Gillette, A. Paulovich, S. L. Pomeroy, T. R. Golub, E. S. Lander, J. P. Mesirov, Gene set enrichment analysis: A knowledge-based approach for interpreting genome-wide expression profiles. *Proc. Natl. Acad. Sci. U. S. A.* **102**, 15545–15550 (2005). doi:10.1073/pnas.0506580102.
58. A. Liberzon, C. Birger, H. Thorvaldsdóttir, M. Ghandi, J. P. Mesirov, P. Tamayo, The Molecular Signatures Database Hallmark Gene Set Collection. *Cell Syst.* **1**, 417–425 (2015). doi:10.1016/j.cels.2015.12.004.
59. D. G. Howe, J. A. Blake, Y. M. Bradford, C. J. Bult, B. R. Calvi, S. R. Engel, J. A. Kadin, T. C. Kaufman, R. Kishore, S. J. F. Lauderkind, S. E. Lewis, S. A. T. Moxon, J. E. Richardson, C. Smith, Model organism data evolving in support of translational medicine. *Lab Anim. (NY)*. **47**, 277–289 (2018). doi:10.1038/s41684-018-0150-4.
60. Y. Hao, S. Hao, E. Andersen-nissen, R. Gottardo, P. Smibert, Y. Hao, S. Hao, E. Andersen-nissen, W. M. M. Iii, S. Zheng, A. Butler, E. Papalexi, E. P. Mimitou, J. Jain, A. Srivastava, T. Stuart, L. M. Fleming, B. Yeung, Resource Integrated analysis of multimodal single-cell data II Integrated analysis of multimodal single-cell data. *Cell*. **184**, 3573–3587.e29 (2021). doi:10.1016/j.cell.2021.04.048.
61. P. L. Germain, M. D. Robinson, A. Lun, C. Garcia Meixide, W. Macnair, Doublet identification in single-cell sequencing data using scDbtFinder. *F1000Research*. **10**, 1–26 (2022). doi:10.12688/f1000research.73600.2.
62. E. M. Kernfeld, R. M. J. Genga, K. Neherin, M. E. Magaletta, P. Xu, R. Maehr, A Single-Cell Transcriptomic Atlas of Thymus Organogenesis Resolves Cell Types and Developmental Maturation. *Immunity*. **48**, 1258–1270.e6 (2018). doi:10.1016/j.immuni.2018.04.015.
63. N. Borchering, N. L. Bormann, G. Kraus, scRepertoire: An R-based toolkit for single-cell immune receptor analysis. *F1000Research*. **9**, 1–17 (2020). doi:10.12688/f1000research.22139.2.
64. S. S. Mangiafico, SUMMARY AND ANALYSIS OF EXTENSION PROGRAM EVALUATION IN R (2016).

Acknowledgements

We thank all present and past LSCB members and in particular Antonius Chrisnandy, Bilge Sen Elci and Moritz Hofer for discussions and sharing materials. We thank Julia Pr bandier for administrative assistance and Katrin Hafen for technical expertise. We acknowledge support and work from the Flow Cytometry, Centre de Ph nog nomique, Gene Expression, Histology and Bioluminescence and Optics EPFL core facilities. We thank all collaborators from the Syn-Thy project, in particular Graham Anderson, Viktorja Major, Joanna Sweetman and Tim Henderson and for their feedback.

Author contributions

TH conceived the study, designed and carried experiments, analyzed results, prepared artwork, and wrote the manuscript. LFLM helped with experimental design, experimental and analysis work and provided feedback on the manuscript. TB performed grafting experiment and analysis and provided feedback. LT and JJL helped with experiments. PR taught methods, provided feedback and shared reagents. CCB and GH provided feedback on the work and edited the manuscript. MPL conceived the work, designed experiments, and carried out the final editing of the manuscript.

Funding

This work was funded by the Wellcome Trust Wellcome Collaborative Award (SynThy, 211944/Z/18/Z) and EPFL.

Competing interests

The authors declare no competing interests.

Data and materials availability

Sequencing data reported in this paper have been deposited in the Gene Expression Omnibus (GEO) public repository under the accession number GSE240698. The SubSeries GSE240696 and GSE240697 corresponds to bulk and single-cell RNA-seq, respectively. Code used for analysis is available upon request and will be published on Github.

Supplementary Materials

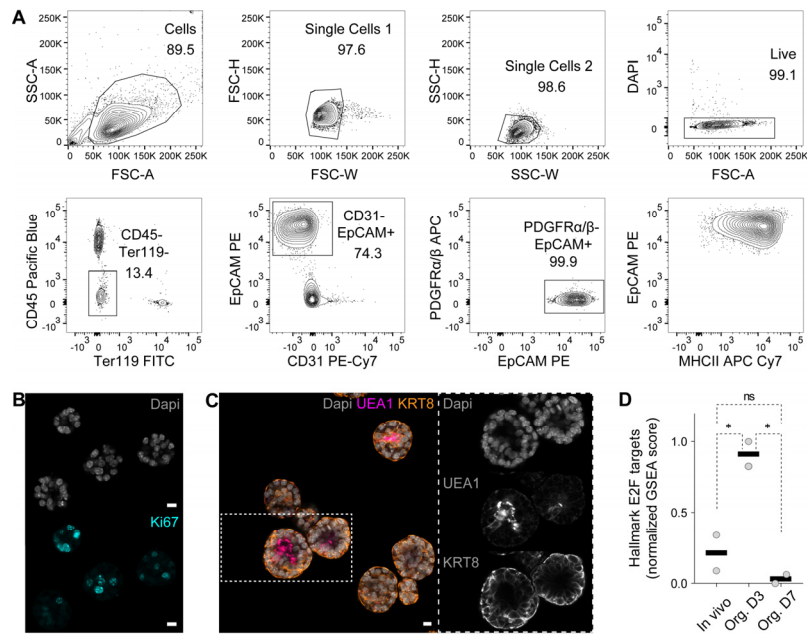


Fig. S1 (A) Sorting strategy to isolate TECs (EpCAM+). Exclusion of CD45+, Ter119+, CD31+ and PDGFRα+ PDGFRβ+ cells. TECs are mostly MHCII+. **(B)** Immunofluorescence images of organoids seven days after seeding showing nuclei (Dapi, top [grey]) and proliferating cells (Ki67, bottom [cyan]). Scale bars, 10µm. **(C)** Immunofluorescence image of organoids showing different cell populations after seven days in culture, here with medullary cells (UEA1-reactivity [bright pink and middle] and cortical cells [KRT8 [amber and bottom]). Dapi counterstains nuclei (grey and top). Scale bar, 10µm. **(D)** Single-sample gene set enrichment analysis (GSEA) demonstrating a proliferation peak (E2F hallmark) for organoids at day 3. ns: $P > 0.05$, *: $P = 0.0241$ (In vivo vs Org. D3) and $P = 0.0126$ (Org. D3 vs Org. D7) (one-way ANOVA with Tukey's multiple comparisons test; $n = 2$ mice per condition). Graph represents individual datapoints with mean.

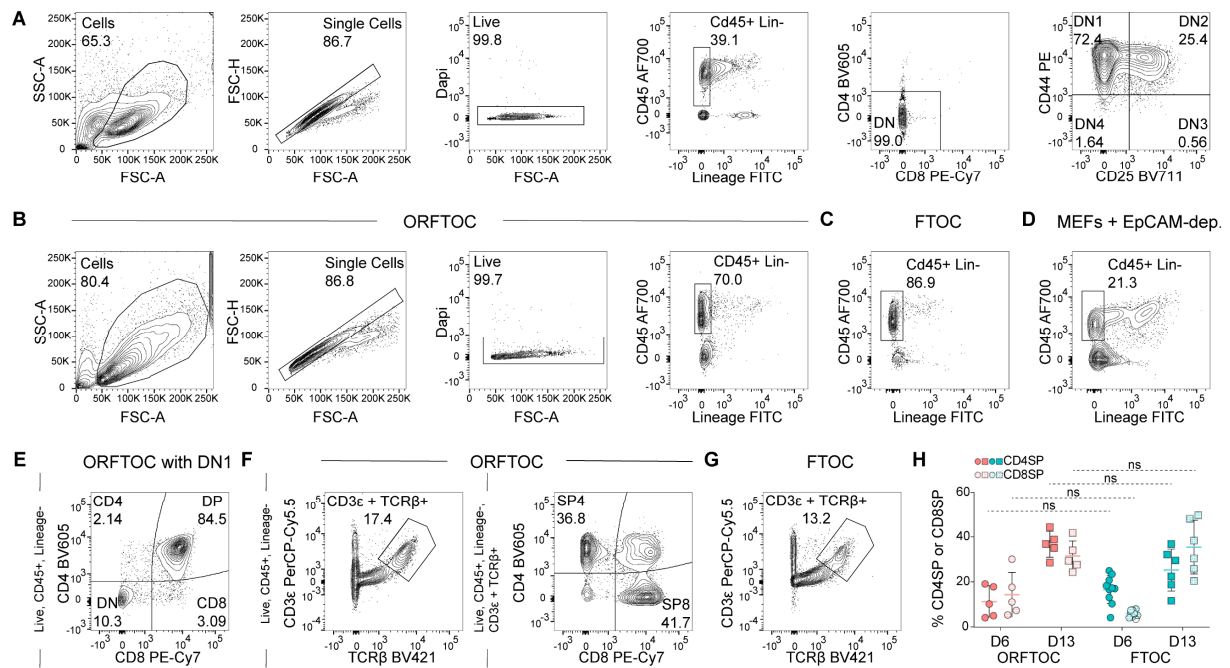


Fig. S2. (A) Flow cytometry plots showing the developmental stage (DN) of thymocytes in E13.5 thymi. (B) Flow cytometry plots showing the gating strategy to analyze thymocyte development in ORFTOCs and control conditions. (C) Flow cytometry plot showing the CD45+ Lineage- population in FTOC controls. (D) Flow cytometry plot showing the CD45+ Lineage- population in control reaggregates with MEFs and the EpCAM-depleted fraction of cells from E13.5 thymi. (E) Flow cytometry plots showing T cell development in ORFTOCs using adult DN1 as T cell input population. Gating strategy is indicated on the left. (F) Flow cytometry plots showing the CD3ε+ TCRβ+ population in ORFTOCs, and its division into CD4SP and CD8SP T cell lineages. Gating strategies are indicated on the left of each plot. (G) Flow cytometry plot showing the CD3ε+ TCRβ+ population in FTOC controls. Gating strategy is as in F (left). (H) Percentage of CD4SP and CD8SP within the CD3ε+ TCRβ+ population, at day 6 and day 13, for both ORFTOCs and FTOC controls. ns: $P > 0.05$ (Brown-Forsythe ANOVA test for both CD4SP and CD8SP with Dunnett's T3 multiple comparisons test; $n = 5$ for all ORFTOC populations and time, $n = 10$ for FTOC populations at day 6 and $n = 6$ for FTOC populations at day 13, from 5 independent experiments). Graph represents individual datapoints with mean + SD.

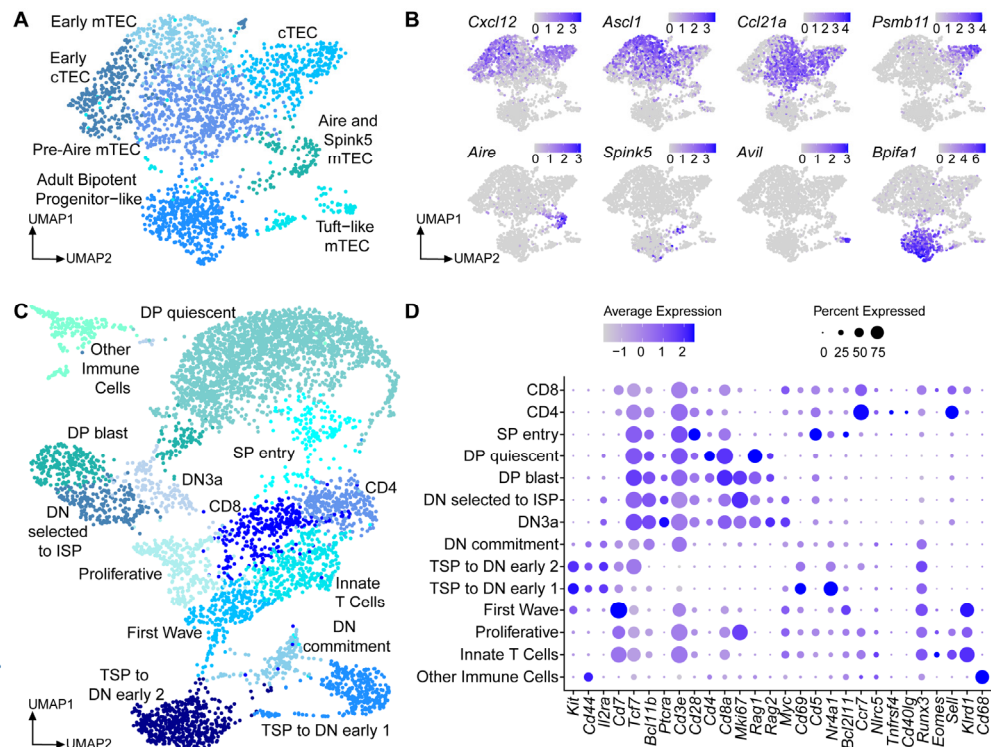


Fig. S3. (A) UMAP showing the different epithelial clusters. (B) UMAP showing characteristic marker expression for each of the epithelial clusters. (C) UMAP showing the different immune clusters. (D) Dot plot summarizing the expression of characteristic markers of T cell development for the different clusters.

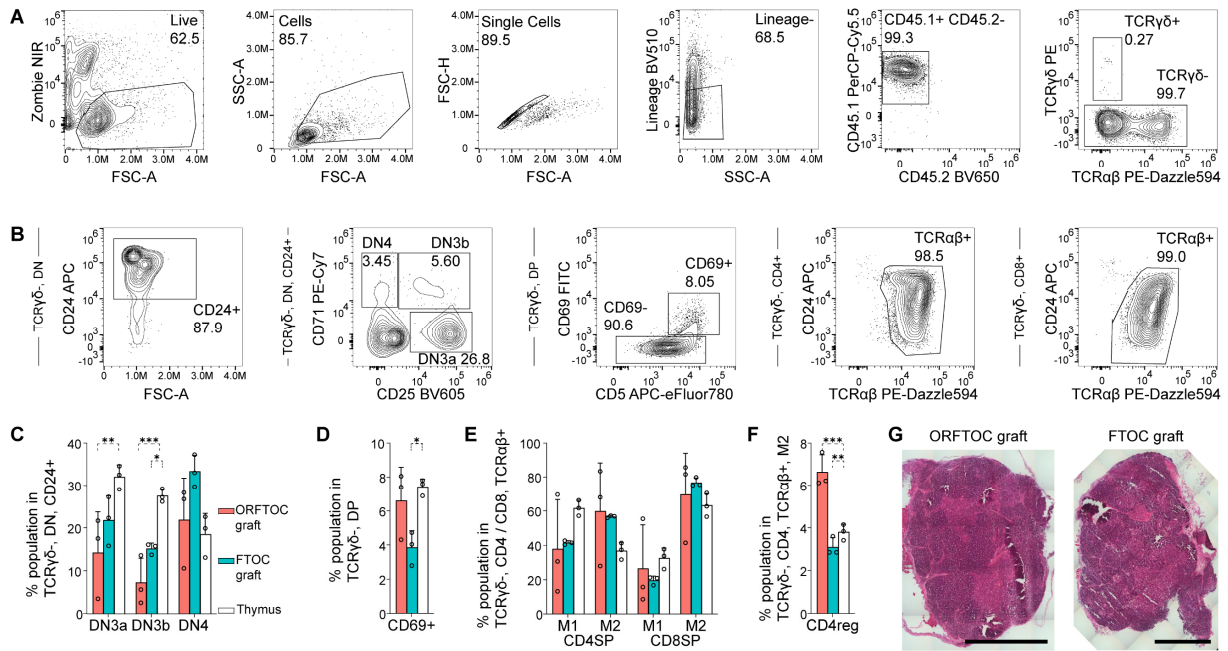


Fig. S4 (A - F) Flow cytometry plots showing the gating strategy to analyze grafts. ORFTOCs (CD45.2) were grafted under the kidney capsule of CD45.1 hosts. Live, single, Lineage negative (CD11b, CD11c, Gr1, Ter119, DX5, NK-1.1, MHCII, F4/80) cells were gated for CD45.1 positivity (**A**) and TCRγδ negative T cells were further analyzed (**B**). CD25 and CD71 expression on CD24+ DN cells were used to enumerate DN3a, DN3b and DN4 subsets, quantified in (**C**) for the different conditions. β-selection occurs at the DN3a to DN3b transition. CD69 expression identifies cells undergoing positive selection and is quantified in (**D**) for the different conditions. Gating on the TCRαβ+ population, mature (M1 and M2) CD4SP and CD8SP T cells are quantified in (**E**) and CD4 regulatory T cells (CD4reg) in (**F**), for the different conditions. For all bar graphs, only significant differences are indicated with stars. * P = 0.0381 (DN3a ORFTOC vs thymus), *** P = 0.0009 (DN3b ORFTOC vs thymus), * P = 0.0116 (DN3b FTOC vs thymus), * P = 0.0373 (Cd69 FTOC vs thymus), ns: P > 0.05 (one-way ANOVA for each subpopulation between conditions, n = 3 grafts/mice for each condition). Bar graphs represent mean and SD, with individual datapoints displayed as circles. **G**, Hematoxylin and eosin (H&E) of ORFTOC and FTOC grafts.

[Movie S1](#)

https://drive.google.com/file/d/1J8zgBQJIXWtEuldunFMsglbxdZQy_rN-/view?usp=sharing

One week time-lapse showing the development of thymic epithelial organoids starting from sorted single thymic epithelial cells seeded in Matrigel and cultured in defined conditions.

Materials and Methods

Mice

For all in vitro experiments, C57BL/6J mice were purchased from Charles River France and maintained in the EPFL animal facility until use. For grafting experiments, Ly5.1 and C57BL/6J mice were bred and maintained in the mouse facility of the Department of Biomedicine at the University of Basel. For timed mating, noon of the day of the vaginal plug was considered as day 0.5 of embryonic development (E0.5). Mice were housed in individual cages at $23^{\circ}\text{C} \pm 1^{\circ}\text{C}$ with a 12 h light/dark cycle, and supplied with food and water ad libitum. All animal work was conducted in accordance with Swiss national guidelines, reviewed and approved by the Cantonal Veterinary Offices of Vaud and of Basel-Stadt, license numbers VD3035.1, VD3823 and BS2321.

Isolation of thymic epithelial cells (TECs)

E16.5 embryonic thymi were dissected and collected in Eppendorf tubes containing FACS buffer (PBS [Gibco Catalog No. 10010-015] + 2% fetal bovine serum [FBS] [Thermo Fisher Scientific, Catalog No. 26140079]). Lobes were rinsed with PBS and digested with 475 μl TrypLE (Gibco Catalog No. 12605-028) for 5 min at 37°C under agitation (Eppendorf, ThermoMixer C). Lobes were pipetted to promote dissociation, 25 μl DNase (Sigma-Aldrich, Catalog No. 10104159001, from 1 mg/ml stock) was added and the tubes were incubated for another 5 min. Lobes were again pipetted to help dissociation, TrypLE was quenched with 1ml Adv. DMEM/F12 (Thermo Fisher Scientific, Catalog No. 12634028) containing 10 % FBS and the cell suspension was filtered through a 40 μm strainer. The cells were pelleted and resuspended in FACS buffer for staining with the following antibodies for 20 min at 4°C : Ter119-FITC (BioLegend, Catalog No. 116205, 1/100), EpCAM-PE (BioLegend, Catalog No. 1198206, 1/80), PDGFR- α -APC (BioLegend, Catalog No. 135907, 1/40), PDGFR- β -ACP (BioLegend, Catalog No. 136007, 1/40), CD31-PE-Cy7 (BioLegend, Catalog No. 102524, 1/160), MHCII-APC/Fire750 (BioLegend, Catalog No. 107651, 1/160), CD45-Pacific Blue (BioLegend, Catalog No. 103126, 1/200). Dapi (Tocris, Catalog No. 4748, 0.5 $\mu\text{g/ml}$) was used to exclude dead cells. After staining, the antibodies were washed and the cells resuspended in FACS buffer for sorting using an Aria Fusion (BD). The sorting strategy for isolating thymic epithelial cells is shown in fig. S1A. Sorted cells were collected in TEC medium (see below) containing 2 % FBS and 2.5 μM Thiazovivin (Stemgen, Catalog No. AMS.04-0017).

Thymic epithelial organoid culture

Sorted thymic epithelial cells were embedded in growth-factor-reduced Matrigel (Corning, Catalog No. 356231) ($\sim 1.55 \times 10^4$ cells per 20 mL drop) and plated in 24-well plates (Corning, Catalog No. 353047, or Ibidi, Catalog No. 82426). After Matrigel polymerization, TEC medium was added. TEC medium consisted of organoid basal medium (Advanced DMEM/F-12 supplemented with 1 \times GlutaMAX [Thermo Fisher Scientific, Catalog No. 35050038], 10 mM HEPES [Thermo Fisher Scientific, Catalog No. 15630056], 100 $\mu\text{g ml}^{-1}$ Penicillin–Streptomycin [Thermo Fisher Scientific, Catalog No. 15140122], 1 \times B-27 supplement [Thermo Fisher Scientific, Catalog No. 17504001], 1 \times N2 supplement [Thermo Fisher Scientific, Catalog No. 17502001], 1 mM N-Acetylcysteine [Sigma-Aldrich, Catalog No. A9165]) plus 100 ng ml^{-1} FGF7 (Peprotech, Catalog No. 100-19). 2.5 μM Thiazovivin was also added to the medium for the first two days. Medium was changed every second day. Organoids were cultured at 37°C with 5% CO_2 .

Organoid proliferation assays

Sorted thymic epithelial cells were embedded in 10 μl Matrigel drops ($\sim 7.5 \times 10^3$ cells/drop) in a 48-well plate (Corning, Catalog No. 353078). On the day of seeding (day 0), at day 1, 3, 5 and 7, 220 μM resazurin (Sigma-Aldrich, Catalog No. R7017) was added to organoid basal medium and incubated with the cells for 4 h at 37 °C. Afterwards, the resazurin-containing medium was collected and replaced by fresh TEC medium with or without FGF7. Organoid proliferation was estimated by measuring the reduction of resazurin to fluorescent resorufin in the medium using a Tecan Infinite F500 microplate reader (Tecan) with 560 nm excitation and 590 nm emission filters. For analysis, data were normalized from minimum to maximum.

Bulk transcriptome profiling

Sorted thymic epithelial cells were culture as indicated above. As controls, sorted thymic epithelial cells from E16.5 embryos were either directly lysed in RLT buffer (QIAGEN, Catalog No. 74004) containing 40 mM DTT (ITW Reagents, Catalog No. A2948) or cultured in 2D on plates coated with 6 $\mu\text{g/ml}$ laminin (R&D Systems, Catalog No. 3446-005-01). Cultures were done in TEC medium. Organoids were collected in cold PBS to dissolve Matrigel and then lysed in RLT buffer with DTT. They were collected after 3 and 7 days. Cells cultured in 2D were directly collected in RLT buffer with DTT. They were collected once a confluent monolayer formed, after 3 days, as prolonged culture in these conditions lead to cell detachment and death. RNA was extracted using QIAGEN RNeasy Micro Kit (QIAGEN, Catalog No. 74004) according to manufacturer's instructions. Purified RNA was quality checked using a

TapeStation 4200 (Agilent), and 88 ng were used for QuantSeq 3' mRNA-Seq library construction according to manufacturer's instructions (Lexogen, Catalog No. 015.96). Libraries were quality checked using a Fragment Analyzer (Agilent) and were sequenced in a NextSeq 500 (Illumina) using NextSeq v2.5 chemistry with Illumina protocol #15048776. Reads were aligned to the mouse genome (GRCm39) using star (version 2.7.0e). R (version 4.1.2) was used to perform differential expression analyses. Count values were imported and processed using edgeR (53). Expression values were normalized using the trimmed mean of M values (TMM) method and lowly-expressed genes (< 1 counts per million) and genes present in less than three samples were filtered out. Differentially expressed genes were identified using linear models (Limma-Voom) (54), and P-values were adjusted for multiple comparisons by applying the Benjamini-Hochberg correction method (55). Voom expression values were used for hierarchical clustering using the function hclust (56) with default parameters, and for heatmap generation. Single sample gene set enrichment analysis (GSEA) (57) was used to score the E2F targets hallmark proliferation gene set (58, 59) between samples.

Whole-mount immunofluorescence staining

Organoid samples were fixed in 4% paraformaldehyde (Thermo Fisher Scientific, Catalog No. 15434389) in PBS for 30 min at room temperature and subsequently washed with PBS. Samples were permeabilized in 0.2 % Triton X-100 (Sigma-Aldrich, Catalog No. T8787), 0.3 M glycine (Invitrogen, Catalog No. 15527-013) in PBS for 30 min at room temperature and blocked in 10 % serum (goat [Thermo Fisher Scientific, Catalog No. 16210064] or donkey [Abcam, Catalog No. ab7475]), 0.01% Triton X100 and 0.3M glycine in PBS for 4h at room temperature. Samples were then incubated with primary antibodies overnight at 4 °C, washed with PBS, incubated with secondary antibodies overnight at 4 °C, and washed with PBS. Mounting was done with Fluoromount-G (SouthernBiotech, Catalog No. 0100-01). The following primary and secondary antibodies were used: MHCII-Biotin (BioLegend, Catalog No. 107603, 1/200), UEA1 (Vector Laboratories Catalog No. B-1065, 1/500), Keratin 5 (BioLegend, Catalog No. 905501, 1/200), Keratin 8 (Abcam Catalog. No. ab53280, 1/200), Ki67 (BD Pharmingen, Catalog No. 550609, 1/200), EpCAM-APC (Invitrogen, Catalog No. 17-5791-82, 1/200), Streptavidin Alexa 488 (Thermo Fisher Scientific, Catalog No. S-11223, 1/500), Streptavidin Alexa 647 (Thermo Fisher Scientific, Catalog No. S-21374, 1/500), Goat anti-Rat Alexa 647 (Thermo Fisher Scientific, Catalog No. A-21247, 1/500), Donkey anti-Mouse Alexa 568 (Thermo Fisher Scientific, Catalog No. A-10037, 1/500), Donkey anti-Rabbit Alexa 488 (Thermo Fisher Scientific, Catalog No. A-21206, 1/500), Donkey anti-Rabbit Alexa 568 (Thermo Fisher Scientific, Catalog No. A-11077, 1/500). Dapi (Tocris, Catalog No. 47481 mg/ml) was used to stain nuclei.

Reaggregate culture

E13.5 embryonic thymi were dissected and collected in Eppendorf tubes containing FACS buffer. Lobes were rinsed with PBS and digested with 475 μ l TrypLE and 25 μ l DNase (from 1 mg/ml stock) for 5 min under agitation. Lobes were pipetted to help dissociation and TrypLE was quenched with 1ml Adv. DMEM/F12 containing 10 % FBS. The cells were pelleted and resuspended in FACS buffer for immunomagnetic cell separation with EpCAM-conjugated beads (Miltenyi Biotec, Catalog No. 130-105-958, 1/4). After 20 min incubation at 4°C, the unbound complexes were washed and the cells processed through magnetic columns (Miltenyi Biotec, Catalog No. 130-042-401) following manufacturer instruction. The EpCAM-depleted fraction was collected and used to prepare reagggregates with dissociated thymic epithelial organoids and mouse embryonic fibroblasts (MEFs).

Thymic epithelial organoids at day 7 of culture were collected in cold Advanced DMEM/F-12 supplemented with 1 \times GlutaMAX, 10 mM HEPES and 100 μ g ml⁻¹ Penicillin–Streptomycin. Organoids were pelleted and digested with 950 μ l TrypLE and 50 μ l DNase (from 1 mg/ml) for 5min at 37 °C. Organoids were pipetted to improve dissociation. In case digestion was insufficient, organoids were further digested for 5 min with Trypsin + 0.25% EDTA (Gibco, Catalog No. 25200-072) at 37 °C and pipetted until the obtention of a single cell suspension. Dissociation was quenched with Adv. DMEM/F12 containing 10 % FBS and the cells pelleted.

Wild-type MEFs were a kind gift from the Blackburn laboratory. MEFs were cultured in Advanced DMEM/F-12 supplemented with 1 \times GlutaMAX, 1x Non-Essential Amino Acids (Gibco, Catalog No. 11140035), 100 μ g ml⁻¹ Penicillin–Streptomycin and 10 % FBS on gelatin-coated dishes (0.1% gelatin in H₂O) (Sigma-Aldrich, Catalog No. G1890). MEFs were harvested using Trypsin EDTA 0.25% for 2 min at 37 °C. Dissociation was quenched with Adv. DMEM/F12 containing 10 % FBS and the cells pelleted.

For reagggregates using adult double negative 1 (DN1) thymocytes as input population, adult thymi were dissected from 4 weeks old female C57BL/6J mice. Thymi were cut in small pieces with a scalpel to liberate thymocytes, which were filtered to a single cell suspension with a 40 μ m strainer. Cells were incubated with APC anti-mouse CD8a Antibody (BioLegend, Catalog No. 100711, 1/50) for 20 min at 4°C in FACS buffer and washed. Cells were then incubated with anti-APC magnetic beads (Miltenyi Biotec, Catalog No. 130-090-855, 1/4) for 20 min at 4°C. The unbound beads were washed away and the cells processed through magnetic columns following manufacturer instruction. The APC depleted fraction was collected and used for staining with the following antibodies: Ter119-FITC (BioLegend, Catalog No. 116205, 1/800), Cd45R-FITC (BioLegend, Catalog No. 103205, 1/800), CD11b-FITC (Thermo Fisher Scientific, Catalog No. 11-0112-82, 1/800), Ly-6G-FITC (BioLegend, Catalog No. 108405,

1/800), Cd11C-FITC (BioLegend, Catalog No. 117306, 1/800), NK-1.1-FITC (BioLegend, Catalog No. 108705, 1/800), CD3-FITC (BioLegend, Catalog No. 100306), CD4-FITC (BioLegend, Catalog No. 100510), CD45-Pacific Blue (BioLegend, Catalog No. 103126, 1/200) or CD45-AF700 (BioLegend, Catalog No. 103127, 1/160), CD44-PE (BioLegend, Catalog No. 103008, 1/160), CD25-BV711 (BioLegend, Catalog No. 102049, 1/160) and Dapi (Tocris, Catalog No. 4748, 0.5 ug/ml). After staining, the antibodies were washed and the cells resuspended in FACS buffer for sorting using an Aria Fusion (BD). The sorting strategy for isolating DN1 thymocytes was gating on cells, single cells, live cells, CD45+ cells, CD44+ CD25- cells. DN1 thymocytes were collected in ORFTOC medium (see below).

Organoids reaggregate fetal thymic organ culture (ORFTOCs) were prepared as previously described (39). Briefly, the cell suspension for each ORFTOC typically contained 10^5 EpCAM-depleted cells, 10^5 thymic epithelial organoid cells, and 10^5 MEFs (or 10^5 thymic epithelial organoid cells, 4×10^4 DN1 thymocytes and 10^5 MEFs). These cells were transferred to an Eppendorf tube and pelleted. The pellet was resuspended in 60 μ l of the medium used for culture, and transferred to a tip sealed with parafilm inside a 15 ml Falcon tube. Cells were pelleted inside the tip for 5 min at 470 rcf. The pellet was then gently extruded on top of a filter membrane (Merck, Catalog No. ATTP01300) floating on culture medium in 24well plate. ORFTOC culture medium consisted of advanced DMEM/F-12 supplemented with 1 \times GlutaMAX, 1x Non-Essential Amino Acids, 100 μ g ml⁻¹ Penicillin–Streptomycin, 2 % FBS and 100 ng/ml FGF7. 2.5 μ M Thiazovivin was added for the first two days of culture and half of the medium volume was changed every second day.

Controls where one of the cell population is absent were made the same way. For FTOC controls, E13.5 dissected lobes were directly placed on top of a filter membrane and also cultured in ORFTOC medium.

All cultures were done at 37°C with 5% CO₂.

Flow cytometry analysis of ORFTOCs and FTOCs

After 6 and 13 days in culture, ORFTOCs, FTOCs, reagggregates with DN1 thymocytes and controls reagggregates were gently detached from the filter membrane by pipetting and transferred to Eppendorf tubes, together with the culture medium to collect recently emigrated T cells. Samples were pelleted, rinsed with PBS and digested with 200 μ l TrypLE for 10 min at 37° C with agitation on an Eppendorf shaker (800 rpm). Dissociation was quenched with 1ml Adv. DMEM/F12 containing 10 % FBS and the cells pelleted. Cells were resuspended in FACS buffer for staining. The cells were incubated for 20 min with the following antibodies: Ter119-FITC (BioLegend, Catalog No. 116205, 1/800), Cd45R-FITC (BioLegend, Catalog No. 103205,

1/800), CD11b-FITC (Thermo Fisher Scientific, Catalog No. 11-0112-82, 1/800), Ly-6G-FITC (BioLegend, Catalog No. 108405, 1/800), Cd11c-FITC (BioLegend, Catalog No. 117306, 1/800), NK-1.1-FITC (BioLegend, Catalog No. 108705, 1/800) together referred as Lineage, CD44-PE (BioLegend, Catalog No. 103008, 1/160), CD69-APC (BioLegend, Catalog No. 104513, 1/160), CD4-BV605 (BioLegend, Catalog No. 100548, 1/40), CD3-PerCP/Cy5.5 (BioLegend, Catalog No. 100327, 1/160), CD8-PE/Cy7 (BioLegend, Catalog No. 100722, 1/160), CD25-BV711 (BioLegend, Catalog No. 102049, 1/160), CD45-AF700 (BioLegend, Catalog No. 103127, 1/160), TCR β -BV421 (BioLegend, Catalog No. 109230, 1/80) and Dapi (Tocris, Catalog No. 4748, 0.5 ug/ml). After staining, the antibodies were washed and the cells resuspended in FACS buffer for analyzing using a LSR Fortessa Cytometer (BD). The gating strategy for analysis is shown in fig. S2B. Beads (UltraComp, Thermo Fisher Scientific Catalog No. 01-3333-42) were used for single color staining for compensation. Gates were based on T cells extracted from a young adult. Flow cytometry data were analyzed using FlowJo (BD, version 10.9.0).

Single-cell transcriptome profiling

After 13 days in culture, ORFTOC and FTOC samples were collected and dissociated as described for flow cytometry analysis. After dissociation, two ORFTOC samples and two FTOC samples were pooled, respectively. For each pool, 500 000 cells were incubated with 1ul TotalSeq Antibody (HTO) (BioLegend, Catalog No. 155863 and 155861) in 50 μ l FACS buffer for 30 min on ice. Antibodies were washed two times with FACS buffer and the single cell suspensions filtered through a 40 μ m strainer. After cell count, samples were mixed in a 1:1 ratio and processed using Chromium Next GEM Single Cell 5' Reagent Kits v2 (Dual Index) with Feature Barcode technology for Cell Surface Protein & Immune Receptor Mapping reagents (10X Genomics, Catalog No. PN-1000265, PN-1000256, PN-1000190, PN-1000287, PN-1000215 and PN-100025) following manufacturer's instruction. Single Cell Mouse TCR amplification Kit (10X Genomics Catalog No. 1000254) was used to prepare TCR libraries. Sequencing was done using NovaSeq v1.5 STD (Illumina protocol #1000000106351 v03) for around 100,000 reads per cell. The reads were aligned using Cell Ranger v6.1.2 to the mouse genome (mm10). Raw count matrices were imported into R and analyzed using Seurat v4.2.0 (60). HTO with less than 100 features and less than 1 count were discarded. Cells with less than 600 features, less than 0.4 or more than 10 percent mitochondrial genes were discarded. Demultiplexing was performed using HTODemux with standard parameters. Doublets were removed using recoverDoublets from scDbiFinder package (61) and based on doublets identified from HTOs. Data were normalized using SCTransform and with cell cycle score as variable to regress. The three clusters representing the main cell types were obtained using

PCA and UMAP with 18 dimensions and a resolution of 0.005. Each cell type was then subset and thresholded based on *EpCAM*, *Ptprc* and *Pdgfra* expression. Epithelial clusters were identified using 18 dimensions and a resolution of 0.4, leading to 7 clusters that were named based on markers from previous datasets (29, 41–44, 62). Immune clusters were identified using 18 dimensions and a resolution of 3. Immune clusters were further merged to obtain 14 clusters representing main T cell developmental stages based on markers from previous datasets (40, 43, 45, 46). The number of cells per clusters in both FTOC and RFTOC samples were calculated to show HTO repartition between both samples. TCR analysis was conducted using scRepertoire (63). Filtered contig output from Cell Ranger was used as input and added to immune cells metadata. Productive cells with both TRA and TRB chains were plotted on the UMAP, and percentage of productive cell (either at least TRB chain with no NA and no double chain, or both TRA and TRB chains with no NA and double chain accepted only for TRA) per cluster calculated. The mouse samples from the dataset from Park et al. (43) were used for alignment. H5ad files were converted to Seurat object, TECs were subset from the stromal dataset and 4 weeks-old T cells from the mouse total dataset. Alignment was performed using SCTransform and canonical correlation analysis (CCA) with the Park dataset labeled as reference and otherwise default parameters.

Kidney capsule grafting and analysis

ORFTOCs were grafted in CD45.1 host mice and FTOC controls in CD45.2 host mice. Mice were treated with the analgesic Carprofen (10 mg/kg in drinking water) 12-24 h prior to transplantation. Mice were anesthetized with Ketalar/Rompun (100 mg/kg Ketamin and 20 mg/kg Xylazin, intraperitoneal). Lacrinorm eye gel (Bausch & Lomb) was administered to avoid dehydration of the cornea during the procedure. Anesthetized mice were shaved laterally and disinfected using Betadine. The surgery was performed on a heating pad in order to minimize body temperature drop. A small incision of approximately 1 cm was done first on the skin and then in the peritoneum. By pulling at the posterior fat of the kidney with forceps, the kidney was exposed outside of the peritoneum and kept wet with PBS. Under the microscope, an incision and a channel were done with watchmaker-forceps on the kidney capsule's membrane and one ORFTOC or FTOC was placed under the membrane. After positioning the kidney back into the peritoneum, the wound was closed with two stitches (resorbable suture material 5/0; Polyactin 910; RB-1 plus; Johnson&Johnson). The skin opening was closed with staples, which were removed 7-10 days later. An analgesic (Temgesic, Buprenorphine 0.1 mg/kg, subcutaneous) was administered at the end of the procedure followed by continuous treatment of transplanted mice by Carprofen (10 mg/kg in drinking water) for 3 days. After the transplants,

mice were monitored daily and weighed every second day to confirm their wellbeing. Grafts were analyzed 5 weeks after transplantation.

At the time of analysis, mice were sacrificed with CO₂ and kidneys retrieved. Grafts were separated from the kidney under the microscope. To collect T cells, grafts were mechanically dissociated by pipetting in FACS buffer. Single cell suspensions were then stained with Zombie NIR (BioLegend, Catalog No. 423105, 1/1000) for 30 min at 4° C. Samples were then washed with FACS buffer and incubated with the following Lineage antibodies for 30 min at 4°C: CD11b Biotin (BioLegend, Catalog No. 101204, 1/1000), CD11c Biotin (BioLegend, Catalog No. 117304, 1/1000), CD19 Biotin (BioLegend, Catalog No. 101504, 1/1000), DX5 Biotin (BioLegend, Catalog No. 108904, 1/1000), MHCII Biotin (BioLegend, Catalog No. 116404, 1/1000), GR1 Biotin (BioLegend, Catalog No. 108404, 1/1000), F4/80 Biotin (BioLegend, Catalog No. 123100, 1/1000), Ter119 Biotin (BioLegend, Catalog No. 116204, 1/1000) and NK-1.1 Biotin (BioLegend, Catalog No. 108704, 1/1000). After washes, samples were incubated with the following antibodies for 30 min at 4°C : CD45.1-PerCP-Cy5.5 (BioLegend, Catalog No. 110728, 1/500), CD45.2-BV650 (BioLegend, Catalog No. 109836, 1/200), CD4-BUV563 (Thermo Fisher Scientific, Catalog No. 365-0042-82, 1/1000), CD8-BUV615 (Thermo Fisher Scientific, Catalog No. 366-0081-82, 1/500), TCRαβ-PE-Dazzle594 (BioLegend, Catalog No. 109220, 1/500), TCRγδ-PE (BioLegend, Catalog No. 118108, 1/500), CD69-FITC (BioLegend, Catalog No. 104506, 1/500), CD24-APC (BioLegend, Catalog No. 101814, 1/1000), CD44-BV785 (BioLegend, Catalog No. 103059, 1/500), Ckit-BUV737 (Thermo Fisher Scientific, Catalog No. 367-1171-82, 1/200), CD71-PE-Cy7 (BioLegend, Catalog No. 113812, 1/200), Sca1-BUV395 (Thermo Fisher Scientific, Catalog No. 363-5981-82, 1/500), CD25-BV605 (BioLegend, Catalog No. 102036, 1/500), CD5-APC-eF780 (Thermo Fischer Scientific, Catalog No. 47-0015-82, 1/500) and Streptavidin-BV510 (Biolegend, Catalog No. 405234, 1/500). After final washes, samples were resuspended in FACS buffer and analyzed on an Aurora flow cytometer (Cytex Biosciences). Flow cytometry data were then analyzed using FlowJo (version 10.9.0).

Sectioning, immunofluorescence staining and RNA scope on sections

Organoids, ORFTOCs, FTOCs and grafts were fixed in 4% paraformaldehyde in PBS for 30 min at room temperature (organoids) to overnight at 4 °C (ORFTOCs, FTOCs, grafts). Samples were then washed with PBS and either processed for cryosectioning or for paraffin embedding. For cryosectioning, samples were incubated in 30% (W/V) sucrose (Sigma-Aldrich, Catalog No. S1888) in PBS until the sample sank. Subsequently, samples were incubated for 12 h in a mixture of Cryomatrix (Eprexia, Catalog No. 6769006) and 30% sucrose (Sigma-Aldrich, Catalog No. 84097) (mixing ratio 50/50), followed by a 12 h incubation in pure Cryomatrix. The

samples were then embedded in a tissue mold, frozen on dry ice or in isopentane cooled by surrounding liquid nitrogen. 10 µm-thick sections were cut at -20°C using a CM3050S cryostat (Leica).

For paraffin embedding, organoid, ORFTOC and FTOC samples were embedded in HistoGel (Thermo Fisher Scientific, Catalog No. HG-4000-012) before being placed into histology cassettes. Cassettes were then processed with a Tissue-Tek VIP 6 All Vacuum Infiltration Processor (Sakura) and embedded in paraffin. 4 µm paraffin sections were obtained with a Leica RM2265 microtome. Slides were processed through de-waxing and antigen retrieval in citrate buffer at pH 6.0 using a heat-induced epitope retrieval PT module (Thermo Fisher Scientific) before proceeding with immunostaining. Sections were then blocked and permeabilized for 30 min in 1% BSA (Thermo Fisher Scientific, Catalog No. 15260-037), 0.2% Triton X100 in PBS and blocked for 30 min in 10% goat or donkey serum in PBS at room temperature. Primary antibodies were incubated O/N at 4 °C in PBS, 1.5% donkey or goat serum. On the following day, slices were washed twice in 1% BSA, 0.2% Triton X-100 in PBS and incubated with secondary antibodies at room temperature for 45 min. Finally, slices were washed twice in 0.2% Triton X-100 in PBS and mounted with Fluoromount-G. The following primary and secondary antibodies were used: UEA1 (Vector Laboratories, Catalog No. B-1065, 1/500), Keratin 5 (BioLegend, Catalog No. 905501, 1/200), Keratin 8 (Abcam, Catalog. No. ab53280, 1/200), CD3ε (Thermo Fisher Scientific, Catalog No. MA5-14524, 1/200), MHCII-Biotin (BioLegend, Catalog No. 107603, 1/200) EpCAM-PE (BioLegend, Catalog No. 118206, 1/200), Aire (Thermo Fischer Scientific, Catalog No. 14-5934-82, 1/50), Streptavidin Alexa 488 (Thermo Fisher Scientific, Catalog No. S-11223, 1/500), Goat anti-Rat Alexa 568 (Thermo Fisher Scientific, Catalog No. A-11077, 1/500), and Donkey anti-Rabbit Alexa 647 (Thermo Fisher Scientific, Catalog No. A-31573, 1/500). Nuclei were again stained with Dapi (Tocris, Catalog No. 4748, 1 µg/ml). RNAscope Multiplex Fluorescent V2 assay (Bio-Techne, catalog no. 323110) was performed according to the manufacturer's protocol. Paraffin sections were hybridized with the probes Mm-Foxn1 (Bio-Techne, catalog no. 482021). Mm-3Plex probes (Bio-Techne, catalog no. 320881) and 3Plex Dapb probes (Bio-Techne, catalog no. 320871) were used as positive and negative controls, respectively. Probes were incubated at 40°C for 2 hours, and the different channels were revealed with TSA Opal570 (Akoya Biosciences, catalog no. FP1488001KT). Tissues were counterstained with Dapi and mounted with ProLong Gold Antifade Mountant (Thermo Fisher Scientific, P36930). Hematoxylin and eosin staining was performed using a Ventana Discovery Ultra automated slide preparation system (Roche).

Microscopy and image analysis

Live brightfield imaging was performed using a Nikon Eclipse Ti2 inverted microscope with 4×/0.13 NA, 10×/0.30 NA, and 40×/0.3 NA air objectives and a DS-Qi2 camera (Nikon Corporation). Time lapse was imaged with a Nikon Eclipse Ti inverted microscope system equipped with a 20×/0.45 NA air objective and a DS-Qi2 camera (Nikon Corporation). Both microscopes were controlled using the NIS-Elements AR software (Nikon Corporation). Extended depth of field (EDF) of brightfield images was calculated using a built-in NIS-Elements function. Fluorescent confocal imaging of fixed whole-mount and sections was done on a Leica SP8 microscope system, equipped with a 20×/0.75 NA air and a 40x/1.25 glycerol objectives, 405 nm, 488 nm, 552nm and 638 nm solid state lasers, DAPI, FITC, RHOD and Y5 filter cubes, a DFC 7000 GT (Black/White) camera and a CCD grayscale chip. Sections were also imaged on a Leica DM5500 upright microscope equipped with a 20x/0.7 NA air and a 40x/1 NA oil objectives, a DFC 3000 (Black/White) or a DMC 2900 (Color) cameras and a CCD grayscale or a CMOS color chip, respectively. Both Leica microscopes were controlled by the Leica LAS-X software (Leica microsystems). For image processing, only standard contrast- and intensity-level adjustments were performed, using Fiji/ImageJ (NIH) (version 2.1.0/1.53c).

Statistics

The number of replicates (n), the number of independent experiments or animals, the type of statistical tests performed, and the statistical significance are indicated for each graph in the figure legend. Statistical significance was analyzed using one- or two-way ANOVA, Brown-Forsythe ANOVA in case of heteroscedasticity or Mood's median test in the absence of normal distribution. For multiple comparisons, one-way ANOVA were followed by Tukey's test, Brown-Forsythe ANOVA by Dunnet's T3 test, and Mood's test results adjusted for false-discovery rate. Data normality and equality of variances were previously tested with Shapiro-Wilk and Brown-Forsythe test, respectively. Grubbs test was used to determine the presence of outliers across scRNAseq subpopulations. In all cases, values were considered significant when $P \leq 0.05$. Graphs show individual datapoints with mean \pm standard deviation (SD). Tests were performed using Prism (GraphPad, version 9.4.0), except Grubbs test which was performed using GraphPad website (<https://www.graphpad.com/quickcalcs/grubbs1/>) and Mood's test which was performed using the package rcompanion (64) in R (version 4.1.2). Graphs were made using Prism.

Chapter III - Bioprinting approach for guiding organoid self-organization for the generation of macroscale (multi)tissue constructs

Recapitulating macro-scale tissue self-organization through organoid bioprinting

Jonathan A. Brassard^{1,*}, Mike Nikolaev^{1,*}, Tania Hübscher^{1,*}, Moritz Hofer¹ and Matthias P. Lutolf^{1,2,#}

¹ Laboratory of Stem Cell Bioengineering, Institute of Bioengineering, School of Life Sciences and School of Engineering, Ecole Polytechnique Fédérale de Lausanne (EPFL), Lausanne, Switzerland.

² Institute of Chemical Sciences and Engineering, School of Basic Science (SB), EPFL, Lausanne, Switzerland.

* These authors contributed equally: Jonathan A. Brassard, Mike Nikolaev, Tania Hübscher.

Corresponding author: matthias.lutolf@epfl.ch

Published in Nature Materials (21 September 2020)

<https://doi.org/10.1038/s41563-020-00803-5>

Abstract

Bioprinting promises enormous control over the spatial deposition of cells in three dimensions¹⁻⁷, but current approaches have had limited success at reproducing the intricate micro-architecture, cell-type diversity and function of native tissues formed through cellular self-organization. We introduce a three-dimensional bioprinting concept that uses organoid-forming stem cells as building blocks that can be deposited directly into extracellular matrices conducive to spontaneous self-organization. By controlling the geometry and cellular density, we generated centimetre-scale tissues that comprise self-organized features such as lumens, branched vasculature and tubular intestinal epithelia with in vivo-like crypts and villus domains. Supporting cells were deposited to modulate morphogenesis in space and time, and different epithelial cells were printed sequentially to mimic the organ boundaries present in the gastrointestinal tract. We thus show how biofabrication and organoid technology can be merged to control tissue self-organization from millimetre to centimetre scales, opening new avenues for drug discovery, diagnostics and regenerative medicine.

Article

Bioprinting has been widely applied in tissue engineering and regenerative medicine due to its powerful ability to control large-scale depositions of cells and biocompatible materials¹. Although robust bioprinting modalities such as multimaterial², *in situ*³, freeform^{4–7} and smart material bioprinting^{8,9} have recently been developed, these methods compromise the suitability of the cellular environment to improve printability and resolution. This tradeoff has precluded the high cellular density and permissiveness necessary to recreate the complexity of native tissue architecture and function.

In vivo, tissue formation relies heavily on a tightly regulated morphogenetic program that allows groups of cells to locally interact and self-organize. Iterative interactions between these locally developing tissue units guide successive cycles of cellular differentiation and patterning that establish biological complexity over a large scale. Because of their unique self-organization potential, stem cell-derived organoids are promising tissue mimetics that are unmatched by engineering methods in terms of reproducing local features of tissue architecture and cell-type composition^{10,11}. However, because organoids cannot be grown beyond the millimetre scale, they lack architectural features of native organs that would allow the emergence of higher-level functional characteristics^{12,13}. An important step towards *in vitro* tissue and organ development for regenerative medicine involves controlling the self-organization potential of mammalian cells at the macroscopic scale, but this remains challenging with existing technologies. A better control over tissue size and architecture could ultimately provide artificial organs to be used for drug screening or eventual organ replacements, lessening the burden on animal testing and removing the long wait times for transplants.

Here we introduce a three-dimensional (3D) bioprinting concept for guiding tissue morphogenesis across more physiologically relevant scales and directly within highly permissive extracellular matrices (ECMs) that facilitate effective multicellular self-organization. Our approach, termed bioprinting-assisted tissue emergence (BATE), uses stem cells and organoids as spontaneously self-organizing building blocks that can be spatially arranged to form interconnected and evolving cellular constructs (Fig. 1a). Hence, each cell or cellular aggregate that would normally develop into a relatively randomly shaped small organoid can be coerced to fuse and reorganize, following the geometry and constraints imposed by 3D printing. Using this versatile strategy, large-scale cellular constructs can be printed with key cell types—for example, parenchyma and its corresponding stroma, or different epithelial cells from the gastrointestinal tract—in an effort to reproduce the tissue–tissue interactions seen in native organ development or in homeostasis.

One critical challenge in bioprinting is to screen for the optimal combination of nozzle diameter, extrusion pressure and printhead speed required depending on the bioink composition, rheological properties and cellular concentration. To solve this costly optimization, we designed an easy-to-build and broadly applicable printing setup consisting of a syringe-based extrusion system coupled to a microscope with a manually controlled stage (Fig. 1a and Extended Data Fig. 1a). Microscope-based bioprinting lowers the need for in-depth expertise on hydrogel rheology and bioink formulation as it facilitates printout optimization by providing direct user feedback for visually controlling and modulating the printing process in real time. Cells can be sequentially aspirated and accurately deposited directly inside liquid precursors of typical ECM hydrogels during their gelation (Supplementary Video 1). By adjusting the nozzle size (50–200 μm), flow rate (5–200nl $\cdot\text{s}^{-1}$) and printing speed (defined by the microscope stage handling), we can control the final cellular density, down to lines of single cells if desired (Fig. 1b and Extended Data Fig. 1b–d). Printing of relatively complex designs, such as discontinuous patterns with various cell densities, can be facilitated by using a programmed dispensing of the syringe.

Due to their favourable viscosity range, a wide variety of commonly used cell and organoid culture matrices such as Matrigel, collagen I or methylcellulose are compatible with BATE, in some cases requiring an optimization of the temperature and bioink concentration to achieve good printing fidelity. The use of these cell-instructive matrices allows high-density cell suspensions (up to 100million cells per ml) to be readily available as bioink for 3D printing without compromising cellular viability (Fig. 1c and Extended Data Fig. 1e) and cell-intrinsic self-organization (Fig. 1d–g).

To illustrate the potential and flexibility of our approach for guiding the macro-scale self-organization of primary cells derived from human tissues, we printed three cell types with known self-organizing (or self-assembling) potentials that originated from tissues that play critical roles during organ morphogenesis and function; namely, epithelial, connective and vascular tissues (Fig. 1d–g). Over the course of several days, human intestinal stem cells (hISCs) printed in a line (here, 5–15mm in length) inside a viscous Matrigel/collagen precursor solution morphed into a connected and polarized epithelial tube in the crosslinked matrix (Fig. 1d–g), recapitulating the tissue organization found in classical hISC-derived organoids¹⁴. The establishment of intestinal epithelial tubes was found to be highly dependent on the ECM type and culture conditions (Extended Data Fig. 2), highlighting the importance of the more bioactive ECM support and media in cellular remodelling and morphogenesis after bioprinting. Similar results were obtained with primary mouse colon and stomach stem cell, as well as with human colon stem cells (Extended Data Fig. 3), indicating that BATE may be broadly applicable to epithelial stem cell-derived organoids.

Human mesenchymal stem/progenitor cells (hMSCs) precisely positioned in a 3D Matrigel and collagen mixture readily migrated and invaded the surrounding ECM, establishing a fibrous connective tissue-like structure (Fig. 1d–g). Furthermore, by 3D printing human umbilical vein endothelial cells (HUVECs), we also formed self-organized branched vascular tubes with a lumen that can be perfused (Fig. 1d–g and Extended Data Fig. 4). When printed in collagen I and stimulated with a high concentration of vascular endothelial growth factor (VEGF), the HUVECs formed de novo capillaries¹⁵ (Fig. 1d–g, Extended Data Fig. 5 and Supplementary Video 2). By timing the exposure to VEGF, angiogenesis was robustly triggered at the tissue scale, resulting in an interconnected vascular network and tubes featuring continuous lumen. Notably, in defective printouts, for example caused by cell aggregation during printing, the multicellular self-organization resulted in the smoothing of small defects or variations while maintaining the prescribed macroscopic geometry (Extended Data Fig. 5). These experiments show that the specific local interactions that control self-organization of a small cellular unit can be multiplied and systematically arranged to form epithelial tubes, connective tissues and vascular networks with a defined geometry.

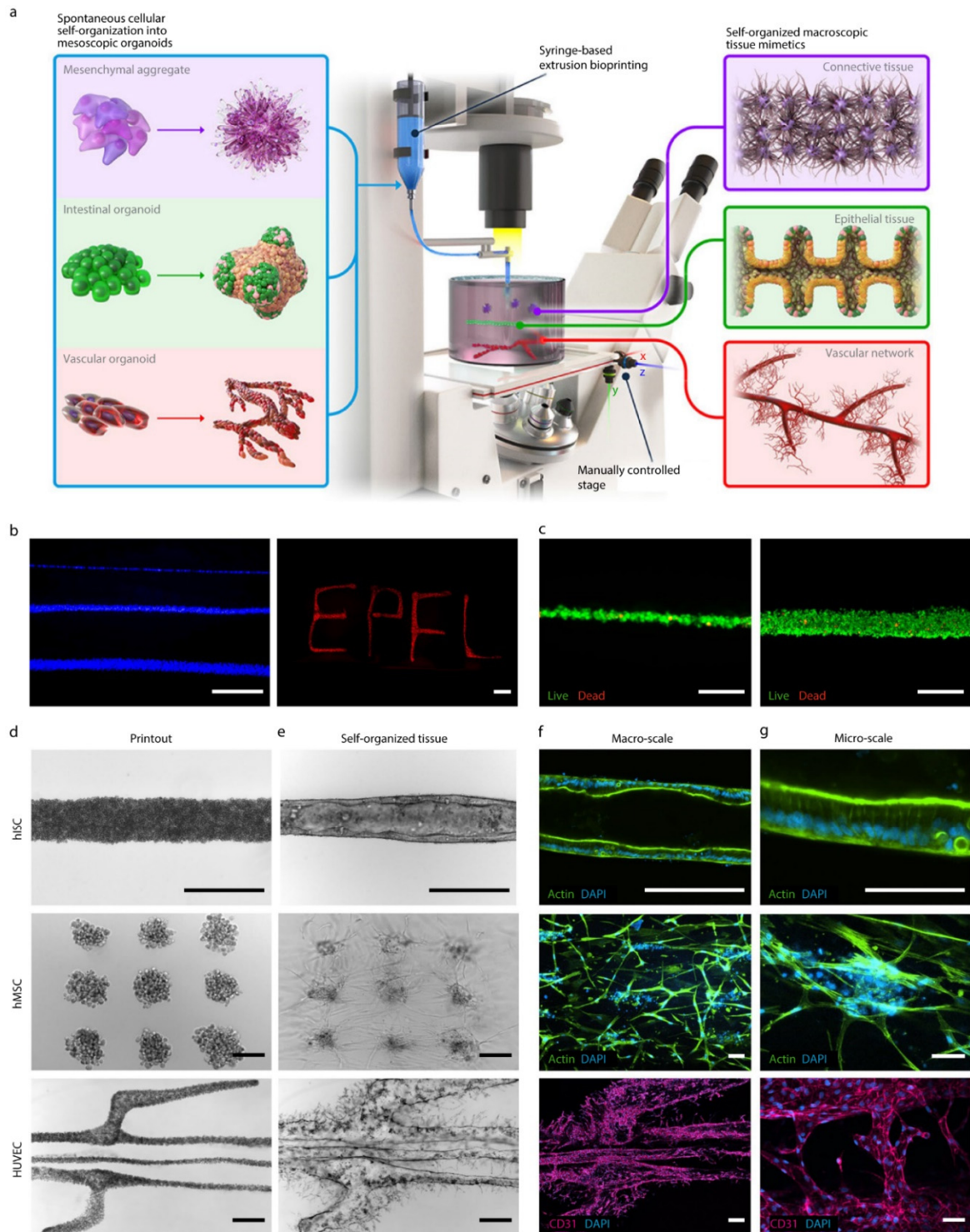


Figure 1 BATE. **a**, Illustration of the BATE concept using spontaneously self-organizing building blocks to create large-scale tissues. **b**, Representative fluorescent images of cells stained with cell tracker dyes showing the modulation of the resolution (left) and printing of complex geometry (right). Scale bars, 500 μm . **c**, Representative images of viability of HUVECs after printing with a low (left) and high (right) density, shown by calcein AM (live, green) and ethidium homodimer-1 (dead, red) cell stainings. See also Extended Data Fig. 1e for quantification. Scale bars, 250 μm . **d,e**, Bright-field images of the cell patterning immediately after printing (**d**) and after self-organization (**e**) of hMSC, hMSC and HUVEC cells. Scale bars, 500 μm . **f,g**, Fluorescence confocal images of macroscopic (**f**) and microscopic (**g**) tissue architecture. Cells are labelled with DAPI (blue) and F-actin (green) or CD31 (pink). All images are representative of $n=3$ biologically independent experiments. Scale bars, 250 μm (**f**) and 75 μm (**g**).

Next, we attempted to reconstruct an intricately patterned tissue at the macro-scale, which required the precise manipulation of geometry, cell–cell interactions, ECM composition and dynamics and the presence of key soluble factors (Fig. 2a). Mouse intestinal stem cells (mISCs), when cultured in Matrigel and supplemented with a defined cocktail of growth factors (EGF, Noggin and R-spondin (ENR)), form organoids bearing crypts and villus-like compartments resembling the epithelium of the small intestine *in vivo*^{16,17}. Dense lines of 3D-printed mISCs, cultured in ENR, developed into epithelial tubes in Matrigel as well as stiffer Matrigel and collagen mixtures (Extended Data Fig. 6 and Supplementary Videos 3 and 4). Guided by the imposed cylindrical geometry, bioprinted ISCs first condense into a thick tubular construct lacking a lumen before expanding as colonies and then fusing soon after into a polarized and lumenized epithelial tissue (Fig. 2b, Supplementary Video 3 and Extended Data Fig. 7). After 4–6days, the epithelial tubes bud (Fig. 2b) in a process that appears to coincide with the emergence of individual Paneth cells, which are distinguishable by their characteristic morphology and darker appearance, interspersed with stem cells expressing the characteristic marker *Lgr5* (Extended Data Fig. 7). This finely spaced salt and pepper-like cellular arrangement is reminiscent of the patterning of Paneth cells and stem cells in the intestinal crypts *in vivo* and in organoids^{16,17}. Even though dead cells are shed inside the epithelium as in classical organoids, intestinal tubes can be cultured for longer periods (≥ 3 weeks) and reach a larger diameter ($>400 \mu\text{m}$) (Fig. 2c,d). During this remodelling process, the length of the tube increases only slightly (less than 10% in 3weeks), demonstrating that the increase in diameter is due to proliferation and growth.

A critical parameter for colony fusion is a very high density of cells, probably because confined colony growth exerts compressive forces and increases colony-colony contact, subsequently promoting fusion. Indeed, although small organoids can also be used for printing, the resulting tubes are often discontinuous and show relatively high variation in their diameter, mainly due to irregular organoid fusion in the absence of the condensation step seen with single-cell printing (Extended Data Fig. 8). Furthermore, tubes printed at lower density (12.5 million cells per ml) not only have a smaller diameter (Fig. 2e), but also suffer from decreased robustness and reproducibility, as exemplified by some discontinuities as well as a heterogeneous distribution of their crypts (Extended Data Fig. 8). Using high single-cell density (≥ 50 million cells per ml), the printed tubes are highly reproducible, each of them having a comparable diameter (Fig. 2e) and featuring a continuous lumen as shown by histological analysis (Fig. 2f). Following matrix degradation, epithelial tubes can then be released and manually handled, indicating a surprising mechanical resiliency (Fig. 2g). Together, these data demonstrate that by spatially arranging spontaneously self-organizing tissue building blocks in permissive ECMs, complex tissue architecture and patterning can be robustly reproduced at the centimetre scale.

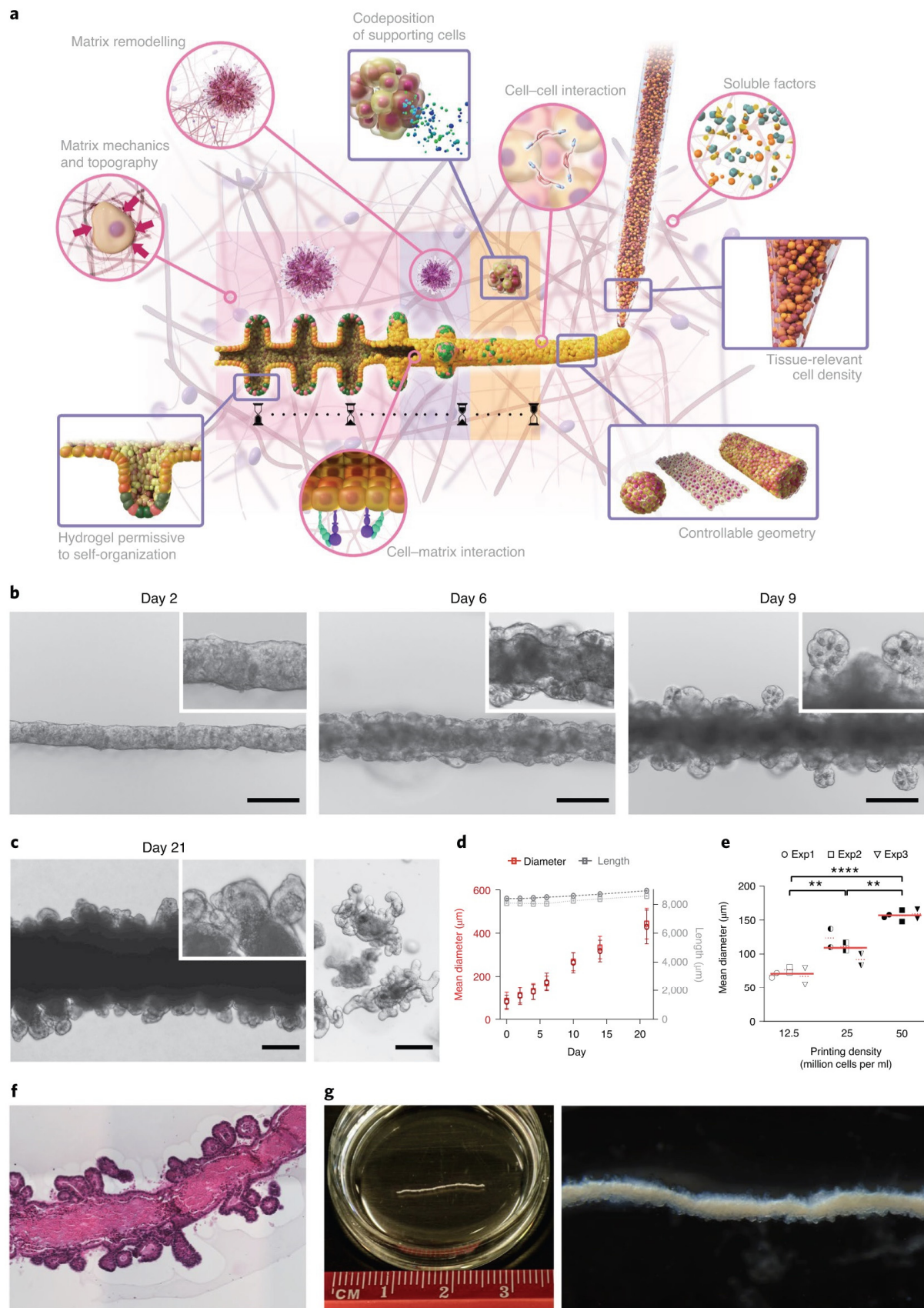
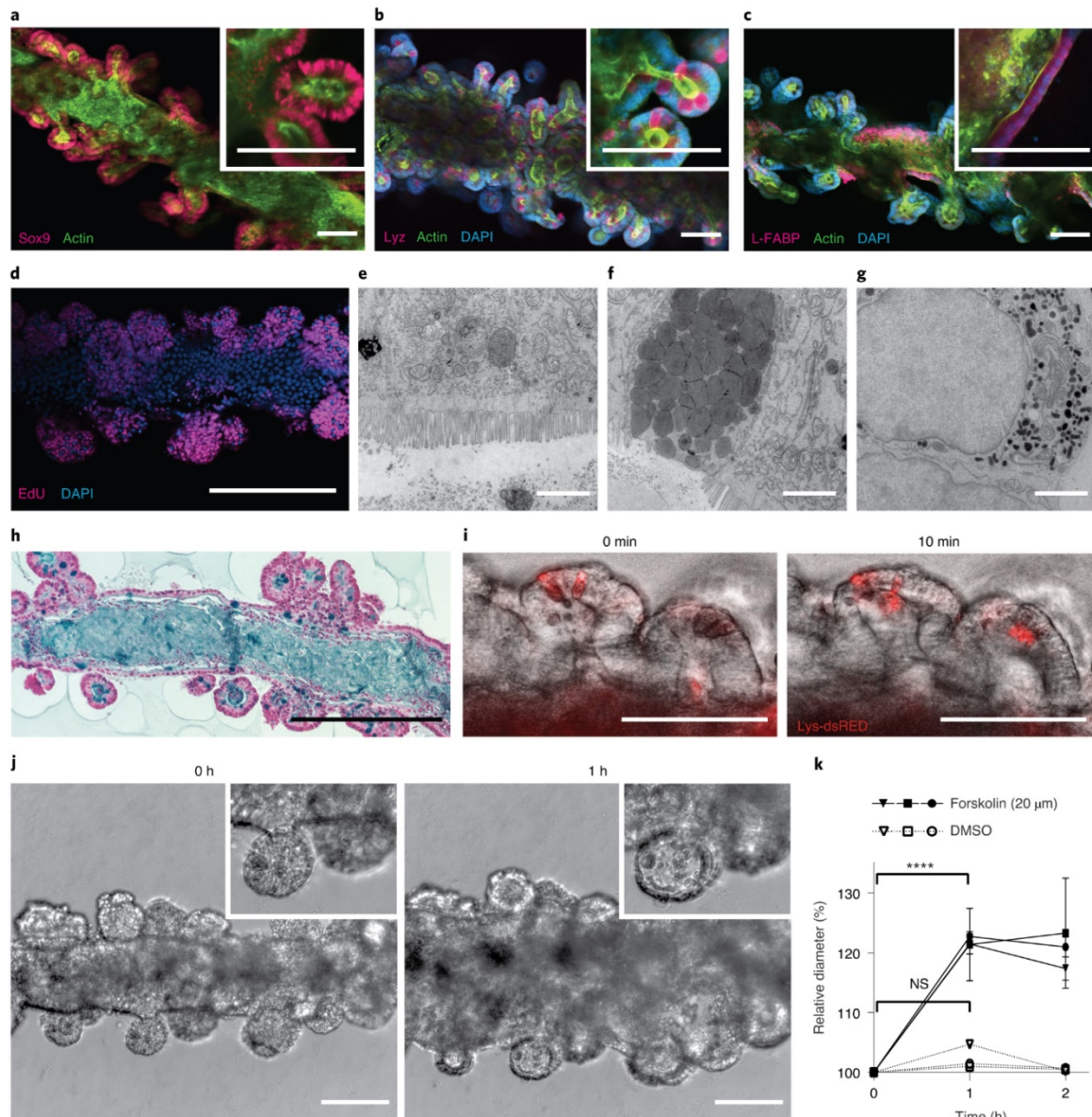


Figure 2 Macroscopic intestinal tube printing. a, Illustration of BATE applied to intestinal tissue engineering. Robust control over cellular density and tissue geometry can be achieved directly inside environments permissive to multicellular self-organization. b, Bright-field images of tube evolution.

Insets show the dense condensation phase (day 2), the formation of a lumen and appearance of budding structures (day 6) and the formation of crypts with dark Paneth cells (day 9). Images are representative of $n > 10$ biologically independent experiments. Scale bars, 200 μm . **c**, Intestinal tube after 21 days of culture showing an intact epithelium despite large accumulation of dead cells (right) and classical organoid culture before passaging (right) for size comparison. Scale bars, 200 μm . **d**, For two tubes, mean tube diameter and total length versus number of days in culture. Standard deviation of the mean along the tube's length is indicated for the diameter. **e**, Influence of bioink cell density on tube diameter after 6 days of culture. Results of three different experiments are shown with two tubes for each. $**P = 0.0074$ (left) and 0.0022 (right), $****P < 0.0001$, determined by one-way ANOVA with Tukey's multiple comparisons test. **f**, Histological cross-section stained with Hematoxylin and Eosin to visualize the continuous lumen and cellular organization. Images are representative of $n = 3$ biologically independent experiments. Scale bar, 200 μm . **g**, Macroscopic images of intestinal tube spanning > 15 mm. Images are representative of $n = 3$ biologically independent experiments.

To characterize the cellular composition of the printed intestinal tissues, eight-day-old tubes were stained to reveal putative crypts (marked by Sox9) with Paneth cells (Lyz), as well as a villus-like domain positive for the enterocyte marker L-FABP (Fig. 3a–c). Proliferative cells, labelled by the thymidine analogue 5-ethynyl-2'-deoxyuridine (EdU), were exclusively found in crypts (Fig. 3d). Transmission electron microscopy demonstrated the presence of mature differentiated cell types in the tubes, such as enterocytes with a characteristic apical brush border, mucus-producing goblet cells and enteroendocrine cells (Fig. 3e–g). Histological analysis using Alcian Blue showed goblet cells and a mucus layer covering the apical side of the epithelium (Fig. 3h).

Next, we assessed the physiological responses of the intestinal tubes to chemical stimuli. Paneth cells are a chief player in innate mucosal immunity and contain large apical secretory granules rich in host defence peptides such as lysozyme and defensins. To assess this secretory response, we used a lysozyme reporter organoid line (Lys-dsRED mISCs)¹⁸. Cells were printed and cultured for 6 days before being exposed basally to 100 μM carbamylcholine to trigger release of lysozyme granules from Paneth cells¹⁹ (Fig. 3i). On chemical treatment, the tubes immediately responded by swelling, followed by liberation of the lysozyme granules in their lumen (Supplementary Video 5). Additionally, we characterized the ability of the intestinal tubes to swell in response to the activation of the cystic fibrosis transmembrane conductance regulator channels²⁰. Eight-day-old intestinal tubes exposed to 20 μM forskolin rapidly swelled, showing expansion of their diameter by more than 20% after 1h (Fig. 3j,k and Supplementary Video 5). These results show that BATE can yield engineered tissues with high physiological relevance, resembling the phenotype and functionalities of their in vivo counterparts.



In the embryo and adult organism, different organ tissues continuously interact to provide precise spatiotemporal cues that ensure robust development and function, although existing cell culture and 3D printing approaches cannot reliably reproduce such physiological tissue–tissue interactions. BATE enables the sequential printing of multiple cell types to form complex geometries and cell-type arrangements with good spatial resolution (Fig. 4a–d). Given their important roles during intestinal development and as a stem cell niche *in vivo*^{21,22}, we explored how mouse intestinal mesenchymal cells (IMCs) could be used to increase the relevance of bioprinted intestinal tubes (Fig. 2). We first tested the simultaneous printing of primary mISCs and IMCs in the same bioink deposited as a dense line (Fig. 4e–h). In this configuration, randomly dispersed IMCs were gradually excluded from the epithelial cell condensate to migrate at the periphery of the forming tube, self-sorting into an intestinal epithelium surrounded by supporting α -SMA-positive mesenchymal cells (Fig. 4e,f and Supplementary Video 6). The co-deposition of IMCs altered the initial phenotype of the self-organizing ISCs from a columnar and highly polarized epithelium to a more squamous one (Fig. 4e–h and Extended Data Fig. 9), mirroring previously described intestinal organoids cultured in the presence of intestinal myofibroblast feeder layers²³. Incidentally, when the tubes were co-cultured with IMCs, complete lumen formation happened after only 1 day compared to 3–4 days without. The tube diameter also increased faster in the presence of IMCs, roughly doubling in size compared to control (Extended Data Fig. 9). Of note, after an initial radial expansion of the tube due to rapid fusion and proliferation, symmetry breaking still occurred, resulting in the highly stereotypical emergence of budding structures around the tube. That these budding structures represent *de novo* crypts was confirmed by the presence of Paneth cells, whereas differentiated cell types, such as enterocytes, were restricted to the non-budding areas (Fig. 4g,h). Similar results were obtained by printing IMCs in parallel lines around the mISCs, or by suspending the IMCs inside the gel before printing (Fig. 4i and Extended Data Fig. 9).

The versatility of BATE is also seen in its ability to control the sequential deposition of supportive cells spatially and temporally (Fig. 4i). Indeed, the integration of the bioprinter into an automated microscope makes it possible to track tissue emergence in real time and, if desired, return to specific locations to precisely place other cell types. Even though the fine nozzle is piercing the hydrogel during subsequent deposition, IMCs can still be deposited at any given time around the self-organizing epithelial tube to locally deliver key mesenchymal signals, for example. This presents the exciting possibility to guide tissue self-organization through cell-secreted temporal cues, potentially mirroring the action of native signalling centres as well as time-sensitive tissue–tissue interactions that may be critical during organ development.

One of the prevalent problems in stem cell-derived epithelial organoids is the physical inaccessibility of their lumen, restricting their lifetime and making it very difficult to study important physiological and pathological processes, such as host–microbe interactions or drug toxicity. In our system, the inclusion of stromal cells accelerates lumen formation and increases lumen diameter (Extended Data Fig. 9). This allows to connect the tissues to a liquid perfusion system to remove dead cells shed into the lumen during tissue turnover, a feature that could not be achieved with the densely filled lumen of intestinal organoids and intestinal tubes (Fig. 4j and Supplementary Video 7). This demonstrates how multicell-type bioprinting, in combination with extrinsically guided self-organization, can be leveraged to increase the relevance of tissue models.

Finally, we tested whether BATE could be used to establish multi-tissue models via combinatorial printing of various epithelial cell types from the gastrointestinal tract. Organoid-forming stem cells from different organs can be aspirated one after the other and dispensed sequentially to generate a cellular gradient flanked by two pure populations (Fig. 4a). Using this approach, stem cells from the stomach and colon, isolated from mTmG-mice that express membrane-localized dTomato protein, were combined with LGR5-eGFP mISCs to create large tubes featuring a gastrointestinal or small/large intestinal junction. Bright-field and fluorescence imaging revealed that the organ-specific identities were conserved after printing and throughout culture, ultimately resulting in a clear distinction between the intestinal zone filled with crypts containing LGR5+ stem cells, the smoother gastric or colonic zone, as well as the organ boundary where the crypt number progressively decreased (Fig. 4k,l and Extended Data Fig. 10). Gene expression analysis confirmed that both tissue identities are preserved within our multi-tissue models, with high expression of both small intestine (Alpi, Lyz1, Muc2) and gastric markers (Muc5ac, Muc6, Pgc) coexisting in the gastrointestinal tubes (Fig. 4m). BATE thus represent a powerful tool to answer unmet needs for multiple tissue or organ integration in organoid culture.

Efforts to create large-scale constructs out of organoids have been attempted by randomly positioning intestinal organoids inside a contracting collagen ring²⁴ or by punctually injecting mammary epithelial cells directly inside crosslinked collagen²⁵. Here, we show how this concept of organoid fusion can be used to produce relatively large-scale tissues using identical building blocks, as well as mimic tissue boundaries by using building blocks from related organs. The local self-organization properties of organoid-forming stem cells can also be modulated by supportive cells to yield constructs with improved growth or altered development.

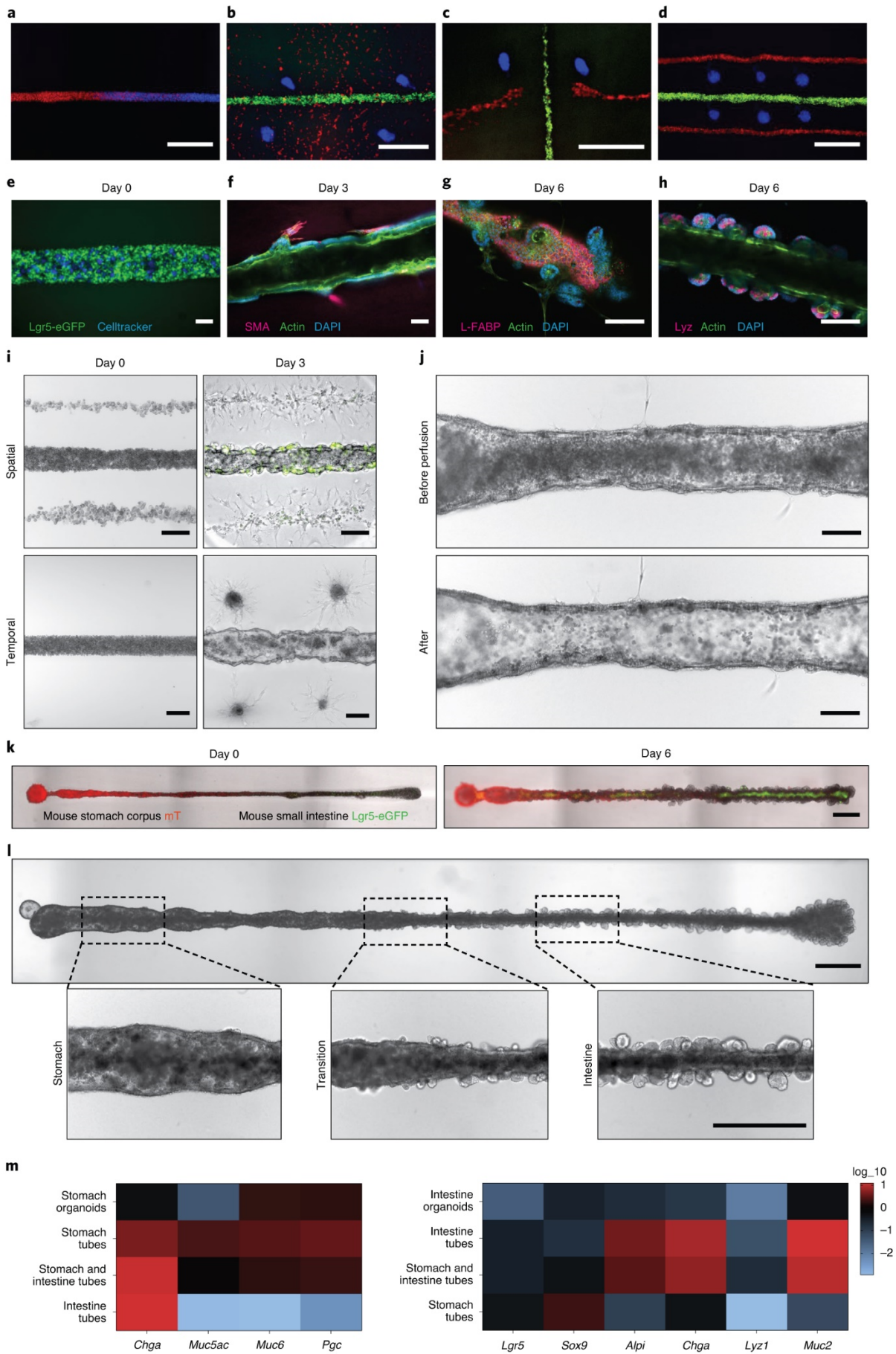


Figure 4 Co-culture printing. **a–d**, Micrographs of cells stained with cell tracker dyes showing the printing of cellular gradient (**a**), two different cell types within a dispersed third one (**b**), discontinuous lines (**c**) and complex multicellular pattern (**d**). Scale bars, 500 μm . **e–h**, Self-sorting of ISCs and IMCs during intestinal tube formation (**e**) IMCs stained with cell tracker (blue) are initially randomly dispersed within the ISCs (green, Lgr5–eGFP). **f**, SMA-positive IMCs (red) are located at the periphery of the tube. **g,h**, After 6 d, enterocytes are located on flatter surface and excluded from crypts (**g**) whereas Paneth cells are located within the crypts (**h**). Scale bars, 100 μm . **i**, Bright-field images of intestinal tube evolution with IMC patterning, demonstrating control over spatial (top) and temporal (bottom) deposition. Scale bars, 200 μm . **j**, Bright-field images of an intestinal tube before (top) and after (bottom) perfusion. Scale bars, 200 μm . **k**, Tubes composed of mouse stomach corpus (mT) and mouse small intestine (Lgr5–eGFP) stem cells directly after printing (left) and 6 d later (right). Scale bar, 500 μm . **l**, High-resolution image with insets representing the stomach part, the transition zone and the intestinal part. Scale bars, 500 μm . **m**, Heatmap of quantitative real-time PCR data showing the relative expression of stomach specific genes (Muc5ac, Muc6, Pgc), intestine specific genes (Alpi, Lyz1, Muc2) as well as Chga and stem/progenitor cells (Lgr5, Sox9) in tubes composed of one or both cell types 4 d after printing. Average expression over two tubes, normalized to organoids in standard culture conditions are shown (see Methods). As a comparison, gene expression levels for organoids originating from single cells and kept in the same medium as the tubes for the same time period are shown. All bright-field and fluorescent images in the figure are representative of $n=3$ biologically independent experiments.

We believe that our cell-printing approach to guide tissue morphogenesis at different scales has several advantages compared to existing bioprinting technologies. Fragile cells such as primary stem cells can be organized into a complex geometry directly within the most potent 3D culture matrices, such as Matrigel. In comparison, previous studies have succeeded in printing cell-only bioink inside a support bath of microgels⁶ or in printing biomaterial-based bioink directly inside self-healing guest–host hydrogels⁷. These strategies have, however, failed to provide the necessary environment for complex self-organization processes. In addition to enabling morphogenetic guidance using tissue–tissue interactions, BATE also reduces printing time and geometrical complexity because the microscopic architecture of the final constructs is created by the cells during subsequent remodelling and self-organization.

We believe that with BATE, local rules of cellular interactions and self-organization specific to a group of cells can be multiplied across different scales, provided that the geometry, cellular density, and the environment are suitable. As such, the conditions that have been optimized for different organoid systems can be seamlessly translated to the macroscopic scale by bioprinting the relevant stem cells in their specific permissive environments. Because these fundamental concepts are broad, we envision that the same design strategy for naturally programmed building blocks could also be applied to tissues from different origins, combining existing organoid systems as well as their relevant supportive cells. This study thus opens new avenues in stem cell biology and regenerative medicine, providing a powerful tool for engineering self-organized tissues and mimicking organ boundaries as well as other tissue–tissue interactions. The fact that the cells contained within these printed tissues follow a well-

regulated physiological morphogenetic program, contrary to the exaggerated spatial confinement or excessive restrictions seen in other bioprinting approaches, may also hold promise in substantially increasing their functionality, integration and maturation in vivo.

References

1. Murphy, S. V. & Atala, A. 3D bioprinting of tissues and organs. *Nat. Biotechnol.* 32, 773–785 (2014).
2. Liu, W. et al. Rapid continuous multimaterial extrusion bioprinting. *Adv. Mater.* 29, 1604630 (2017).
3. Keriquel, V. et al. In situ printing of mesenchymal stromal cells, by laser-assisted bioprinting, for in vivo bone regeneration applications. *Sci. Rep.* 7, 1778 (2017).
4. Hinton, T. J. et al. Tree-dimensional printing of complex biological structures by freeform reversible embedding of suspended hydrogels. *Sci. Adv.* 1, e1500758–e1500758 (2015).
5. Lee, A. et al. 3D bioprinting of collagen to rebuild components of the human heart. *Science* 365, 482–487 (2019).
6. Bhattacharjee, T. et al. Writing in the granular gel medium. *Sci. Adv.* 1, e1500655–e1500655 (2015).
7. Highley, C. B., Rodell, C. B. & Burdick, J. A. Direct 3D printing of shear-thinning hydrogels into self-healing hydrogels. *Adv. Mater.* 27, 5075–5079 (2015).
8. Jamal, M. et al. Bio-origami hydrogel scaffolds composed of photocrosslinked PEG bilayers. *Adv. Healthc. Mater.* 2, 1142–1150 (2013).
9. Villar, G., Graham, A. D. & Bayley, H. A tissue-like printed material. *Science* 340, 48–52 (2013).
10. Clevers, H. Modeling development and disease with organoids. *Cell* 165, 1586–1597 (2016).
11. Lancaster, M. A. & Knoblich, J. A. Organogenesis in a dish: modeling development and disease using organoid technologies. *Science* 345, 1247125–1247125 (2014).
12. Laurent, J. et al. Convergence of microengineering and cellular self-organization towards functional tissue manufacturing. *Nat. Biomed. Eng.* 1, 939 (2017).
13. Brassard, J. A. & Lutolf, M. P. Engineering stem cell self-organization to build better organoids. *Cell Stem Cell* 24, 860–876 (2019).
14. Sato, T. et al. Long-term expansion of epithelial organoids from human colon, adenoma, adenocarcinoma, and Barrett’s epithelium. *Gastroenterology* 141, 1762–1772 (2011).
15. Blatchley, M. R. & Gerecht, S. Reconstructing the vascular developmental milieu in vitro. *Trends Cell Biol.* 30, 15–31 (2020).
16. Sato, T. et al. Single Lgr5 stem cells build crypt-villus structures in vitro without a mesenchymal niche. *Nature* 459, 262 (2009).
17. Sato, T. et al. Paneth cells constitute the niche for Lgr5 stem cells in intestinal crypts. *Nature* 469, 415–418 (2011).
18. Es, J. Hvan et al. Enteroendocrine and tuft cells support Lgr5 stem cells on Paneth cell depletion. *Proc. Natl Acad. Sci. USA* 116, 26599–26605 (2019).
19. Yokoi, Y. et al. Paneth cell granule dynamics on secretory responses to bacterial stimuli in enteroids. *Sci. Rep.* 9, 2710 (2019).
20. Dekkers, J. F. et al. A functional CFTR assay using primary cystic fibrosis intestinal organoids. *Nat. Med.* 19, 939–945 (2013).
21. Wells, J. M. & Spence, J. R. How to make an intestine. *Development* 141, 752–760 (2014).
22. Stzepourginski, I. et al. CD34+ mesenchymal cells are a major component of the intestinal stem cells niche at homeostasis and after injury. *Proc. Natl Acad. Sci. USA* 114, E506–E513 (2017).
23. Farin, H. F., Van Es, J. H. & Clevers, H. Redundant sources of Wnt regulate intestinal stem cells and promote formation of Paneth cells. *Gastroenterology* 143, 1518–1529.e7 (2012).
24. Sachs, N., Tsukamoto, Y., Kujala, P., Peters, P. J. & Clevers, H. Intestinal epithelial organoids fuse to form self-organizing tubes in floating collagen gels. *Development* 144, 1107–1112 (2017).

25. Reid, J. A., Mollica, P. A., Bruno, R. D. & Sachs, P. C. Consistent and reproducible cultures of large-scale 3D mammary epithelial structures using an accessible bioprinting platform. *Breast Cancer Res.* 20, 122 (2018).

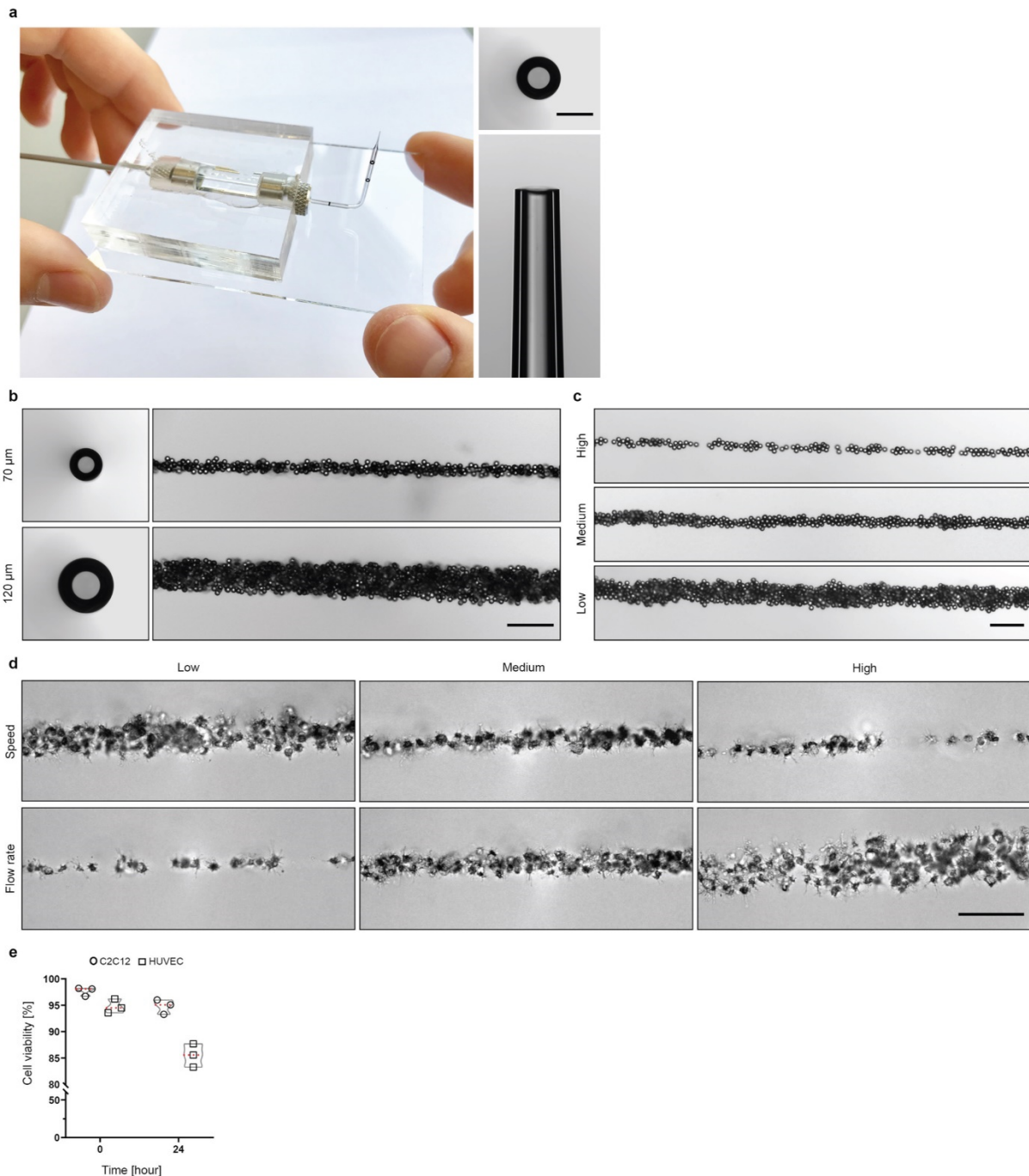
Acknowledgements

We thank N. Gjorevski and A. Martinez Arias for valuable feedback on the manuscript. We thank S. Li and D. Dutta for deriving organoid lines from intestinal tissues of mTmG and Lys-dsRED reporter mice, respectively. We thank O. Mitrofanova for help with human intestinal organoid culture and tube printing, S. Giger for providing hMSCs and A. Manfrin and A. Chrisnandy for the qPCR primers for intestinal genes. We thank R. Guet and O. Burri from EPFL's BioImaging and Optics Platform for help with intestinal tube analysis. We thank J. van Es and H. Clevers for providing intestinal tissues of Lys-dsRED reporter mice and J. McKinney for providing intestinal tissues of mTmG reporter mice. This work was funded by support from the EU Horizon 2020 Project INTENS (no. 668294-2), the Swiss National Science Foundation research grant no. 310030_179447, the National Center of Competence in Research (NCCR) 'Bio-Inspired Materials' (<https://www.bioinspired-materials.ch/>), the PHRT-PM/PH Research Project Proposal 2017, the Wellcome Trust Collaborative Award 211944/Z/18/Z, and EPFL.

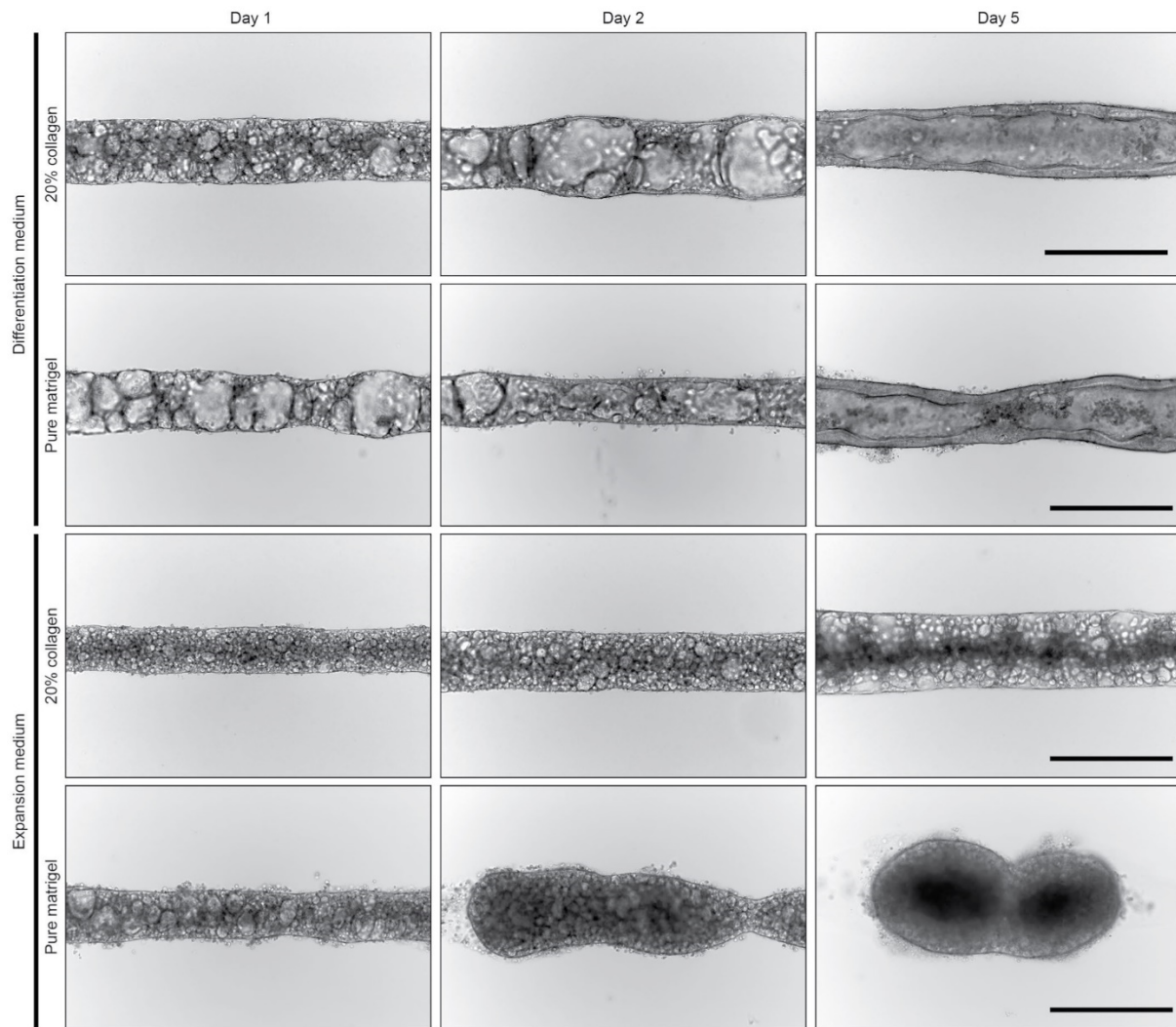
Author contributions

M.P.L. and M.N. conceived the initial idea. J.A.B., M.N., T.H. and M.P.L. conceived the study, designed experiments and analysed the data. M.P.L. and J.A.B. wrote the manuscript. T.H. performed multi-gastrointestinal cell-type printing. M.H. was involved in performing and analysing stomach tube printing experiments. All authors provided feedback on the manuscript.

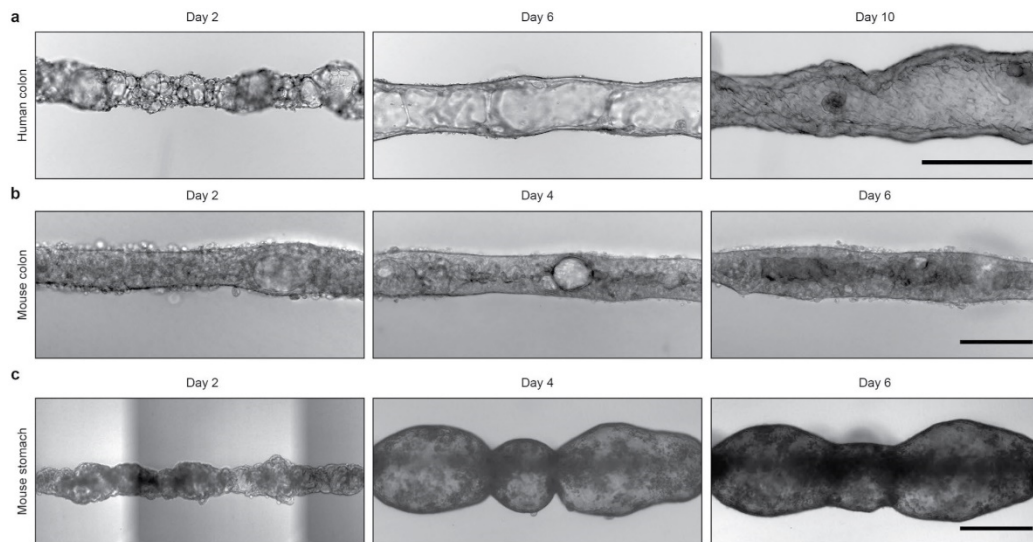
Extended data figures and supplementary videos



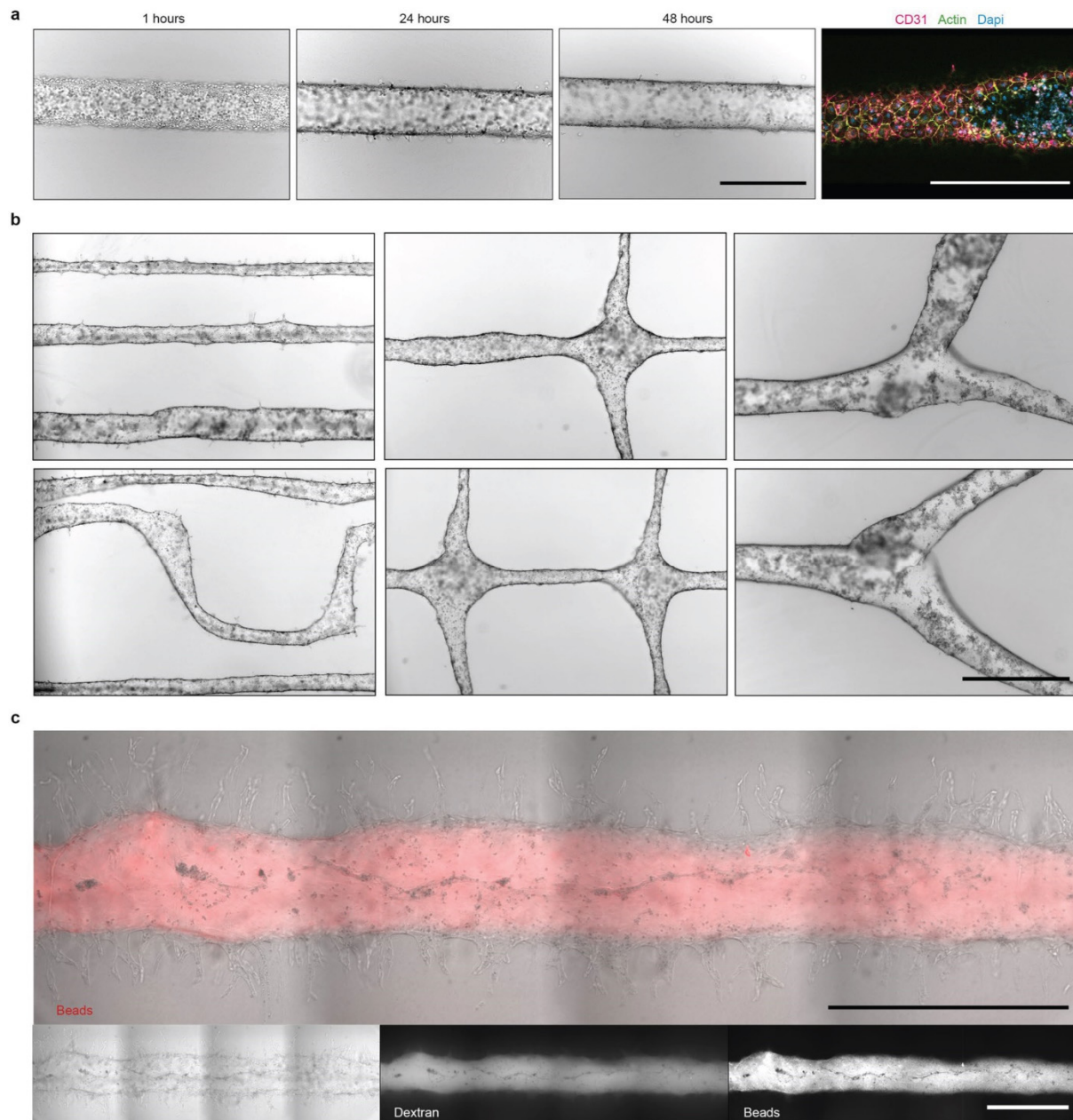
Extended Data Fig. 1 Bioprinter setup and proof-of-concept. **a**, Picture of the nozzle to be mounted on the microscope. The nozzle after pulling and breaking of the tip has a long taper and a clear cut. Scale bar, 200 μm . **b**, Printing with beads showing that resolution and printing thickness can be modulated by changing the nozzle size or (**c**) the speed of the stage movement. Images are representative of $n = 3$ independent experiments. Scale bars, 200 μm . **d**, Printing with HUVECs showing that resolution and cell density can be controlled by modifying the flow rate (syringe-based extrusion) or the printing speed (stage movement). Images are representative of $n = 3$ biologically independent experiments. Scale bar, 200 μm . **e**, Viability of C2C12 (circles) and HUVECs (squares) right after printing and 24 hours later. Data represented as percentage of live cells for three replicates ($n = 3$ biologically independent experiments), with the mean for each condition shown as a dot line.



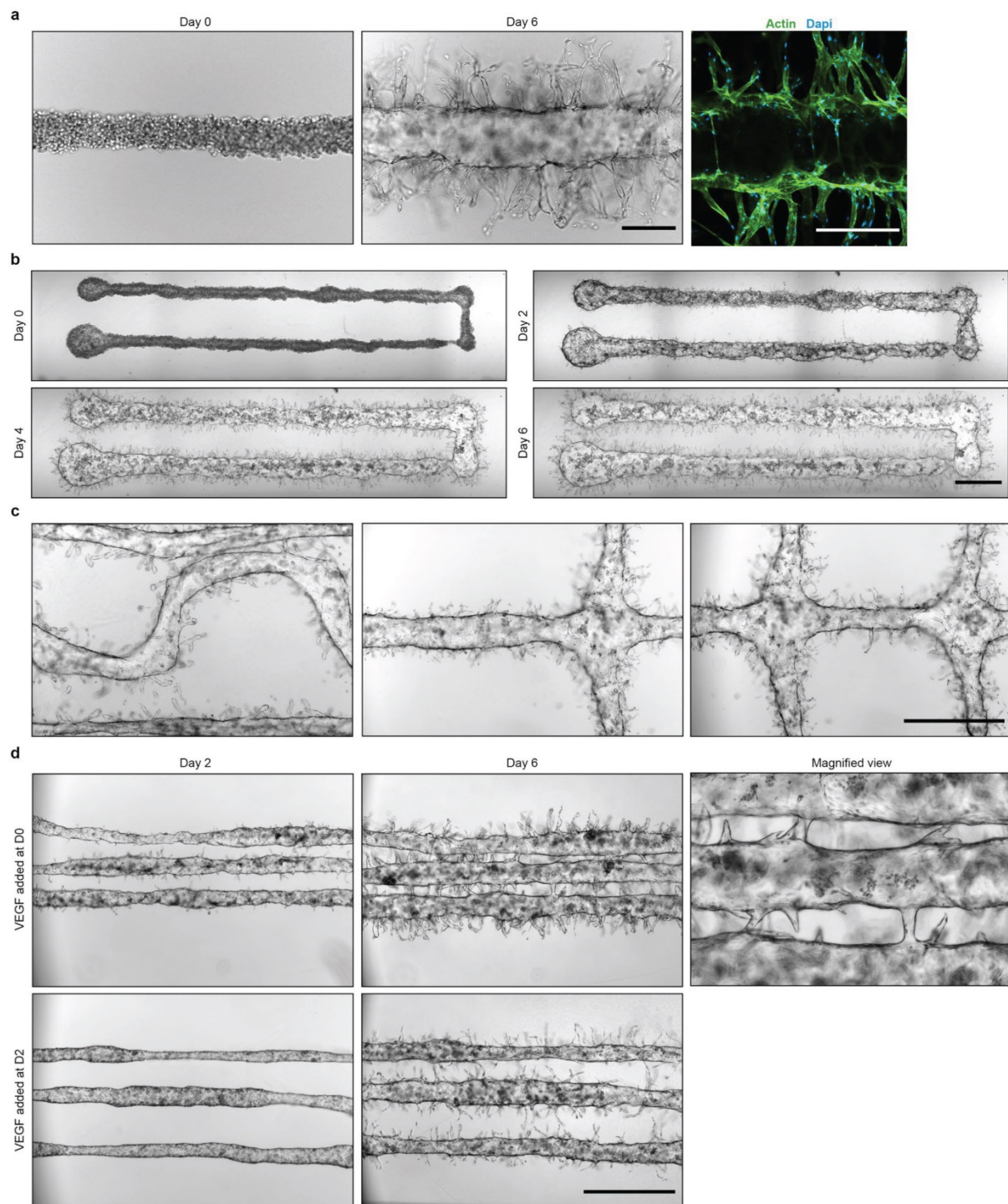
Extended Data Fig. 2 Printing human intestinal tubes. Bright-field images showing the evolution of human intestinal stem cells printed as a line. Differentiation medium promotes the rapid formation of a continuous lumen. Increasing the matrix stiffness, by addition of collagen in the support hydrogel, allows to maintain the printed geometry better, preventing collapse of the tube due to cell remodelling. Images are representative of $n = 3$ biologically independent experiments. Scale bars, 500 μm .



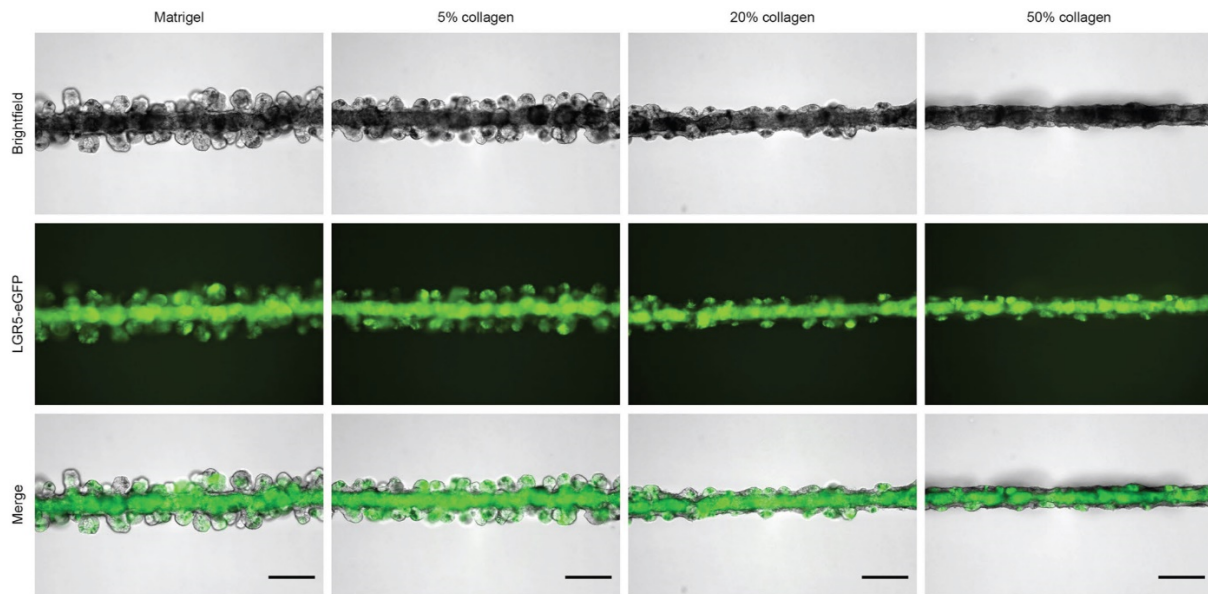
Extended Data Fig. 3 BATE of colon and stomach epithelial tubes from mouse and human primary cells. **a**, Bright-field images of tube evolution from human and **(b)** mouse colon stem cells and **(c)** mouse stomach stem cells. In all cases, a thick tubular epithelium is formed by colony growth and fusion at high density. Images are representative of $n = 3$ biologically independent experiments. Scale bars, 500 μm .



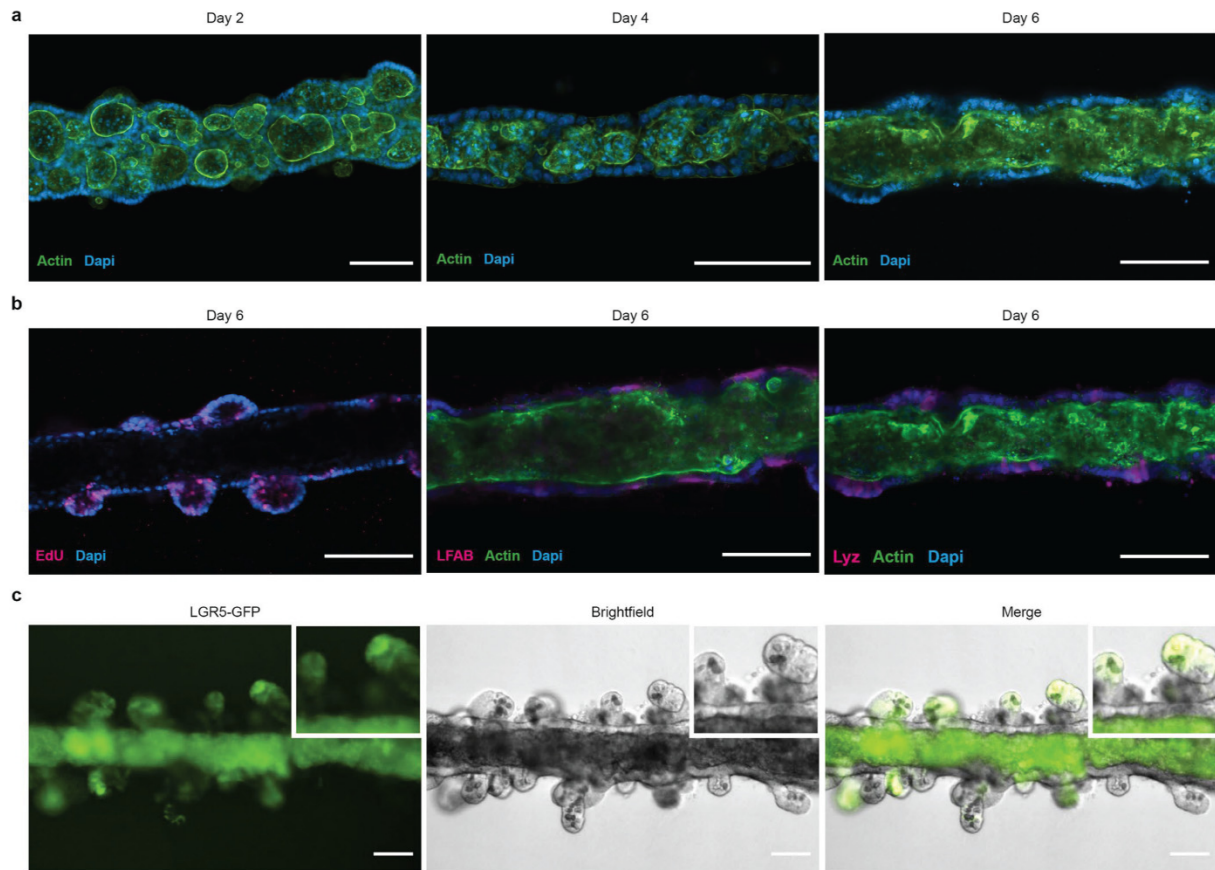
Extended Data Fig. 4 BATE of vascular endothelial tubes. **a**, Evolution of a printed line of HUVECs, showing rapid reorganization into an endothelial tube with a single macroscopic lumen. Images are representative of $n = 3$ biologically independent experiments. Scale bar, 500 μm . **b**, Different geometries can be printed to form branched vascular tubes and other complex structures. Images are representative of $n = 3$ biologically independent experiments. Scale bar, 1000 μm . **c**, Bright-field and fluorescent images showing vascular tube perfusion with fluorescently labelled dextran (2000 kDa) or fluorescently labelled beads (0.1 μm). Images are representative of $n = 3$ biologically independent experiments. Scale bars, 1000 μm .



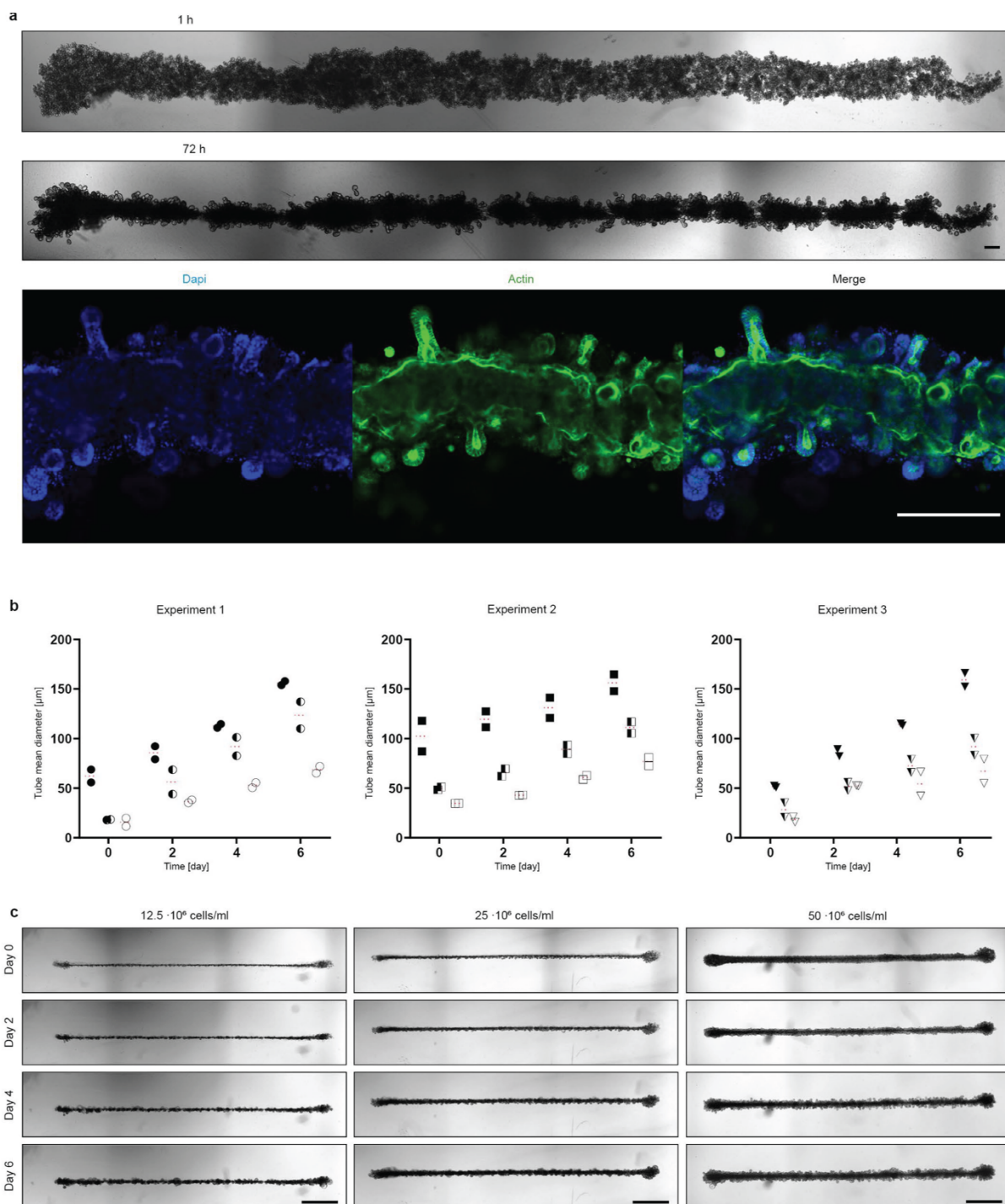
Extended Data Fig. 5 Induction of angiogenesis in bioprinted vascular tubes. **a**, Evolution of a printed vascular tube exposed to high VEGF concentration. Many capillaries are formed de novo while maintaining the continuous lumen. Scale bars, 250 μm . **b**, Evolution of a printout with straight angles showing good conservation of the printing geometry over time. Scale bar, 1000 μm . **c**, Complex geometries can also be printed, resulting in branched vascular networks with strong angiogenesis potential. Scale bar, 1000 μm . **d**, Bright-field images showing the evolution of printed vascular tube with addition of VEGF at different time points. Angiogenesis can be triggered at a desired time, promoting formation of capillaries that can connect with other tubes. Images are representative of $n = 3$ biologically independent experiments. Scale bar, 1000 μm .



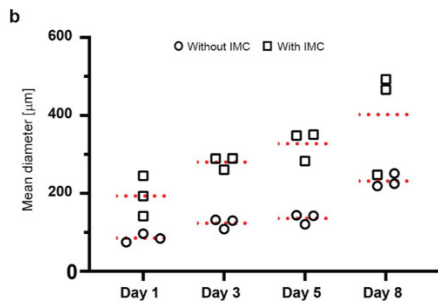
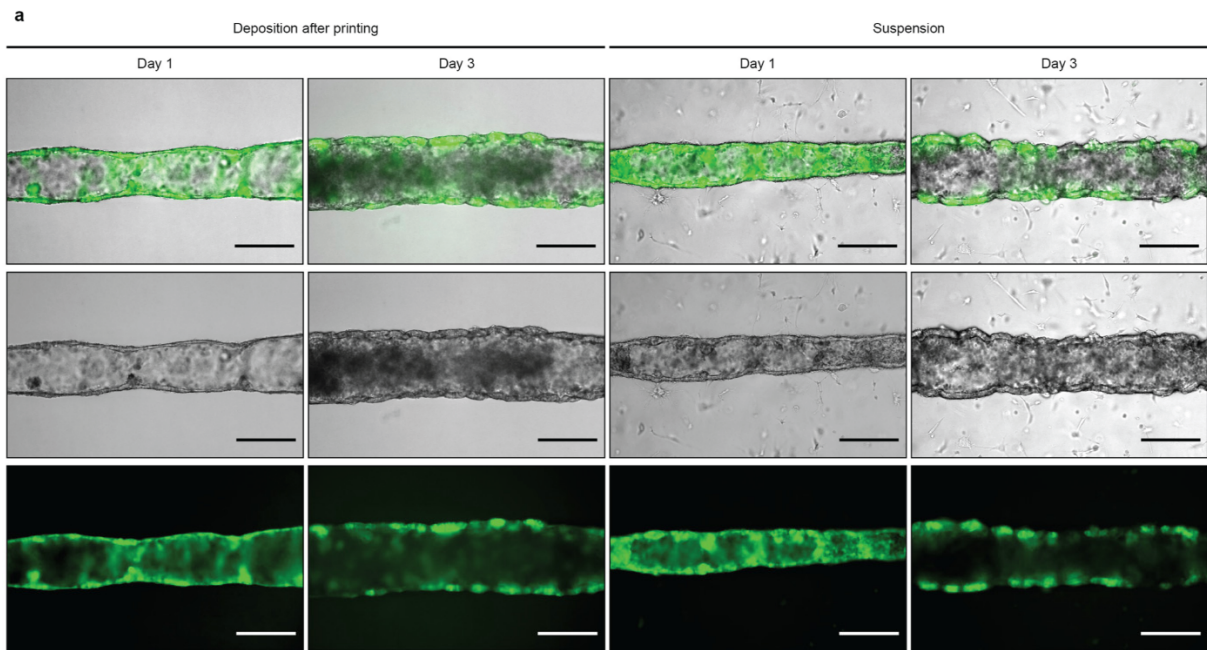
Extended Data Fig. 6 Intestinal tube morphogenesis: influence of collagen content in the support hydrogel. Addition of collagen I increases the stiffness of the support hydrogel, limiting extensive budding of the tubes. Of note: when the gel is disrupted, budding can occur even at later time points also for initially stiffer hydrogels. Images are representative of $n = 3$ biologically independent experiments. Scale bars, 200 μm .



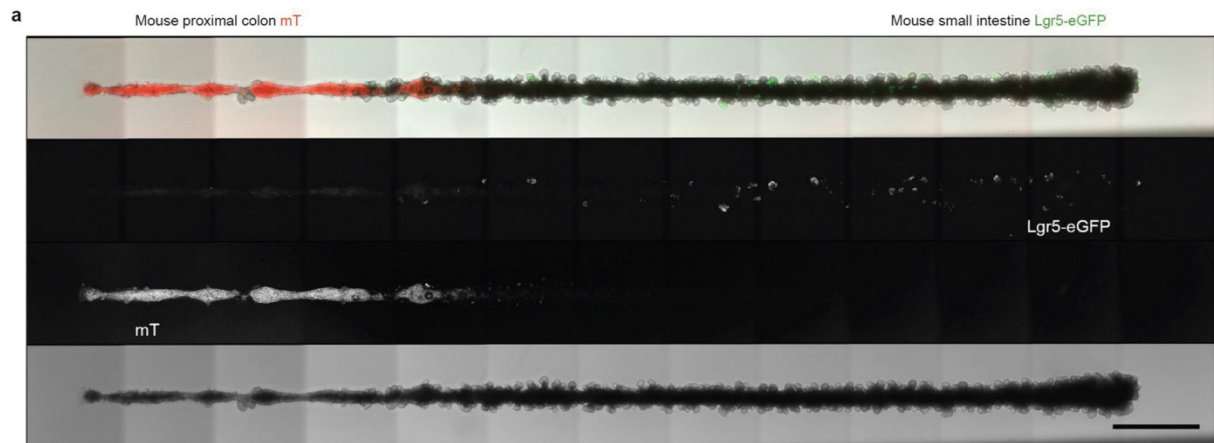
Extended Data Fig. 7 Intestinal epithelial tube staining. **a**, Confocal fluorescent images showing the formation of a continuous lumen by colony fusion. Images are representative of $n = 3$ biologically independent experiments. Scale bars, $100 \mu\text{m}$. **b**, Staining of the intestinal tubes after six days of culture. Proliferation (EdU, left) and Paneth cells (Lyz, right) are restricted to the crypt-like structures whereas enterocytes (LFAB, middle) are found on flatter surfaces. Images are representative of $n = 3$ biologically independent experiments. Scale bars, $100 \mu\text{m}$. **c**, fluorescent image of LGR5-eGFP and corresponding bright-field image of a tube after seven days, showing darker Paneth cells intercalated in between stem cells inside the crypts. Note that the autofluorescence of dead cells in the lumen does not overlap with the intact epithelium in the merged picture. Images are representative of $n = 3$ biologically independent experiments. Scale bars, $100 \mu\text{m}$.



Extended Data Fig. 8 Influence of printing cell density on tube formation and diameter. a, Representative tube printed from small intestinal organoids (that is not single cells). Top: 1 hour after printing, Middle: 72h after printing, Bottom: staining (Dapi labelling the nuclei, Actin) of the tube showing a lumen and crypt structures. Scale bars, 200 μm . **b,** Change of mean tube diameter over time at three different cell densities: 12,5 million (white symbol), 25 million (white and black symbol) and 50 million (black symbol) cells/ml. The experiment was repeated three times and two tubes are shown for each cell density. **c,** Evolution over time of one representative tube for each initial cell density from one of the three experiment is shown. Scale bars, 1000 μm .



Extended Data Fig. 9 Effect of IMC co-culture in bioprinted intestinal tubes. **a**, Bright-field images and corresponding fluorescent images of Lgr5-eGFP three days after printing, showing the effect of IMC co-culture on tube formation. IMCs were either deposited after printing for adherence on the well bottom and hydrogel (left), or directly suspended inside the hydrogel before and during printing (right). In all cases, a continuous lumen was formed after only one day, and the tubes comprise many Lgr5+ buds after 3 days. Images are representative of $n = 3$ biologically independent experiments. Scale bars, 250 μm . **b**, Difference in evolution of the tube diameter if co-cultured with IMCs or not. For each day, the mean diameter (dotted line) of tubes with and without myofibroblasts were compared ($n=3$ tubes for each day).



Extended Data Fig. 10 Continuous epithelial tube composed of mouse small intestine and colon stem cells. Top: merged (max Z projection) image of the tube in bright-field as well as showing red (mT) and green (Lgr5-eGFP) fluorescent cells, each color being shown separately below. Middle: colon cells expressing mT and intestinal cells expressing Lgr5-eGFP. Bottom: bright-field. Images are representative of $n = 3$ biologically independent experiments. Scale bar, 1000 μm .

[Supplementary Video 1](#)

https://static-content.springer.com/esm/art%3A10.1038%2Fs41563-020-00803-5/MediaObjects/41563_2020_803_MOESM3_ESM.mp4

BATE technology. Real-time demonstration of BATE technology, with sequential cellular aspiration and deposition within liquid ECM precursors.

[Supplementary Video 2](#)

https://static-content.springer.com/esm/art%3A10.1038%2Fs41563-020-00803-5/MediaObjects/41563_2020_803_MOESM4_ESM.mp4

Angiogenesis of the bioprinted vascular network. Z-stacks of bright-field and fluorescent images showing the morphology of the vascular network, highlighting the formation and maintenance of a continuous lumen in the presence and absence of VEGF supplementation. The stacks also show connections between different vascular tube through angiogenesis.

[Supplementary Video 3](#)

https://static-content.springer.com/esm/art%3A10.1038%2Fs41563-020-00803-5/MediaObjects/41563_2020_803_MOESM5_ESM.mp4

Intestinal tube morphogenesis. Five-day time-lapse showing the evolution of the intestinal tube. Right after the printing process, cells condense into a tightly packed line before starting to polarize and giving rise to Paneth cell emergence and subsequent budding formation.

[Supplementary Video 4](#)

https://static-content.springer.com/esm/art%3A10.1038%2Fs41563-020-00803-5/MediaObjects/41563_2020_803_MOESM6_ESM.mp4

Matrix softening promotes intestinal crypt morphogenesis. Three-day time-lapse showing intestinal crypt morphogenesis after treatment of the tube with collagenase. Matrix degradation results in homogeneous elongation of budding structure into crypts with darker Paneth cells at the bottom.

[Supplementary Video 5](#)

https://static-content.springer.com/esm/art%3A10.1038%2Fs41563-020-00803-5/MediaObjects/41563_2020_803_MOESM7_ESM.mp4

Physiological response to chemical stimuli in intestinal tubes. Carbamylcholine treatment triggers release of lysozyme granules from Paneth cells. Intestinal tubes exposed to Forskolin rapidly swelled, as a response to the activation of the cystic fibrosis transmembrane conductance regulator channels.

[Supplementary Video 6](#)

https://static-content.springer.com/esm/art%3A10.1038%2Fs41563-020-00803-5/MediaObjects/41563_2020_803_MOESM8_ESM.mp4

Multicellular self-assembly of intestinal epithelial and stromal cells. Two-day time-lapse showing the evolution of intestinal tube morphogenesis when mouse ISC are printed together with mouse IMCs. Tube formation and lumen genesis are faster. Some IMC migrating at the periphery of the tube can also be seen.

[Supplementary Video 7](#)

https://static-content.springer.com/esm/art%3A10.1038%2Fs41563-020-00803-5/MediaObjects/41563_2020_803_MOESM9_ESM.mp4

Large-scale self-organization allows lumen accessibility and perfusion. Demonstration of the perfusion process of the intestinal tube to remove the dead cells that are shed during culture as in the normal turnover of the tissue.

Methods

Mouse strains

The following mouse lines were used for organ extraction and organoid culture establishment: 6–13-week-old heterozygous *Lgr5*⁺ eGFP-IRES-CreERT2 (Jackson Laboratory), *Lyz2*^{dsRED18}, *mTmG26* or wild-type C57BL/6. All mouse work was conducted in accordance with animal experimentation protocols prescribed by EPFL and the Federation of European Laboratory Animal Science Associations. The establishment of organoid culture from mouse stomach, small intestines and colons was approved by the responsible ethical committee in compliance with local animal welfare laws, guidelines and policies.

Murine intestinal and colonic crypt isolation and culture

Murine intestinal crypts were isolated and cultured as previously described¹⁴. Briefly, the middle part of the intestine (roughly corresponding to the jejunum) was collected and washed thoroughly with ice-cold PBS without calcium and magnesium (Gibco) containing Gentamicin/Amphotericin (Gibco). Luminal content and villi were scraped with a glass slide to only keep the crypts and remove the rest of the epithelium. After washing with ice-cold PBS, intestinal sections were minced using two razor blades, collected in a 50-ml Falcon tube and washed again 5–10 times. The minced intestinal fragments were then incubated on ice for 20min in PBS containing 20mM EDTA (Gibco). After sedimentation of the fragments, EDTA was removed and replaced by PBS supplemented with 10% fetal bovine serum (FBS) (Gibco). The first fraction of the crypts was released by gentle vortexing of the tube and collected in another tube mounted with a 70- μ m strainer (BD Bioscience). To collect the second fraction of the crypts, 10ml of cold PBS was added, and intestinal fragments were triturated 10–20 times before being passed through a 70- μ m strainer. The two fractions were analysed under the microscope and then combined and centrifuged at 100g before being resuspended in cold Advanced DMEM/F12 medium (Invitrogen). After a second centrifugation, crypts were resuspended in Matrigel (Corning, growth factor reduced, phenol red-free formulation), deposit as 20–25 μ l droplets in 24-well plates and incubated for 10min in hanging-drop position at 37 °C in 5% CO₂. After polymerization, 500 μ l of organoid basal medium (Advanced DMEM/F12 containing GlutaMax, HEPES, penicillin-streptomycin, B27, N2 (all from Invitrogen) and 1 μ M N-acetylcysteine (Sigma-Aldrich)) was added and supplemented with 5 μ M of Thiazovivin (Stemgent, only for the first 2d), mEGF (50ngml⁻¹, Peprotech), Noggin (100ngml⁻¹, produced in-house), R-spondin (500ngml⁻¹, produced in-house), CHIR99021 (3 μ M, Millipore) and valproic acid (1mM, Sigma). Passaging of the cells was done every 3–4d by mechanical disruption of the organoids through a glass pipet followed by reembedding in Matrigel. ISCs

were maintained at 37 °C in 5% CO₂ humidified air during culture. Murine colonic crypts were isolated using the same protocol with longer EDTA incubation (30–40min) and cultured in organoid basal medium supplemented with growth factors and small molecules, including mEGF, Noggin, R-spondin and CHIR99021 (same concentration as ISC culture) as well as Wnt3A (50ngml⁻¹, Time Bioscience) or in WNR-conditioned medium supplemented with mEGF (50ngml⁻¹) and Primocin (100µgml⁻¹, InvivoGen). Colon organoids were passaged every 5–7d. Medium was changed every 2d for all cultures.

Murine stomach gland isolation and culture

The extracted stomach was cut along the inner curvature, folded up and washed in PBS. The forestomach was removed, and the remaining glandular stomach split to the antrum and corpus part, respectively. Separately for both regions, the glands were extracted and cultured as organoids according a previously published protocol²⁷. In brief, the stomach tissue was washed and minced in chelation buffer (sterile distilled water with 5.6mM Na₂HPO₄, 8.0mM KH₂PO₄, 96.2mM NaCl, 1.6mM KCl, 43.4mM sucrose, 54.9mM d-sorbitol, 0.5mM dl-dithiothreitol, pH7) and digested in EDTA-containing chelation buffer for 30min at 4 °C with occasional swirling. Glands were extracted by applying mechanical pressure and subsequently separated from the larger fragments by letting the latter sediment in Advanced DMEM/F-12 medium. Glands and fragments thereof were seeded in Matrigel analogous to extracted intestinal crypts and cultured in WRN-conditioned medium supplemented with 1× B27, 1mM N-acetylcysteine, 50ngml⁻¹ of mEGF, 100ngml⁻¹ of FGF 10 (Peprotech), 10nM Gastrin (Tocris) and 0.5mM Anaplastic lymphoma kinase (ALK)-inhibitor (A83-01, Tocris). Medium was replaced every 2–3d. Passaging of the cells was done every 5–6d by dissociation with TrypLE (Gibco) (4min at 37 °C) followed by reembedding in Matrigel. During the initial phases of culture after initial seeding or after passaging, 10µM Rho-associated, coiled-coil containing protein kinase (ROCK)-inhibitor (Y27632, Selleckchem) was added to the medium. During the first three passages, the medium was supplemented with Primocin.

Conditioned medium

Triple Wnt/R-Spondin/Noggin (WRN)-conditioned medium was produced using L-WRN cells (ATCC, CRL-3276) according to a modified version of a previously published protocol²⁸. In brief, L-WRN cells were grown until confluency in Advanced DMEM/F-12 medium supplemented with 10mM HEPES, 1× GlutaMax, 20% FBS and 50Uml⁻¹ of penicillin-streptomycin. After reaching confluency, medium was replaced and collected every 24h for 9d. Collections of three consecutive days were pooled and diluted 1:1 in fresh medium without

FBS (final FBS concentration: 10%), sterile filtered and stored at -20°C . Frozen aliquots were used within 4 months and kept at 4°C for a maximum of 1 week after thawing. Cell lines HEK293 used to produce Noggin, R-spondin and Wnt conditioned medium were acquired from the Hubrecht Institute (Utrecht, Netherlands).

Murine myofibroblast isolation and culture

IMCs were isolated from 6–13-week-old C57BL/6 mice following a previously published protocol, with few modifications²⁹. Briefly, the small intestine was prepared and used for intestinal crypt isolation as described in the corresponding section. Intestinal fragments were then washed and incubated in DMEM containing Collagenase IV (300Uml^{-1} , Invitrogen) and Dispase (0.08Uml^{-1} , Roche) for 30 min at 37°C in a shaking water bath. The supernatant was then collected, centrifuged at $280g$ for 5 min and resuspended in DMEM supplemented with 10% FBS, penicillin-streptomycin, L-glutamine, non-essential amino acids and insulin-transferrin-selenium (Invitrogen). Cells were then transferred to culture flasks and medium was changed after cell adhesion (4–5 h) and every 2 d after. Cells were split 1:2 as needed and used between passages 3 and 8.

Human small intestinal organoid culture

Human small intestinal organoids were provided by the laboratory of H. Clevers (Hubrecht Institute) within the framework of a collaboration agreement. Human small intestinal organoids were cultured in human ISC expansion medium composed of 50% L-WRN-conditioned medium, supplemented with $1\times$ B27 supplement (Gibco), $1\mu\text{M}$ N-acetylcysteine (Sigma-Aldrich), 50ngml^{-1} EGF (Peprotech), 500nM A83-01 (Tocris), 10nM gastrin (Sigma-Aldrich), 10mM nicotinamide (Sigma-Aldrich), $10\mu\text{M}$ SB202190 (Seleckchem), 10nM prostaglandin E2 (Tocris). Y-27632 ($10\mu\text{M}$, Seleckchem) was used in the first 48 hours after single-cell dissociation to prevent detachment-induced cell apoptosis. The medium was changed every two days and the expanding organoids were passaged every six to eight days by mechanical dissociation using a fire-polished glass Pasteur pipette. Organoids were used between passage number 10 and 20.

Cell lines

C2C12 cells (ATCC) were maintained in DMEM supplemented with 10% FBS, L-glutamine, sodium pyruvate, HEPES and penicillin-streptomycin (all from Invitrogen). HUVECs (Lonza) were maintained using EGM-2 Bulletkit medium (Lonza) and used until passage 10. To trigger

angiogenesis, VEGF (50ngml⁻¹ , R&D systems) was added. hMSCs (Lonza) were obtained as passage 1 cells and expanded up to passage 10 in α MEM supplemented with 10% FBS, 2mM GlutaMax, 100Uml⁻¹ of penicillin and 100 μ gml⁻¹ of streptomycin (all from Gibco) and human FGF2 (1ngml⁻¹ , Peprotech). Medium was changed every 2d for all cultures.

Bioprinting hardware

All 3D printing was performed on a custom-built extrusion-mode printer fabricated by combining a syringe pump (neMESYS, Cetoni) with either a Zeiss Axiovert 200M microscope or a Nikon Eclipse Ti inverted microscope. During the printing processes, the microscope controller was used to precisely control the positions, while the syringe pump was used to control the flow of the extruded cell suspension. For the nozzle, a PCR micropipette (Drummond) was pulled using a DMZ micropipette puller (Zeitz Instruments) using empirically defined settings for optimal printing. The pulled glass capillaries have a long conical taper that can be broken by carefully applying pressure on the tip at the desired position, obtaining the internal diameter needed for the printing of beads, cells or aggregates. The long taper ensures lower deformation of the surrounding environment when printing. Nozzle with internal diameters ranging from 20 to 200 μ m were fabricated depending on the needs, examined under a microscope to ensure a clear and homogeneous cut, treated with Sigmacote (Sigma-Aldrich) to prevent adhesion of the cells for a few minutes and dried for several hours. The glass capillary was then bended under a flame and connected to 1/16" polyetheretherketone tubing with a dual small hub RN coupler and RN compression fittings for glass capillary and polyetheretherketone tubing (all from Hamilton). The connector was arranged in between a polydimethylsiloxane (PDMS) slab and a glass slide to increase stability and an easy mounting part was fabricated using reverse moulding of the condenser in PDMS. The perfectly fitting PDMS block then allowed mounting of the nozzle in the field of view of the microscope by bonding of the PDMS with the glass slide holding the nozzle. The microscope heating/cooling system 'the cube' (Life Imaging Services) was used to maintain the environment at the desired temperature.

Bioprinting process

Hydrogel precursor preparation. For the hydrogel precursor mixture, a native bovine dermis collagen type I solution (5mgml⁻¹ , Kouken) was neutralized and reconstituted on ice with 10% v/v of 10 \times DMEM (Invitrogen), 8% Advanced DMEM/F12 medium, 2% v/v of sodium bicarbonate 0.5M to a 4mgml⁻¹ final solution. The collagen solution was mixed with ice-cold

Matrigel in the following ratios: 50% for beads, 50% for MSCs, 0–50% for experiments on matrix stiffness, 20% for intestinal, stomach and colon stem cells, 100% collagen for HUVECs.

Cell preparation.

Single-cell suspensions were prepared following established protocol for the different cell types. Briefly, IMCs, HUVECs, MSCs and C2C12 were washed with PBS and incubated with TripLE Express (Life Technologies) for 3–5min at 37 °C. Cells were then collected in a 15-ml Falcon tubes with culture medium containing 10% FBS and filtered through a 40- μ m strainer to avoid clogging of the nozzle by cell aggregates. Cells were centrifuged and resuspended in their respective medium supplemented with 1.5mM EDTA.

Stomach, intestinal and colon organoids were dissociated at 37 °C for 8min (mouse stomach and intestine) or 15–17min (human intestine, mouse and human colon) using TrypLE Express supplemented with DNase I (2,000Uml⁻¹ ; Roche), N-acetylcysteine (0.5mM) and Y27632 (10 μ M). Cells were also passed through a cell strainer and resuspended in ENR or WNR-conditioned medium supplemented with EDTA (2mM). For mouse colon stem cells, an extra 10% FBS was added. Cells were kept on ice until printing.

Cells were resuspended at concentrations ranging from 10⁷ to 10⁸ cells per ml to be used for printing.

For organoid printing, organoids were retrieved from the Matrigel 2d after having been seeded as single cells. Matrigel was mechanically disrupted using cold organoid basal medium, collected in a Falcon and centrifuged (200g, 4min, 4 °C). The supernatant was removed, and organoids were washed once more with cold basal medium. They were then incubated with Dispase (0.08Uml⁻¹) and Collagenase IV (10%), N-acetylcysteine (0.5mM) and Y27632 (10 μ M) at 37 °C for 5min. The organoids were then washed three times with basal medium and resuspended in ENR supplemented with EDTA.

Bioprinting.

Two small rectangular 2–3-mm-thick PDMS spacers were cut, sterilized with ethanol and placed on the bottom of 6- or 12-well plates to reduce the amount of hydrogel used for printing. The nozzle was washed for several minutes in ethanol and then rinse thoroughly with sterile water or PBS before printing. A droplet of cell suspension (5–10 μ l) was placed in an empty well before being aspirated by the nozzle at a volumetric flow rate of 50–100 μ ls⁻¹ . The ice-cold hydrogel was then added in between two PDMS blocks before starting to print. Cells were dispensed directly in the hydrogel by extrusion of the suspension at a volumetric flow rate of 15–100 μ ls⁻¹ depending on the cellular density and geometrical thickness desired. For hydrogels that are too liquid at low temperature (4 °C), the temperature can be controlled in the bioprinting periphery to obtain optimal viscosity. The user can print for 2–5min before the nozzle starts dragging the gelling hydrogel too much. Cellular density, flow rate and stage

speed can then be modulated depending on the construct to print. For example, the standard intestinal and gastrointestinal tubes were generated using a 90–100- μm nozzle diameter, a cell density of 50million cells per ml, a flow rate of 35nl s^{-1} and a temperature of 25–32 °C. For multiple cell printing, sequential aspirations and depositions were used depending of the printing (gradient or separate prints). Tissue geometries were printed directly by the user controlling the stage while looking through the microscope. The embedded construct was incubated for 10min at 37 °C to finalize crosslinking before adding the medium with the intended growth factors. For intestinal, stomach and colon stem cells the Rock inhibitor Thiazovivin (2.5 μM) was added to the medium for the first 2d to prevent anoikis.

Epithelial tubes were cultured using the following medium: mouse intestine (organoid basal medium+mEGF, Noggin, R-spondin), stomach (WNR-conditioned medium+B27, N-acetylcysteine, Gastrin, mEGF, FGF10 and A83-01), colon (WNR-conditioned medium+mEGF and Primocin), coculture of stomach and intestine (WNR-conditioned medium+Gastrin, mEGF and FGF10) and coculture of intestine and colon (WNR-conditioned medium+mEGF and Primocin), human intestine expansion medium (EGF, 10% Noggin-conditioned medium, 25% R-Spondin-conditioned medium, 50% Wnt3a-conditioned medium, nicotinamide, gastrin, A83-01, SB202190, prostaglandin E2), human intestine differentiation medium (EGF, 10% Noggin-conditioned medium, 25% R-Spondin-conditioned medium, gastrin, A83-01), using the same concentration as described above. Medium was changed every two days for all cultures.

Matrix degradation.

Collagenase type IV was diluted at 5mgml $^{-1}$ (1,450Uml $^{-1}$) directly into the relevant medium before being used as a 10 \times concentrated solution that could be directly added to the wells of the printed constructs. The printouts were treated with collagenase for 12min, washed twice with PBS and put back in their growth medium.

Temporal deposition.

Printed intestinal constructs were put back under the microscope coupled to the bioprinter with temperature controlled at 37 °C. A droplet of IMCs (0.5 $\times 10^8$ cells per ml) was then deposited on an adjacent well and aspirated. The user can navigate the previous printouts and deposit cells inside the hydrogel by looking into the microscope and manually adjusting the height of the nozzle. Dots of IMCs were patterned by lifting the nozzle and punching through the hydrogel before deposition. A programmed syringe push allowed the deposition of a similar number of cells for every injection. Of note, the hydrogel was locally disrupted by the nozzle, but did not preclude cellular deposition if cellular density was high enough.

Cell viability measurements

C2C12 and HUVECs were printed according to the protocol described above. For qualitative imaging, the constructs were then incubated with calcein AM (4mM) and Ethidium homodimer-1 (2mM) for 30–40min following the live/dead kit instructions (Thermo Fisher Scientific). Incubation was done on different printouts at different time points with 30min incubation in saponin (0.3%) for positive staining of dead cells. Pictures were taken after washing twice with PBS. For quantitative imaging, constructs were stained with Hoechst 33342 (5 µgml⁻¹, Thermo Fisher Scientific) and Ethidium homodimer-1 (2mM, Thermo Fisher Scientific), because calcein AM did not allow to distinguish single cells after considerable remodelling and thus hindered precise cell counting. Three different printing experiments (n=3) were performed for each cell line and time point (immediately after printing, and after 24h).

Multiple cell printing using cell trackers

C2C12 cells were incubated with calcein AM, Cell tracker deep red dye or Cell tracker blue dye (all from Thermo Fisher Scientific) following the manufacturer's protocols. Cell tracker blue was used at a final concentration of 10µM, whereas deep red cell tracker was diluted to a final concentration of 1µM and calcein AM was used at 4mM. Cells were washed and incubated with their respective cell trackers during 30min at 37 °C, then dissociated and prepared for printing as detailed before. Pictures were taken after ECM gelation and medium addition.

Forskolin and carbamylcholine treatment

Tubes with crypt structures (days 6–8) were treated with forskolin (20µM, Selleckchem), carbamylcholine (100 µM, Sigma) or dimethylsulfoxide (Thermo Fisher Scientific).

Immunofluorescence staining

Printed constructs were rinsed twice with PBS and fixed with 4% paraformaldehyde (Thermo Fisher Scientific) in PBS for 25min at room temperature. Following fixation, tissues were transferred onto glass slides with a homemade PDMS spacer and permeabilized with 0.2% Triton X-100 in PBS for 1h at room temperature. They were then blocked with 10% goat serum in PBS containing 0.01% Triton X-100 for 3h at room temperature. The samples were then incubated for 36h at 4°C with the primary antibody diluted in blocking buffer against lysozyme (1:50; Thermo Fisher Scientific), L-FABP (1:50; Santa Cruz) or Sox9 (1:50; Abcam) for intestinal tubes, CD31 (1:200; Cell Signalling Tech) for vascular tubes and alpha smooth muscle actin (1:100; Agilent) for IMCs. After washing for 3–5h at room temperature, samples

were incubated overnight at 4°C with secondary antibody Alexa 647 donkey- α -rabbit (1:500 in blocking solution; Invitrogen) or Alexa 647 donkey- α -mouse (1:500 in blocking solution; Invitrogen), DAPI (1:2,000) and phalloidin-Alexa 488 (1:200; Invitrogen). After at least 3h of washing, samples were mounted in fluoromount-G (Thermo Fisher Scientific) before imaging. Proliferative cells were stained with a Click-iT EdU Alexa Fluor 647 imaging kit (Thermo Fisher Scientific) following the manufacturer's instructions.

Microscopy and image processing

Bright-field and fluorescent (mT, green fluorescent protein (GFP), dsRED, viability dye, cell trackers) images of printouts were taken using a Nikon Eclipse Ti inverted microscope system equipped with a $\times 4/0.20$ numerical aperture (NA), $\times 10/0.30$ NA and $\times 20/0.45$ NA air objectives; 395-, 470-, 555- and 632-nm filters and controlled by NIS software or a Leica SP8 system equipped with a $\times 10/0.30$ NA air objective, a $\times 25/0.95$ NA water objective, a 440-nm pulsed laser (40MHz–312.5 kHz) as well as a Supercontinuum White Light Laser (80–10MHz+Manual) controlled by LEICA LAS-X software. Fixed samples were imaged with an inverted confocal microscope (INVERT Zeiss Axio Observer Z1) equipped with $\times 10/0.30$ NA and $\times 20/0.80$ NA air objectives; 405-, 488- and 555-nm lasers and controlled by ZEN 2009 imaging software (Zeiss). Image processing was performed using Fiji/ImageJ (NIH) and further processed using Photoshop CC (Adobe) using only standard contrast and intensity level adjustments. Animated videos were rendered using Premiere Pro (Adobe).

Tube diameter analysis

A tiled image of the tube was taken with stored position for imaging on multiple days. Image analysis was carried out using the following pipeline in Fiji. Images of the same tubes at different time points were stacked and registered using the StackReg plugin (Rigid Body). Then a segmented line with a width larger than the tube was drawn along the tube and used to straighten it. This line was saved and used for each image of the stack, which were further processed independently. Each image was filtered using Subtract Background. An automatic threshold was applied to the image and it was converted to mask and holes were filled if required. The plugin Local Thickness was run on this mask. Eventually, a horizontal line separating the image exactly in the middle was drawn and the profile of the tube along that line was measured and saved.

Statistics

Graphs and statistical analysis were made in GraphPad Prism. For the influence of cell density on tube diameter, a one-way analysis of variance (ANOVA) with Tukey's multiple comparisons test was performed, comparing the mean diameter of tubes at day 6 after printing. The experiment was repeated three times, each with two tubes per density and values were averaged per experiment before being compared. Test details were as follows: 50×10⁶ cells per ml versus 25×10⁶ cells per ml, $q=8.555$ d.f.=6; 50×10⁶ cells per ml versus 12.5×10⁶ cells per ml, $q=15.3$ d.f.=6 and 25×10⁶ cells per ml versus 12.5×10⁶ cells per ml, $q=6.745$ d.f.=6. For forskolin-induced swelling, a repeated measures two-way ANOVA with Tukey's multiple comparisons test was performed, comparing the increase in tube diameter for the control and for the treated condition between before and 1h after the treatment. Tubes were used 8d after printing and from three different experiments, each with one control and two treated tubes. For the treated condition, values were averaged per experiment before being compared. Test details are as follows. For the control sample: before treatment versus 1h after treatment, $q=2.887$ d.f.=2; before treatment versus 2h after treatment, $q=4.862$ d.f.=2 and 1h after treatment versus 2h after treatment, $q=2.111$, d.f.=2. For the treated sample: before treatment versus 1h after treatment, $q=72.77$ d.f.=2; before treatment versus 2h after treatment $q=16.86$ d.f.=2 and 1h after treatment versus 2h after treatment $q=1.075$ d.f.=2. For the evolution of the tube diameter over 3weeks, the mean and the standard deviation of the diameter as well as the length were plotted for each tube.

Histology

Samples were prepared together with the EPFL Histology Core Facility in accordance with their standard procedures. Briefly, samples were fixed in 4% paraformaldehyde overnight at 4 °C and washed three times with PBS. Fixed samples were placed on an even surface and covered by HistoGel (Thermo Fisher Scientific) previously heated to 50 °C. The sample was then cooled before being embedded in paraffin as standard protocol. Sectioning was done on a Leica cryostat CM3050S at -30 °C. For staining, the 10- μ m sections were either immersed in Alcian Blue pH2.5 solution for 25min and counterstained with Nuclear Fast Red, or immersed in Hematoxylin Eosin solution. Samples were then dehydrated and mounted with xylene-based glue. Sections were imaged on a LEICA DM 5500 microscope, DMC 2900 Color camera. Image processing was made in ImageJ (NIH).

Transmission electron microscopy

Samples were chemically fixed in a buffered mix of 2.5% glutaraldehyde and 2.0% paraformaldehyde in 0.1M phosphate buffer (pH7.4), and left for 4h. Then samples were washed thoroughly with cacodylate buffer (0.1M, pH7.4), postfixed for 40min in 1.0% osmium tetroxide with 1.5% potassium ferrocyanide, followed by 40min in 1.0% osmium tetroxide alone. They were finally stained for 30min in 1% uranyl acetate in water before being dehydrated through increasing concentrations of alcohol and then embedded in Durcupan ACM (Fluka) resin. The samples were then placed in moulds and the resin polymerized at 65 °C for 24h. Thin sections of 50-nm thicknesses were cut with a diamond knife, and collected onto single slot copper grids with a pioloform support film. Sections were contrasted with lead citrate and uranyl acetate, and images taken with a transmission electron microscope at 80 kV (Tecnai Spirit, FEI Company with Eagle CCD camera).

Perfusion setup

Sterile scissors were used to create two clear cuts at the extremities of the intestinal tubes. The intestinal tubes were then placed under the microscope with the bioprinter and kept at 37 °C and 5% CO₂ during the perfusion process. The perfusion nozzle was prepared such as the printing nozzle but was made smaller (~50 µm) and bent in a Z shape. This nozzle was mounted on the bioprinter and inserted inside the intestinal tubes using the manually controlled stage. Perfusion was controlled by a house-made LabVIEW (National Instruments) interface linked to neMESYS software (Cetoni). For endothelial tubes, a glass nozzle (tip, 30µm) was mounted on a mouth pipetting device and the perfusion process controlled by hand. Then 2,000-kDa of luorescein isothiocyanate dextran (Invitrogen) or 0.1µm of red fluorescent beads (Invitrogen) diluted in cell culture medium were injected.

Real-time quantitative PCR (qPCR)

Stomach and intestinal organoids in Matrigel were collected using the RLT buffer from the RNeasy Micro Kit (Qiagen) supplemented with 40mM dithiothreitol (Sigma). Tubes printed in Matrigel collagen mix were collected according to the following protocol: one wash with cold organoid medium, 3min incubation at 37 °C with 200µl Collagenase IV (300Uml⁻¹), one wash with PBS 1× and RLT buffer supplemented with dithiothreitol. The lysates were then kept at -80 °C until further processing. The RNA extraction was performed using a RNeasy Micro Kit and complementary

Online content

Any methods, additional references, Nature Research reporting summaries, source data, extended data, supplementary information, acknowledgements, peer review information; details of author contributions and competing interests; and statements of data and code availability are available at <https://doi.org/10.1038/s41563-020-00803-5>.

Conclusion

Conclusion and outlook

This thesis work presents the application of bioengineering approaches to generate functional organoid models across scales.

The development of organoids from many different tissues and organs revolutionized fundamental research in the field of stem cell biology, and organoids also started to reveal their translational potential, for example for personalized medicine. However, organoids present several inherent limitations. These are either due to our still uncomplete understanding of and inability to recapitulate the biological processes leading to tissue and organ development, or due to the absence of the guiding environment that cells would encounter *in vivo*. In both cases, bioengineering approaches can help overcome these issues. This can be done either 1) by disturbing native biological processes and studying the consequences of these perturbations, 2) by trying to create simplified models of the tissue or organ, therefore leading to the understanding of the minimal requirements for its functionality, or 3) by providing external cues to guide biological processes such as tissue/organ development or to recapitulate multi-tissue interactions *ex vivo*.

In chapter I, we used bioengineering approaches at the cellular level to generate cells responsive to light. We relied on lentiviral vectors encoding a two-step inducible (drug and blue light) optogenetic system controlling the expression of Cre recombinase. We used light responsiveness to control the induction of cancer driver mutations in space and time in *Apc^{fl/fl};Kras^{LSL-G12D/+};Trp53^{fl/f}* (AKP) colon organoids. We also leveraged a colon-on-a-chip platform to obtain a defined topology compatible with long-term culture and imaging of the colon organoids. This model allowed us to gain insights into tumor initiation and development processes, which cannot be well studied with either standard organoid or animal models. This is mostly because organoids cannot be cultured without passaging for long enough¹ and critically do not allow the formation of pathophysiologically relevant tumors, or because while tumors are observable in mice for example with bioluminescence methods, these do not provide high enough resolution to study initial tumor development². More specifically, we showed that our model recapitulated *in vivo*-like responses to microbiota metabolites and could be used to test new tumor-suppressive drugs, here exemplified with Tiopronin, an inhibitor of glutathione peroxidases. This model thus provides an interesting animal-free alternative for functional studies. Overall, our work demonstrated the potential of combining bioengineering approaches, here at the cellular level, and organoids or organoid-on-a-chip.

In chapter II, I developed a new model from one of the few remaining organs were bona-fide organoids did not exist yet. I capitalized on the knowledge gained from other endoderm-derived cell types, and generated thymic epithelial organoids. I characterized these organoids and

compared them to standard 2D cultures of thymic epithelial cells, which lose their ability to mediate thymopoiesis. Since thymic epithelial organoids were more closely resembling *in vivo* TECs than 2D-cultured TECs, I probed their ability to mediate T cell development by reaggregating them with T cell progenitors. These experiments proved the capacity of thymic epithelial organoid-derived cells to educate T cells in a way reminiscent of the native thymus. Finally, we grafted the reagggregates in mice and showed their ability to attract new T cell progenitors, thus mimicking another crucial feature of the native thymus. This work demonstrated for the first time that sorted individual TECs cultured independently of other cell types can maintain their functionality *in vitro*. In general, this chapter tried to bridge the gap between the fields of organoids and immunology, an interface that remains relatively poorly explored.

In chapter III, we stepped into the macroscopic world and developed a new bioprinting approach to generate larger tissue constructs compared to classical organoids. We modified a microscope with a motorized stage into an extrusion printer by coupling it to a syringe-pump system and a printing nozzle. This easy-to-use printing setup presents the advantage of allowing real-time visual control and modulation of the printing process. We printed single cell suspensions obtained from organoids directly in classical organoid matrices such as Matrigel and collagen hydrogels. Using a cell-only bioink and matrices with relatively well-known properties and effects on the cells simplified the technology development process and ensured high viability of the printed tissues. The printed cells self-organized into tissues recapitulating certain aspects of their *in vivo* counterparts. We generated centimeter-scale tissues with multiple cell types, for example an intestinal tube with supportive cells such as fibroblasts and endothelial cells. We also printed sequentially different cells of the gastrointestinal tract, generating a construct with stomach and intestine or intestine and colon cells and mimicking organ boundaries. Finally, we tested the functionality of the printed tissues by monitoring their response to different stimuli, for example to Forskolin, a drug inducing swelling in a CFTR-dependent manner and used to assess drug responses among cystic fibrosis patients³. This part demonstrated the potential of using bioengineering approaches such as bioprinting to guide tissue shape and organization at a macroscopic level, here in combination with organoid-derived stem cells.

For each of the chapters, there are obvious next steps that should be taken. In chapter I, an improvement in resolution to be able to target and induce mutations truly at the single cell level would be very interesting, as it would allow to follow tumor development from one single mutated cell. Further work is however required to be able to precisely target light to one particular cell in the organoid-on-a-chip, but advances in multiphoton stimulation methods seem promising strategies^{4,5}. In chapter II, the long-term ability of thymic epithelial cells

cultured as organoids to mediate thymopoiesis still poses a challenge. Using single-cell omics techniques to study pathways involved in the crosstalk between TECs and other cell types might identify candidates to optimize the culture conditions. In preliminary work, I leveraged a microwell platform⁶ allowing the formation of reproducible, miniature and easily imageable organoids to perform a small screen. By testing the influence of different growth factors on TECs, I noticed for example that the TGF β inhibitor A83-01 led to organoids growing larger over time. This is in accordance with previous results indicating that TGF β inhibition supports the proliferation of epithelial progenitors *in vitro*⁷. Beside soluble signals, the ECM is also important to support cells. Contrary to many organs, ECM atlases do not incorporate the thymus⁸, and current knowledge about thymic ECM composition is mostly based on immunostaining and histology. To remedy this, I performed an in-depth characterization of embryonic, neonatal, young and old adult thymi by liquid chromatography coupled to tandem mass spectrometry. While providing insights into the ECM composition and how it changes over time, until now these data could not be translated into an improvement of TEC cultures. Therefore, future work will be needed to identify the growth factors and matrix composition required to maintain TEC functionality in the long term. In chapter III, further developing the printing setup to be able to generate more complex forms resembling other organs would be of interest. Another improvement would be to optimize the matrix to be able to control precise gelation upon cell deposition. Synthetic matrices, such as the ones based on polyethylene glycol (PEG) hydrogels functionalized with ECM molecules^{9,10} might present interesting possibilities for a tighter control over gel properties. More work will however be required to optimize these synthetic hydrogels to reflect the permissive and self-healing properties of Matrigel and other natural ECMs.

As a general limitation, while this thesis work presents several interesting new insights, it has the inconvenient of mostly involving mouse cells. This is at least partially explained by the fact that for most organs, murine organoids were developed first. Culture conditions for murine organoids are also better defined in many cases, because mouse biology is better understood than human biology thanks to animal studies, or simply because mouse cells require less complex culture conditions¹¹. The more robust culture conditions and organoid development process obtained with mouse cells facilitate their combination with bioengineering approaches. In addition, many genetically engineered mouse models already exist, here exemplified by the inducible AKP cells. Ethical constraints and rules are also less severe when working with mouse cells. Moreover, obtaining patient-derived samples is very complicated for some internal organs such as the thymus, even more so as it involutes early in life.

However, despite the fact that mouse models have been and can still be very useful to study human biology, there are also differences in certain processes that require specific models

involving human cells. Focusing on organoids, they can be derived from human tissue-resident or from pluripotent stem cells. Luckily, in some cases culture conditions established for mouse cells can be relatively well translated to human cells, generally with some additions. This is true for example for human colonic organoids, as adding inhibitors of TGF β (A83-01) and of p38 (SB202190) pathways to the classical Wnt, Noggin, R-spondin and EGF used with mouse cells is sufficient for their growth¹¹. However, even when culture conditions are relatively well established, human organoids might lack certain cell types or not recapitulate their native organ patterning as faithfully as murine organoids¹², complicating their integration with bioengineering approaches.

In addition to healthy human organoids, cancer organoids can also be grown. They are derived from surgically resected specimens, biopsies, or circulating cancer cells^{13,14}. Some on-going work in our lab uses a similar colon-on-a-chip approach as we did in Chapter I with patient-derived colorectal cancer organoids. While this model and organoids in general are great to study patient-specific features of the disease, they do not allow to study cancer initiation and to follow tumor development. Moreover, patient-derived samples often contain only healthy or only mutated tissue, but not both. Therefore, an alternative approach is to engineer mutations in healthy human colon organoids¹⁵ to be able to study cancer initiation and progression. Genetic engineering is most of the time done by CRISPR-Cas9. During the revisions of this work, we used this technique to knockout *Gpx2* in AKP organoids, and could thus apply a similar approach to mutate human cells in the future. Human inducible colorectal cancer organoids could then be cultured long term in our chip platform, as we did here for mouse AKP organoids, and allow to study in real time what happens between the appearance of oncogenic mutations and tumor formation.

Another current focus in the cancer field is the tumor microenvironment and its influence on tumor development¹⁶. While cancer organoids often only mimic the epithelial compartment, tumors usually contain fibroblasts, immune cells and vasculature. Traditional approaches to study the influence of the environment rely on patient-derived xenograft models. However, there is more and more pressure to reduce animal use¹⁶. Therefore, integrating tumor microenvironment cells to our colon-on-a-chip platform is an interesting alternative. In a proof-of-concept, we already cultured mouse tumor-derived fibroblasts with AKP organoids in the chip, and work with human tumor and microenvironment cells is also on-going in the lab. Overall, this model hopefully will allow to test different drugs in vitro, and to assess not only their effect on cancer cells, but how tumor microenvironment modulates it and how the healthy tissue is adversely affected.

In chapter II, I developed a new type of organoids to try to overcome one of the main limitations in the field, namely the fact that thymic epithelial cells lose their functional ability to mediate T

cell development when cultured independently of other cells types and of a complex 3D environment. I hope that once conditions maintaining TEC functionality in the long term have been identified, they could be translated to human thymic epithelial organoids. It would indeed be extremely useful to grow human TECs able to select human T cells in a native-like fashion. Currently, the most common strategies to mediate T cell development in vitro try to completely circumvent the use of TECs and rely on stromal cell lines (e.g. OP9 and MS5) engineered to express Notch ligands. However, the extent to which stromal cell lines are able to mediate either positive selection or negative selection is controversial. They cannot process peptides in the same way as cTECs do to mediate positive selection. In addition, they do not express MHCII, leading to a bias towards the development of CD8+ T cells¹⁷. Stromal cells lines are also unable to perform promiscuous gene expression, and thus cannot mediate negative selection against tissue-restricted antigens¹⁸. In any case, OP9 and MS5 being murine cell lines, selection processes are based on murine peptides and MHC, and their use for the maturation of human hematopoietic progenitor cells would lead to functionless and autoreactive cells if they were to be transplanted to humans. Engineered beads and plates have been used to replace stromal cells, but also lack the ability to mediate selection processes^{19,20}. To overcome this issue, research in the field follows two strategies. The first one is to generate immature T cell precursors, and let them undergo positive and negative selection in the host thymus²¹. The second is based on engineering a specific TCR known to be compatible with the patient and to be reacting against a certain target antigen²². However, none of these solutions allows to obtain in vitro a T cell repertoire that is both diverse and self-tolerant.

Alternatively, TECs could be derived from pluripotent stem cells. This would provide the additional advantage of permitting the obtention of patient-specific cells. Indeed, even if thymic epithelial organoid lines could be grown from tissue-resident stem cells²³, there would still be an HLA mismatch if they would be used to select T cells obtained from another donor. Up to now however, differentiating TECs from pluripotent stem cells remains challenging and often does not pass the TEPCs stage without transplantation in mice. Nevertheless, taking advantage of the crosstalk with other cell types and of a 3D architecture, a very recent study seems to have found a way to obtain mature TECs able to perform T cell maturation in vitro²⁴. Hopefully this work will be followed and allow the expansion of the use of pluripotent stem cell-derived TECs and their clinical application. Indeed, regenerating the thymus is of high interest, not only in ageing conditions, but also after immunological insults²⁵. Regarding this, one personal curiosity that I would like to address is to understand if the loss of TEC functionality observed in culture actually mimics what is happening during thymic involution but in a much faster way²⁶.

In Chapter III, it is evident that in order to create organoid-derived tissues suitable for transplantation, the starting point must be human cells. We performed a proof-of-concept using human intestinal and colon organoids as well as human mesenchymal cells. Even though we could generate centimeter-scale tissue constructs, this is still far from the real size of human organs. Current printing approaches already applied in the clinics work relatively well for tissues such as cartilage and bones^{27,28}. However, their use for tissues with higher vascularization and cell type complexity remains challenging. Therefore, one of the main needs in the field is to develop robust ways to integrate vasculature. There is promising research underway for organoids^{29,30}, and hopefully more strategies applicable to larger tissues will also arise soon. The development of a bioprinting method that would allow the integration of multiple cell types with high viability and would generate organ-size constructs is not for tomorrow³¹. However, it is interesting to note the potential of leveraging the natural properties of cells instead of capitalizing solely on engineering approaches.

Overall, I believe that many future scientific developments will be at the interface between different domains, such as here biology and engineering, and that the next generation of functional organoid models will accelerate the revolution happening in the fields of cell therapy, regenerative medicine, in vitro diagnostics and drug discovery¹.

References

1. Zhao, Z. *et al.* Organoids. *Nat. Rev. Methods Prim.* **2**, (2022).
2. Cosette, J. *et al.* Bioluminescence-based tumor quantification method for monitoring tumor progression and treatment effects in mouse lymphoma models. *J. Vis. Exp.* **2016**, 1–9 (2016).
3. Boj, S. F. *et al.* Forskolin-induced Swelling in Intestinal Organoids : An In Vitro Assay for Assessing Drug Response in Cystic Fibrosis Patients. 1–12 (2017). doi:10.3791/55159
4. Shemesh, O. A. *et al.* Temporally precise single-cell-resolution optogenetics. *Nat. Neurosci.* **20**, 1796–1806 (2017).
5. Adesnik, H. & Abdeladim, L. Probing neural codes with two-photon holographic optogenetics. *Nat. Neurosci.* **24**, 1356–1366 (2021).
6. Brandenburg, N. *et al.* High-throughput automated organoid culture via stem-cell aggregation in microcavity arrays. *Nat. Biomed. Eng.* **4**, 863–874 (2020).
7. Suzuki, D., Pinto, F. & Senoo, M. Inhibition of TGF- β signaling supports high proliferative potential of diverse p63+ mouse epithelial progenitor cells in vitro. *Sci. Rep.* **7**, 1–14 (2017).
8. McCabe, M. C., Saviola, A. J. & Hansen, K. C. A mass spectrometry-based atlas of extracellular matrix proteins across 25 mouse organs. (2022).
9. Gjorevski, N. *et al.* Designer matrices for intestinal stem cell and organoid culture. *Nature* **539**, 560–564 (2016).
10. Chrisnandy, A., Blondel, D., Rezakhani, S., Broguiere, N. & Lutolf, M. P. Synthetic dynamic hydrogels promote degradation-independent in vitro organogenesis. **21**, (2022).
11. Kim, J., Koo, B.-K. & Knoblich, J. A. Human organoids: model systems for human biology and medicine. *Nat. Rev. Mol. Cell Biol.* **21**, 571–584 (2020).
12. He, G. *et al.* Optimized human intestinal organoid model reveals interleukin-22-dependency of paneth cell formation II II Optimized human intestinal organoid model reveals interleukin-22-dependency of paneth cell formation. *Cell Stem Cell* **29**, 1333–1345 (2022).
13. Fujii, M. *et al.* A Colorectal Tumor Organoid Library Demonstrates Progressive Loss of Niche Factor Requirements during Tumorigenesis. *Cell Stem Cell* **18**, 827–838 (2016).
14. Bose, S., Clevers, H. & Shen, X. Promises and challenges of organoid-guided precision medicine. *Med* **2**, 1011–1026 (2021).
15. Drost, J. *et al.* Sequential cancer mutations in cultured human intestinal stem cells. *Nature* **521**, 43–47 (2015).
16. LeSavage, B. L., Suhar, R. A., Broguiere, N., Lutolf, M. P. & Heilshorn, S. C. Next-generation cancer organoids. *Nat. Mater.* **21**, 143–159 (2022).
17. Bird, L. From stem cell to T cell in vitro. *Nat. Rev. Immunol.* **4**, 320 (2004).
18. Montel-Hagen, A. *et al.* In Vitro Recapitulation of Murine Thymopoiesis from Single Hematopoietic Stem Cells. *Cell Rep.* **33**, 108320 (2020).
19. Trotman-Grant, A. C. *et al.* DL4- μ beads induce T cell lineage differentiation from stem cells in a stromal cell-free system. *Nat. Commun.* **12**, 1–11 (2021).
20. Reimann, C. *et al.* Human T-lymphoid progenitors generated in a feeder-cell-free delta-like-4 culture system promote T cell reconstitution in NOD/SCID/ γ c-/- mice. *Stem Cells* **30**, 1771–1780 (2012).
21. Singh, J. & Zúñiga-Pflücker, J. C. Producing proT cells to promote immunotherapies. *Int. Immunol.* **30**, 541–550 (2018).
22. Montel-Hagen, A. *et al.* Organoid-Induced Differentiation of Conventional T Cells from Human Pluripotent Stem Cells. *Cell Stem Cell* **24**, 376–389.e8 (2019).
23. Ragazzini, R. *et al.* Defining the identity and the niches of epithelial stem cells with highly pleiotropic multilineage potency in the human thymus. *Dev. Cell* 1–19 (2023). doi:10.1016/j.devcel.2023.08.017
24. Ramos, S. A. *et al.* Generation of functional thymic organoids from human pluripotent

- stem cells. *Stem cell reports* **18**, 829–840 (2023).
25. Velardi, E., Tsai, J. J. & van den Brink, M. R. M. T cell regeneration after immunological injury. *Nat. Rev. Immunol.* **21**, 277–291 (2021).
 26. Hale, L. P. *et al.* T cell-depleted cultured pediatric thymus tissue as a model for some aspects of human age-related thymus involution. *GeroScience* **43**, 1369–1382 (2021).
 27. Zhang, Q. *et al.* 3D printing method for bone tissue engineering scaffold. *Med. Nov. Technol. Devices* **17**, 100205 (2023).
 28. Onderková, A. & Kalaskar, D. M. Bioprinting 3D bioprinting for auricular reconstruction : A review and future perspectives. *International J. Bioprinting* **X**, (2023).
 29. Grebenyuk, S. & Ranga, A. Engineering organoid vascularization. *Front. Bioeng. Biotechnol.* **7**, 1–12 (2019).
 30. Zhao, X. *et al.* Review on the Vascularization of Organoids and Organoids-on-a-Chip. *Front. Bioeng. Biotechnol.* **9**, 1–10 (2021).
 31. Jo, Y., Hwang, D. G., Kim, M., Yong, U. & Jang, J. Bioprinting-assisted tissue assembly to generate organ substitutes at scale. *Trends Biotechnol.* **41**, 93–105 (2023).

Acknowledgements

My deepest gratitude goes to everyone who contributed, from closer or further, to this adventure. This thesis would not have existed without you, thank you.

First, I would like to thank my thesis director Prof. Matthias Lütolf. Thank you for giving me the opportunity to join your laboratory. Thank you for your support and continuous motivation, for the freedom to explore different projects in a truly multidisciplinary environment, and for your contagious enthusiasm about new discoveries.

Secondly, I thank very much my thesis committee, Prof. Li Tang, Prof. Marcel Van den Brink, and Dr Jennifer Cowan. Thank you for your involvement in the work. Receiving feedback from world experts is an incredible opportunity, and discussions during ThymOz were extremely helpful to finalize the thymus project. Thank you as well for your presence during the thesis defense, it was very interesting and nice.

Thank you very much also to Prof. David Suter, for agreeing to preside the defense and for your support and scientific advises.

Prof. Freddy Radtke, Prof. Selman Sakar and Dr Loïc Dayon, thank you as well for your involvement in my candidacy proposal and annual reports.

Thirdly, I would like to thank all the collaborators of the Syn-Thy project. With you I learnt so much, and your feedbacks during my entire PhD were extremely valuable. In particular, thanks to Prof. C. Clare Blackburn for welcoming me in your lab at the very beginning and sharing your passion about the thymus. Thanks to Paul Rouse for everything you taught me and for the nice time spent together in Scotland. Thanks also to Joanna Sweetman and to Tim Henderson. Special thanks to Viktoria Major for an unforgettable conference in Australia. Thanks to Prof. Georg Holländer for interesting discussions and collaborations. Thanks to Dr Thomas Barthlott for the experiments done together in Basel and for your support. Thanks to Prof. Graham Anderson for your extremely valuable inputs.

This work could not have been done without the help of the EPFL core facilities. In particular, thanks to the flow cytometry facility team, Dr Miguel Garcia, Valérie Glütz, Francesco Palumbo and André Mozes. Thanks to the histology facility staff, Dr Jessica Dessimoz, Agnès Hautier, Gian-Filippo Mancini and Nathalie Müller. Thanks to the Phenogenomics center, in particular to Julie Parchet-Piccand, Sonia Verp and Arnaud Legay as well as Khaled El Khwildy and Christine Di Natale. Thanks also to the BioImaging and Optics platform and to the Gene expression core facility.

Thanks to everyone who contributed to my scientific adventures before the PhD. In particular thanks to Dr Gernot Neumayer, Prof. Marius Wernig, Dr Moritz Mall, Sarah Grieder, Dr. Daniel Strebinger, Prof. David Suter, Dr Bianca Silva, Prof. Johannes Gräff and Dr Charles Baur.

Thanks to all LSCB members for the great fun and amazing time spent in and outside the lab together. I could not have dreamt of a better place to do a PhD. Thanks to my past desk neighbors Saba and Delphine for your support and laughs. Thanks to Sonja, Andrea and Giuliana for your scientific inputs as well as for the great time spent together even since you left the lab. Also thanks to Aleks for all the nice moments together. Thanks to Mehmet and François for the great atmosphere in the lab at the beginning of my PhD. Thanks to JiSoo and Stefano for your kindness. Thanks to Olga for sharing this PhD adventure. Thanks to Mike for the bioprinting work done together. Thanks to Nicolas and Hwanseok for the karaoke evenings. Thanks to Ian, DJ, Sophia and Nikita for the interesting discussions. Thanks to Yann, Jakob and Hao-An for being an amazing new generation of PhD students. Thanks also to Nathalie and Sylke for your friendship and support. Thanks to Lucie, Julia and Stefanie for making this lab such a good working place. Thanks to Jonathan for teaching me what you knew about organoids at the very beginning and for involving me in the bioprinting work. Thanks to Fran for sharing the tumor initiation project with me, for your invaluable inputs and all the nice moments spent together.

To Antonius, Bilge and Moritz, you are indissociable from this PhD work; it simply would not have been possible without you. Heartfelt thanks for your continuous support, inspiration, and most importantly for all the great fun together. I will forever remember these years spent with you and I really hope that not too much will change after we all graduated.

To Juliane, Feli, and also to Suzane, your support was invaluable during the years of this PhD, thank you.

To my friends from the Bachelor studies, Alessandro, Thaïs, Delphine, Melanie and Alexandra. We started the biology endeavor together, and your support was very important. I'm extremely grateful to count you as friends since then.

To my volleyball friends, thanks for being still a team after all these years and for all the nice moments spent together on and off the court since then. Thank you Leticia, Magali, Cindy, Marie and Diane. Special thanks to Fabienne, for being this incredible friend who brings us together most of the time. Special thanks also to Ariane, for being like a sister and for the gift of making me the godmother of your son.

To Carolane for being there since all these years, for knowing me so well and staying by my side, your friendship is invaluable, thank you.

To Alex, thank you for being who you are. No words can describe everything you give me.

Finally, thank you to the bottom of my heart to my family.

To Lauriane et Florian, thank you for the endless support and for the fun times spent together. Especially thank you for the Island trip, it will forever stay in my memories and was a most welcome break during this PhD.

To my mum and dad, thank you for offering me an amazing environment to grow and develop my passions, for giving me the opportunity to study what I wanted to and for supporting me continuously since the beginning. To you I dedicate this thesis.

Curriculum Vitae

Tania Hübscher

Current address: Route du Lac 14, 1026 Denges, Switzerland

Phone number: +41 79 126 49 65

Email address: tania.hubscher@gmail.com

Nationality: Swiss

Education

PhD in Biotechnology and Bioengineering Program (EDBB) 2018-2023

Laboratory of Stem Cell Bioengineering (LSCB), Prof. Matthias Lütolf

École Polytechnique Fédérale de Lausanne, EPFL, Switzerland

PhD Thesis title: Bioengineering functional organoid models across scales

Master's in Life Sciences and technology, orientation Neurosciences and 2014-2017

Neuroengineering

École Polytechnique Fédérale de Lausanne, EPFL, Switzerland

Thesis work carried out at Stanford university

Wernig Laboratory, Prof. Marius Wernig

Master thesis title: Shedding light on the formation of induced neuronal cells

Mention of excellence

Bachelor of Science in Biology 2011-2014

Université de Neuchâtel, UNINE, Switzerland 2011-2014

Magma Cum Laude, best student of the promotion and Jean Landry award

Maturité Fédérale

Lycée Jean Piaget, Neuchâtel, Switzerland

2008-2011

Cum Laude

Publications

Adam E. Handel et al. Developmental dynamics of the neural crest–mesenchymal axis in creating the thymic microenvironment. *Sci. Adv.* 8, eabm9844 (2022).

<https://www.science.org/doi/10.1126/sciadv.abm9844>

Rossi, G., Giger, S., Hübscher, T. et al. Gastruloids as in vitro models of embryonic blood development with spatial and temporal resolution. *Sci Rep* 12, 13380 (2022).

<https://doi.org/10.1038/s41598-022-17265-1>

Zhang, Y.S., Haghashtiani, G., Hübscher, T. et al. 3D extrusion bioprinting. *Nat Rev Methods Primers* 1, 75 (2021). <https://doi.org/10.1038/s43586-021-00073-8>

Banterle, N., Nievergelt, A.P., de Buhr, S. et al. Kinetic and structural roles for the surface in guiding SAS-6 self-assembly to direct centriole architecture. *Nat Commun* 12, 6180 (2021).

<https://doi.org/10.1038/s41467-021-26329-1>

Brassard, J.A., Nikolaev, M., Hübscher, T. et al. Recapitulating macro-scale tissue self-organization through organoid bioprinting. *Nat. Mater.* 20, 22–29 (2021).

<https://doi.org/10.1038/s41563-020-00803-5>

Oral and poster presentations

Poster presentation, BaCell 3D – Building Advanced Multicellular Systems in 3D, Basel, Switzerland 2022

Oral presentation, ThymOz International Conference on Thymus and T cell Biology, Heron Island, Australia 2022

Professional experience

Laboratory technician 2017-2018
Gönczy Lab - Cell and Developmental Biology, Prof. Pierre Gönczy

Additional training

Innosuisse Business Concept Training EPFL Innovation Park Consortium, EPFL, Lausanne	2021
Advanced Technical Presentation Damian Conway, Online	2021
Statistic 4 – Experimental design Dr. Frédéric Schütz, UNIL, Lausanne	2021
Statistic 2 – "Statistics in practice: a refresher" Dr. Marc-Olivier Boldi, UNIL, Lausanne	2020
From Blank Page to Manuscript Draft – Manuscript Writing Workshop Dr. Kaycie Butler, Online	2020
Introductory Course in Laboratory Animal Science (Module 1), Dr. Fabienne Chabaud, UNIL, Lausanne	2019